U.PORTO
FEUP FACULDADE DE ENGENHARIA
UNIVERSIDADE DO PORTO

Methodology for Analysis of Open and Filled Holes in Aircraft Composite Laminate Structures

Gabriel Soares

Supervisor
Prof. Dr. Carolina Silva
Dr. Pedro Albuquerque
Jorge Trigo

Master's in Mechanical Engineering
Faculdade de Engenharia
Universidade do Porto

"In flying, the probability of survival
is inversely proportional to the angle of arrival".

Neil Armstrong

Abstract

The incorporation of composite materials in commercial aircraft structures, exemplified by the Boeing 787 Dreamliner and Airbus A350 XWB, has created a demand for efficient and reliable methods to design structures using anisotropic materials. While composites offer significant weight reduction, fuel efficiency, and improved performance, they pose significant challenges in stress and failure analysis, particularly in regions with stress concentrations such as open and filled holes. These features are critical in aerospace structures, where they are used for cable passages, antennas, and fastened joints.

This thesis introduces a tool using analytical methods for fast and accurate stress and failure analysis of open and filled hole configurations in composite laminates, reducing preprocessing effort and reducing the need for detailed local numerical models to capture stress concentrations. Infinite-domain problems are solved using Lekhnitskii's complex potential formalism, which is extended to finite-width plates through auxiliary functions and potentials that enforce boundary conditions, following the approach of Nguyen-Hoang and Becker. The framework is further expanded to address biaxial loading in finite plates. To ensure compatibility with industrial workflows, the tool integrates a load-extraction procedure from finite element results and employs the conservative First Ply Failure criterion for laminate failure prediction.

The tool was systematically verified and validated against finite element simulations to ensure its correct application and to define the limits of its applicability. The resulting framework provides an efficient means of supporting preliminary structural design in aerospace applications, enabling reliable assessment of stress concentrations and failure in composite open and filled hole configurations, while remaining adaptable to industry needs.

Keywords: Composite laminates; open hole; filled hole; stress concentrations; finite-width plates; Lekhnitskii complex potentials; biaxial loading; first ply failure.

Resumo

A incorporação de materiais compósitos em estruturas de aeronaves comerciais, exemplificada pelo Boeing 787 Dreamliner e pelo Airbus A350 XWB, criou a necessidade de métodos eficientes e fiáveis para o dimensionamento de estruturas com materiais anisotrópicos. Embora os compósitos ofereçam reduções significativas de peso, maior eficiência no consumo de combustível e melhor desempenho, colocam desafios relevantes na análise de tensões e de falhas, sobretudo em regiões com concentrações de tensão, como furos abertos e furos preenchidos. Estas características são críticas em estruturas aeroespaciais, onde são utilizadas para passagens de cabos, antenas e ligações aparafusadas.

Esta tese apresenta uma ferramenta com base em métodos analítics para uma análise rápida e precisa de tensões e falhas em configurações de furos abertos e preenchidos em laminados compósitos, reduzindo o esforço de pré-processamento e diminuindo a necessidade de recorrer a modelos numéricos locais detalhados para captar concentrações de tensão. Problemas em domínios infinitos são resolvidos utilizando o formalismo do potencial complexo de Lekhnitskii, que é estendido a placas de largura finita através de funções e potenciais auxiliares que impõem as condições de fronteira, seguindo a abordagem de Nguyen-Hoang e Becker. O enquadramento é ainda expandido para considerar carregamentos biaxiais em placas finitas. Para garantir compatibilidade com fluxos de trabalho industriais, a ferramenta integra um procedimento de extração de cargas a partir de resultados de elementos finitos e emprega o critério conservador de First Ply Failure para previsão de falha do laminado.

A ferramenta foi sistematicamente verificada e validada contra simulações de elementos finitos, assegurando a sua correta aplicação e definindo os limites da sua aplicabilidade. O enquadramento resultante fornece um meio eficiente de apoio ao projeto estrutural preliminar em aplicações aeroespaciais, permitindo uma avaliação fiável das concentrações de tensão e da falha em configurações de furos abertos e preenchidos em compósitos, mantendo-se adaptável às necessidades da indústria.

Acknowledgements

First, I would like to thank Prof. Dr. Carolina Silva and Dr. Pedro Albuquerque for making possible this collaboration between FEUP and Jet Aviation Madrid, I am sincerely grateful for the opportunity.

I would like to thank Prof. Dr. Carolina Silva for her invaluable guidance throughout the thesis, for her constant availability to provide support, and for her dedication to ensuring the quality and clarity of this work.

I thank Dr. Pedro for all the support he provided during the development of my thesis at Jet Aviation in Madrid. He assumed the role of a mentor, serving as a valuable role model for my future career.

I thank Jorge Trigo, who guided me through coding challenges and helped me develop a stronger understanding of finite element analysis and programming logic. I also wish to thank the entire team at Jet Aviation for their constant availability and support throughout my thesis.

A special thanks to all my friends in Porto and Viseu, whose support made these five years truly special. I am especially grateful to Ruben, my collaborator on numerous university projects, and to Madalena for her assistance in preparing the figures, and all support throughout the year.

Finally, I would like to thank my family. My father, for teaching me the value of hard work. My sister, who has been a role model, a teacher, and a friend. And finally, my mother, to whom I am most grateful, whose strength is my greatest inspiration in life.

Contents

List of Figures

List of Tables

Nomenclature

Abbreviations

2D	two-dimensional
3D	three-dimensional
API	Application Programming Interface
BC	Boundary Condition
CBUSH	1D bushing element (*Femap Nastran*)
CFRP	Carbon Fibre Reinforced Polymer
CLT	Classical Laminate Theory
CPS8	Continuum Plane Stress element with 8 nodes (*Abaqus*)
CQUAD4	4-node quadrilateral shell element (*Femap Nastran*)
DOF	Degree of Freedom
FE	Finite Element
FPF	First Ply Failure
MS	Margin of Safety
MPC	Multi-Point Constraint
SCF	Stress Concentration Factor
SDG	Sustainable Development Goals
RBE3	Rigid Body Element, type 3 (*Femap Nastran*)
S8R	8-node shell element with reduced integration (*Abaqus*)
XWB	Extra Wide Body

Indices and notations

$\mathrm{Average}\,(\Box)$	average operator
$\min(\Box)$	minimum operator
$\mathrm{PA}(\Box)$	operator for periodic arrangement
$\hat{\Box}$	amplitude
$\Box'$	derivative with respect to complex variable
$\widetilde{\Box}$	field quantity produced by unit remote load
$\Box_0$	remote or far field

Nomenclature

$\square_f$	fastener
$\square_{\mathrm{Bea}}$	bearing
$\square_{\mathrm{By}}$	bypass
$\square_d$	diameter
$\square_{\mathrm{s}}$	symmetric
$\square^{\perp}$	perpendicular
$\square^{\mathrm{dev}}$	deviation
$\square^{\mathrm{FH}}$	filled hole
$\square_{\mathrm{Fo}}$	Fourier series
$\square^{\mathrm{HBC}}$	hole boundary conditions
$\square^{\mathrm{HE}}$	horizontal edges
$\square^{\mathrm{inf}}$	infinite
$\square^{\mathrm{mv}}$	multivalued
$\square^{\mathrm{OH}}$	open hole
$\square^{\mathrm{sv}}$	single-valued
$\square^{\mathrm{VE}}$	vertical edges

Symbols

$\mathbf{A}$, A_{ij}	matrix of extensional stiffnesses and its components
b	experimental fitting parameter involved in the R-curve
d	hole and fastener diameter
e	end distance
E, $\hat{E}$	Young's modulus; effective Young's modulus
f, g	Fourier-series coefficients
F	Airy stress function
G, $\hat{G}$	shear modulus; effective shear modulus
h_s	coefficient characterising angle-ply laminates
K_{t0}	stress concentration factor with remote stress as reference value
l_{F0}	wavelength of Fourier-series expansion
l	iteration step
L	number of iterations
n_x, n_y	number of horizontal and vertical auxiliary plates
$\mathbf{n}$	normal vector
N	number of terms
N_x, N_y, N_{xy}	normal stress resultants
p_x, p_y	loading functions

P	force; load
Q_{ij}	reduced stiffnesses with respect to the local coordinate system
$\bar{Q}_{ij}$	reduced stiffnesses with respect to the global coordinate system of the laminate
r	radial coordinate
R	hole and fastener radius
s	coefficient in governing equations for an orthotropic plate
s, $\tilde{s}$	arc-length parameter
S_{ij}	components of compliance tensor stored in matrix form
t	thickness
t_s	coefficient characterising angle-ply laminates
$\mathbf{u}$, u_i	displacement vector and its components
w	width
x, y, z	spatial coordinates
X_n, Y_n	components of external force

Greek symbols

α, β	complex coefficients of Fourier-series expansions of loading functions
α	ratio of bypass load perpendicular to the material axes to the sum of bypass loads in longitudinal and transverse directions
β	load factor; ratio of bearing to total load
γ	engineering shear strain
ε	strain
$\boldsymbol{\varepsilon}$	linearised strain tensor
ζ	mapping function
$\boldsymbol{\kappa}$	plate-curvature vector
μ	complex constant
ν, $\hat{\nu}$	Poisson's ratio; effective Poisson's ratio
ξ	relative or dimensionless coordinate
$\Delta\xi$	relative or dimensionless crack length
ϱ	hyperbolic function
σ, $\bar{\sigma}$	normal stress; average normal stress
$\boldsymbol{\sigma}$, σ_{ij}	Cauchy stress tensor and its components
τ	shear stress
φ	circumferential coordinate
ϕ	hyperbolic function involved in the Airy stress function
Φ	complex potential
χ	convergence criterion for load transfer
ψ	convergence criterion for free edge

1. Introduction

1.1 Motivation and Background

The aerospace industry is among the most competitive in the world, driving a continuous pursuit of performance and efficiency improvements in aircraft design. One of the key strategies for achieving these goals has been adopting lighter materials, particularly advanced composite materials. The Boeing 787 Dreamliner was the first large commercial airplane in the world to use composite materials as the primary material in its structure and is Boeing's most fuel-efficient airplane. In response to the Boeing 787 Dreamliner, Airbus created the A350 XWB also in composites. This new generation of aircraft features more than 50% of the structural weight in carbon fibre reinforced polymer (CFRP) [1]. The use of this type of material results in greater fuel efficiency due to the aircraft's lower weight, and as a consequence pollutant emissions are lower and noise is reduced. There is also an increase in passenger comfort and a decrease in the need for maintenance [2]. One major drawback of using composite materials is the increased complexity in their design, as, unlike isotropic materials, whose properties remain the same in all directions, composite materials are, in most cases, anisotropic, and therefore their mechanical properties vary depending on the direction of the applied load. Hence, significant changes in design models have been necessary [3]. Aiming to work with composite airplanes, Jet Aviation, a company specializing in modifications of large aircraft, primarily for Airbus and Boeing, proposed this thesis, focusing on the structural design process for composite materials. Jet Aviation is a global leader in business aviation services, providing aircraft management, maintenance, modifications, charter, and staffing at more than 50 locations worldwide, with a workforce of over 4000 employees. This work was carried out at the company's engineering office, in Madrid, within the Structural Analysis Department.

In the context of this thesis, particular attention is given to improving the modeling of stress concentration zones near holes. Both open and filled hole configurations will be examined to accurately represent such features in plates and joints. In aircraft design, open holes are commonly used, for example, to accommodate antennas or to allow electrical cables to pass through sections of the airframe. Additionally, fastened joints are a widely used method for connecting thin plate structures, being widely used due to their ease of manufacturing and structural reliability. This thesis aims to develop a tool capable of delivering fast and accurate stress analyses of open and filled holes in composite laminates used in aircraft structures. The tool is intended for use in the preliminary design phase, helping to reduce the number of finite element (FE) simulations needed during the early stages of development and minimizing the meshing effort needed around stress concentration zones, which also enables the creation of lighter models with reduced preprocessing requirements. Since we are looking for simplicity, efficiency, and accuracy, the tool will be constructed using analytical methods.

The tool is designed for global models with multiple holes, which may be either filled or open, but it does not treat the model as a single global problem domain that encompasses all holes. Instead, each hole and its surrounding region of the plate is modeled as a two-dimensional individual plane stress boundary value problem, dividing it into multiple simpler problems with specified bearing and bypass loads applied as inputs. These inputs are obtained by direct extraction of bypass and bearing loads from FE results. In large scale models, fasteners are typically represented using multi-point constraints (MPC), without explicitly modeling either the fastener or the corresponding hole. Moreover, when holes are included, the mesh is generally not refined in order to reduce model complexity and minimize preprocessing efforts. Thus, stress concentrations are not accurately captured; however, bypass and bearing loads can still be determined with high accuracy, enabling the analysis of stress concentration zones without the need for detailed modeling. The methodology developed in this thesis can only analyse the regions of the global model within the following configurations: uniaxial and biaxial open hole under in-plane normal loadings; filled hole problem under in-plane loading, with both pure bearing and bearing-bypass loading. Holes that fall outside the model's capabilities should be analysed numerically using a localised model.

When holes lie close to a plate edge, the stress field around the hole is modified by free-edge effects. Most analytical solutions for composite materials assume an infinite plate and thus neglect proximity to boundaries. However, in practical finite plates, nearby edges perturb the stress distribution and can significantly change local stress concentrations around the hole, in this case, we have to solve a finite-domain problem. For example, a common approach for narrow plates, relies on heuristic methods, which, although yielding good results for the open hole problem [4–7], are accurate more by coincidence than by physical justification. Consequently, their applicability to other scenarios cannot be reliably established. Nguyen-Hoang and Becker [8, 9], developed an analytical approach to the problem that intends to satisfy the boundary conditions at selected discrete points or in average along a predefined section, by incorporating auxiliary functions and potentials to the infinite-domain solution.

Being proposed by an aerospace-related company, it is important that the tool can be adapted to the company's capabilities and integrated with its existing design practices. Consequently, this thesis presents a novel approach tailored to industry needs, which builds upon the state-of-the-art analytical finite-width solution for stress field computation developed by Nguyen-Hoang and Becker [8, 9], while employing Lekhnitskii's [10] formalism to address the infinite-domain problem. Moreover, to the best of the author's knowledge, no study has yet addressed the biaxial loading case by superposing Nguyen-Hoang and Becker's [9] solution for the open hole uniaxial finite-width problem. Additionally, the extraction of bypass and bearing loads was carried out in accordance with the company's FE modeling guidelines. Furthermore, a key requirement from the company was that the tool should conservatively predict failure. Thus, First Ply Failure (FPF) was employed, meaning the failure of a single ply implies the failure of the entire laminate. This philosophy, under the assumptions made, also offers a straightforward and accurate way to determine failure using simple analytical formulae.

Finally, this thesis supports the United Nations Sustainable Development Goals, especially SDGs 9, 12, and 13. It delivers a practical method to analyse open and filled holes in composite laminates for preliminary design, encouraging the wider use of composite materials by making their assessment faster. By shortening design loops and improving confidence in joint sizing, the approach enables lighter aircraft and lower lifecycle CO_2 emissions (SDG 13). Conservative First Ply Failure checks keep the methodology safe and serviceable (SDG 12). The tool follows existing industrial guidelines, easing adoption in real programmes and strengthening innovation capacity in aerospace engineering (SDG 9). The workflow supports repair-over-replacement practices and better resource use (SDG 12), and builds collaboration and knowledge transfer with industry and academia (SDGs 17 and 4).

1.2 Objectives

The objectives of this thesis are:

- implementation and validation of analytical solutions to predict the stress field in open and filled holes in composite infinite and finite plates;
- implementation and validation of first ply failure criteria;
- implementation and validation of a load extraction methodology;
- development of a tool aligned with the industry design practices and definition

of its range of applicability.

1.3 Outline

In Equation 2.2.3.3, the theoretical framework of this thesis will be briefly covered. Starting by the fundamentals of the Theory of Elasticity, focusing on plane problems. Following, the Classical Laminate Theory is introduced as a core concept for laminate level analysis. Furthermore, the solution for the generalized plane stress problem in a homogeneous anisotropic plate is described, detailing the complex potential method in the formalism by Lekhnitskii [10].

In Figure 3.2 the mechanical idealisation is presented, reducing the real scenario to a simplified model suitable for analysis, adopting a linear 2D plane stress approach. Subsequently, the FE methodology employed throughout the thesis is defined, serving for verification, validation, and assessment of the limitations of the analytical model. A mesh convergence study is carried out in order to establish a generalised meshing methodology that can be applied to the different geometries considered in this work.

In section 4.6 the development of the stress calculus based on the complex potential methods was formulated, following Lekhnitskii's [10] formalism to solve the infinite-domain open and filled hole problems. Furthermore, the finite-dimension problem is addressed for the filled and open hole problems, following the approach of Nguyen-Hoang and Becker [11–14], which enforces the plate's boundary conditions by incorporating auxiliary functions and potentials to the infinite-domain solution. Both formulations were then verified, and their limitations assessed. The finite-domain solution was then expanded to the biaxial loading case, which was again validated against FE results. At last, the finite filled hole problem under bearing-bypass load is solved by superposition of the open and filled hole problems.

Failure assessment is carried out in Equation 5.2.4, where First Ply Failure is employed and validated against FE results. This approach is chosen for its high level of conservatism and its suitability for analytical implementation within the developed tool.

In Table 6.3, a methodology for extracting bearing and bypass loads from FE results is presented. The chapter first introduces the joint representation adopted by the company for which the tool was developed. Subsequently, the load extraction methodology is described, based on defining an extraction area determined by the relative position of the hole to the plate edges and to adjacent holes. Finally, the methodology is tested and its results analysed.

In section 7.4 a schematics of the tool workflow is presented, along with its main assumptions and a summary of the tool's range of applicability. Finally, we present an example of application of the tool and conclude with an overview of the tool's overall performance.

Lastly, section 8.2 provides a summary and outlook of the thesis, highlighting its gaps and proposing directions for future work.

2. Literature Review

This chapter starts by presenting an overview of the literature regarding analytical methods for the stress analysis of open and filled holes. It then provides a mathematical background of the essential concepts for computing the stress field in orthotropic homogeneous composite plates under plane stress, laying the foundation for the open and filled hole solutions presented in detail in section 4.6.

2.1 Overview

An overview of the existing methods for computation of the stresses in open and filled holes is reviewed in this Section, with a focus on analytical approaches.

The stress analysis of open and filled holes varies in complexity depending on factors such as material orthotropy, finite plate dimensions, the shape of the hole, and loading conditions.

2.1.1 Open Hole

Concerning the open hole problem, the stress field of an isotropic, infinite plate with a central circular opening under uniform tension was analysed by Kirsch [15] using the Airy stress function; the analytical solution can be found in references [16–18]. Inglis [19] derived the stress concentration around an elliptical hole in an infinite plate subjected to remote loading. The strain energy of a cracked body was calculated by deriving the stress field for an infinite plate with a through-thickness central crack under biaxial loading, using Inglis's solution [19]. Westergaard [20] developed a new solution for the stress field around a crack by deriving an Airy stress function using complex numbers, which describes the stress field in an infinite plate containing a crack. Westergaard's solution presents improvement upon Inglis's approach by presenting a formulation that applies directly to cracks, rather than to an ellipse that approximates a crack in the limiting case. Irwin [21] was the first to introduce the concept of the stress intensity factor (SIF), which describes the stress state at the crack tip, is related to the rate of crack growth, and is used to establish fracture failure criteria. Irwin's solution defined a near-crack-tip approximation to

Westergaard's complete solution for the stress field around a crack, significantly simplifying Westergaard's result in the region immediately surrounding the crack tip. The complex potentials formulation for the stress functions was initially introduced by Kolosov [22] and later formalized by Muskhelishvili [23], becoming known as the Kolosov-Muskhelishvili formalism. One limitation of this formulation is its restriction to linear elasticity; to address this, Szachter et al. [24] proposed a nonlinear extension to the Kolosov-Muskhelishvili formalism. Savin [25] analysed the stress concentration around elliptical holes in an infinite, isotropic plate under various loading conditions using the complex potential formulation. Similarly, Lekhnitskii [10] applied the complex potentials formulation to solve problems related to infinite homogeneous anisotropic plates, including stress distribution in plates with elliptical or circular openings, both unfilled and filled with rigid or elastic materials of varying properties under different loading conditions. Lekhnitskii's solutions can only be applied for solving stress concentration problems in symmetric laminates; Becker [26] extended this to unsymmetrical laminates by developing a complex potential method for plate problems with bending-extension coupling in an infinite anisotropic plate. Ukadgaonker and Rao [27, 28] presented a general solution for hole problems in unsymmetrical laminates based on Becker's complex potential method. Their approach accommodates any shape of hole, considers arbitrarily oriented uniaxial, biaxial, and shear stresses at infinity, as well as uniform tangential force and uniform pressure around the hole, and is applicable to various laminate geometries, being extended to multilayered plates.

2.1.2 Filled Hole

Regarding filled hole, existing solutions can be classified into two main approaches, those that employ a detailed bolt-plate contact model, and those that idealise the bolt interaction by prescribing a predefined stress distribution along a portion of the hole boundary. In the latter case, a sinusoidal distribution of radial tractions is commonly assumed, this was studied by Waszczak and Cruse [29]. For modeling the bolt contact, there are studies addressing conformal contact problems, this area focuses on contact between bodies where the contact area is relatively large compared to the radius of curvature, making the half-plane assumption invalid [30]. Therefore, Hertzian contact theory should not be employed [31]. The study of frictionless conformal contacts was first initiated by Persson [32]. A more comprehensive overview of developments in this field can be found in the literature surveys by Gladwell [33], and Ciavarella et al. [34]. Additionally, still regarding frictionless contact, To et al. [35] covers a finite pin-loaded plate with a reinforced hole. A particularly relevant set of contributions on conformal contacts with friction is given by Sundaram and Farris [30, 36], who developed general solutions for rigid and elastic pins under complex loading conditions. Depending on the application, additional insights can be drawn from Ho and Chau [37], who considered an infinite plate loaded by a rivet of different materials and Hou and Hills [37], who addressed interference fits, where the fastener is slightly larger than the hole and clearance fit, where the pin is slightly smaller than the hole. A number of studies have applied complex potential methods within Lekhnitskii's [10] formalism to model orthotropic plates with bolted joints. Zhang and Ueng [38, 39] addressed friction and arbitrary load directions in infinite plates, while Hyer and Klang [40, 41] considered additional effects such as bolt elasticity and clearance. An important observation in the context of conforming contacts is that, under frictionless conditions and perfect bolt-hole fit, the contact area initially decreases with increasing load but eventually stabilizes. Dundurs and Stippes [42] considered this behavior as receding contact. In this regime, field quantities scale linearly with the external load. Similar trends have been observed in the presence of friction by Ciavarella et al. [34]. These findings justify the use of linear models for bolted-joint problems, and particularly support the widespread adoption of the sinusoidal load idealisation introduced by Waszczak and Cruse [29], which greatly simplifies the development of analytical solutions. Catalanotti and Camanho [43] as well as Nguyen-Hoang and Becker [12], derive failure loads based on this linear sinusoidal idealisation and demonstrate good agreement with experimental data. Therefore, the assumptions and idealisations, including those related to bolt contact, can be considered valid for the quasi-isotropic cases examined in the referenced studies.

2.1.3 Finite-Domain Solutions

For finite-width problems, Tan's approach [5, 7] uses a heuristic method with correction factors to scale the infinite solution for an ellipse under uniform tension by Lekhnitskii [10], ensuring the integrated stresses along the width of the finite plate equilibrate the external load. This is further refined by adapting the stresses to Heywood's formula [44] from photoelasticity, yielding good correlation for stress concentrations and their decay in the hole vicinity [6]. However, Nguyen-Hoang and Becker demonstrated that the heuristic approach yields erroneous results for single-fastener bolted joints, both in isotropic [12, 13] and orthotropic [8] plate materials, as well as for open hole configurations with finite dimensions [11], particularly when assessing stresses along the entire net-section plane. Additionally, Tan's scaling method is based on practical experience rather than a strict theoretical foundation, assuming stress decay in a finite plate is similar to that in an infinite plate, therefore; it is not applicable to other problems.

Calculi that account for finite plate dimensions in bolted joints typically assume frictionless bolt contact rendered as sinusoidal radial hole tractions. For isotropic plates, Bickley [45] addressed the infinite domain with Airy stress functions and Knight [46] capture finite width, without considering finite end distance, also using Airy stress functions. For orthotropic plates, following Lekhnitskii's [10] complex potentials, de Jong [47] treated the infinite plate and de Jong and Vuil [48] extended the formulation to arbitrary load directions. Berbinau and Soutis developed a general mixed-boundary methodology for partially loaded holes [49]. To account for finite plate dimensions, de Jong [50] proposed correction factors that heuristically adjust the infinite-domain solution so that its uniform remote stresses equilibrate the applied load across the actual plate width. The method, however, fails to satisfy stress-free boundary conditions at the edges parallel to the loading, making it reliable primarily in cases where finite-width effects remain small, as the case of wider width-to-hole diameter ratios. Echavarría et al. [51], in orther to reduce computational cost, truncated the stress series representation and validated against de Jong [50]. However, direct comparison to the actual boundary-value problem and edge-decay behavior is missing, an important limitation for nonlocal failure analyses.

Regarding works fulfilling the boundary conditions of the finite-domain problem, Ogonowski [52] employed the boundary collocation technique combined with a complex variable method to analyse the stress distribution in anisotropic plates with finite geometry and stress concentrations under arbitrary loadings. This study, conducted in a doubly connected anisotropic region, demonstrated results consistent with the stress concentration factors reported by Pilkey [53] for a quasi-isotropic laminate within the width-to-diameter ratio range $2 \leq w/d \leq 12$ and regarding the circumferential stresses for a $[0^\circ_5\,/\,(\pm 45^\circ)_2\,/\,90^\circ]_\mathrm{s}$ laminate with a value of $w/d = 8$ with FE values. Hufenbach and Kroll [54] presented a solution for stress concentration in anisotropic plates under mechanical and hygrothermal loading, using complex stress functions in combination with conformal mapping, showing strong agreement with FE results for $w/d = 4$ in unbalanced laminates of $[30^0]$ and $[60^0]$. Hufenbach et al. [55] presented a solution method for stress concentration in fibre- and textile-reinforced multilayered composites, considering circular or elliptical cut-outs and finite outer boundaries, using complex-valued displacement functions, conformal mappings, boundary collocation, and least squares methods, obtaining good agreement with experimentally determined strains for $w/d = \{2, 5\}$. Moreover, Hufenbach et al. [56] also consider non-constant tractions along the straight boundaries with an arbitrarily oriented elliptical hole drilled in the plate. For the case of uniform tension, they present accurate results for an elliptical hole with geometric ratios $w/(2a) = 1.67$ and $b/a = 3$, where a represents the major semi-axis and b the minor semi-axis. Nguyen-Hoang and Becker [11] presented a solution to the finite-domain problem for isotropic materials using Airy stress function, taking the stress field of corresponding infinite-domain problem and supplementing it with auxiliary functions enabling to continuously model traction-free edges. Later, they extended this methodology using the complex potential method to represent the stress state for orthotropic laminates [9], presenting excellent agreement to FE analysis. For bolted-joints problems, Kratochvil and Becker [57] approximated the rectangular plate geometry as an ellipse, revealing good correlation to FE calculations in the circumferential stresses for $[\pm 45°]$ laminates with $w/d = 3$, as well as $[0°/90°]_s$ laminates with $w/d = 5$. Grüber et al. [58] treat bending extension coupling showing good agreement with FE analyses for $w/d = \{15, 45\}$, an aspect ratio range with slight or even negligible finite-width effects. This approach is extended to multi-layered composite bolted joints with interference fit subjected to thermal loading [59]. An approach for the computation of the stress field in finite-dimension bolted joints with isotropic plates using Airy stress function is presented by Nguyen-Hoang and Becker [13]. The solution is obtained by taking the infinite-domain stress field and applying auxiliary functions that ensure traction-free edges are satisfied continuously, they later expanded the solution for for orthotropic laminates by using the complex potential method [8]. Nguyen-Hoang and Becker [14] analysed the bolted joint under combined bearing–bypass loading in composite laminates by superimposing the open hole and filled hole problems, and concluded that the filled hole case represents the most critical condition.

2.1.4 Final Remarks

In this thesis, the infinite-domain problems for open and filled holes are addressed using Lekhnitskii's [10] complex potential formalism. Then, Nguyen-Hoang and Becker's finite-domain solution is employed to address the open hole problem in composite laminates under uniaxial loading [9], as well as the filled hole problem in composite laminates [8].

2.2 Mathematical Background

This section outlines the theoretical foundations used to compute stress fields in orthotropic homogeneous plates under plane stress conditions. It begins with the fundamental equations of elasticity, including equilibrium conditions, strain–displacement relations, and the constitutive behavior of anisotropic materials. Next, Classical Laminate Theory (CLT) is introduced to enable laminate-level analysis of multi-layered composites. The formulation is then reduced to two dimensions, enabling the use of the Airy stress function in conjunction with complex potentials to obtain the stress and displacement fields of an orthotropic homogeneous plate under plane stress.

2.2.1 Basic Equations of Theory of Elasticity of an Anisotropic Body

This subsection presents the governing equations of anisotropic elasticity, following reference [60].

For a body described in Cartesian coordinates, the equilibrium equations are expressed in terms of the stress components σ_x, σ_y, σ_z (normal stresses) and τ_{xy}, τ_{yz}, τ_{xz} (shear stresses). These equations take the form:

$$\begin{aligned} \frac{\partial \sigma_x}{\partial x} + \frac{\partial \tau_{xy}}{\partial y} + \frac{\partial \tau_{xz}}{\partial z} + X = 0, \\ \frac{\partial \tau_{xy}}{\partial x} + \frac{\partial \sigma_y}{\partial y} + \frac{\partial \tau_{yz}}{\partial z} + Y = 0, \\ \frac{\partial \tau_{xz}}{\partial x} + \frac{\partial \tau_{yz}}{\partial y} + \frac{\partial \sigma_z}{\partial z} + Z = 0. \end{aligned} \tag{2.1}$$

In cylindrical coordinates, the stress components in this system include σ_r, σ_θ, σ_z (normal stresses), and $\tau_{r\theta}$, $\tau_{\theta z}$, τ_{rz} (shear stresses). The corresponding equilibrium equations are:

$$\begin{aligned} \frac{\partial \sigma_r}{\partial r} + \frac{1}{r}\frac{\partial \tau_{r\theta}}{\partial \theta} + \frac{\partial \tau_{rz}}{\partial z} + \frac{\sigma_r - \sigma_\theta}{r} + R = 0, \\ \frac{\partial \tau_{r\theta}}{\partial r} + \frac{1}{r}\frac{\partial \sigma_\theta}{\partial \theta} + \frac{\partial \tau_{\theta z}}{\partial z} + \frac{2\tau_{r\theta}}{r} + \Theta = 0, \\ \frac{\partial \tau_{rz}}{\partial r} + \frac{1}{r}\frac{\partial \tau_{\theta z}}{\partial \theta} + \frac{\partial \sigma_z}{\partial z} + \frac{\tau_{rz}}{r} + Z = 0. \end{aligned} \tag{2.2}$$

where X, Y, Z and R, Θ, Z are the body forces referred to a unit volume in directions x, y, z and r, θ, z.

For small deformations, the strain components can be directly related to the displacement field. These relations are essential for coupling the equilibrium equations with the constitutive behavior of the material. Let (u, v, w) be the displacement components in the x, y, and z directions. The strain–displacement relations are given by:

$$\begin{aligned} \varepsilon_x &= \frac{\partial u}{\partial x}, & \gamma_{yz} &= \frac{\partial v}{\partial z} + \frac{\partial w}{\partial y}, \\ \varepsilon_y &= \frac{\partial v}{\partial y}, & \gamma_{xz} &= \frac{\partial w}{\partial x} + \frac{\partial u}{\partial z}, \\ \varepsilon_z &= \frac{\partial w}{\partial z}, & \gamma_{xy} &= \frac{\partial u}{\partial y} + \frac{\partial v}{\partial x}. \end{aligned} \tag{2.3}$$

For the displacement components (u_r, u_θ, u_z) in the radial, circumferential, and axial directions, the strain–displacement relations are expressed as:

$$
\begin{aligned}
\varepsilon_r &= \frac{\partial u_r}{\partial r}, & \gamma_{\theta z} &= \frac{\partial u_\theta}{\partial z} + \frac{1}{r}\frac{\partial u_z}{\partial \theta}, \\
\varepsilon_\theta &= \frac{1}{r}\frac{\partial u_\theta}{\partial \theta} + \frac{u_r}{r}, & \gamma_{rz} &= \frac{\partial u_z}{\partial r} + \frac{\partial u_r}{\partial z}, \\
\varepsilon_z &= \frac{\partial u_z}{\partial z}, & \gamma_{r\theta} &= \frac{1}{r}\frac{\partial u_r}{\partial \theta} + \frac{\partial u_\theta}{\partial r} - \frac{u_\theta}{r}.
\end{aligned}
\tag{2.4}
$$

These expressions are valid for both elastic and inelastic continuous bodies and form the fundamental basis for formulating boundary value problems in solid mechanics.

Based on the generalized Hooke's law, the strain–stress relationships for a generally anisotropic, linearly elastic material expressed in the global cartesian coordinate system are given by:

$$
\begin{bmatrix} \varepsilon_x \\ \varepsilon_y \\ \varepsilon_z \\ \gamma_{xy} \\ \gamma_{yz} \\ \gamma_{xz} \end{bmatrix}
=
\begin{bmatrix}
S_{11} & S_{12} & S_{13} & S_{14} & S_{15} & S_{16} \\
S_{12} & S_{22} & S_{23} & S_{24} & S_{25} & S_{26} \\
S_{13} & S_{23} & S_{33} & S_{34} & S_{35} & S_{36} \\
S_{14} & S_{24} & S_{34} & S_{44} & S_{45} & S_{46} \\
S_{15} & S_{25} & S_{35} & S_{45} & S_{55} & S_{56} \\
S_{16} & S_{26} & S_{36} & S_{46} & S_{56} & S_{66}
\end{bmatrix}
\begin{bmatrix} \sigma_x \\ \sigma_y \\ \sigma_z \\ \tau_{xy} \\ \tau_{yz} \\ \tau_{xz} \end{bmatrix}
\tag{2.5}
$$

In this formulation, the coefficients S_{ij} represent the components of the compliance matrix, which defines the linear elastic response of the material. For a fully anisotropic material, the compliance matrix contains 21 independent constants.

2.2.2 Classical Laminate Theory for Orthotropic Laminates

Classical Laminate Theory (CLT) provides a framework to evaluate the overall behavior of laminated composite structures, facilitating the transition from the properties of a single lamina to the response of a multilayered laminate. The information presented in this Subsection is based on references [61, 62].

In this review, each lamina is assumed to be a linearly elastic orthotropic material, meaning that the mechanical properties vary along three mutually orthogonal directions, which are typically aligned with the fibre direction, the in-plane transverse direction, and the thickness direction.

For laminate composites, it is useful to define two coordinate systems, the first is the local material coordinate system associated with each individual lamina, referred to as the 1–2–3 system. In this system, the 1-axis aligns with the fibre direction, the 2-axis lies within the plane of the lamina and is perpendicular to the fibers, and the 3-axis is normal to the lamina plane.

The second is the global coordinate system, typically denoted by the Cartesian axes x–y–z, which describes the overall orientation of the laminate structure. When a lamina is not aligned with the global axes, its stiffness contributions must be transformed accordingly. In such cases, the resulting laminate stiffness matrix can include nonzero bending–extension coupling terms due to misalignment between the local and global axes.

2.2.2.1 Transformation of Local Lamina Properties to the Global Coordinate System

The lamina's compliance and stiffness matrices, denoted by $\boldsymbol{S}$ and $\boldsymbol{Q}$, respectively, characterize the mechanical response of an individual ply when loads and strains are expressed in the local material coordinate system. However, when a lamina is oriented at an arbitrary angle θ, these matrices must be transformed to the global coordinate system for laminate-level analysis.

To transform the compliance $\boldsymbol{S}$ and stiffness $\boldsymbol{Q}$ matrices from the local 1-2 material axes to the global x-y coordinate system using engineering strain notation, the transformation matrices for stress and strain are defined as:

$$\boldsymbol{T}_\sigma = \begin{bmatrix} \cos^2\theta & \sin^2\theta & 2\sin\theta\cos\theta \\ \sin^2\theta & \cos^2\theta & -2\sin\theta\cos\theta \\ -\sin\theta\cos\theta & \sin\theta\cos\theta & \cos^2\theta - \sin^2\theta \end{bmatrix}, \tag{2.6}$$

$$\boldsymbol{T}_\varepsilon = \begin{bmatrix} \cos^2\theta & \sin^2\theta & \sin\theta\cos\theta \\ \sin^2\theta & \cos^2\theta & -\sin\theta\cos\theta \\ -2\sin\theta\cos\theta & 2\sin\theta\cos\theta & \cos^2\theta - \sin^2\theta \end{bmatrix}. \tag{2.7}$$

The transformed compliance and stiffness matrices in the global coordinate system are obtained using engineering strain notation, where the shear strain component is defined as $\gamma_{xy} = 2\varepsilon_{xy}$. Due to this, the strain and stress transform differently, and the transformation requires distinct matrices $\boldsymbol{T}_\varepsilon$ and $\boldsymbol{T}_\sigma$. Using these, the transformed compliance and stiffness matrices in the global coordinate system are obtained as:

$$\bar{\boldsymbol{S}} = \boldsymbol{T}_\varepsilon^{-1}\,\boldsymbol{S}\,\boldsymbol{T}_\sigma, \qquad \bar{\boldsymbol{Q}} = \boldsymbol{T}_\sigma^{-1}\,\boldsymbol{Q}\,\boldsymbol{T}_\varepsilon \tag{2.8}$$

The resulting transformed compliance matrix $\bar{\boldsymbol{S}}$ and the transformed stiffness matrix $\bar{\boldsymbol{Q}}$ are the following:

$$\bar{\boldsymbol{S}} = \begin{bmatrix} \bar{S}_{11} & \bar{S}_{12} & \bar{S}_{16} \\ \bar{S}_{12} & \bar{S}_{22} & \bar{S}_{26} \\ \bar{S}_{16} & \bar{S}_{26} & \bar{S}_{66} \end{bmatrix}, \bar{\boldsymbol{Q}} = \begin{bmatrix} \bar{Q}_{11} & \bar{Q}_{12} & \bar{Q}_{16} \\ \bar{Q}_{12} & \bar{Q}_{22} & \bar{Q}_{26} \\ \bar{Q}_{16} & \bar{Q}_{26} & \bar{Q}_{66} \end{bmatrix}. \tag{2.9}$$

To simplify the evaluation of transformed properties, Tsai and Pagano [63] introduced trigonometric identities to express the stiffness and compliance matrices components in terms of angle-invariant parameters as follows:

$$\begin{aligned}
\bar{Q}_{11} &= U_1 + U_2\cos 2\theta + U_3\cos 4\theta, & \bar{S}_{11} &= V_1 + V_2\cos 2\theta + V_3\cos 4\theta, \\
\bar{Q}_{12} &= \bar{Q}_{21} = U_4 - U_3\cos 4\theta, & \bar{S}_{12} &= \bar{S}_{21} = V_4 - V_3\cos 4\theta, \\
\bar{Q}_{22} &= U_1 - U_2\cos 2\theta + U_3\cos 4\theta, & \bar{S}_{22} &= V_1 - V_2\cos 2\theta + V_3\cos 4\theta, \\
\bar{Q}_{16} &= \frac{1}{2}U_2\sin 2\theta + U_3\sin 4\theta, & \bar{S}_{16} &= V_2\sin 2\theta + 2V_3\sin 4\theta, \\
\bar{Q}_{26} &= \frac{1}{2}U_2\sin 2\theta - U_3\sin 4\theta, & \bar{S}_{26} &= V_2\sin 2\theta - 2V_3\sin 4\theta, \\
\bar{Q}_{66} &= U_5 - U_3\cos 4\theta, & \bar{S}_{66} &= V_5 - 4V_3\cos 4\theta.
\end{aligned} \tag{2.10}$$

with the corresponding invariants defined as:

$$\begin{aligned}
U_1 &= \frac{1}{8}\left(3Q_{11} + 3Q_{22} + 2Q_{12} + 4Q_{66}\right), & V_1 &= \frac{1}{8}\left(3S_{11} + 3S_{22} + 2S_{12} + S_{66}\right), \\
U_2 &= \frac{1}{2}\left(Q_{11} - Q_{22}\right), & V_2 &= \frac{1}{2}\left(S_{11} - S_{22}\right), \\
U_3 &= \frac{1}{8}\left(Q_{11} + Q_{22} - 2Q_{12} - 4Q_{66}\right), & V_3 &= \frac{1}{8}\left(S_{11} + S_{22} - 2S_{12} - S_{66}\right), \\
U_4 &= \frac{1}{8}\left(Q_{11} + Q_{22} + 6Q_{12} - 4Q_{66}\right), & V_4 &= \frac{1}{8}\left(S_{11} + S_{22} + 6S_{12} - S_{66}\right), \\
U_5 &= \frac{1}{2}\left(U_1 - U_4\right), & V_5 &= 2\left(V_1 - V_4\right).
\end{aligned} \tag{2.11}$$

These invariants simplify the computation of the $\bar{\boldsymbol{Q}}$ and $\bar{\boldsymbol{S}}$ matrices.

2.2.2.2 Strain and Stress Variation in a Laminate

The stress–strain relationship for the k$^{\text{th}}$ lamina within a multilayered laminate is defined as:

$$\boldsymbol{\sigma}_{\text{k}} = \bar{\boldsymbol{Q}}_{\text{k}}\,\boldsymbol{\varepsilon}_{\text{k}}, \tag{2.12}$$

From the linear distribution of the strain value in the thickness direction it is taken that the laminate strains are linearly related to the distance from the mid-plane as

$$\boldsymbol{\varepsilon}(z) = \boldsymbol{\varepsilon}^0 + z\,\boldsymbol{\kappa} \tag{2.13}$$

where $\boldsymbol{\varepsilon}^0 = [\varepsilon^0_{xx},\, \varepsilon^0_{yy},\, \gamma^0_{xy}]^T$ represents the midplane strain vector, while to denote the curvature vector, which included both bending and twisting curvatures, there is $\boldsymbol{\kappa} = [\kappa_{xx},\, \kappa_{yy},\, \kappa_{xy}]^T$. The variable z denotes the through-thickness coordinate measured from the mid-plane as pictured in Figure 2.1.

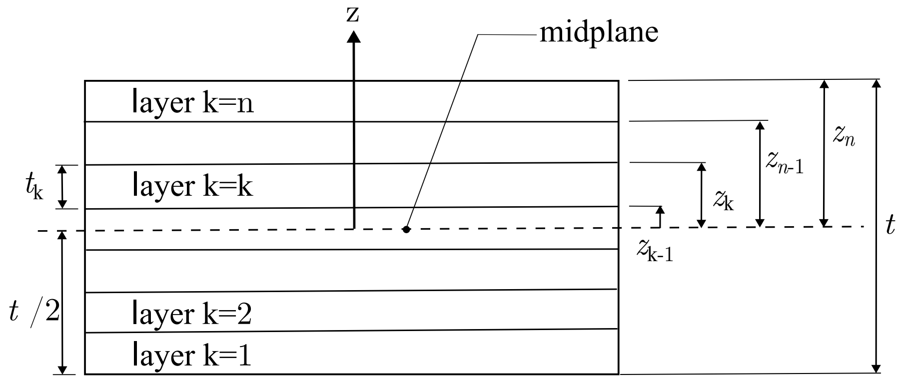

Figure 2.1: Through-thickness schematic of a composite laminate showing mid-plane, z-coordinate, interface positions z_{k-1} and z_k, ply thickness t_k, and total thickness t.

2.2.2.3 Resultant Forces and Moments in the Laminate

Because ply stresses vary through the laminate thickness, the stress field is represented by equivalent midplane resultants in-plane forces and bending–twisting moments as illustrated in Figure 2.2.

The in-plane force resultants $\boldsymbol{N}$ and bending moment resultants $\boldsymbol{M}$ are defined as integrals of the in-plane stresses across the laminate thickness:

$$\boldsymbol{N} = \int_{-t/2}^{t/2} \boldsymbol{\sigma}(z)\, dz = \sum_{\mathrm{k}=1}^{N} \int_{z_{\mathrm{k}-1}}^{z_k} \boldsymbol{\sigma}_{\mathrm{k}}(z)\, dz \tag{2.14}$$

$$\boldsymbol{M} = \int_{-t/2}^{t/2} \boldsymbol{\sigma}(z)\, z\, dz = \sum_{\mathrm{k}=1}^{N} \int_{z_{\mathrm{k}-1}}^{z_k} \boldsymbol{\sigma}_{\mathrm{k}}(z)\, z\, dz \tag{2.15}$$

By incorporating the linear variation of strain with respect to the laminate thickness and applying the constitutive relation for each lamina, the force and moment

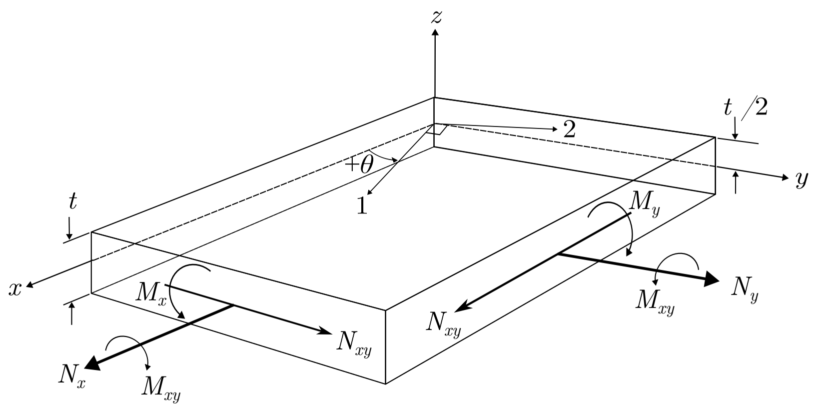

Figure 2.2: Schematic of a multilayered laminate showing the global axes (x, y, z) and the lamina's local material axes $(1, 2)$ oriented by the ply angle θ. Through-thickness stresses are represented on the mid-surface by the CLT resultants: in-plane forces N_x, N_y, N_{xy} and bending–twisting moments M_x, M_y, M_{xy}; t is the laminate thickness (with $t/2$ to each face).

resultants can be expressed in terms of the midplane strains $\boldsymbol{\varepsilon}^0$ and curvatures $\boldsymbol{\kappa}$ as follows:

$$\boldsymbol{N} = \mathbf{A}\,\boldsymbol{\varepsilon}^0 + \mathbf{B}\,\boldsymbol{\kappa} \tag{2.16}$$

$$\boldsymbol{M} = \mathbf{B}\,\boldsymbol{\varepsilon}^0 + \mathbf{D}\,\boldsymbol{\kappa} \tag{2.17}$$

In this formulation, **A**, **B**, and **D** represent the extensional stiffness, bending–extension coupling stiffness, and bending stiffness matrices, respectively. These matrices are computed by integrating the transformed stiffness matrix $\bar{\boldsymbol{Q}}_k$ of each ply over its thickness interval:

$$\begin{aligned} A_{ij} &= \sum_{\mathrm{k}=1}^{N} \left(\bar{Q}_{ij}\right)_{\mathrm{k}} \left(z_{\mathrm{k}} - z_{\mathrm{k}-1}\right), \\ B_{ij} &= \frac{1}{2}\sum_{\mathrm{k}=1}^{N} \left(\bar{Q}_{ij}\right)_{\mathrm{k}} \left(z_{\mathrm{k}}^2 - z_{\mathrm{k}-1}^2\right), \\ D_{ij} &= \frac{1}{3}\sum_{\mathrm{k}=1}^{N} \left(\bar{Q}_{ij}\right)_{\mathrm{k}} \left(z_{\mathrm{k}}^3 - z_{\mathrm{k}-1}^3\right), \end{aligned} \tag{2.18}$$

where N is the number of single plies.

2.2.2.4 Effective Stiffnesses of the Laminate

In this thesis we consider laminates that are symmetric about the midplane and subjected to in-plane loading; under these assumptions, $\boldsymbol{\kappa} = [0, 0, 0]$. Therefore we get

$$\begin{bmatrix} N_x \\ N_y \\ N_{xy} \end{bmatrix} = \underbrace{\begin{bmatrix} A_{11} & A_{12} & A_{16} \\ A_{12} & A_{22} & A_{26} \\ A_{16} & A_{26} & A_{66} \end{bmatrix}}_{=\mathbf{A}} \begin{bmatrix} \varepsilon_x \\ \varepsilon_y \\ \gamma_{xy} \end{bmatrix}. \tag{2.19}$$

When an orthotropic laminate is subjected to in-plane loading only, it is commonly idealised as an equivalent orthotropic plate. The laminate's effective in-plane stiffnesses must then be assigned. Let t denote the laminate thickness, and let A_{ij}^{-1} be the components of $\mathbf{A}^{-1}$, the inverse of the extensional stiffness matrix. The in-plane effective properties are:

$$\hat{E}_x = \frac{1}{A_{11}^{-1}\, t}, \qquad \hat{E}_y = \frac{1}{A_{22}^{-1}\, t}, \qquad \hat{G}_{xy} = \frac{1}{A_{66}^{-1}\, t}, \qquad \hat{\nu}_{xy} = -\frac{A_{12}^{-1}}{A_{11}^{-1}}, \qquad \hat{\nu}_{yx} = -\frac{A_{12}^{-1}}{A_{22}^{-1}}. \tag{2.20}$$

2.2.3 Stress Field of an Orthotropic Homogeneous Plate under Plane Stress

This Subsection follows reference [10], introducing Lekhnitskii's formalism and deriving the complex potential formulation for representing stress fields in anisotropic plates.

2.2.3.1 Generalised Plane Stress State in a Homogeneous Plate

For analysing a thin orthotropic plate under generalized plane stress, the average stresses and displacements with respect to the thickness are computed. These represent the mean values across the plate thickness h, being defined as:

$$\begin{aligned} \bar{\sigma}_x &= \frac{1}{h}\int_{-h/2}^{h/2} \sigma_x \, dz, \quad \bar{\sigma}_y = \frac{1}{h}\int_{-h/2}^{h/2} \sigma_y \, dz, \quad \bar{\tau}_{xy} = \frac{1}{h}\int_{-h/2}^{h/2} \tau_{xy} \, dz, \\ \bar{u} &= \frac{1}{h}\int_{-h/2}^{h/2} u \, dz, \quad \bar{v} = \frac{1}{h}\int_{-h/2}^{h/2} v \, dz. \end{aligned} \tag{2.21}$$

The out-of-plane stress component $\bar{\sigma}_z$ is negligible in the context of plane stress.

By integrating the full three-dimensional equilibrium equations over the plate thickness (from $z = -h/2$ to $z = h/2$), and applying the plane stress assumptions ($\sigma_z = \tau_{xz} = \tau_{yz} = 0$), the following in-plane equilibrium equations for the averaged stresses are obtained:

$$\begin{aligned} \frac{\partial \bar{\sigma}_x}{\partial x} + \frac{\partial \bar{\tau}_{xy}}{\partial y} + \bar{X} = 0, \\ \frac{\partial \bar{\tau}_{xy}}{\partial x} + \frac{\partial \bar{\sigma}_y}{\partial y} + \bar{Y} = 0, \end{aligned} \tag{2.22}$$

where

$$\bar{X} = \frac{1}{h}\int_{-h/2}^{h/2} X\,dz, \quad \bar{Y} = \frac{1}{h}\int_{-h/2}^{h/2} Y\,dz. \tag{2.23}$$

$\bar{X}$ and $\bar{Y}$ are the average body forces per unit volume and the generalized Hooke's law for a generally anisotropic material becomes:

$$\begin{aligned} \bar{\varepsilon}_x &= S_{11}\bar{\sigma}_x + S_{12}\bar{\sigma}_y + S_{16}\bar{\tau}_{xy}, \\ \bar{\varepsilon}_y &= S_{12}\bar{\sigma}_x + S_{22}\bar{\sigma}_y + S_{26}\bar{\tau}_{xy}, \\ \bar{\gamma}_{xy} &= S_{16}\bar{\sigma}_x + S_{26}\bar{\sigma}_y + S_{66}\bar{\tau}_{xy}. \end{aligned} \tag{2.24}$$

The quantities $\bar{\varepsilon}_x$, $\bar{\varepsilon}_y$, and $\bar{\gamma}_{xy}$ represent the thickness-averaged in-plane deformation components and are defined in terms of the mean displacements $\bar{u}$ and $\bar{v}$ as follows:

$$\bar{\varepsilon}_x = \frac{\partial \bar{u}}{\partial x}, \quad \bar{\varepsilon}_y = \frac{\partial \bar{v}}{\partial y}, \quad \bar{\gamma}_{xy} = \frac{\partial \bar{u}}{\partial y} + \frac{\partial \bar{v}}{\partial x}. \tag{2.25}$$

By differentiating these deformation expressions, the following compatibility equation for in-plane deformation is obtained:

$$\frac{\partial^2 \bar{\varepsilon}_x}{\partial y^2} + \frac{\partial^2 \bar{\varepsilon}_y}{\partial x^2} - \frac{\partial^2 \bar{\gamma}_{xy}}{\partial x\,\partial y} = 0. \tag{2.26}$$

2.2.3.2 General Expression for Stress Functions

In the absence of body forces, the stress components can be expressed through the Airy stress function F, which inherently satisfies the equilibrium conditions. The cartesian stress components are

$$\sigma_x = \frac{\partial^2 F}{\partial y^2}, \quad \sigma_y = \frac{\partial^2 F}{\partial x^2}, \quad \tau_{xy} = -\frac{\partial^2 F}{\partial x \partial y}, \tag{2.27}$$

and in polar coordinates, the corresponding stress components are

$$\sigma_r = \frac{1}{r}\frac{\partial F}{\partial r} + \frac{1}{r^2}\frac{\partial^2 F}{\partial \varphi^2}, \quad \sigma_\varphi = \frac{\partial^2 F}{\partial r^2}, \quad \tau_{r\varphi} = -\frac{\partial}{\partial r}\left(\frac{1}{r}\frac{\partial F}{\partial \varphi}\right). \tag{2.28}$$

Substituting the expressions for the in-plane strains from Equation 2.24 and representing the stress components in terms of the Airy stress function F, the governing differential equation that the stress function must satisfy is

$$S_{22}\frac{\partial^4 F}{\partial x^4} - 2S_{26}\frac{\partial^4 F}{\partial x^3 \partial y} + (2S_{12} + S_{66})\frac{\partial^4 F}{\partial x^2 \partial y^2} - 2S_{16}\frac{\partial^4 F}{\partial x \partial y^3} + S_{11}\frac{\partial^4 F}{\partial y^4} = 0. \tag{2.29}$$

Where if the material is an composite laminate, the corresponding effective compliances need to be inserted. The general solution to the governing differential equation can be obtained by expressing it symbolically using four first-order linear differential operators. This leads to the compact form

$$D_1 D_2 D_3 D_4 F = 0, \tag{2.30}$$

where each operator D_k $(k = 1, 2, 3, 4)$ is defined as

$$D_k = \frac{\partial}{\partial y} - \mu_k \frac{\partial}{\partial x}, \tag{2.31}$$

and μ_k are the roots of the associated characteristic equation

$$S_{11}\mu^4 - 2S_{16}\mu^3 + (2S_{12} + S_{66})\mu^2 - 2S_{26}\mu + S_{22} = 0. \tag{2.32}$$

For orthotropic laminates, Equation 2.32 takes the form

$$\mu^4 + \left(\frac{\hat{E}_x}{\hat{G}_{xy}} - 2\hat{\nu}_{xy}\right)\mu^2 + \frac{\hat{E}_x}{\hat{E}_y} = 0. \tag{2.33}$$

The roots of the characteristic equation may be complex or purely imaginary, but do not admit real solutions when all the coefficients are finite and non-zero [10]. Under these conditions, the roots are denoted as μ_1, μ_2, $\bar{\mu}_1$, and $\bar{\mu}_2$, with their form depending on the relation between the elastic constants. Two distinct cases are possible:

1. **All roots are distinct:**

$$\mu_1 = \alpha + \beta i, \quad \mu_2 = \gamma + \delta i, \quad \bar{\mu}_1 = \alpha - \beta i, \quad \bar{\mu}_2 = \gamma - \delta i \tag{2.34}$$

   where α, β, γ, and δ are real numbers such that $\beta > 0$ and $\delta > 0$.

2. **The roots are equal in complex-conjugate pairs:**

$$\mu_1 = \mu_2 = \alpha + \beta i, \quad \bar{\mu}_1 = \bar{\mu}_2 = \alpha - \beta i \quad (\beta > 0). \tag{2.35}$$

For isotropic plates:

$$\mu_1 = \mu_2 = i, \quad \bar{\mu}_1 = \bar{\mu}_2 = -i, \quad \alpha = 0, \quad \beta = 1. \tag{2.36}$$

Based on Equation 2.29, Equation 2.30, and Equation 2.31, the general solution for the stress function F is

$$F = F_1(x + \mu_1 y) + F_2(x + \mu_2 y) + F_3(x + \bar{\mu}_1 y) + F_4(x + \bar{\mu}_2 y), \tag{2.37}$$

where F_1, F_2, F_3, and F_4 are arbitrary analytic functions of the complex variables $(x + \mu_k y)$ and $(x + \bar{\mu}_k y)$. To simplify notation, it is introduced the following variable substitutions:

$$z_1 = x + \mu_1 y, \quad z_2 = x + \mu_2 y, \quad \bar{z}_1 = x + \bar{\mu}_1 y, \quad \bar{z}_2 = x + \bar{\mu}_2 y. \tag{2.38}$$

Taking into account that the stress function F must be a real-valued function of x and y, the general solution can be rewritten as

$$F = 2\,\mathrm{Re}\left[F_1(z_1) + F_2(z_2)\right], \tag{2.39}$$

where $\mathrm{Re}[\cdot]$ denotes the real part of a complex expression.

2.2.3.3 Stress Field Representation Using Complex Potentials

Once the Airy stress function F is properly defined, the expressions for both the stress and displacement fields can be derived. To facilitate this, the following definitions for the complex stress potentials are introduced:

$$\Phi_1(z_1) = \frac{dF_1}{dz_1}, \quad \Phi_2(z_2) = \frac{dF_2}{dz_2}, \quad \Phi_1'(z_1) = \frac{d\Phi_1}{dz_1}, \quad \Phi_2'(z_2) = \frac{d\Phi_2}{dz_2}, \tag{2.40}$$

where $\Phi_1(z_1)$ and $\Phi_2(z_2)$ denote the complex stress potentials associated with the analytic functions F_1 and F_2. Furthermore, the normal and tangential stress components on a plane with an arbitrarily oriented normal vector $\mathbf{n}$ can be obtained using the following expressions

$$\begin{aligned} \sigma_n &= \sigma_x \cos^2(n,x) + \sigma_y \cos^2(n,y) + 2\tau_{xy} \cos(n,x)\cos(n,y), \\ \tau_n &= (\sigma_y - \sigma_x)\cos(n,x)\cos(n,y) + \tau_{xy}\left[\cos^2(n,x) - \cos^2(n,y)\right], \end{aligned} \tag{2.41}$$

where $\cos(n,x)$ and $\cos(n,y)$ are the direction cosines of the normal vector with respect to the x and y axes, respectively. Consequently, the stress components can be expressed as follows:

$$\begin{aligned} \sigma_x &= 2\,\mathrm{Re}\left[\mu_1^2 \Phi_1'(z_1) + \mu_2^2 \Phi_2'(z_2)\right], \\ \sigma_y &= 2\,\mathrm{Re}\left[\Phi_1'(z_1) + \Phi_2'(z_2)\right], \\ \tau_{xy} &= -2\,\mathrm{Re}\left[\mu_1 \Phi_1'(z_1) + \mu_2 \Phi_2'(z_2)\right], \end{aligned} \tag{2.42}$$

$$\begin{aligned} \sigma_r &= 2\,\mathrm{Re}\Big[(\sin\varphi - \mu_1\cos\varphi)^2\,\Phi_1'(z_1) + (\sin\varphi - \mu_2\cos\varphi)^2\,\Phi_2'(z_2)\Big], \\ \sigma_\varphi &= 2\,\mathrm{Re}\Big[(\cos\varphi + \mu_1\sin\varphi)^2\,\Phi_1'(z_1) + (\cos\varphi + \mu_2\sin\varphi)^2\,\Phi_2'(z_2)\Big], \\ \tau_{r\varphi} &= 2\,\mathrm{Re}\Big[(\sin\varphi - \mu_1\cos\varphi)(\cos\varphi + \mu_1\sin\varphi)\,\Phi_1'(z_1) \\ &\quad + (\sin\varphi - \mu_2\cos\varphi)(\cos\varphi + \mu_2\sin\varphi)\,\Phi_2'(z_2)\Big]. \end{aligned} \tag{2.43}$$

2.2.4 Final Remarks

In this Section we presented the theoretical foundation of our work, which will then be further developed in section 4.6. Here the objective was to present the principal formulation used to define the stress field for orthotropic plates under plane stress. Since this thesis follows a sequence of implementation and verification, the remaining theoretical formulations are introduced alongside the validation of their implementation, in order to illustrate the step-by-step process that led to the development of the final tool.

3. Mechanical Idealisation and Finite Element Methodology

In this chapter, the problem is first mechanically idealised, reducing the real-case scenario to a simplified model suitable for analysis. Subsequently, the FE methodology adopted for the verification, validation, and limit testing of the formulation throughout the thesis is presented and discussed.

3.1 Mechanical Idealisation

The load transfer in bearing involves a contact problem with a fully 3D stress state. This includes in-plane stresses that vary through the thickness as well as out-of-plane components. Clamping pressure reduces stress concentrations and thereby raises the static failure load as well. Additionally, the clearence between the fastener and the hole should be minimized, as it leads to lower contact area and therefore higher bearing stresses [64]. Accurately capturing all of these effects, however, is computationally demanding and impractical for developing efficient analytical models. For this reason, the problem is mechanically idealised as a 2D linear plane stress case, which still captures the dominant mechanisms governing tensile failure. When adopting a linear 2D plane stress approach, the effects of contact elasticity, three-dimensional stresses, and secondary bending are not accounted for. Accordingly, the model applies only to joints that are symmetric about the midplane, which are typically connections with an even number of plates (e.g., a double-lap joint) and laminates that exhibit no bending–extension coupling [14].

In the open hole load case, remote uniform tensile stresses are assumed, as pictured in Figure 3.1. For the filled hole load case representing bearing, a frictionless perfect fit between fastener and hole is assumed. The bolt contact is idealised by sinusoidal radial tractions distributed along half of the hole edge following Waszczak and Cruse [29] approach, as shown in Figure 3.2. For the fastened joint under combined bearing–bypass loading (Figure 3.3), the model is constructed as a superposition of the open and filled hole cases, as suggested in the literature [65] and depicted in Figure 3.4. The superposition of two perpendicular uniaxial loading cases approach is taken for the open hole under biaxial loading as pictured in Figure 3.5. The distance from the center of the hole to either the edge where the load is applied or where a constraint is applied is e_{load}, w is the finite plate width and d the hole diameter. Assuming a perfect fit, the fastener diameter, d_f, equals that of the hole, $d_f = d$. The component σ_0 denotes the uniaxial far-field total stress, which equilibrates the bearing load P_{Bea} introduced by the fastener, and the remote bypass $P_{\text{By}} = \sigma_{\text{By}} \cdot w$. The total force is $P = P_{\text{Bea}} + P_{\text{By}}$, where $\sigma_0 = P \cdot w$ and the forces are given per plate thickness. In the open hole there is no bearing, therefore, $\sigma_0 = \sigma_{\text{By}}$. Additionally, note that the open hole case is symmetric about both the x- and y-axes, whereas the filled hole case is symmetric only about the y-axis, except when $e = e_{\text{load}}$.

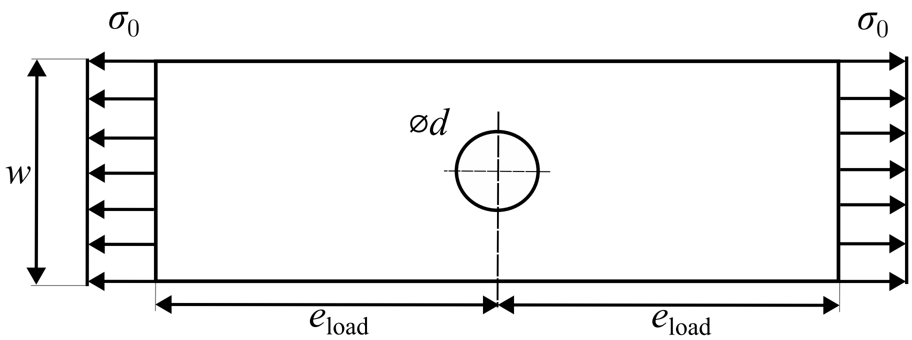

Figure 3.1: Finite-plate open hole tension configuration: a rectangular plate of width w with a central circular hole of diameter d, subjected to uniform remote uniaxial tension σ_0; e_{load} denotes the distance to the loaded edges.

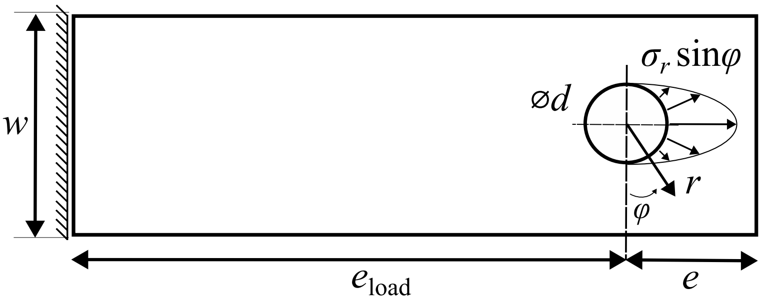

Figure 3.2: Finite-plate filled hole pure bearing configuration: a rectangular plate of width w with a central circular hole of diameter d, the bolt contact is modeled as sinusoidal radial tractions acting over half of the hole circumference; e_{load} denotes the distance to the constraint edge and e the end distance.

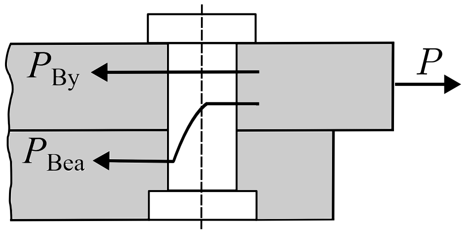

Figure 3.3: Fastened joint under combined bearing–bypass loading, where the total load P is carried partly by the fastener through the bearing load P_{Bea} and partly by the plate through the bypass load P_{By}.

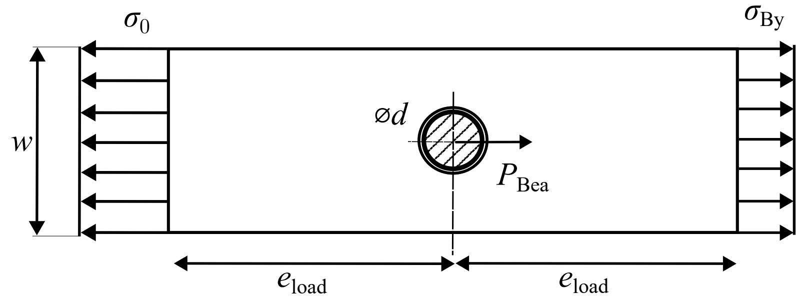

Figure 3.4: Finite-plate filled hole configuration under bypass and bearing: a rectangular plate of width w with a central circular hole of diameter d, subjected to uniform remote uniaxial tension σ_0; e_{load} denotes the distance to the loaded edges.

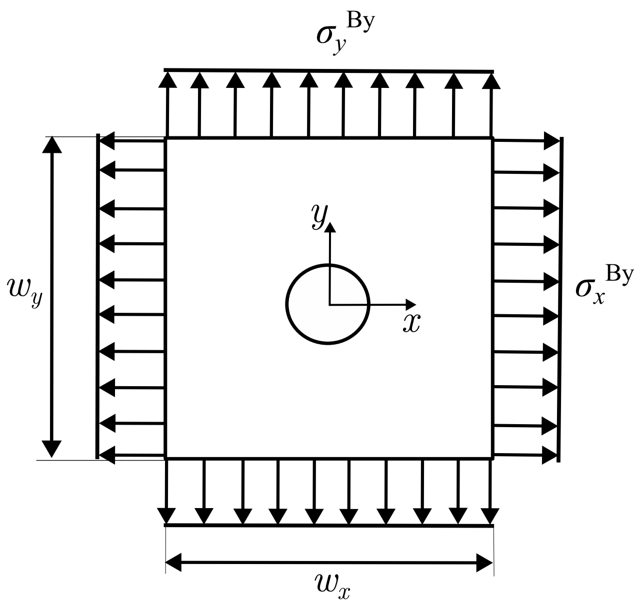

Figure 3.5: Finite-plate open hole under biaxial bypass loading: a rectangular plate of width w_x and height w_y with a central circular hole of diameter d, subjected to uniform remote bypass stresses σ_x^{By} and σ_x^{By} on the x- and y-edges, respectively.

3.2 Finite Element Methodology

In section 4.6, an analytical approach for computing the stress field in an orthotropic plate with open and filled holes will be presented. FE analysis plays a central role in this work, serving to verify, validate, and assess the limitations of the analytical model. The FE simulations were performed using *Abaqus*, with *Python*-based scripting employed for model setup and automation. In this section, the modeling of the different cases is described, together with convergence tests used to verify that the stresses in the concentration zones are accurately captured. We will target numerical convergence to the third decimal place (tolerance $\leq 10^{-3}$), which conservatively allows us to report relative errors to two decimal places.

The geometry and boundary conditions follow those shown in Figure 3.1, Figure 3.4, and Figure 3.5, with $d = 2$ mm. The model is defined using the International System of Units (SI), with dimensions expressed in millimeters. Instead of applying the remote load on each edge of the plate, one side is constrained in the loading direction while the opposite side is subjected to the applied load. In all cases, the plate was modeled using CPS8 continuum plane stress elements, containing 8 nodes. The laminate elastic properties were defined using the option *Engineering Constants*, using the effective stiffness of the laminate. Note that we will only be dealing with orthotropic laminate composites; therefore, throughout this thesis, the following five different layups, which are widely employed in composite aircraft structures, were considered: $[0°]$, $[0°/\pm 45°/90°]_s$ (quasi-isotropic), $[0°/90°]_s$, $[\pm 45°]_s$ and $[0^{\circ}_5\,/\,(\pm 45°)_2\,/\,90°]_s$. The equivalent elastic properties of the laminates are summarized in Table 3.1. The elastic properties of the lamina can be inferred from the $[0°]$ column. This setup was adopted to allow direct comparison with the results of Nguyen-Hoang and Becker [8, 9], who used the lamina properties originally reported by Camanho et al. [66].

Table 3.1: Effective elastic properties of various laminate configurations using Hexcel IM7-8552 ply properties (adapted from Camanho et al. [66]). Throughout this thesis, ply angles are measured counterclockwise, with $[0°]$ aligned with the y-axis.

	$[0°]$	$[\pm 45°]_s$	$[0°/90°]_s$	$[0^{\circ}_5\,/\,(\pm 45°)_2\,/\,90°]_s$	Quasi-isotropic
$\hat{E}_x$ [GPa]	9.10	17.75	90.60	39.52	64.52
$\hat{E}_y$ [GPa]	171.40	17.75	90.60	100.05	64.52
$\hat{E}_y/\hat{E}_x$	18.84	1.00	1.00	2.53	1.00
$\hat{G}_{xy}$ [GPa]	5.30	36.51	5.30	20.77	24.64
$\hat{\nu}_{xy}$	0.016	0.775	0.030	0.169	0.309

For the uniaxial loading case, the bypass remote loads were applied using the *Surface Traction* option. The bearing load was introduced through radial hole tractions with a sinusoidal distribution, representing the bolt–hole contact idealisation, and was applied using the *Surface Traction* option, with

$$\sigma_r(R,\varphi) = \begin{cases} -\dfrac{2}{\pi}\dfrac{P_{\mathrm{Bea}}}{R}\sin\varphi & \text{for} \quad 0 \le \varphi \le \pi, \\ 0 & \text{for} \quad \pi \le \varphi \le 2\pi. \end{cases} \tag{3.1}$$

Nguyen-Hoang and Becker [8] performed a convergence study, where they concluded that a minimum of 72 elements should be placed along the hole edge to match the accuracy of the FE results reported by Catalanotti and Camanho [43]. In the tests conducted in this thesis, a mesh with 160 elements around the hole was used. Although this increases the computational cost of the simulation, it ensures stress results at every 2.25° angle and represents a conservative approach to accurately capture the stress concentration. For this analysis, the stresses will be taken from the nodes located at one point at the edge of the hole. Element size changes radially, decreasing toward the hole boundary to provide local refinement near the edge. The mesh is locally refined within a square-shaped patch whose side length is set by projecting the smallest plate dimension onto the square's diagonal, $L = \sqrt{2}\min\{e_{\mathrm{load}}, w/2, e\}$. In *Abaqus*, this refinement can be prescribed using the bias ratio r, defined along the diagonal as $r = L_{\max}/L_{\min}$, where $L_{\min}$ is the smallest distance between two consecutive nodes of the square's diagonal and $L_{\max}$ is the largest distance between two consecutive nodes of the square's diagonal. A schematic is shown in Figure 3.6.

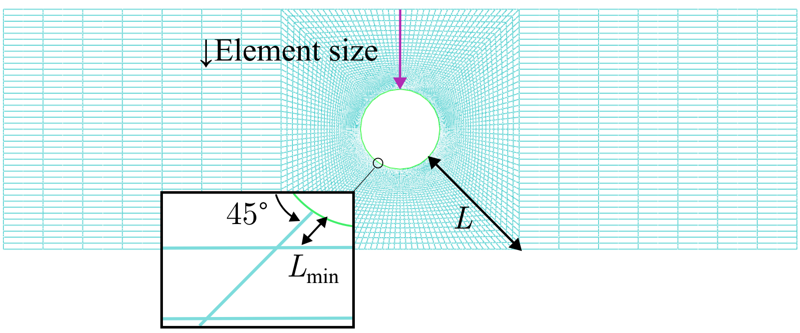

Figure 3.6: Local mesh-refinement strategy around the hole. The element size decreases toward the hole's boundary. Refinement is defined along the 45° diagonal of length L, with the minimum distance between two consecutive nodes being $L_{\min}$ ($L = \sqrt{2}\,\min\{e_{\mathrm{load}}, w/2, e\}$).

Assuming a geometric progression of N elements of the diagonal, the minimum distance between two consecutive nodes of the square's diagonal is

3.2. Finite Element Methodology

$$L_{\min} = L\,\frac{r^{\frac{1}{N-1}} - 1}{r^{\frac{N}{N-1}} - 1}. \tag{3.2}$$

The goal is to choose the number of elements so that the element adjacent to the hole edge is no larger than $L_{\min}$, independent of the plate's overall dimensions. Accordingly, we determine the number of elements N in the direction normal to the hole edge to ensure convergence, while fixing the mesh bias ratio at $r = 10$. Figure 3.7 and Figure 3.8 show the mesh convergence studies for the open hole and filled hole cases and a representation of the FE model. The stress field is normalized by σ_0 for the open hole case and by σ_d for the filled hole case, where $\sigma_d = P_{\mathrm{Bea}}/d$. For consistency throughout this thesis, the following dimensionless coordinate was introduced:

$$\xi = \frac{x - R}{w/2 - R}, \tag{3.3}$$

where $\xi = 0$ corresponds to the hole edge and $\xi = 1$ to the free straight boundary. Hence, the analysis primarily focuses on the stress state at the hole edge at the point $(\xi = 0, y = 0)$, which is where the maximum net-section stresses are located, except for the $[\pm 45°]_{\mathrm{s}}$-laminate, which can be found at a some distance from the hole edge. Under tension, higher stress concentrations occur when edge effects become more significant, specifically for lower values of w in the open hole case and for lower values of both e and w in the filled hole case. Throughout this thesis, the conditions $e/d \geq 2.5$ and $w/d \geq 3$ are maintained. Accordingly, for the open hole case, $w/d = 3$ was adopted, while for the filled hole case, $w/d = 3$ and $e/d = 2.5$ were used, which gives $L = \sqrt{2}\,w/2$. Additionally, we use $N = \{5, 10, 20, 40, 80, 20, 160\}$, yielding $L_{\min} = \{0.1967, 0.1038, 0.0531, 0.0269, 0.0135, 0.0090, 0.0068\}$ mm. The study allows to conclude that for all cases, convergence happens until the third decimal place if $N = 120$. Therefore, following Equation 3.2, we arrive to the conclusion that $L_{\min} = 0.0090$ mm for both the open and filled hole cases.

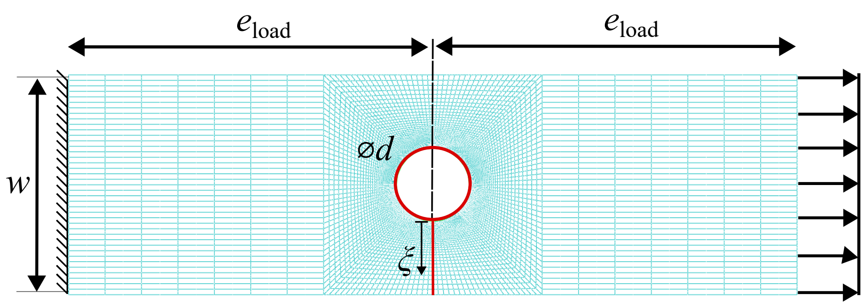

(a) Finite Element model representation of the open hole problem. For the convergence test $w/d = 3$ and $e_{\text{load}}/d = 20$, with $d = 2$ mm.

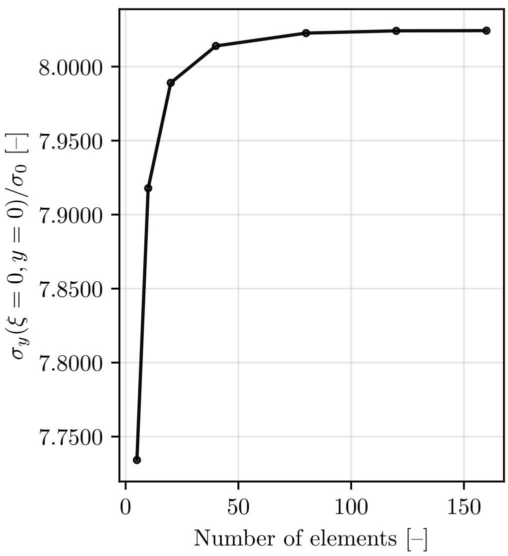

(b) Quasi-isotropic laminate.

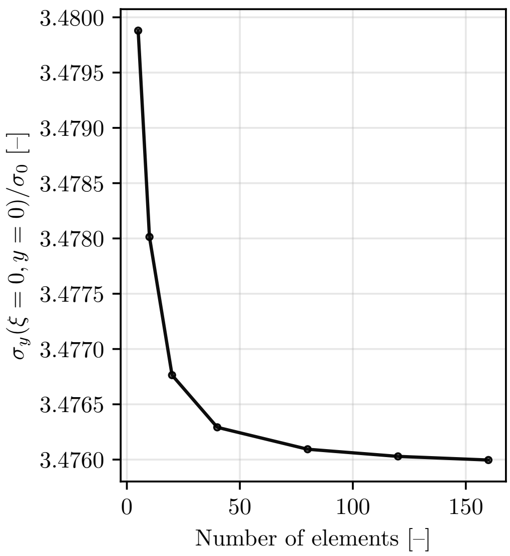

(c) [0°]-laminate.

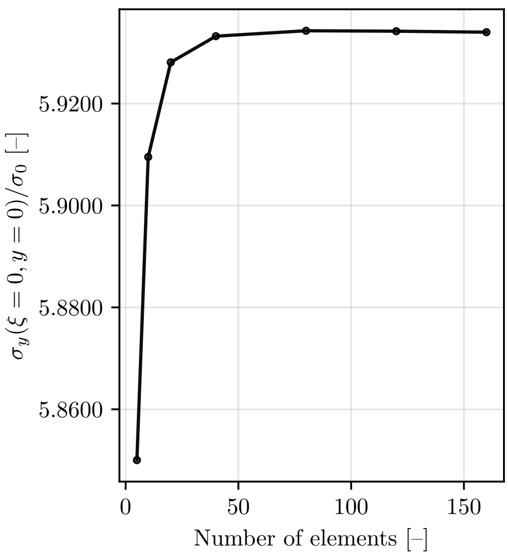

(d) $[0°/90°]_s$-laminate.

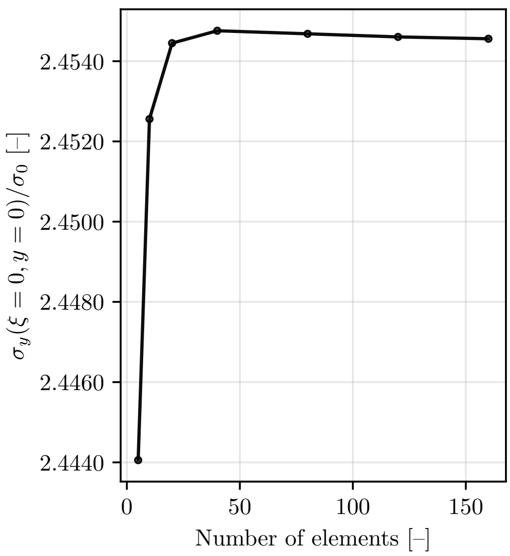

(e) $[\pm 45°]_s$-laminate.

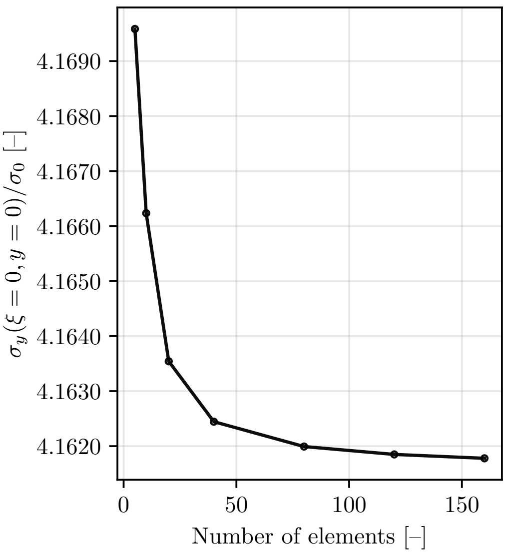

(f) $[0^\circ_5\,/\,(\pm 45°)_2\,/\,90°]_s$-laminate.

Figure 3.7: Open hole tension: mesh convergence of normalised axial stress. (a) FE model used in the study. (b–f) $\sigma_y(\xi = 0, y = 0)/\sigma_0$ with respect to the number of elements $N = \{5, 10, 20, 40, 80, 120, 160\}$ for the laminates indicated. Results converge to three decimal places.

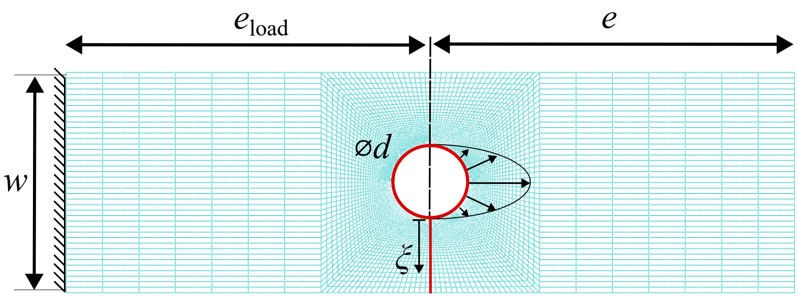

(a) FE model representation of the filled hole problem. For the convergence test $w/d = 3$, $e/d = 2.5$ and $e_{\text{load}}/d = 20$, , with $d = 2$ mm.

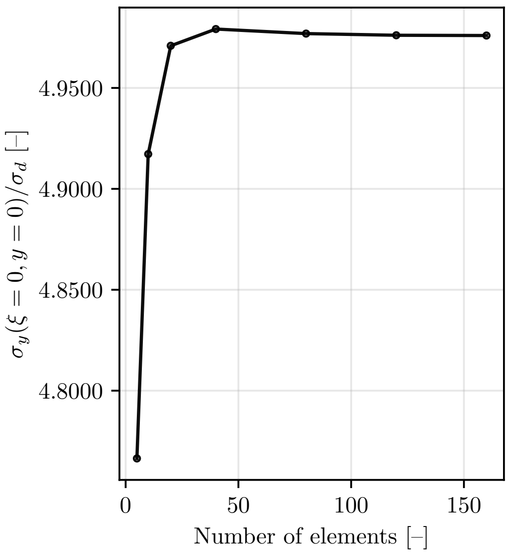

(b) [0°]-laminate.

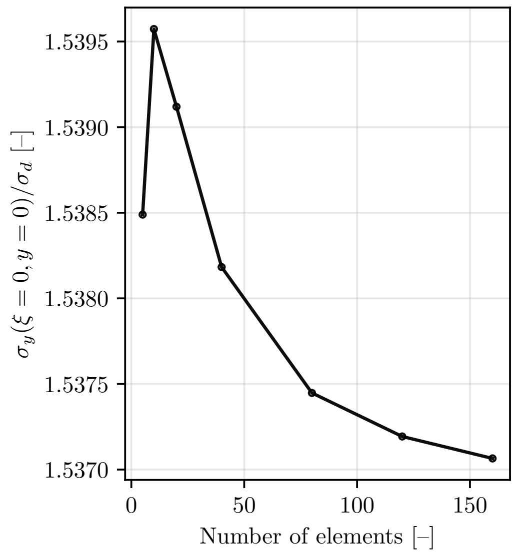

(c) Quasi-isotropic laminate.

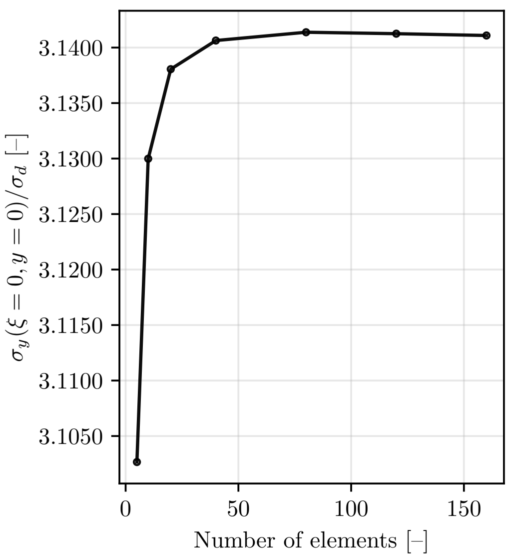

(d) $[0°/90°]_{\text{s}}$-laminate.

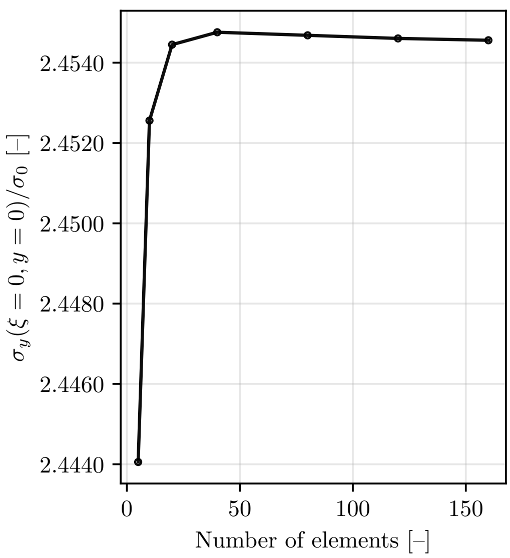

(e) $[\pm 45°]_{\text{s}}$-laminate.

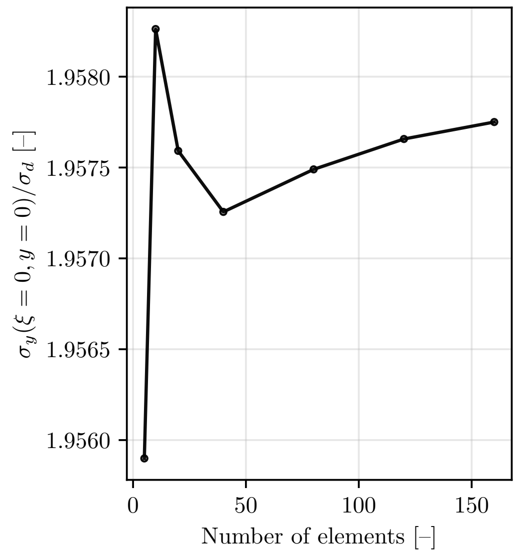

(f) $[0^\circ_5 \,/\, (\pm 45^\circ)_2 \,/\, 90^\circ]_s$-laminate.

Figure 3.8: Filled hole bearing: mesh convergence of normalised axial stress. (a) FE model used in the study. (b–f) $\sigma_y(\xi = 0, y = 0)/\sigma_d$ with respect to the number of elements $N = \{5, 10, 20, 40, 80, 120, 160\}$ for the laminates indicated. Results converge to three decimal places.

4. Stress Analysis

In this chapter, we develop a methodology for determining the stress field in open and filled holes using analytical methods, with all formulations implemented in *Python* and verified against numerical results, obtained from *Abaqus*. We begin by presenting Lekhnitskii's [10] infinite-domain solution, which employs complex potentials and conformal mapping to compute the stress field, and assess both its implementation and its range of validity. Next, we introduce the finite-domain approach of Nguyen-Hoang and Becker [8, 9, 14], which extends the infinite-domain formulation by incorporating auxiliary functions and potentials to enforce boundary conditions, thereby solving the boundary-value problem for an orthotropic finite-width plate under uniaxial tension. Its accuracy and applicability are likewise evaluated against numerical solutions. Finally, we formulate a finite-domain solution for the open hole under biaxial tension and validate its performance through comparison with numerical results.

4.1 Infinite-Domain Problem

This Section solves the infinite-domain problem using Lekhnitskii's [10] solution. It starts by reviewing the fundamentals for imposing boundary conditions on circular domains and introducing the general concepts of complex potentials for modelling open and filled holes in an infinite plate. Then, the particular potentials for each setting are presented. Finally, the formulation is verified and its limitation analysed, using FE solutions.

4.1.1 Application of Boundary Conditions on Circular Domains via Conformal Mapping

Traction along any curved contour represented by the coordinates s are typically applied, with complex potentials, using the loading functions

$$\begin{aligned} p_x(s) &= 2\,\mathrm{Re}\left[\mu_1 \Phi_1(z_1) + \mu_2 \Phi_2(z_2)\right], \\ p_y(s) &= 2\,\mathrm{Re}\left[\Phi_1(z_1) + \Phi_2(z_2)\right]. \end{aligned} \tag{4.1}$$

4.1. Infinite-Domain Problem

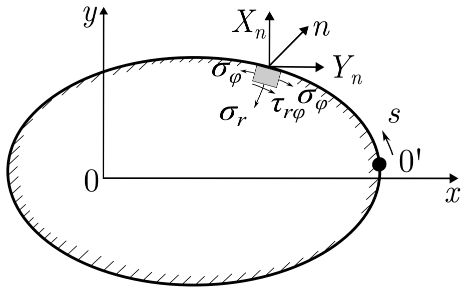

Figure 4.1: External resultant forces X_n and Y_n acting along the outer contour, equilibrated by the boundary tractions from the stress components σ_{rr}, $\sigma_{\varphi\varphi}$, and $\tau_{r\varphi}$. The arc-length coordinate s, outward normal n and $0'$ marks the origin of s.

For illustration of the following explanation, see Figure 4.1. The general case of multiple connected regions enclosed by a single external boundary and one or more internal boundaries, the relationship between the stress components σ_x, σ_y, τ_{xy}, and the loading functions is given by:

$$
\begin{aligned}
p_x(s) &= \pm \int_0^s X_n \, d\tilde{s}, \qquad X_n = \sigma_x \cos(n, x) + \tau_{xy} \cos(n, y), \\
p_y(s) &= \mp \int_0^s Y_n \, d\tilde{s}, \qquad Y_n = \tau_{xy} \cos(n, x) + \sigma_y \cos(n, y).
\end{aligned} \tag{4.2}
$$

The quantities X_n, Y_n denote the components of the external force along the arc length parameter s, and are in equilibrium with the internal stress component. The choice of the upper or lower sign in the equations depends on whether the integration contour is tangent to an external or internal boundary, respectively.

To address circular hole problems, conformal mapping is used, projecting the infinite open hole domain onto the circular unit domain, enabling the application of tractions on the corresponding single external boundary. Conformal mapping is a transformation of the form $\zeta_k = f(z_k)$, where $f(\zeta_k)$ is a single-valued, holomorphic function defined in a connected region of the complex ζ_k-plane. The mapping is assumed to be continuous up to the boundary and reversible, ensuring a one-to-one correspondence between points in the physical z_k-plane and the parametric ζ-plane as seen in Figure 4.2. This transformation is called conformal, as it preserves the sense of the angle [25]. For a hole with radius $R = d/2$, the conformal mapping functions are given by

$$
\zeta_k = \frac{z_k \pm \sqrt{z_k^2 - R^2(1+\mu_k^2)}}{R(1 - i\mu_k)}, \tag{4.3}
$$

which map back to the z_k-plane. The appropriate sign in the mapping function $\zeta_k(z_k)$ is selected to ensure that the resulting stress fields are continuously differentiable

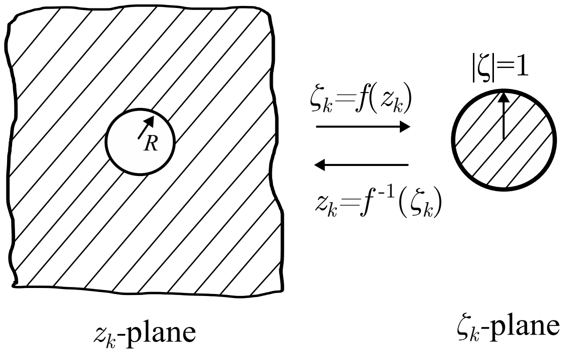

Figure 4.2: Illustration of conformal mapping transformation in between the z_k-plane and the ζ_k-plane, using the mapping functions $f^{-1}(\zeta_k)$ and $f(z_k)$, which depend on the original domain's shape.

and physically valid along any path, which can be verified by checking whether the imposed stress boundary conditions are satisfied. When conformal mapping is applied to a circular domain with only an external boundary subjected to tractions, the upper sign is used.

$$\cos(n,x) = \pm\frac{dy}{ds}, \qquad \cos(n,y) = \mp\frac{dx}{ds}. \tag{4.4}$$

it is obtained

$$\int_0^s X_n\,ds = \int_0^s \tilde{\sigma}_x\,dy - \tilde{\tau}_{xy}\,dx, \qquad \int_0^s Y_n\,ds = \int_0^s \tilde{\tau}_{xy}\,dy - \tilde{\sigma}_y\,dx. \tag{4.5}$$

Along the circular hole with the radius $r = R$ and the relations

$$x = R\cos\varphi, \qquad y = R\sin\varphi \quad \Rightarrow \quad dx = -R\sin\varphi\,d\varphi, \quad dy = R\cos\varphi\,d\varphi, \tag{4.6}$$

leading to the following equations:

$$\begin{aligned} \int_0^s X_n\,ds &= R\int_0^\varphi \tilde{\sigma}_r(R,\varphi)\cos\varphi - \tilde{\tau}_{r\varphi}(R,\varphi)\sin\varphi\,d\varphi, \\ \int_0^s Y_n\,ds &= R\int_0^\varphi \tilde{\tau}_{r\varphi}(R,\varphi)\cos\varphi + \tilde{\sigma}_r(R,\varphi)\sin\varphi\,d\varphi. \end{aligned} \tag{4.7}$$

Relating Equation 4.2 with Equation 4.7 eventually allows to arrive to the loading functions:

$$\begin{aligned} p_x(s) &= R\int_0^\varphi \tilde{\sigma}_r(R,\varphi)\cos\varphi - \tilde{\tau}_{r\varphi}(R,\varphi)\sin\varphi\,d\varphi, \\ p_y(s) &= R\int_0^\varphi \tilde{\tau}_{r\varphi}(R,\varphi)\cos\varphi + \tilde{\sigma}_r(R,\varphi)\sin\varphi\,d\varphi. \end{aligned} \tag{4.8}$$

Equation 4.8 will be further used to select the complex potentials in such a way that the corresponding stresses satisfy the prescribed stress BCs.

4.1.2 Complex Potentials - General Considerations

For an accurate evaluation of the tractions along the hole boundary, the loading functions are decomposed into two components: the first accounts for the contribution of the net force acting on the boundary, this is the multivalued (mv) component, while the second captures the fluctuating part of the load distribution, which is single-valued (sv) and expressed as a Fourier series. Accordingly, Equation 4.2 can be rewritten as:

$$\begin{aligned} p_x(\varphi) &= \overbrace{-\frac{P_x}{2\pi}\varphi}^{=p_x^{\mathrm{mv}}(\varphi)} + \overbrace{\beta_0 + \sum_{n=1}^{\infty}\left(\beta_n e^{in\varphi} + \bar{\beta}_n e^{-in\varphi}\right)}^{=p_x^{\mathrm{Fo,sv}}(\varphi)}, \\ p_y(\varphi) &= \underbrace{+\frac{P_y}{2\pi}\varphi}_{=p_y^{\mathrm{mv}}(\varphi)} + \underbrace{\alpha_0 + \sum_{n=1}^{\infty}\left(\alpha_n e^{in\varphi} + \bar{\alpha}_n e^{-in\varphi}\right)}_{=p_y^{\mathrm{Fo,sv}}(\varphi)}. \end{aligned} \tag{4.9}$$

where, P_x and P_y denote the resultant forces associated with the distributions X_n and Y_n, per unit length. The coefficients α_n and β_n are generally complex-valued and depend on the specific loading conditions applied along the boundary and their complex conjugates are represented by $\bar{\alpha}_n$ and $\bar{\beta}_n$, these coefficients are single-valued. The constants α_0 and β_0 are arbitrary and arise as part of the general solution. Note that the Fourier series is expressed as a sum involving each term and its complex conjugate, which ensures that the imaginary parts cancel out, resulting in a purely real expression. The complex Fourier coefficients are

$$\begin{aligned} \alpha_n &= \frac{1}{2\pi}\int_0^{2\pi} p_y(\varphi)\, e^{-in\varphi}\, d\varphi, \\ \beta_n &= \frac{1}{2\pi}\int_0^{2\pi} p_x(\varphi)\, e^{-in\varphi}\, d\varphi. \end{aligned} \tag{4.10}$$

By equating Equation 4.9 with Equation 4.1, it is arrived to the following complex potentials:

$$
\begin{aligned}
\Phi_1(z_1) &= c_1 + B_1 \ln \zeta_1 + \sum_{n=1}^{\infty} \frac{\bar{\beta}_n - \mu_2 \bar{\alpha}_n}{\mu_1 - \mu_2}\, \zeta_1^{-n}, \\
\Phi_2(z_2) &= c_2 + B_2 \ln \zeta_2 - \sum_{n=1}^{\infty} \frac{\bar{\beta}_n - \mu_1 \bar{\alpha}_n}{\mu_1 - \mu_2}\, \zeta_2^{-n}.
\end{aligned}
\tag{4.11}
$$

Where the values c_k are arbitrary constants, while the coefficients A_k correspond to the coefficients of the multivalued function $\ln \zeta_k$. This term is essential to ensure the reversibility of the mapping functions, as the regions in the z_k-plane and the ζ_k-plane may be either finite or infinite. In particular, one region may be finite while the other is infinite, which implies that the transformation function $f(\zeta_k)$ must become infinite at some point [25]. These coefficients are determined by the following system of equations:

$$
\begin{aligned}
B_1 + B_2 - \bar{B}_1 - \bar{B}_2 &= \frac{P_y}{2\pi h i}, \\
\mu_1 B_1 + \mu_2 B_2 - \bar{\mu}_1 \bar{B}_1 - \bar{\mu}_2 \bar{B}_2 &= -\frac{P_x}{2\pi h i}, \\
\mu_1^2 B_1 + \mu_2^2 B_2 - \bar{\mu}_1^2 \bar{B}_1 - \bar{\mu}_2^2 \bar{B}_2 &= -\frac{S_{16}}{S_{11}} \cdot \frac{P_x}{2\pi h i} - \frac{S_{12}}{S_{11}} \cdot \frac{P_y}{2\pi h i}, \\
\frac{1}{\mu_1} B_1 + \frac{1}{\mu_2} B_2 - \frac{1}{\bar{\mu}_1} \bar{B}_1 - \frac{1}{\bar{\mu}_2} \bar{B}_2 &= \frac{S_{12}}{S_{22}} \cdot \frac{P_x}{2\pi h i} + \frac{S_{26}}{S_{22}} \cdot \frac{P_y}{2\pi h i}.
\end{aligned}
\tag{4.12}
$$

The complex potentials presented in Equation 4.11 allow us to define the stresses due to tractions along the hole boundary, meaning it provides the contribution of the hole's edge effect on the stress field (see Figure 4.3). This should approach zero with increasing distance from the opening. The final general solution includes an additional term representing uniform stress state BCs. Additionally, c_k can be disregarded, as the stress field, is derived using the derivatives of the potentials. Therefore, the general form of the complex potentials suitable for modelling infinite open and filled hole problems is the following:

$$
\begin{aligned}
\Phi_1(z_1) &= A_1 z_1 + B_1 \ln \zeta_1 + \sum_{n=1}^{\infty} \frac{\bar{\beta}_n - \mu_2 \bar{\alpha}_n}{\mu_1 - \mu_2}\, \zeta_1^{-n}, \\
\Phi_2(z_2) &= A_2 z_2 + B_2 \ln \zeta_2 - \sum_{n=1}^{\infty} \frac{\bar{\beta}_n - \mu_1 \bar{\alpha}_n}{\mu_1 - \mu_2}\, \zeta_2^{-n}.
\end{aligned}
\tag{4.13}
$$

Where the coefficients A_k impose the uniform stress state BCs.

The conformal mapping function $\zeta_k = f(z_k)$ is presented in Equation 4.3 and is used to apply the hole tractions. The sign convention in the mapping is carefully

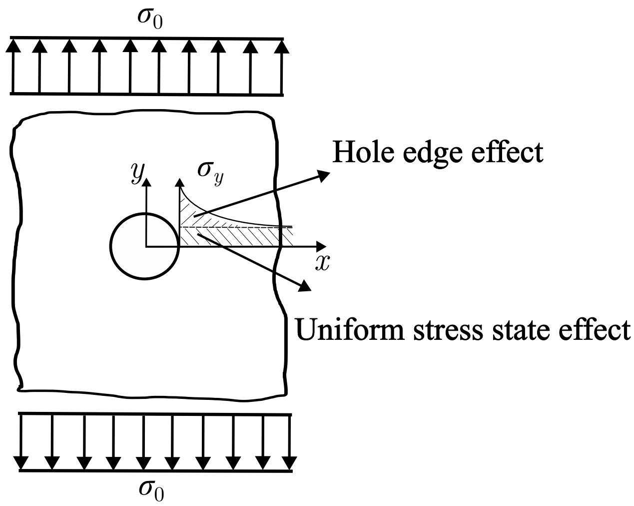

Figure 4.3: Schematic of the infinite-width open hole boundary conditions and the predicted stress distribution around the hole, highlighting the contribution from the hole-edge effect and from the uniform stress state.

selected to ensure that the complex stress potentials, expressed in terms of ζ_k, remain continuously differentiable and yield physically meaningful stress distributions throughout the domain. To ensure this behavior, the following piecewise definition of the mapping branch is adopted:

$$\zeta_k = \begin{cases} \zeta_k^+, & \text{for } 0 \le \varphi \le \pi/2 \quad \text{and} \quad 3\pi/2 < \varphi \le 2\pi \\ \zeta_k^-, & \text{for } \pi/2 < \varphi \le 3\pi/2 \end{cases} \tag{4.14}$$

A singularity in the mapping function arises when the condition $R(1 - i\mu_k) = 0$ is satisfied, which happens in quasi-isotropic laminates, as $\mu_1 = \mu_2 = -i$. To avoid this issue, a small artificial anisotropy can be introduced by slightly perturbing the stiffness matrix coefficients. Tung [67] addressed this singularity by proposing an approximate solution in which the roots are slightly separated, stating that when the root difference remains within 2%, being set to 1% above and 1% below their average, the resulting error is less than 0.01%, making the approximation highly accurate while avoiding the singular behavior not accounted for in Lekhnitskii's [10] original formulation.

Furthermore, when calculating stresses along the vertical edge $x = \pm w/2$, a sign change must be accounted for if the real part of the complex constants μ_k is non-zero [9]. This situation commonly arises in cases such as $[\pm 45°]_s$ laminates. The position y_k^* at which this sign change occurs, y_k^*, can be determined by solving

$$\left.\sqrt{(x + \mu_k y_k^*)^2 - R^2(1 + \mu_k^2)}\right|_{x=\pm w/2} = 0. \tag{4.15}$$

4.1.3 Open hole

The stress analysis of a plate with an open hole is carried out using the principle of superposition where the stress field resulting from the presence of a circular hole is superimposed onto the original stress distribution that exists in an equivalent, hole-free plate subjected to arbitrary external loading. The solution is of the form

$$\Phi_k^{\text{OH,inf}}(z_k) = \underbrace{\Phi_k^{\text{OH-I,inf}}(z_k)}_{\text{plain plate under uniform tension}} + \underbrace{\Phi_k^{\text{OH-II,inf}}(z_k)}_{\text{cancellation of hole tractions}} . \tag{4.16}$$

The complex potential representing the plain plate under uniform tension, which corresponds to the uniform stress state BCs is

$$\Phi_k^{\text{OH-I,inf}}(z_k) = A_k z_k \tag{4.17}$$

and it must fulfill the following relations (see Figure 4.3):

$$\lim_{x\to\pm\infty} \sigma_x(x,y) = 0, \quad \lim_{y\to\pm\infty} \sigma_y(x,y) = \sigma_0, \quad \lim_{\substack{x\to\pm\infty \\ y\to\pm\infty}} \tau_{xy}(x,y) = 0. \tag{4.18}$$

In practice, these boundary conditions are not directly applicable since the load is always applied at a finite distance, for instance, in the presence of consecutive fasteners or when the hole is located near boundaries or loaded edges. To account for this, a numerical study is conducted in subsection 4.1.5 to determine the minimum end-distance-to-diameter ratio, e_{load}/d, at which the load can be applied for the assumption to be valid.

Since $\Phi_k'^{\text{OH-I}} = A_k$, it is constant throughout the plate, which is consistent with its role in enforcing the BC corresponding to a uniform stress state. The resulting stress field solution will take the form:

$$\begin{aligned}
\sigma_x^{\text{OH,inf}}(x,y) &= \sigma_x^{\text{OH-II,inf}}(x,y) \\
\sigma_y^{\text{OH,inf}}(x,y) &= \sigma_0 + \sigma_y^{\text{OH-II,inf}}(x,y) \\
\tau_{xy}^{\text{OH,inf}}(x,y) &= \tau_{xy}^{\text{OH-II,inf}}(x,y)
\end{aligned} \tag{4.19}$$

The boundary of the hole is traction-free and must therefore satisfy the following BCs, where R denotes the radius of the hole:

$$\sigma_r(R,\varphi) = \tau_{r\varphi}(R,\varphi) = 0. \tag{4.20}$$

The complex potentials $\Phi_k^{\text{OH-II,inf}}$ cancel the boundary tractions generated by the bypass loads applied along both principal directions, which are given by Equation 2.43. Hence, $\Phi_k^{\text{OH-II,inf}}$ produces tractions on the hole boundary that are equal in magnitude but opposite in sign to those induced by $\Phi_k^{\text{OH-I}}$, leading to

$$\begin{aligned} \sigma_r^{\text{OH-II,inf}}(R,\varphi) &= -\sigma_0 \sin^2\varphi, \\ \tau_{r\varphi}^{\text{OH-II,inf}}(R,\varphi) &= -\sigma_0 \sin\varphi\cos\varphi. \end{aligned} \tag{4.21}$$

The complex potentials $\Phi_k^{\text{OH-II,inf}}$ represent single-valued and non-zero hole tractions; therefore, have the general form:

$$\begin{aligned} \Phi_1^{\text{OH-II,inf}}(z_1) &= \sum_{n=1}^{\infty} \frac{\bar{\beta}_n - \mu_2\bar{\alpha}_n}{\mu_1-\mu_2}\,\zeta_1^{-n}, \\ \Phi_2^{\text{OH-II,inf}}(z_2) &= -\sum_{n=1}^{\infty} \frac{\bar{\beta}_n - \mu_1\bar{\alpha}_n}{\mu_1-\mu_2}\,\zeta_2^{-n}, \end{aligned} \tag{4.22}$$

which, when equated with the loading functions obtained from Equation 4.8 allows to determine the coefficients. Leading to:

$$\begin{aligned} \Phi_1^{\text{OH-II,inf}}(z_1) &= R\,\frac{\sigma_0\,\mu_2}{2(\mu_1-\mu_2)}\,\zeta_1^{-1}, \\ \Phi_2^{\text{OH-II,inf}}(z_2) &= -R\,\frac{\sigma_0\,\mu_1}{2(\mu_1-\mu_2)}\,\zeta_2^{-1}. \end{aligned} \tag{4.23}$$

The derivatives of the complex potentials, which are required to compute the stress field components, are the following:

$$\begin{aligned} \Phi_1'^{\,\text{OH-II,inf}}(z_1) &= -R\,\frac{\sigma_0\,\mu_2}{2(\mu_1-\mu_2)\sqrt{z_1^2-R^2(1+\mu_1^2)}}\,\zeta_1^{-1}, \\ \Phi_2'^{\,\text{OH-II,inf}}(z_2) &= R\,\frac{\sigma_0\,\mu_1}{2(\mu_1-\mu_2)\sqrt{z_2^2-R^2(1+\mu_2^2)}}\,\zeta_2^{-1}. \end{aligned} \tag{4.24}$$

In Figure 4.6, we present the map of normalised net-section stresses (σ_y/σ_0) computed with the analytical solution for infinite-domain open holes in a $[0°]$ laminate. The plate is considered infinite; however, results are shown only within $x \in [-10, 10]$ mm and $y \in [-10, 10]$ mm.

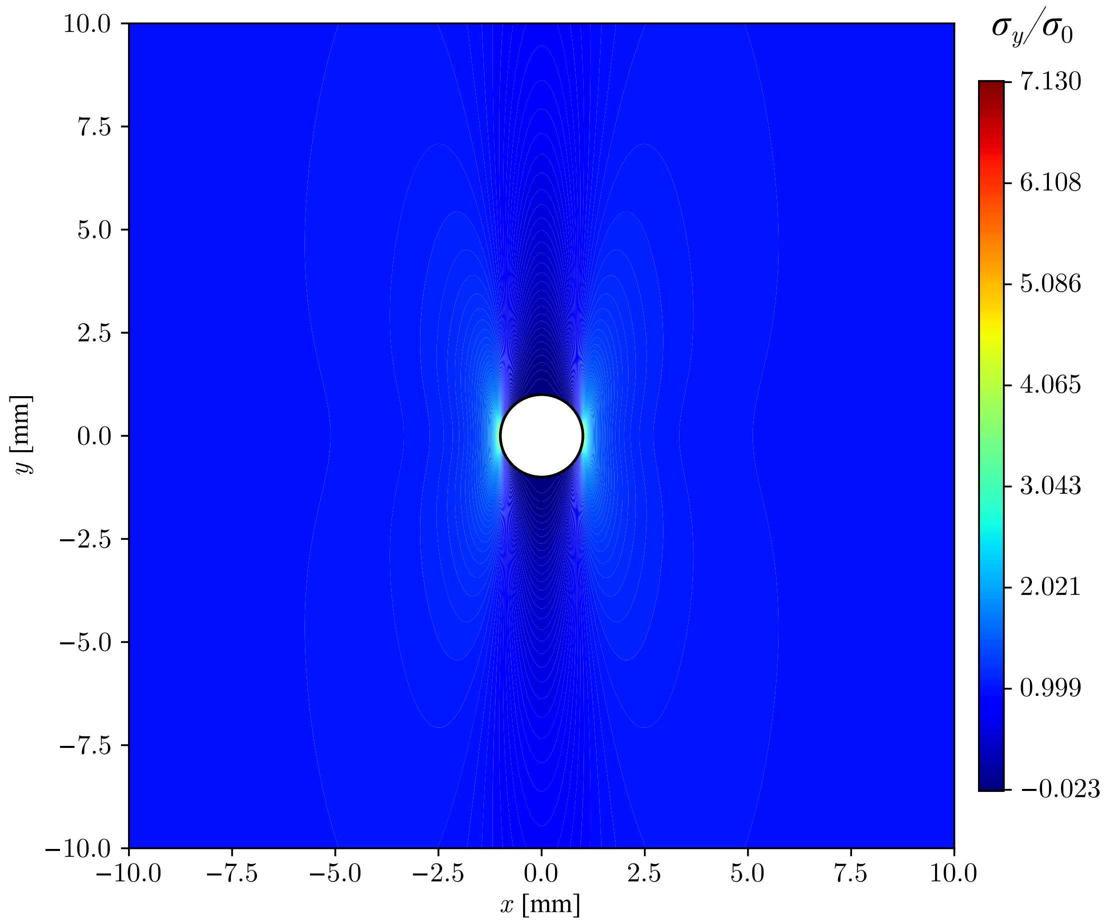

Figure 4.4: Normalised net-section stress field (σ_y/σ_0) around an open hole in an infinite [0°] laminate, computed with the present formulation; contours shown for $x, y \in [-10, 10]$ mm.

4.1.4 Filled Hole

To represent the stress field in the infinite-domain filled hole problem, it is necessary to determine the complex potentials $\Phi_k^{\text{FH,inf}}$ that generate multivalued loading functions of the form given in Equation 4.9. These loading functions are decomposed into single-valued and multivalued components, and accordingly the complex potentials are expressed as the sum of a single-valued part, $\Phi_k^{\text{HBC,sv}}$, and a multivalued part, $\Phi_k^{\text{HBC,mv}}$, having the structure

$$\begin{aligned}
\Phi_1^{\text{FH-inf}}(z_1) &= \Phi_1^{\text{HBC,mv}} + \Phi_1^{\text{HBC,sv}} = B_1 \ln \zeta_1 + \sum_{n=1}^{\infty} \frac{\bar{\beta}_n - \mu_2 \bar{\alpha}_n}{\mu_1 - \mu_2}\, \zeta_1^{-n}, \\
\Phi_2^{\text{FH-inf}}(z_2) &= \Phi_2^{\text{HBC,mv}} + \Phi_2^{\text{HBC,sv}} = B_2 \ln \zeta_2 - \sum_{n=1}^{\infty} \frac{\bar{\beta}_n - \mu_1 \bar{\alpha}_n}{\mu_1 - \mu_2}\, \zeta_2^{-n}.
\end{aligned} \tag{4.25}$$

The filled hole BCs are:

$$
\begin{aligned}
\sigma_r(R,\varphi) &= \begin{cases} -\dfrac{2}{\pi}\dfrac{P_{\mathrm{Bea}}}{R}\cos\varphi & \text{for } -\dfrac{\pi}{2} \leq \varphi \leq \dfrac{\pi}{2}, \\[2ex] 0 & \text{for } \dfrac{\pi}{2} \leq \varphi \leq \dfrac{3\pi}{2}, \end{cases} \\
\tau_{r\varphi}(R,\varphi) &= \quad 0 \qquad\qquad\qquad \text{for } \quad 0 \leq \varphi \leq 2\pi.
\end{aligned}
\tag{4.26}
$$

For illustration of how the BCs were analytically represented see Figure 4.5. Expressing the BCs using a Fourier series expansion and normalizing them by the bearing stress, the BCs can be expressed as

$$
\begin{aligned}
\frac{\sigma_r(R,\varphi)}{\sigma_d} &= -\frac{2}{\pi}\cos\varphi \underbrace{- \frac{4}{\pi^2} - \sum_{n=1}^{N}(-1)^n \frac{4}{\pi^2}\frac{1+\cos 2n\pi}{1-4n^2}\cos 2n\varphi}_{\text{sine Fourier series of } |-2/\pi\cos\varphi|}, \\
\frac{\tau_{r\varphi}(R,\varphi)}{\sigma_d} &= 0.
\end{aligned}
\tag{4.27}
$$

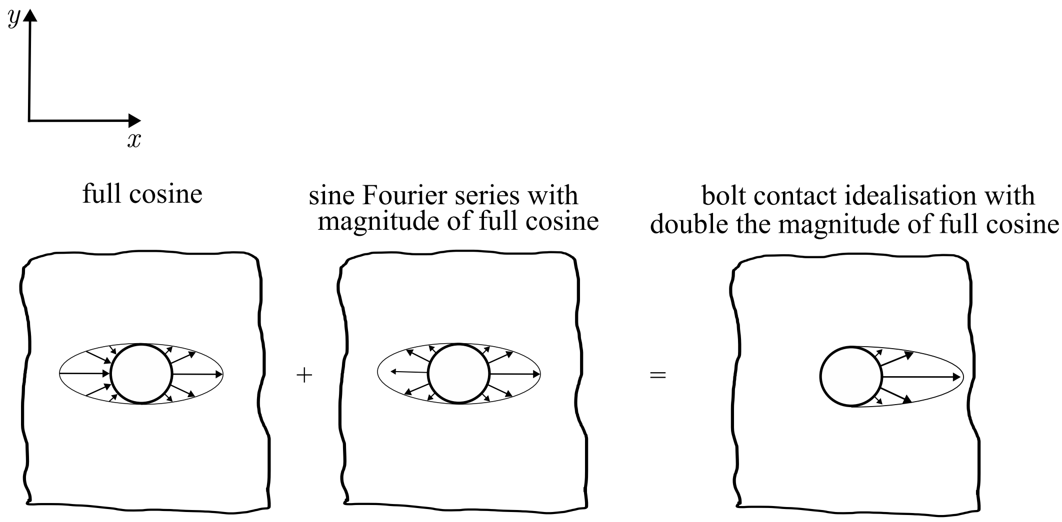

Figure 4.5: Representation of the filled hole BCs by superposition of a full cosine distribution and a cosine Fourier series, resulting in the bolt contact idealisation with sinusoidal radial tractions applied over half of the hole's edge.

Inserting the normalised radial hole traction into Equation 4.8, yields the loading functions:

$$\begin{aligned}
p_x(\varphi) =& R\left(\frac{8(-1)^n\left(2n\sin(2n\varphi)\cos(\varphi)-\sin(\varphi)\cos(2n\varphi)\right)}{(4n^2-1)^2}\right)\frac{\sigma_d}{\pi^2} \\
& -4R\sin(\varphi)\frac{\sigma_d}{\pi^2}-R\left(\varphi+\frac{\sin(2\varphi)}{2}\right)\frac{\sigma_d}{\pi} \\
p_y(\varphi) =& R\left(\frac{8(-1)^n\left(2n\sin(2n\varphi)\sin(\varphi)+\cos(\varphi)\cos(2n\varphi)\right)}{(4n^2-1)^2}\right)\frac{\sigma_d}{\pi^2} \\
& +4R\cos(\varphi)\frac{\sigma_d}{\pi^2}-R\sin^2(\varphi)\frac{\sigma_d}{\pi}.
\end{aligned} \tag{4.28}$$

The loading function $p_x(\varphi)$ is multivalued due to the presence of the linear term φ, which arises from the component $-\frac{2}{\pi}\cos\varphi$. This term allows the model to account for any nonzero force resultants P_x and P_y. In this problem, $P_x = P_{\text{Bea}}$ and $P_y = 0$, as only $p_x(\varphi)$ exhibits multivalued behavior. By solving Equation 4.12, the coefficients B_k can be computed, the system of equations can also be expressed in the matrix form $\mathbf{A}\cdot\mathbf{x} = \mathbf{b}$, and its solution is easily found by inversion. The remaining quantities $p_x^{\text{Fo,sv}}(\varphi)$ and $p_y^{\text{Fo,sv}}(\varphi)$ can be denoted by Fourier series expansions that are capable of representing any periodic and single-valued loading function $p_x^{\text{sv}}(s)$, $p_y^{\text{sv}}(s)$, and by equating them with the single-valued terms in Equation 4.9, the coefficients $\bar{\alpha}_n$ and $\bar{\beta}_n$ for the filled hole problem are

$$\begin{aligned}
\bar{\alpha}_m &= \begin{cases} \dfrac{2P_{bea}}{\pi^2}\dfrac{\sin\frac{\pi}{2}n}{n(n^2-4)} & \text{for } n \neq 1, \\ -\dfrac{P_{bea}}{8\pi} & \text{for } n = 1, \end{cases} \\
\bar{\beta}_m &= \begin{cases} \dfrac{4P_{bea}}{\pi^2}\,i\,\dfrac{\sin\frac{\pi}{2}n}{n^2(n^2-4)} & \text{for } n \neq 1, \\ -\dfrac{P_{bea}}{8\pi}\,i & \text{for } n = 1. \end{cases}
\end{aligned} \tag{4.29}$$

Although the formulation was presented for the bearing load aligned with the x-axis, we will henceforth rotate the coordinate system by $\pi/2$ rad so that the bearing is aligned with the y-axis. This matches the convention of Nguyen–Hoang and Becker [8] for filled holes, enabling direct comparison and agreement of solutions. The complex conjugate values of $\bar{\alpha}_n$ and $\bar{\beta}_n$ for a y-aligned bearing are obtained by solving the BCs for a sine distributed bearing load. In Figure 4.6, we present the map of normalised net-section stresses (σ_y/σ_d) computed with the analytical solution for infinite-domain filled holes in a $[0°]$ laminate, with the bearing load aligned with the y-axis. The plate is considered infinite; however, results are shown only within $x \in [-10, 10]$ mm and $y \in [-10, 10]$ mm.

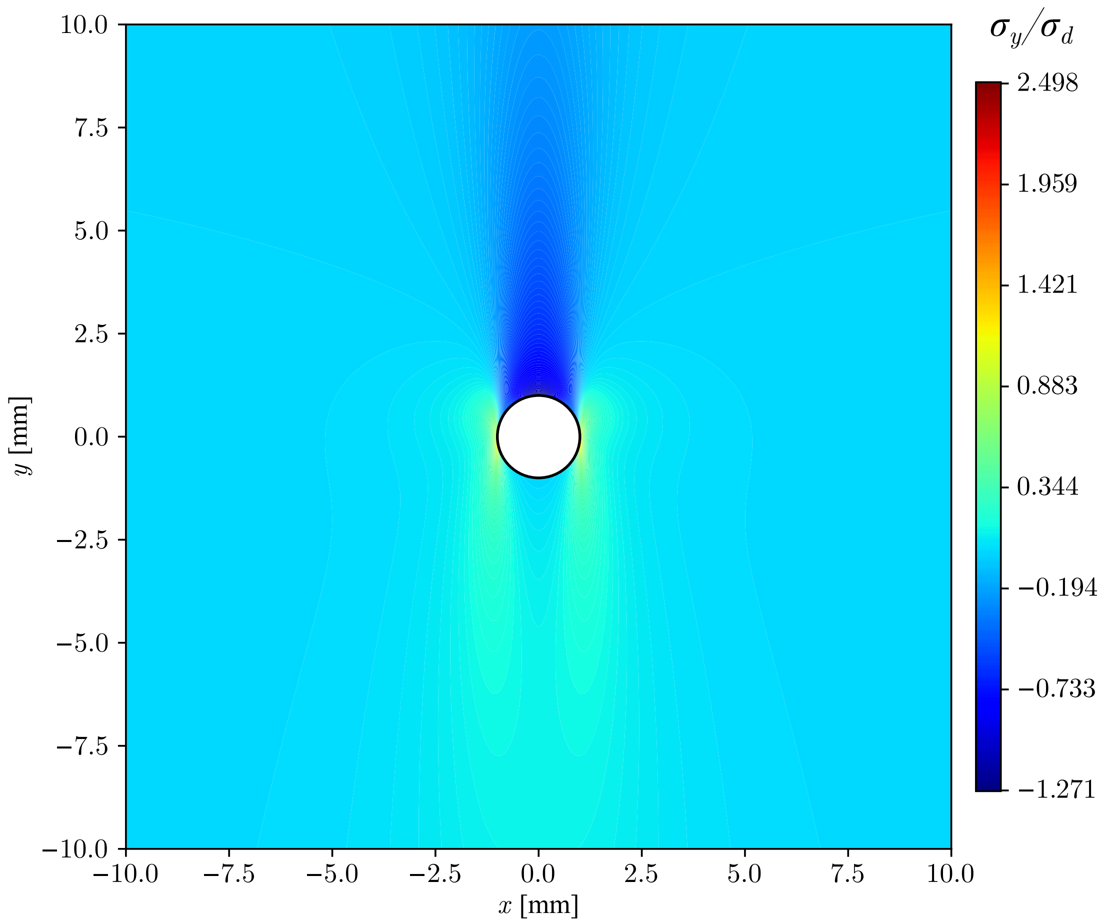

Figure 4.6: Normalised net-section stress field (σ_y/σ_d) around a filled hole in an infinite [0°] laminate, computed with the present formulation; contours shown for $x, y \in [-10, 10]$ mm.

4.1.5 Analysis of the Load Application Distance

The mathematical formulation assumes that the load is applied at infinity. In practice, however, the load is applied at a finite distance, such as in the presence of consecutive fasteners, or when the hole is located near BCs or loaded edges. To address this, a FE analysis was conducted to determine the minimum distance, e_{load}/d, at which the load can be applied (open hole) or the boundary condition imposed (filled hole), such that the stress field is not influenced by it. This analysis was employed for the following sets of dimensions: $e_{\text{load}}/d = \{2.5, 5, 10, 20\}$, $w/d = \{3, 5, 10, 20\}$. For the filled hole case, additional values of $e/d = \{2.5, 10, 20\}$ were considered.

In Figure 4.7 and Figure 4.8, the normalized stresses for the open hole and filled hole cases are presented, respectively. These results correspond to $w/d = 3$ and, for the filled hole case, $w/d = 3$ with $e/d = 2.5$. Additional graphs for the remaining geometric configurations are provided in section A.1.

The first conclusion from this analysis, which can be taken by observation of the plots, for both open and filled holes, is that a smaller w/d ratio reduces the influence of the load application distance on the stress field, whereas a larger $\hat{E}_x/\hat{G}_{xy}$ increases its sensitivity to the load application distance. This conclusion is consistent with reference [68], where it is reported that the characteristic decay length over which end effects remain significant in both isotropic and orthotropic materials, particularly under generalized plane strain and plane stress conditions, is on the order of $b\left(\frac{E}{G}\right)^{1/2}$, where b denotes the maximum dimension perpendicular to the fibers, and E and G represent the longitudinal Young's modulus and shear modulus, respectively.

The relative error (e_r) is calculated at the critical point for each laminate. For all laminates, this point is located at ($\xi = 0, y = 0$), except for the [±45°]s laminate, where it lies at a distance from the hole edge. In addition, the error is evaluated with respect to the reference case $e_{\text{load}}/d = 20$.

Open Hole

For the open hole configuration, if $e_{\text{load}}/d \geq 10$, the largest absolute relative error observed occurs for the [0°] laminate at $w/d = 20$, with $e_r = 0.73\%$. The second-largest error, $|e_r| = 0.25\%$, occurs for the [0°/90°]s laminate. If lower accuracy is acceptable, $e_{\text{load}}/d \geq 5$ can also provide reasonable results. For the [0°] laminate at $w/d = 3$, $|e_r| = 0.89\%$, but for bigger values of w/d, the error exceeds 2%. Among the remaining laminates, the maximum error is $|e_r| = 1.40\%$, which occurs for the $[0°/90°]_\text{s}$ laminate at $w/d = 20$.

Filled Hole

For the filled hole configuration, an additional variable, e/d, is introduced into the analysis. In this case, e_{load}/d denotes the distance from the hole to the constraint in the direction of the applied bearing load. Smaller values of e/d improve the results for the stress field when e_{load} is lower. For $e_{\text{load}} \geq 5$, if $w/d = 3$, the most critical relative error is 0.16%, happening for the [0°] laminate at $e/d = 20$, additionally, for $w/d = 5$, great results can still be obtained with a maximum absolute relative error of 1.81% for the [0°] laminate with $e/d = 20$. Both the [0°] and [0°/90°]s laminates at $w/d = 20$ and $e_{\text{load}}/d \geq 10$ exhibit lower accuracy compared to the other laminates, with minimum absolute relative errors of 3.00% and 2.31%, respectively, at $e/d = 10$. At $w/d = 10$, these laminates show maximum absolute relative errors of 2.00% and 0.80%, respectively, at $e/d = 20$. The remaining laminates display good agreement for $eload/d \geq 10$, with the highest absolute relative error being 0.90% for the $[0^\circ_5\,/\,(\pm 45^\circ)_2\,/\,90^\circ]_\text{s}$ laminate at $w/d = 20$ and $e/d = 20$.

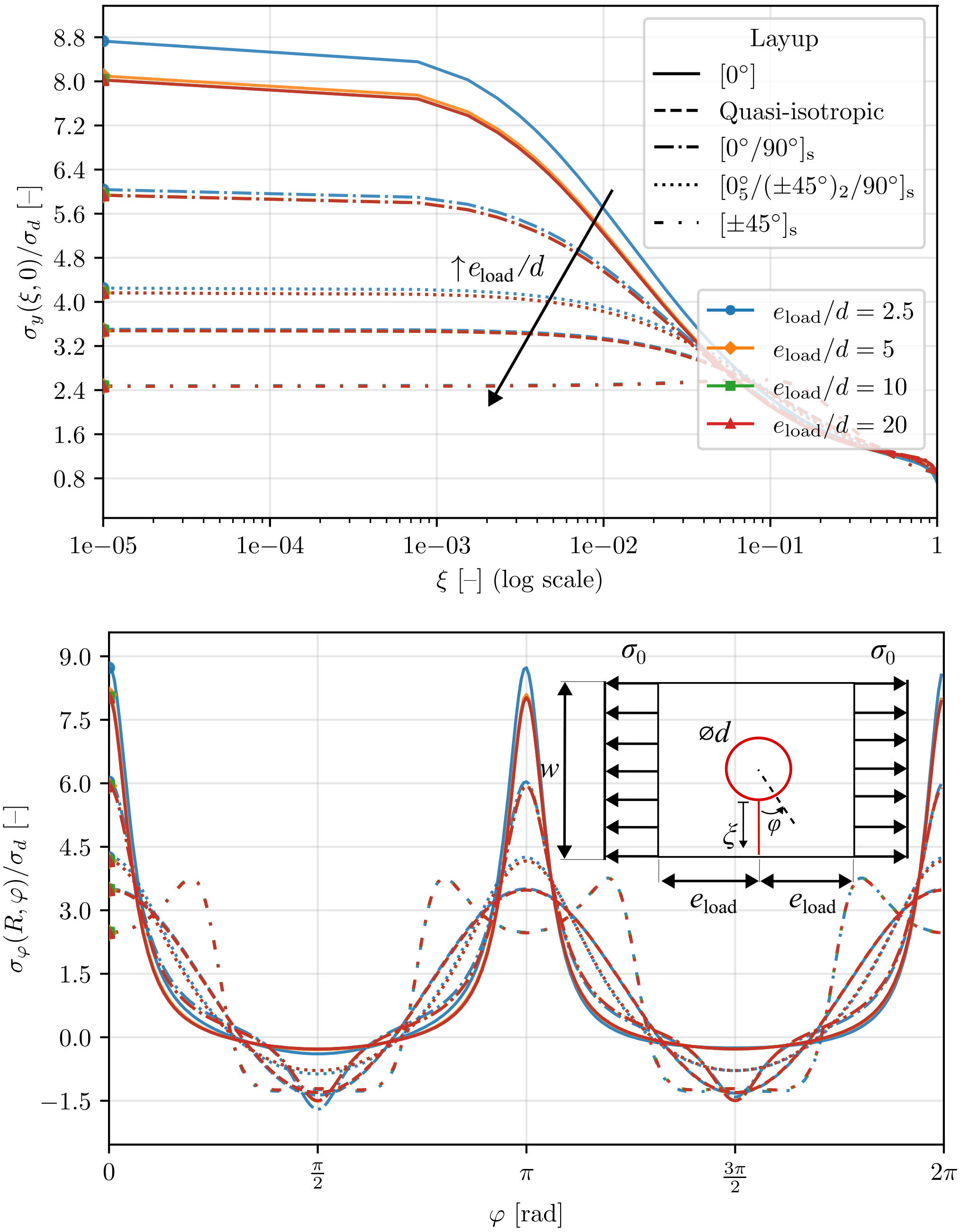

Figure 4.7: Open hole tension stresses for each laminate at different e_{load}/d values, with $w/d = 3$. The upper plot shows the normalized net-section stresses, while the lower plot shows the normalized circumferential stresses.

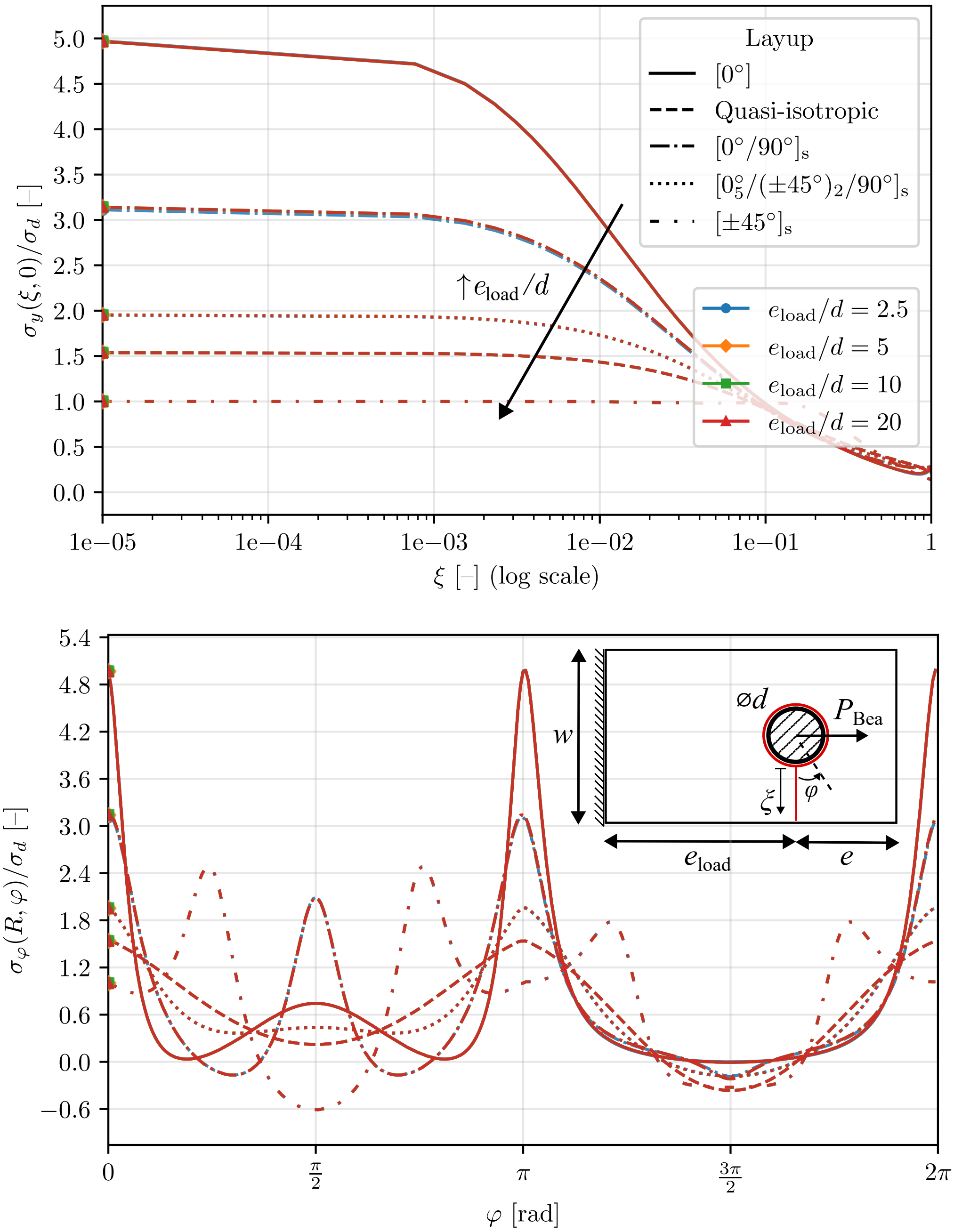

Figure 4.8: Filled hole stresses for each laminate at different e_{load}/d values, with $w/d = 3$ and $e/d = 2.5$. The upper plot shows the normalized net-section stresses, while the lower plot shows the normalized circumferential stresses.

4.1.6 Analysis of Characteristic Stresses

Having established the limitations associated with the load application distance, we now proceed to verify and perform limit testing of the infinite-domain formulation for both the open hole under uniaxial loading and the filled hole configurations. This will be done by comparing the results obtained from the analytical formulation against FE analysis results. The infinite-domain is represented by the condition $w \gg d$. This comparison confirms the accuracy of the complex potentials formalism by Lekhnitskii [10]. Furthermore, it also allows us to determine, for each laminate, the range of w/d values beyond which the plate can be treated as an infinite-domain problem. Since the infinite-domain formulation is computationally less demanding, its use is preferable in order to optimize the overall performance of the tool while minimizing the reliance on the finite-domain methodology. In both analysis the relative error will be evaluated with respect to the infinite-domain analytical solution and will be calculated in the critical point of the laminate, where the stresses are higher.

4.1.6.1 Analysis of the Infinite-Domain Solution: Open Hole

In Figure 4.9, 4.10, 4.11, 4.12, 4.13 are presented the stress distribution in the plates for each laminate. This graphs allow for a comparison of the analytical solution against FE solutions with the following set of width-to-diameter ratios: $w/d = \{5, 10, 20, 40\}$, additionally, the FE models used $e_{\text{load}}/d = 20$. The relative error is evaluated with respect to the infinite-domain analytical solution, and its values are presented in Table 4.1. Increasing w/d leads to convergence of the response curves and $w/d = 40$ provides the closest approximation to the infinite-domain solution. The proximity from the FE solutions to the analytical solution proofs the analytical approach was correctly implemented, and it could be used with errors bellow 1 % for $w/d \geq 20$. Excluding the $[\pm 45°]_s$ laminate, which exhibits the highest errors in almost all configurations, all other laminates show relative errors below 1.5% for $w/d = 10$. Note that the analytical solution provides values smaller than the FE solution in all laminates, therefore it is non conservative to use. Additionally, in cases such as the [0°] laminate, which exhibits higher stress concentrations, the relative error may be lower, yet the absolute difference between the analytical and numerical solutions can be larger. For instance, at $w/d = 5$, the [0°] laminate shows a deviation in the normalised maximum stress of 0.25, whereas the $[\pm 45°]_s$ laminate, despite having nearly twice the relative error, exhibits a smaller deviation of 0.19.

Table 4.1: Maximum stress relative error (%) in open hole tension for various laminate configurations compared with the infinite-domain analytical solution, at different w/d ratios.

	[0°]	Quasi-isotropic	$[0°/90°]_s$	$[\pm 45°]_s$	$[0^\circ_5\,/\,(\pm 45°)_2\,/\,90°]_s$
$w/d = 5$	-3.28%	-4.83%	-3.35%	-8.48%	-4.22%
$w/d = 10$	-1.27%	-1.18%	-0.80%	2.53%	-1.16%
$w/d = 20$	-0.79%	-0.29%	-0.19%	-0.83%	-0.41%
$w/d = 40$	-0.69%	-0.07%	-0.04%	-0.39%	-0.23%

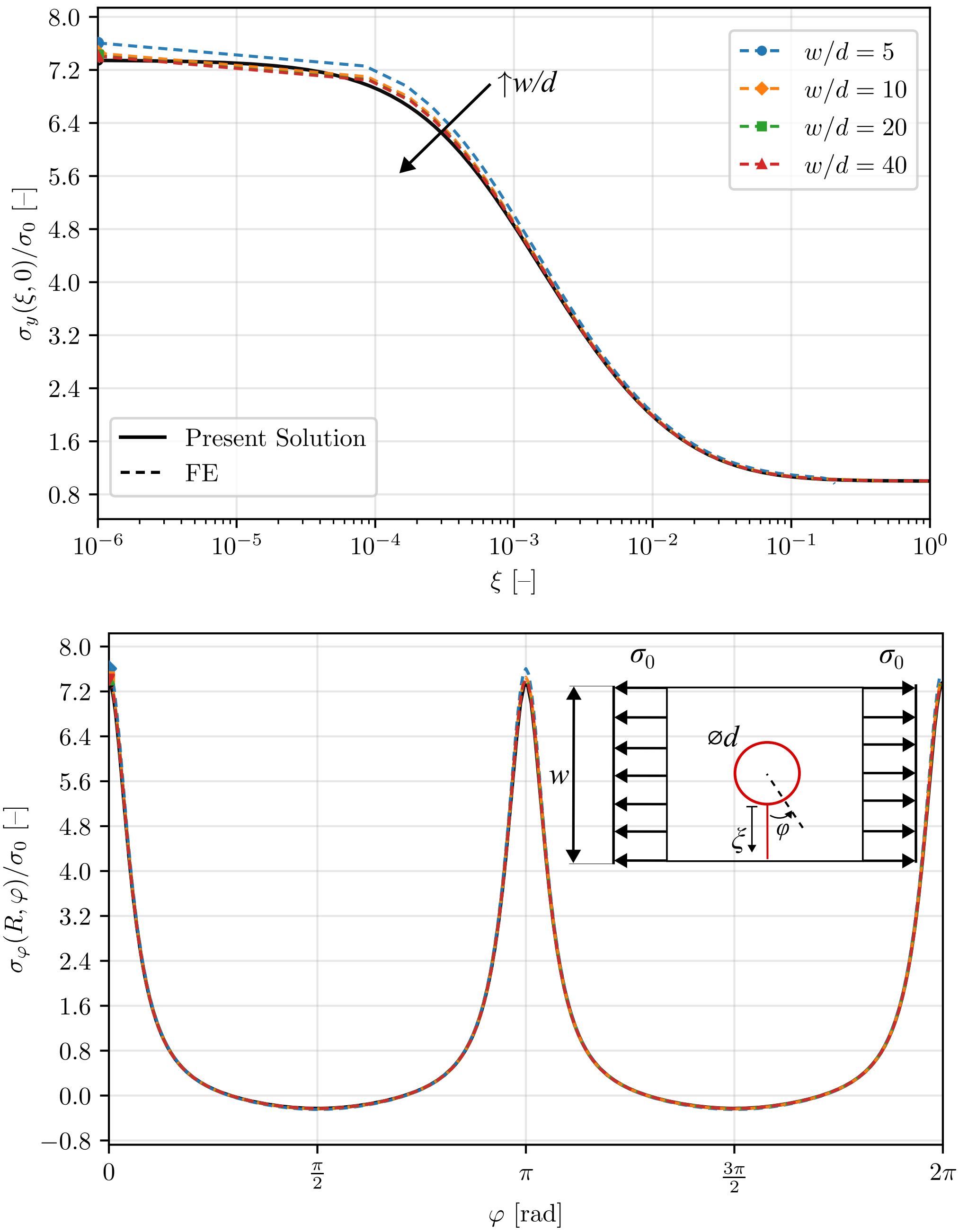

Figure 4.9: Open hole tension infinite plate, comparison between analytical and FE solutions for the $[0°]$ laminate, for $w/d = \{5, 10, 20, 40\}$. The upper plot shows the normalised net-section stresses, while the lower plot shows the normalised circumferential stresses.

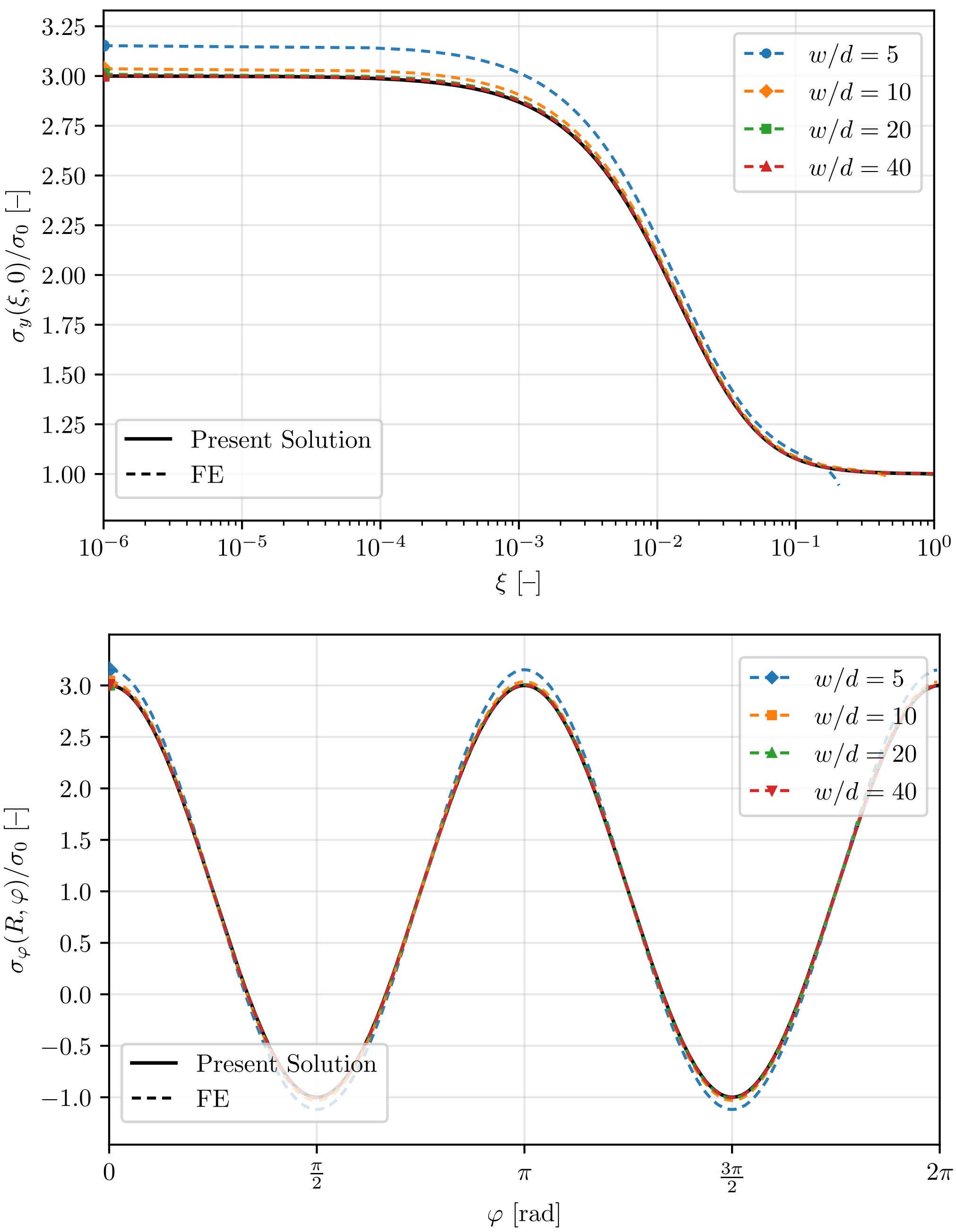

Figure 4.10: Open hole tension infinite plate, comparison between analytical and FE solutions for the quasi-isotropic laminate, for $w/d = \{5, 10, 20, 40\}$. The upper plot shows the normalised net-section stresses, while the lower plot shows the normalised circumferential stresses.

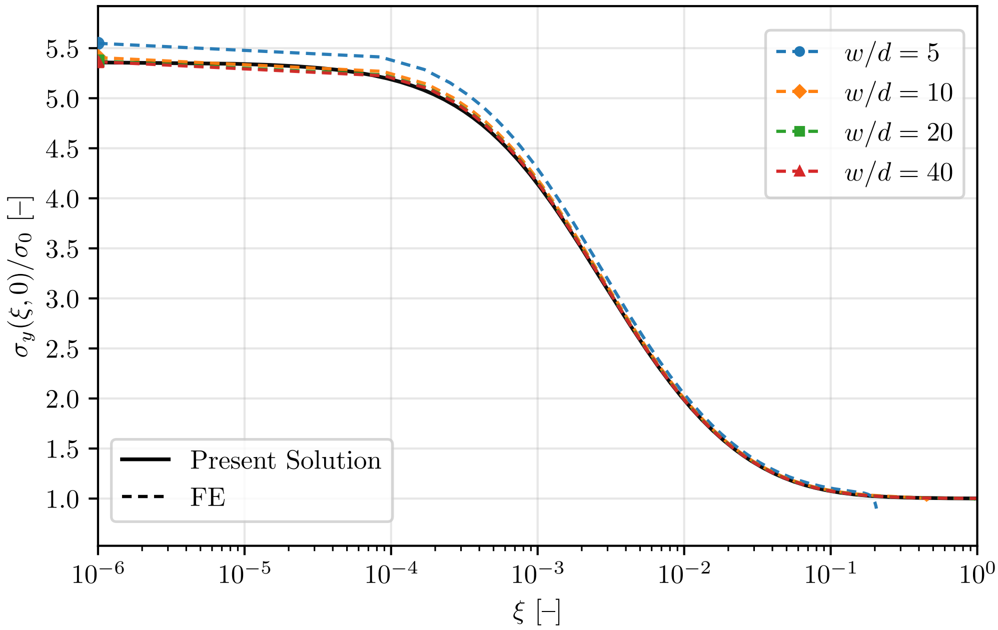

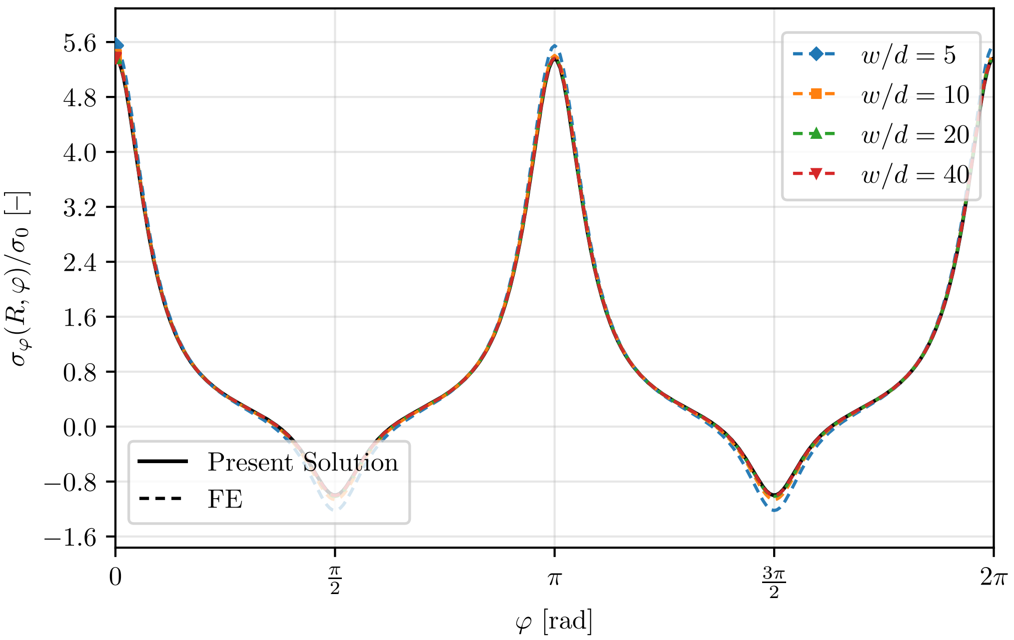

Figure 4.11: Open hole tension infinite plate, comparison between analytical and FE solutions for the $[0°/90°]_s$ laminate, for $w/d = \{5, 10, 20, 40\}$. The upper plot shows the normalised net-section stresses, while the lower plot shows the normalised circumferential stresses.

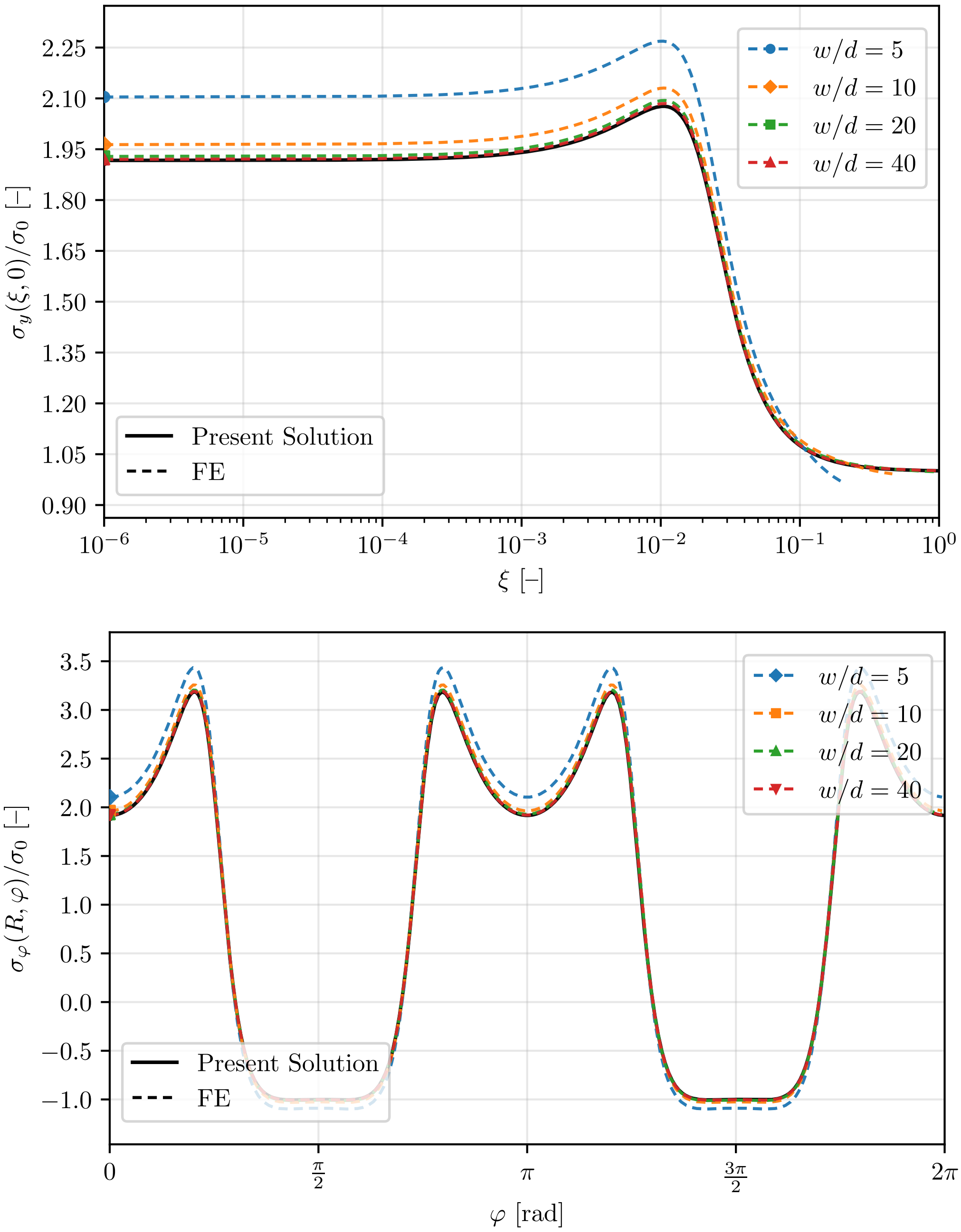

Figure 4.12: Open hole tension infinite plate, comparison between analytical and FE solutions for the $[\pm 45°]_s$ laminate, for $w/d = \{5, 10, 20, 40\}$. The upper plot shows the normalised net-section stresses, while the lower plot shows the normalised circumferential stresses.

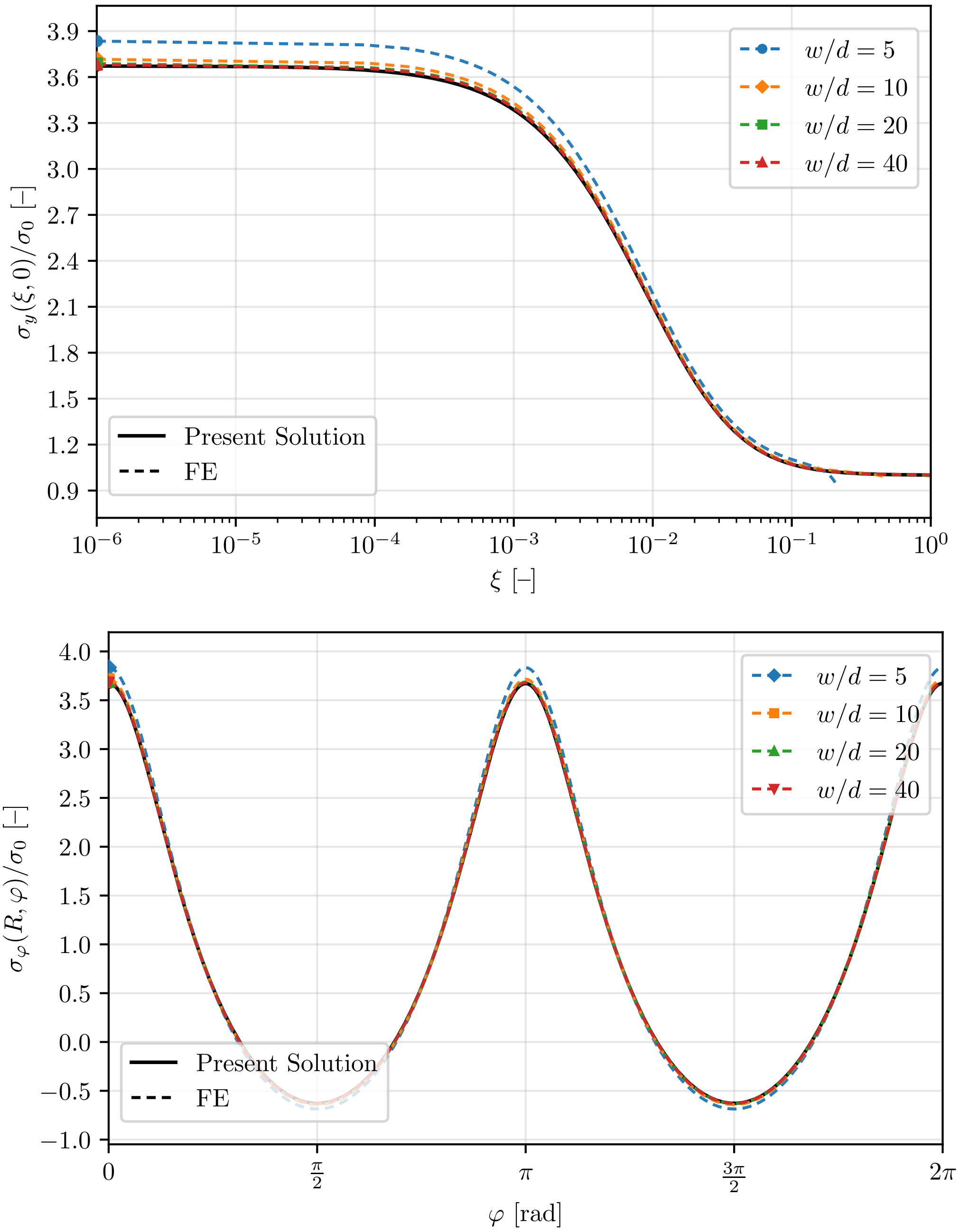

Figure 4.13: Open hole tension infinite plate, comparison between analytical and FE solutions for the $[0^\circ_5\,/\,(\pm 45^\circ)_2\,/\,90^\circ]_\mathrm{s}$ laminate, for $w/d = \{5, 10, 20, 40\}$. The upper plot shows the normalised net-section stresses, while the lower plot shows the normalised circumferential stresses.

4.1.6.2 Analysis of the Infinite-Domain Solution: Filled Hole

The filled hole analysis was carried out for width-to-diameter ratios of $w/d = \{10, 20, 40, 80\}$ and end distance-to-diameter ratios of $e/d = \{2.5, 20, 80\}$. The stress distributions for each laminate at $e/d = 80$ are shown in Figure 4.14, Figure 4.15, Figure 4.16, Figure 4.17, and Figure 4.18. The results for the remaining geometrical configurations, corresponding to $e/d = 2.5$ and $e/d = 20$, are provided in section A.2. The distance at which the boundary is imposed is $e_{\mathrm{load}}/d = 40$. Increasing w/d and e/d leads to convergence of the response curves and $w/d = 80$ with $e/d = 80$ provides the provides the closest approximation to the infinite-domain solutions. The relative error is evaluated with respect to the infinite-domain analytical solution, and its values are presented in Table 4.1, for $e/d = 80$. The analytical infinite-domain solution can be used with lower accuracy than open hole one. For $e/d = 2.5$ and for $e/d = 20$, the minimum absolute relative errors are 25.48% and 3.71%, respectively, with the [0°] laminate presenting the worst solutions. For $e/d = 80$ and $w/d = 80$, the maximum relative error is 3.46% for the [0°] laminate, while all other laminates exhibit errors below 2.2%. These results confirm that the analytical solution for the infinite-domain filled hole problem was correctly implemented; however, its performance proves to be less reliable than that of the open hole model, with errors systematically above 1%.

Table 4.2: Maximum stress relative error (%) in filled hole under bearing for various laminate configurations compared with the infinite-domain analytical solution, at different w/d ratios, with $e/d = 80$.

	[0°]	Quasi-isotropic	$[0°/90°]_s$	$[\pm 45°]_s$	$[0^\circ_5\,/\,(\pm 45°)_2\,/\,90°]_s$
$w/d = 10$	-13.38%	-16.50%	-13.44%	-23.11%	-15.21%
$w/d = 20$	-7.38%	-8.42%	-7.06%	-11.15%	-7.87%
$w/d = 40$	-4.31%	-4.07%	-3.62%	-4.73%	-3.91%
$w/d = 80$	-3.46%	-1.81%	-2.18%	-1.45%	-1.88%

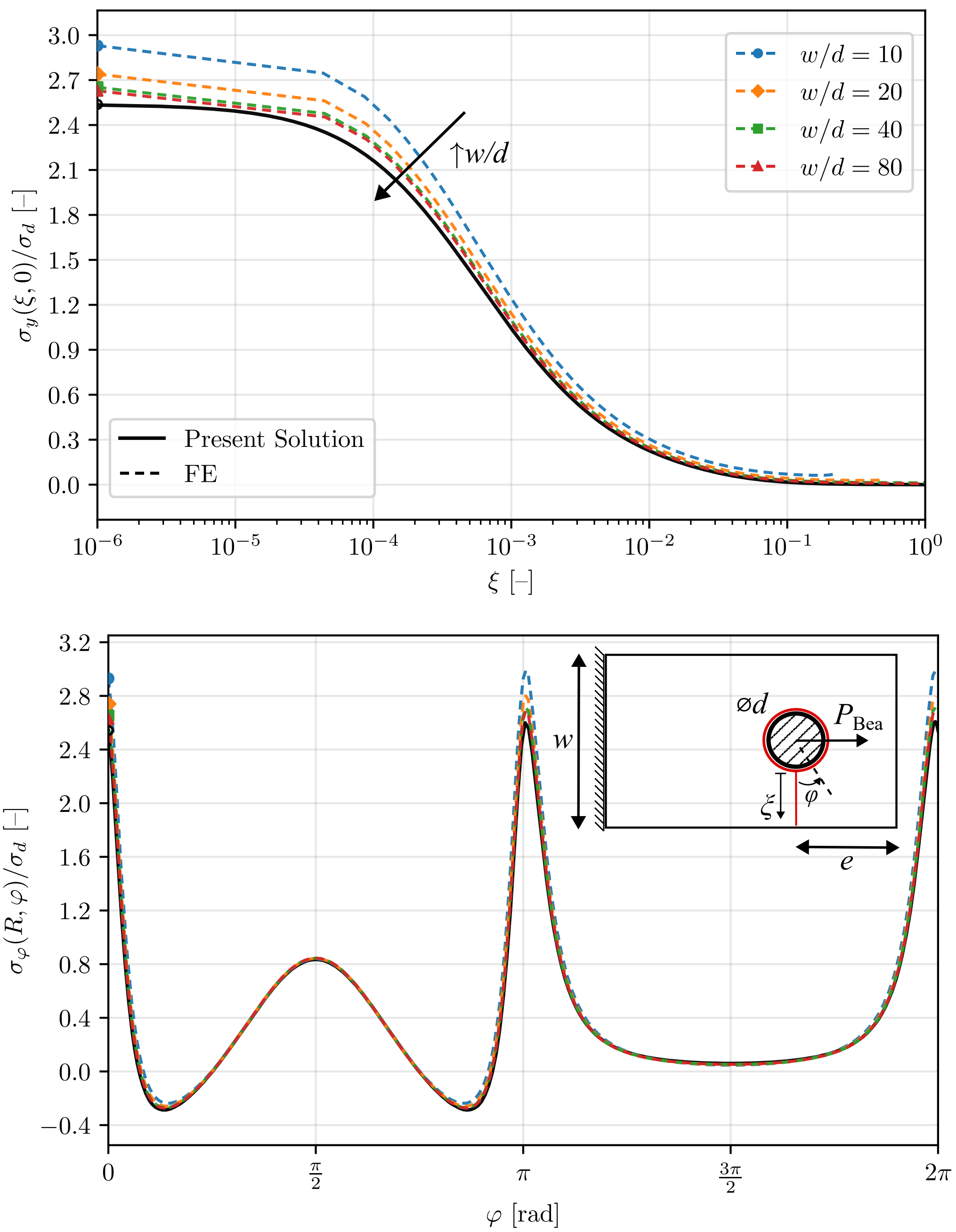

Figure 4.14: Filled hole infinite plate, comparison between analytical and FE solutions for the [0°] laminate, for $w/d = \{10, 20, 40, 80\}$ and $e/d = 80$. The upper plot shows the normalised net-section stresses, while the lower plot shows the normalised circumferential stresses.

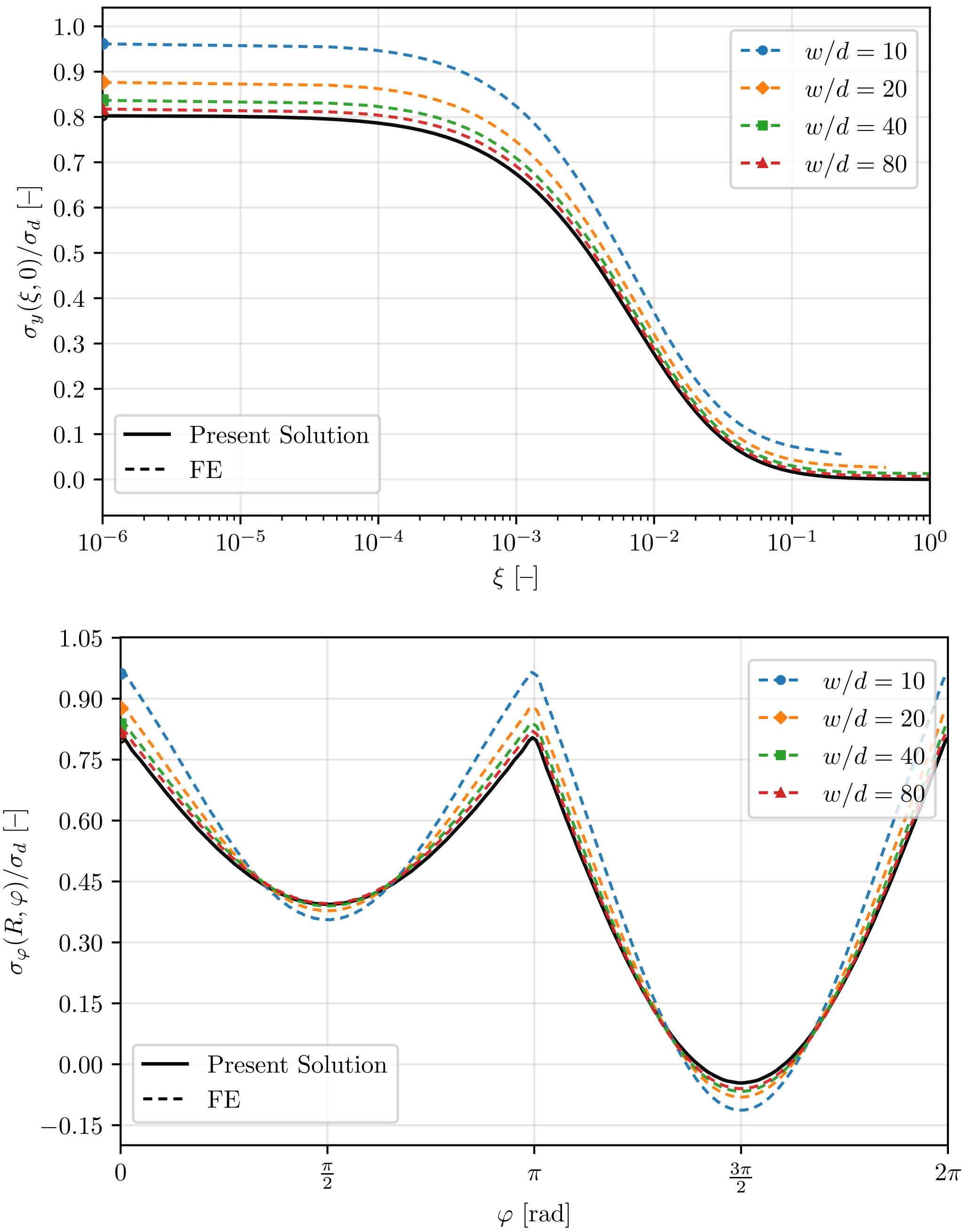

Figure 4.15: Filled hole infinite plate, comparison between analytical and FE solutions for the quasi-isotropic $[0^\circ_5\,/\,(\pm 45^\circ)_2\,/\,90^\circ]_\mathrm{s}$ laminate, for $w/d = \{10, 20, 40, 80\}$ and $e/d = 80$. The upper plot shows the normalised net-section stresses, while the lower plot shows the normalised circumferential stresses.

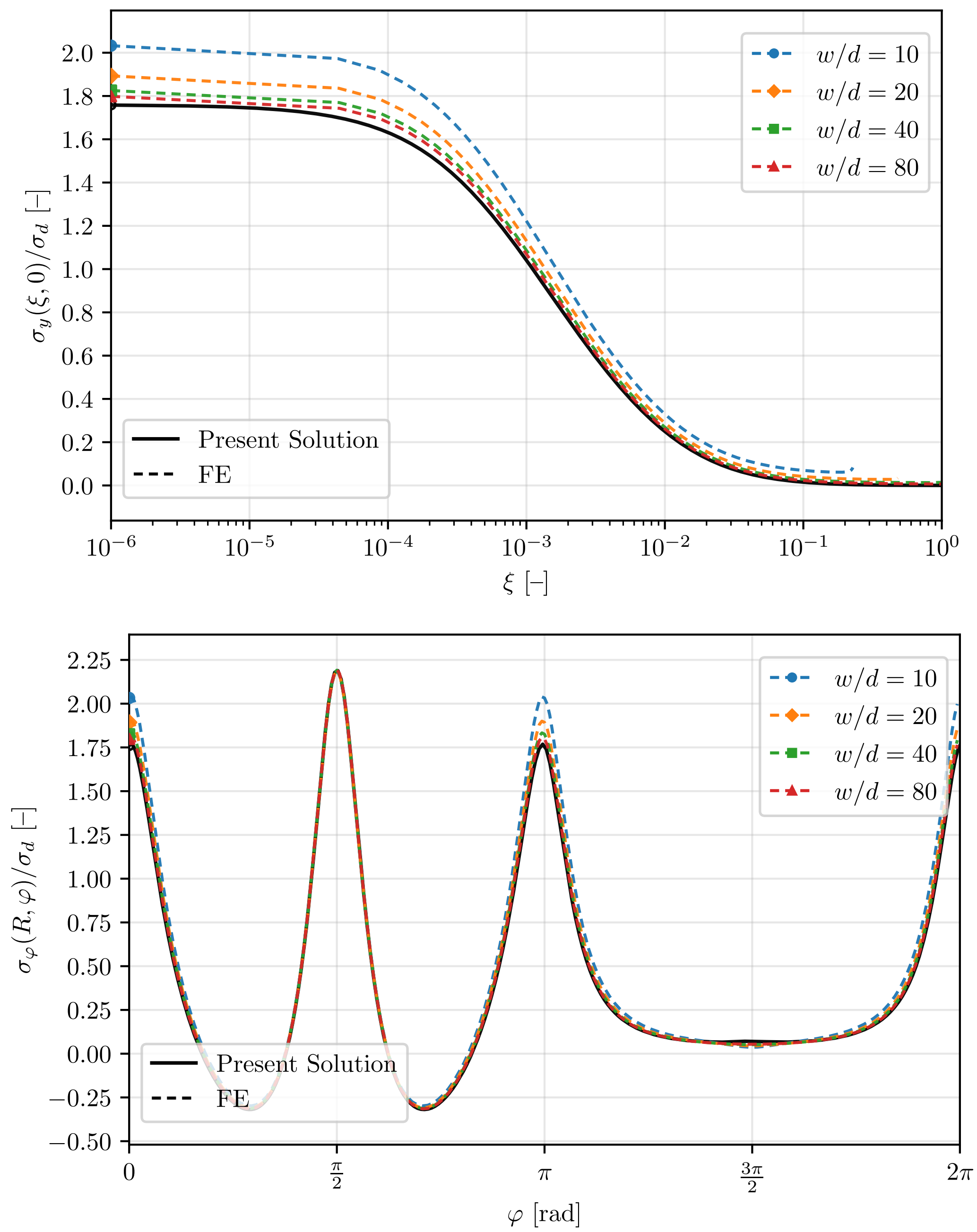

Figure 4.16: Filled hole infinite plate, comparison between analytical and FE solutions for the $[0°/90°]_s$ laminate, for $w/d = \{10, 20, 40, 80\}$ and $e/d = 80$. The upper plot shows the normalised net-section stresses, while the lower plot shows the normalised circumferential stresses.

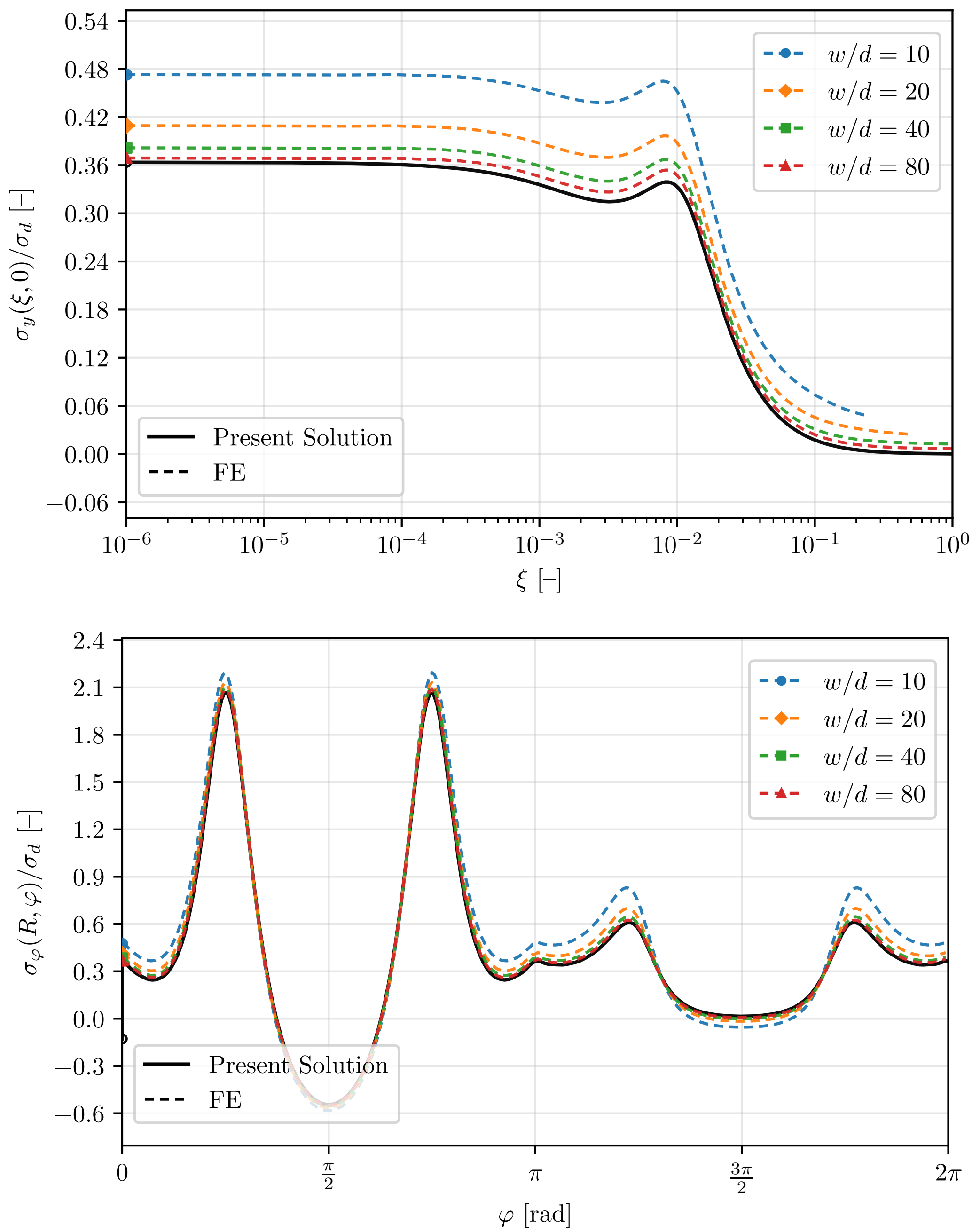

Figure 4.17: Filled hole infinite plate, comparison between analytical and FE solutions for the $[\pm 45°]_\mathrm{s}$ laminate, for $w/d = \{10, 20, 40, 80\}$ and $e/d = 80$. The upper plot shows the normalised net-section stresses, while the lower plot shows the normalised circumferential stresses.

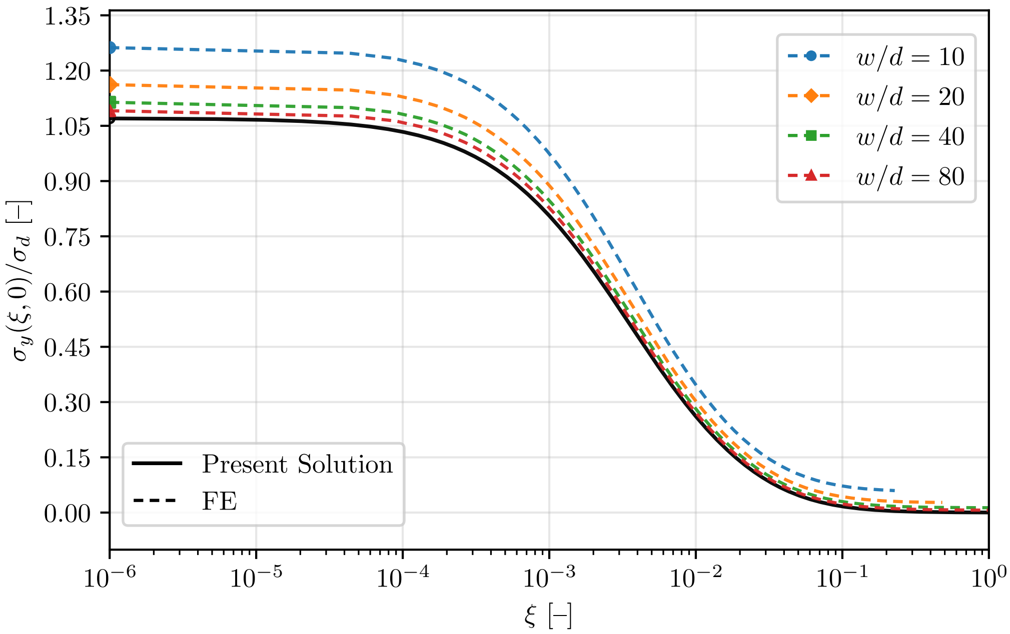

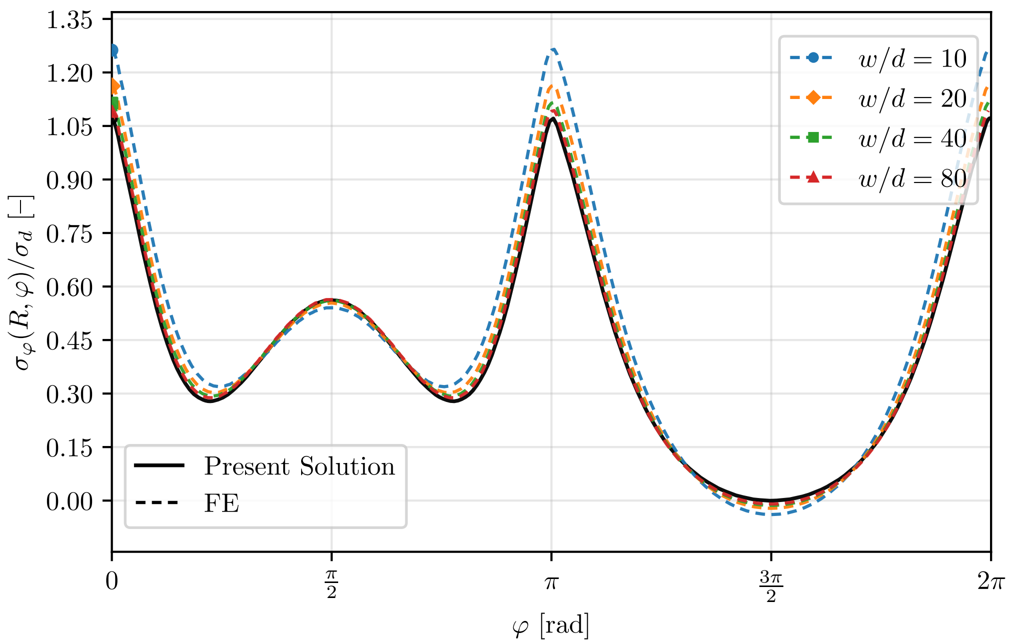

Figure 4.18: Filled hole infinite plate, comparison between analytical and FE solutions for the $[0^\circ_5\,/\,(\pm 45^\circ)_2\,/\,90^\circ]_\mathrm{s}$ laminate, for $w/d = \{10, 20, 40, 80\}$ and $e/d = 80$. The upper plot shows the normalised net-section stresses, while the lower plot shows the normalised circumferential stresses.

4.2 Finite-Domain Problem

In the last Section it was presented a solution for the open and filled hole problem, which is only applicable to infinite plates. Additionally, we tried to under to understand when can a plate be considered infinite with negligible errors. The solution we will present now is applicable to finite-width plates, meaning the assumption that the load is applied at infinity maintains, as well as the assumption that the bearing load is transferred toward a boundary at an infinite distance. To address the finite-width problem, the infinite plate formulation was expanded by incorporating auxiliary functions and potentials to enforce boundary conditions, following Nguyen-Hoang and Becker [11–13] methodology. Both the filled hole and open hole cases will be addressed in parallel, as their formulations are closely related. In addition to the hole's BCs, which are defined for the infinite-domain solution, the finite-domain problem requires satisfying the free-edge conditions, which are illustrated in Figure 4.19. Accordingly, the stress BCs for the open hole are given by:

$$\lim_{x\to\pm\infty} \sigma_x(x,y) = 0, \quad \lim_{y\to\pm\infty} \sigma_y(x,y) = \sigma_0, \quad \lim_{\substack{x\to\pm\infty \\ y\to\pm\infty}} \tau_{xy}(x,y) = 0, \tag{4.30}$$

$$\sigma_r(R,\varphi) = \tau_{r\varphi}(R,\varphi) = 0. \tag{4.31}$$

$$\sigma_x\left(\pm w/2, y\right) = \tau_{xy}\left(\pm w/2, y\right) = 0. \tag{4.32}$$

Furthermore, for filled hole the BCs are:

$$\begin{aligned}
\sigma_r(R,\varphi) &= \begin{cases} -\dfrac{2}{\pi}\dfrac{P_{\text{Bea}}}{R}\sin\varphi & \text{for} \quad 0 \le \varphi \le \pi, \\[2ex] 0 & \text{for} \quad \pi \le \varphi \le 2\pi, \end{cases} \\
\tau_{r\varphi}(R,\varphi) &= \quad 0 \qquad\qquad\qquad \text{for} \quad 0 \le \varphi \le 2\pi.
\end{aligned} \tag{4.33}$$

$$\sigma_x\left(\pm w/2, y\right) = \tau_{xy}\left(\pm w/2, y\right) = 0. \tag{4.34}$$

$$\sigma_y(x,e) = \tau_{xy}(x,e) = 0. \tag{4.35}$$

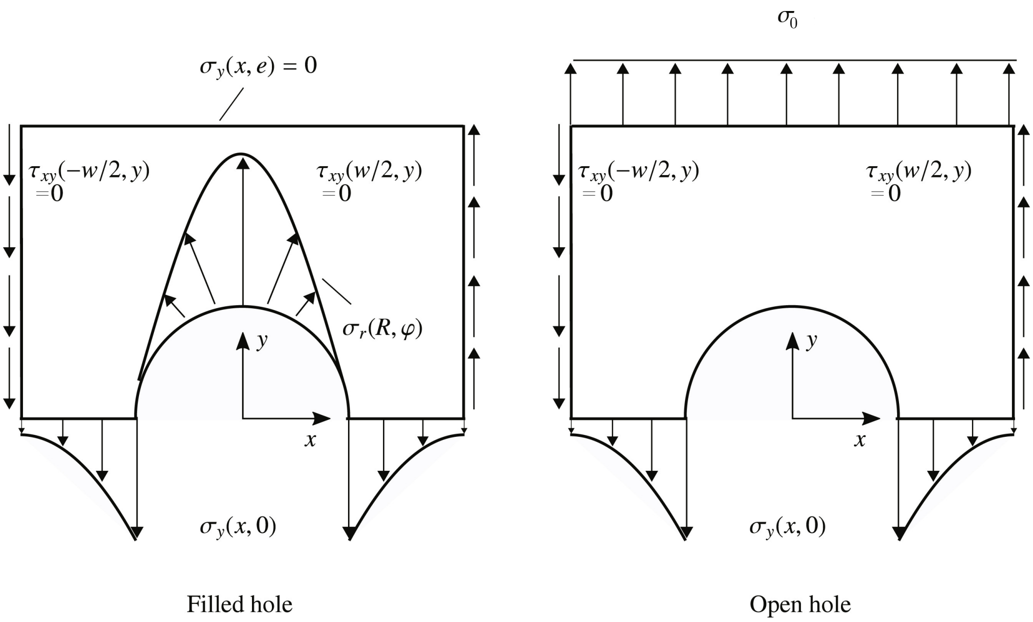

Figure 4.19: Free-form bodies with only the tractions relevant to equilibrium in the loading y direction shown. Using the periodic arrangement technique, the edge shear stresses $\tau_{xy}(\pm w/2, y)$ become negligible, so the external load is carried solely by the net-section stress $\sigma_y(x, 0)$, adapted from reference [14].

4.2.1 Elimination of Tractions Parallel to the Loading Direction

The objective of this section is to eliminate the nonzero traction parallel to the loading direction along the vertical edges, ensuring the conditions $\tau_{xy}\,(\pm w/2, y) = 0$ for the open hole case, and $\sigma_y(x, e) = 0$ together with $\tau_{xy}\,(\pm w/2, y) = 0$ for the filled hole case. The approach employs a cancellation method applicable to any plane problem possessing at least one axis of symmetry. The method involves superimposing virtual auxiliary plates, generated by shifting and periodically replicating the stress field, under the assumption of symmetry about the y-axis, this technique is pictured in Figure 4.20. The stress field considered is that of the infinite-domain solution, expressed in terms of its Airy stress function F^{inf}. F_{11}^{inf} represents the central plate, which is duplicated and placed horizontally to form F_{12}^{inf} and F_{13}^{inf}. Each auxiliary plate eliminates the shear stresses $\tau_{xy}\,(\pm w/2, y)$ along one side edge , but in doing so introduces new shear stresses at the opposite edge. As a result, residual shear tractions remain along both vertical boundaries. There magnitude depend on the number of horizontally aligned auxiliary plates, vanishing when it tends to infinity. For the filled hole case, the normal stresses $\sigma_y(x, e)$ at the horizontal edge $y = e$ are removed by vertically duplicating F^{inf}, reversing its sinusoidal tractions to tension, and rotating it by π rad about the hole boundary, producing the boundary plate F_{21}^{inf}. However, the horizontal auxiliary plates F_{1j}^{inf} introduce additional σ_y^-

along $y = e$; therefore, they are vertically mirrored as applied to F_{11}^{inf}, to ensure complete cancellation of the tractions parallel to the loading direction. This step is unnecessary in doubly symmetric problems, such as the orthotropic open hole configuration, where no horizontal edges are present. The following formulae summarize the methodology described above:

$$F_{ij}^{\text{inf}}(x,y) = \underbrace{(-1)^{i+1}}_{\text{Tension/Compression}} \cdot F^{\text{inf}} \underbrace{\left((-1)^{i+1}x_j,\ (-1)^{i+1}y_i\right)}_{\text{load shifting along hole}}, \tag{4.36}$$

$$\text{with} \quad [x_j] = [x_1\ x_2\ x_3\ x_4\ \ldots] = [x \quad x-w \quad x+w \quad x-2w \quad \ldots], \tag{4.37}$$

$$[y_i] = \begin{cases} [y] & \text{open hole,} \\ [y_1\ y_2] = [y \quad y-2e] & \text{filled hole.} \end{cases} \tag{4.38}$$

The auxiliary plates stress fields are superimposed using:

$$\text{PA}(F^{\text{inf}}) = \sum_{i=1}^{n_y} \sum_{j=1}^{n_x} F_{ij}^{\text{inf}}, \tag{4.39}$$

where n_x represents the number of horizontally, n_y the number of vertically aligned plates and PA($\square$) is the operator executing this arrangement for any infinite-domain stress field symmetric to the y-axis. Additionally, for open hole $n_y = 1$ and for filled hole $n_y = 2$. The value of n_x is determined based on the error in load transfer caused by the residual shear stresses along the vertical boundaries, $\psi_{\tau_{xy}}$. With that the formulation for the cancellation of tractions parallel to the load direction has been summarized. For problems symmetric to the x-axis the whole setup is rotated by $\pi/2$ rad.

4.2.2 Elimination of Tractions Perpendicular to the Loading Direction

The objective of this section is to eliminate the nonzero tractions perpendicular to the loading direction along the vertical edges in both open and filled hole problems ensuring the fulfillment of the condition $\sigma_x\,(\pm w/2, y) = 0$. These tractions result from the periodic auxiliary field introduced in the infinite-domain problems to cancel tractions perpendicular to the load direction. The stress function $F_l^{\text{VE}\perp}$ is an expansion of the boundary violations in a Fourier series, where the index l serves as a placeholder for any arbitrary stress function whose associated nonzero

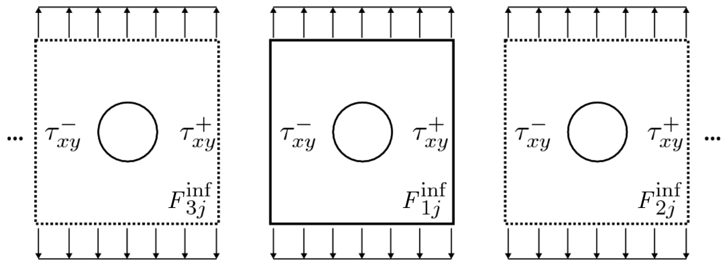

(a) Open hole, adapted from reference [8].

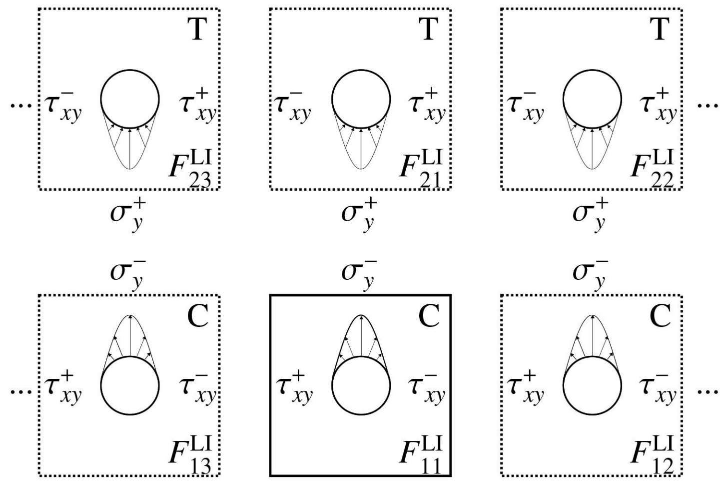

(b) Filled hole, adapted from reference [9].

Figure 4.20: Periodic arrangement used to cancel nonzero tractions along straight edges in load direction. The solid-outlined plate F_{11}^{inf} is the non-shifted original plate obtained from the infinite-domain solution. In (a) the finite domain open-hole problem is bounded at $x = \pm w/2$, and therefore the the arrangement is done only horizontally. For the filled hole in (b), tractions at $y = e$ must also vanish, and therefore F^{inf} has to be vertically duplicated. The sinusoidal tractions are reversed from compression to tension, and the duplicated plate rotated by π rad about the hole boundary, producing the boundary plate F_{12}^{inf}. In the filled hole plate, C denotes compression and T tension.

tractions must be eliminated. For the open hole case, the superimposed field is symmetric with respect to both the x- and y-axes, whereas for the filled hole case, it is symmetric about the y-axis and antisymmetric about $y = e$. Consequently, when specifying the stress deviation along the vertical edges, the following conditions must be satisfied:

$$\begin{aligned} \sigma_{x,l}^{\mathrm{dev}}(\pm w/2, y) &= \sigma_{x,l}^{\mathrm{dev}}(\pm w/2, -y) && \text{open hole,} \\ \sigma_{x,l}^{\mathrm{dev}}(\pm w/2, y^*) &= -\sigma_{x,l}^{\mathrm{dev}}(\pm w/2, -y^*) \quad \text{with} \quad y^* = y - e && \text{filled hole.} \end{aligned} \tag{4.40}$$

Recognizing these symmetries allows the Fourier series expansions over the virtual wavelength l_{Fo} to be simplified as follows.

Open hole:

$$\frac{\sigma_{x,l}^{\mathrm{VE}\perp}(\pm w/2, y)}{\sigma_0} = \sum_{n=1}^{N_l} f_{l,n}^{\sigma_x} \cos \alpha_n y \quad \text{with} \tag{4.41}$$

$$\alpha_n = \frac{2n\pi}{l_{\mathrm{Fo}}}, \quad f_{l,n}^{\sigma_x} = \frac{2}{l_{\mathrm{Fo}}} \int_0^{l_{\mathrm{Fo}}} \sigma_{x,l}^{\mathrm{dev}}(\pm w/2, y) \cos \alpha_n y \; dy. \tag{4.42}$$

Filled hole:

$$\frac{\sigma_{x,l}^{\mathrm{VE}\perp}(\pm w/2, y^*)}{\sigma_d} = \sum_{n=1}^{N_l} g_{l,n}^{\sigma_x} \sin \alpha_n y^* \quad \text{with} \tag{4.43}$$

$$\alpha_n = \frac{2n\pi}{l_{\mathrm{Fo}}}, \quad g_{l,n}^{\sigma_x} = \frac{2}{l_{\mathrm{Fo}}} \int_0^{l_{\mathrm{Fo}}} \sigma_{x,l}^{\mathrm{dev}}(\pm w/2, y^*) \sin \alpha_n y^* \; dy^*. \tag{4.44}$$

It should be noted that the stress deviations at the lower and upper limits of the integral are not equal, as expressed by the following inequalities:

$$\sigma_{x,l}^{\mathrm{dev}}(\pm w/2, y = 0) \neq \sigma_{x,l}^{\mathrm{dev}}(\pm w/2, y = l_{\mathrm{Fo}}) \quad \text{open hole,} \tag{4.45}$$

$$\sigma_{x,l}^{\mathrm{dev}}(\pm w/2, y^* = 0) \neq \sigma_{x,l}^{\mathrm{dev}}(\pm w/2, y^* = l_{\mathrm{Fo}}) \quad \text{filled hole.} \tag{4.46}$$

This mismatch gives rise to the Gibbs phenomenon, producing overshoots in the associated Fourier series expansions, whereas the true deviation should decrease smoothly with increasing distance from the hole. For this reason, this type of approximation function is regarded as less reliable than the periodic arrangement technique. Moreover, employing a stress function of the form $F^{\mathrm{VE}\perp}$ necessitates an additional Fourier series expansion, making it more computationally demanding than the periodic arrangement method. To reduce the influence of periodicity and the Gibbs' phenomenon on the characteristic stresses near the hole, the virtual wavelength $l_{\mathrm{Fo}} = 40\,d$ is selected, ensuring that an undisturbed uniaxial stress state can develop in the far field ($|y| \gg d$).

The tractions of the open hole can be modelled by the Airy stress function of the form

$$\frac{F_l^{\mathrm{VE}\perp}}{\sigma_0} = a_l\, y^2 + \sum_{n=1}^{N_l} \phi_n(x)\, A_{l,n}^{\mathrm{VE}\perp} \cos \alpha_n y, \tag{4.47}$$

and the of the filled hole by

$$\frac{F_l^{\mathrm{VE}\perp}}{\sigma_d} = \sum_{n=1}^{N_l} \phi_n(x)\, A_{l,n}^{\mathrm{VE}\perp} \sin \alpha_n y^*. \tag{4.48}$$

Therein, the entities $\phi_n(x)$ denote unknown functions with respect to x. For an orthotropic plate material, the governing equations can be reduced to:

$$\frac{d^4\phi_n}{dx^4} - \left(\frac{E_y}{G_{xy}} - 2\nu_{xy}\frac{E_y}{E_x}\right)\frac{d^2\phi_n}{dx^2} + \frac{E_y}{E_x}\,\phi_n = 0. \tag{4.49}$$

The corresponding characteristic equation is

$$s^4 - E_y\left(\frac{1}{G_{xy}} - 2\frac{\nu_{xy}}{E_x}\right)s^2 + \frac{E_y}{E_x} = 0. \tag{4.50}$$

- **Case I:** The characteristic roots are identical and real, a situation found in quasi-isotropic laminates, where $s = s_1 = s_2 = 1$.
- **Case II:** The characteristic roots are real but have different values. For the laminates examined in this study, this behavior is observed in the layups [0°], $[0°/90°]_\mathrm{s}$, and $[0^\circ_5\,/\,(\pm45°)_2\,/\,90°]_\mathrm{s}$.
- **Case III:** The roots are complex and take the form $h_s \pm \mathrm{i}t_s, -h_s \pm \mathrm{i}t_s; h_s, t_s \in \mathbb{R}$. This configuration occurs in angle-ply laminates, like $[\pm45°]_\mathrm{s}$.

The general solution for Equation 4.49, is proposed by Nguyen-Hoang and Becker [9] as the following hyperbolic and trigonometric basis functions:

$$\begin{aligned}
\phi_n^{\mathrm{I}} &= C_1^{\phi_n}\cosh\alpha_n x + C_2^{\phi_n}\sinh\alpha_n x + C_3^{\phi_n} x\cosh\alpha_n x + C_4^{\phi_n} x\sinh\alpha_n x,\\
\phi_n^{\mathrm{II}} &= C_1^{\phi_n}\cosh s_1\alpha_n x + C_2^{\phi_n}\sinh s_1\alpha_n x + C_3^{\phi_n}\cosh s_2\alpha_n x + C_4^{\phi_n}\sinh s_2\alpha_n x,\\
\phi_n^{\mathrm{III}} &= \left(C_1^{\phi_n}\cosh h_s\alpha_n x + C_2^{\phi_n}\sinh h_s\alpha_n x\right)\cos t_s\alpha_n x\\
&\quad + \left(C_3^{\phi_n}\cosh h_s\alpha_n x + C_4^{\phi_n}\sinh h_s\alpha_n x\right)\sin t_s\alpha_n x.
\end{aligned} \tag{4.51}$$

The stress components of $F_l^{\mathrm{VE}\perp}$ are calculated using Equation 2.27, leading to the following expressions:

Open hole:

$$\frac{\sigma_{x,l}^{\mathrm{VE}\perp}}{\sigma_0} = 2a_l - \sum_{n=1}^{N_l} \alpha_n^2\, \phi_n(x)\, A_{l,n}^{\mathrm{VE}\perp} \cos\alpha_n y, \tag{4.52}$$

$$\frac{\sigma_{y,l}^{\mathrm{VE}\perp}}{\sigma_0} = \sum_{n=1}^{N_l} \frac{d^2\phi_n}{dx^2}\, A_{l,n}^{\mathrm{VE}\perp} \cos\alpha_n y, \tag{4.53}$$

$$\frac{\tau_{xy,l}^{\mathrm{VE}\perp}}{\sigma_0} = \sum_{n=1}^{N_l} \alpha_n \frac{d\phi_n}{dx}\, A_{l,n}^{\mathrm{VE}\perp} \sin\alpha_n y. \tag{4.54}$$

Filled hole:

$$\frac{\sigma_{x,l}^{\mathrm{VE}\perp}}{\sigma_d} = -\sum_{n=1}^{N_l} \alpha_n^2\, \phi_n(x)\, A_{l,n}^{\mathrm{V,EL}} \sin\alpha_n y^*, \tag{4.55}$$

$$\frac{\sigma_{y,l}^{\mathrm{VE}\perp}}{\sigma_d} = \sum_{n=1}^{N_l} \frac{d^2\phi_n}{dx^2}\, A_{l,n}^{\mathrm{V,EL}} \sin\alpha_n y^*, \tag{4.56}$$

$$\frac{\tau_{xy,l}^{\mathrm{VE}\perp}}{\sigma_d} = -\sum_{n=1}^{N_l} \alpha_n \frac{d\phi_n}{dx}\, A_{l,n}^{\mathrm{VE}\perp} \cos\alpha_n y^*. \tag{4.57}$$

The derivatives of ϕ_n are

$$\begin{aligned}\frac{d\phi_n^{\mathrm{I}}}{dx} = \alpha_n \Big(& C_1^{\phi_n} \sinh(\alpha_n x) + C_2^{\phi_n} \cosh(\alpha_n x)\Big) \\ & + C_3^{\phi_n} \left(\alpha_n x \sinh(\alpha_n x) + \cosh(\alpha_n x)\right) \\ & + C_4^{\phi_n} \left(\alpha_n x \cosh(\alpha_n x) + \sinh(\alpha_n x)\right),\end{aligned} \tag{4.58}$$

$$\begin{aligned}\frac{d^2\phi_n^{\mathrm{I}}}{dx^2} = \alpha_n^2 \Big(& C_1^{\phi_n} \cosh(\alpha_n x) + C_2^{\phi_n} \sinh(\alpha_n x)\Big) \\ & + C_3^{\phi_n} \left(\alpha_n^2 x \cosh(\alpha_n x) + 2\alpha_n \sinh(\alpha_n x)\right) \\ & + C_4^{\phi_n} \left(\alpha_n^2 x \sinh(\alpha_n x) + 2\alpha_n \cosh(\alpha_n x)\right),\end{aligned} \tag{4.59}$$

$$\begin{aligned}\frac{d\phi_n^{\mathrm{II}}}{dx} = \alpha_n \Big(& s_1 C_1^{\phi_n} \sinh(s_1\alpha_n x) + s_1 C_2^{\phi_n} \cosh(s_1\alpha_n x)\Big) \\ & + s_2 C_3^{\phi_n} \sinh(s_2\alpha_n x) + s_2 C_4^{\phi_n} \cosh(s_2\alpha_n x),\end{aligned} \tag{4.60}$$

$$\begin{aligned}\frac{d^2\phi_n^{\mathrm{II}}}{dx^2} &= \alpha_n^2 \left(s_1^2 C_1^{\phi_n} \cosh\left(s_1\alpha_n x\right) + s_1^2 C_2^{\phi_n} \sinh\left(s_1\alpha_n x\right)\right) \\ &\quad + s_2^2 C_3^{\phi_n} \cosh\left(s_2\alpha_n x\right) + s_2^2 C_4^{\phi_n} \sinh\left(s_2\alpha_n x\right),\end{aligned} \tag{4.61}$$

$$\begin{aligned}\frac{d\phi_n^{\mathrm{III}}}{dx} &= \alpha_n \Big\{ \cosh\left(h_s\alpha_n x\right) \left[\left(C_2^{\phi_n} h_s + C_3^{\phi_n} t_s\right) \cos\left(t_s\alpha_n x\right) + \left(C_4^{\phi_n} h_s - C_1^{\phi_n} t_s\right) \sin\left(t_s\alpha_n x\right)\right] \\ &\quad + \sinh\left(h_s\alpha_n x\right) \left[\left(C_1^{\phi_n} h_s + C_4^{\phi_n} t_s\right) \cos\left(t_s\alpha_n x\right) + \left(C_3^{\phi_n} h_s - C_2^{\phi_n} t_s\right) \sin\left(t_s\alpha_n x\right)\right] \Big\},\end{aligned} \tag{4.62}$$

$$\begin{aligned}\frac{d^2\phi_n^{\mathrm{III}}}{dx^2} &= \alpha_n^2 \Big\{ \cosh\left(h_s\alpha_n x\right) \Big[\left(2C_4^{\phi_n} h_s t_s + C_1^{\phi_n}\left(h_s+t_s\right)\left(h_s-t_s\right)\right) \cos\left(t_s\alpha_n x\right) \\ &\quad + \left(C_3^{\phi_n}\left(h_s+t_s\right)\left(h_s-t_s\right) - 2C_2^{\phi_n} h_s t_s\right) \sin\left(t_s\alpha_n x\right)\Big] \\ &\quad + \sinh\left(h_s\alpha_n x\right) \Big[\left(C_2^{\phi_n}\left(h_s+t_s\right)\left(h_s-t_s\right) + 2C_3^{\phi_n} h_s t_s\right) \cos\left(t_s\alpha_n x\right) \\ &\quad + \left(C_4^{\phi_n}\left(h_s+t_s\right)\left(h_s-t_s\right) - 2C_1^{\phi_n} h_s t_s\right) \sin\left(t_s\alpha_n x\right)\Big] \Big\}.\end{aligned} \tag{4.63}$$

The coefficients $C_i^{\phi_n}$ are obtained by imposing the following conditions:

$$\phi_n(\pm w/2) = 1, \tag{4.64}$$

$$\tau_{xy,l}^{\mathrm{VE}\perp}(\pm w/2, y) = 0 \quad \Rightarrow \quad \left.\frac{d\phi_n}{dx}\right|_{x=\pm w/2} = 0. \tag{4.65}$$

The first condition sets ϕ_n to one at the vertical edge for computational convenience. The coefficients for each case are the following:

Case I:

$$\begin{aligned} C_1^{\phi_n} &= \frac{2\sinh\left(\frac{w}{2}\alpha_n\right) + \alpha_n w \cosh\left(\frac{w}{2}\alpha_n\right)}{\sinh\left(w\alpha_n\right) + w\alpha_n}, \\ C_2^{\phi_n} &= C_3^{\phi_n} = 0, \\ C_4^{\phi_n} &= -\frac{2\alpha_n \sinh\left(\frac{w}{2}\alpha_n\right)}{\sinh\left(w\alpha_n\right) + w\alpha_n}. \end{aligned} \tag{4.66}$$

Case II:

$$
\begin{aligned}
C_1^{\phi_n} &= \frac{s_2}{s_2 \cosh\left(s_1 \frac{w}{2}\alpha_n\right) - s_1 \coth\left(s_2 \frac{w}{2}\alpha_n\right) \sinh\left(s_1 \frac{w}{2}\alpha_n\right)}, \quad C_2^{\phi_n} = 0, \\
C_3^{\phi_n} &= \frac{s_1}{s_2 \coth\left(s_1 \frac{w}{2}\alpha_n\right) \sinh\left(s_2 \frac{w}{2}\alpha_n\right) - s_1 \cosh\left(s_2 \frac{w}{2}\alpha_n\right)}, \quad C_4^{\phi_n} = 0.
\end{aligned}
\tag{4.67}
$$

Case III:

$$
\begin{aligned}
C_1^{\phi_n} &= \frac{4h_s \cosh\left(h_s \frac{w}{2}\alpha_n\right) \sin\left(t_s \frac{w}{2}\alpha_n\right) + 2t_s \cos\left(t_s \frac{w}{2}\alpha_n\right) \sinh\left(h_s \frac{w}{2}\alpha_n\right)}{h_s \sin\left(t_s \frac{w}{2}\alpha_n\right) + t_s \cosh\left(h_s \frac{w}{2}\alpha_n\right)}, \\
C_2^{\phi_n} &= C_3^{\phi_n} = 0, \\
C_4^{\phi_n} &= \frac{2t_s \cosh\left(h_s \frac{w}{2}\alpha_n\right) \sin\left(t_s \frac{w}{2}\alpha_n\right) - 2h_s \cos\left(t_s \frac{w}{2}\alpha_n\right) \sinh\left(h_s \frac{w}{2}\alpha_n\right)}{h_s \sin\left(t_s \frac{w}{2}\alpha_n\right) + t_s \sinh\left(h_s \frac{w}{2}\alpha_n\right)}.
\end{aligned}
\tag{4.68}
$$

From Equation 4.41, 4.52 plus Equation 4.43, 4.55, respectively, and taking into account Equation 4.64, leads to:

$$
a_l = \frac{f_{l,0}^{\sigma_x}}{4}, \qquad A_{l,n}^{\mathrm{VE}\perp} = \begin{cases} \dfrac{f_{l,n}^{\sigma_x}}{\alpha_n^2}, & \text{open hole}, \\[2ex] \dfrac{g_{l,n}^{\sigma_x}}{\alpha_n^2}, & \text{filled hole}. \end{cases}
\tag{4.69}
$$

This concludes the definition of $F_l^{\mathrm{VE}\perp}$, providing a formulation capable of canceling the tractions perpendicular to the load direction in the vertical edges, $x = \pm w/2$. The filled hole problem is bounded by the horizontal edge $y = e$, and therefore, the shear tractions $\tau_{xy}(x, e)$, which are perpendicular to the load direction, have not been canceled. The shear stresses are antisymmetric with respect to the y-axis, and therefore $\tau_{xy}(x, y) = -\tau_{xy}(-x, y)$. By adapting Equation 4.48 to satisfy the shear stress antisymmetry condition, the following stress function is obtained:

$$
\frac{F_l^{\mathrm{HE}\perp}}{\sigma_d} = \sum_{n=1}^{N_l} \varrho_n(y), A_{l,n}^{\mathrm{HE}\perp}, \sin\left(\beta_n x\right),
\tag{4.70}
$$

where $\varrho_n(y)$ has the same form as $\phi_n(x)$ in Equation 4.51. This form leads to unbounded stresses as the hole distance increases, $|y| \to \infty$, which would significantly disturb the stress-free condition along the vertical edges. Consequently, the condition $\tau_{xy}(x, e)$ is not included in the present formulation. The implications of this simplification will be examined later in this chapter.

4.2.3 Enforcement of Hole Boundary Conditions

The free-edge BCs have been satisfied through PA(F^{inf}) and $F^{\text{VE}\perp}$; however, the tractions on the hole boundary have thus far been neglected. As a result, superimposing these correction functions and potentials onto the infinite open or filled hole solution will lead to incorrect hole BCs. These can be corrected by superimposing additional complex potentials $\Phi_k^{\text{HBC,sv}}$, with the general form of Equation 4.22. To construct the correction field, the coefficients $\bar{\beta}_m$ and $\bar{\alpha}_m$ are evaluated using Equation 4.10. The loading functions required for the Fourier coefficients are derived from Equation 4.8, where the stresses used in defining these loading functions are obtained through the Fourier series expansion of the boundary condition violations. The index l denotes any arbitrary stress field and the hole tractions $\sigma_{r,l}^{\text{dev}}(R,\varphi)$ and $\tau_{r\varphi,l}^{\text{dev}}(R,\varphi)$ differ from the prescribed boundary conditions at the hole, given by Equation 4.31 for the open hole and Equation 4.33 for the filled hole. These deviations in the hole boundary conditions can be expressed through a Fourier series expansion

$$\sigma_{r,l}^{\text{HBC}}(R,\varphi)/\sigma_0 = \frac{f_{l,0}^{\sigma_r}}{2} + \sum_{n=1}^{N} f_{l,n}^{\sigma_r}\cos n\varphi + \sum_{n=1}^{N} g_{l,n}^{\sigma_r}\sin n\varphi, \tag{4.71}$$

$$\tau_{r\varphi,l}^{\text{HBC}}(R,\varphi)/\sigma_0 = \frac{f_{l,0}^{\tau_{r\varphi}}}{2} + \sum_{n=1}^{N} f_{l,n}^{\tau_{r\varphi}}\cos n\varphi + \sum_{n=1}^{N} g_{l,n}^{\tau_{r\varphi}}\sin n\varphi. \tag{4.72}$$

Where stress deviations can be normalized to σ_0 for open hole and to σ_d when dealing with the filled hole problem. The Fourier coefficients can be calculated using

$$\begin{aligned}
f_{l,n}^{\sigma_r} &= \frac{1}{\pi\,\sigma_0}\int_0^{2\pi} \sigma_{r,l}^{\text{dev}}(R,\varphi)\cos n\varphi\, d\varphi,\\
g_{l,n}^{\sigma_r} &= \frac{1}{\pi\,\sigma_0}\int_0^{2\pi} \sigma_{r,l}^{\text{dev}}(R,\varphi)\sin n\varphi\, d\varphi,\\
f_{l,n}^{\tau_{r\varphi}} &= \frac{1}{\pi\,\sigma_0}\int_0^{2\pi} \tau_{r\varphi,l}^{\text{dev}}(R,\varphi)\cos n\varphi\, d\varphi,\\
g_{l,n}^{\tau_{r\varphi}} &= \frac{1}{\pi\,\sigma_0}\int_0^{2\pi} \tau_{r\varphi,l}^{\text{dev}}(R,\varphi)\sin n\varphi\, d\varphi.
\end{aligned} \tag{4.73}$$

All necessary tools to handle both the straight edges and the hole boundary are now available. However, each correction function or potential targets only a specific subset of boundary tractions and may even interact with or influence the others. Hence, the next section introduces an iterative procedure aimed at reducing the boundary condition violations along all edges simultaneously.

4.2.4 Boundary Conditions Enforced via Iterative Corrections

In order to fulfill all considered BCs, the correction functions are applied in an iterative manner until the residual errors are reduced to a negligible level. Summarizing their behavior, the periodic arrangement function $\mathrm{PA}(F^{\mathrm{inf}})$ enforces $\tau_{xy}(\pm w/2, y) = 0$ and $\sigma_y(x, e) = 0$, but simultaneously disturbs the hole BCs, namely $\sigma_x(\pm w/2, y) = 0$, as well as $\tau_{xy}(x, e) = 0$. The correction function $F_l^{\mathrm{VE}\perp}$ ensures the condition $\sigma_x(\pm w/2, y) = 0$, yet it also interferes with the hole BCs and $\tau_{xy}(x, e) = 0$. Lastly, the correction function F_l^{HBC} explicitly addresses the hole BCs, but in doing so it affects all BCs along the straight edges. The iterative procedure is described by the flowchart in Figure 4.21.

First, the infinite-domain stress field is established in a way that satisfies the hole BC. Next, the periodic arrangement operator, $\mathrm{PA}(F^{\mathrm{inf}})$, is applied to the infinite-domain problem, followed by the correction function $F_l^{\mathrm{VE}\perp}$. Both corrections, however, introduce violations of the hole BC, which are then compensated through the use of F_l^{HBC}, though this in turn affects the free-edge condition in the vertical and horizontal edges. To mitigate this issue, the stress field produced by F_l^{HBC} is also arranged periodically, in the same manner as F^{inf}, after which an additional correction function, $F_{l+1}^{\mathrm{VE}\perp}$, is superimposed to cancel the new tractions perpendicular to the load direction along the vertical edges, reintroducing interference with the hole BCs. It should be noted that this is the only correction function that does not require periodic arrangement, since it already accounts for the condition $\tau_{xy}(\pm w/2, y) = 0$ when defining the stress function. Furthermore, for finite-domain problems bounded by the horizontal edge $y = e$, the stress-free condition $\sigma_y(x, e) = 0$ remains unaffected. This is because the stress function $F_l^{\mathrm{VE}\perp}$ is constructed with antisymmetry about the axis $y = e$, consistent with the antisymmetry inherent in the periodic auxiliary field, thereby ensuring that the tractions normal to the horizontal edge also vanish. Through successive iterations, the procedure ensures the simultaneous satisfaction of all prescribed BCs, leading to the following expression for the stress function of the complete finite-domain solution:

$$F = \underbrace{\sum_{i=1}^{n_y} \sum_{j=1}^{n_{x,\min}} F_{ij}^{\mathrm{inf}}}_{\text{periodic field of } F^{\mathrm{inf}}} + \sum_{l=1}^{L} \left\{ F_l^{\mathrm{VE}\perp} + \underbrace{\sum_{i=1}^{n_y} \sum_{j=1}^{n_{x,\min}} F_{l,ij}^{\mathrm{HBC}}}_{\text{periodic field of } F_l^{\mathrm{HBC}}} \right\}. \tag{4.74}$$

Here, L denotes the number of iterations required until the BCs are sufficiently satisfied. The adequacy of this can be verified by evaluating the load transfer values

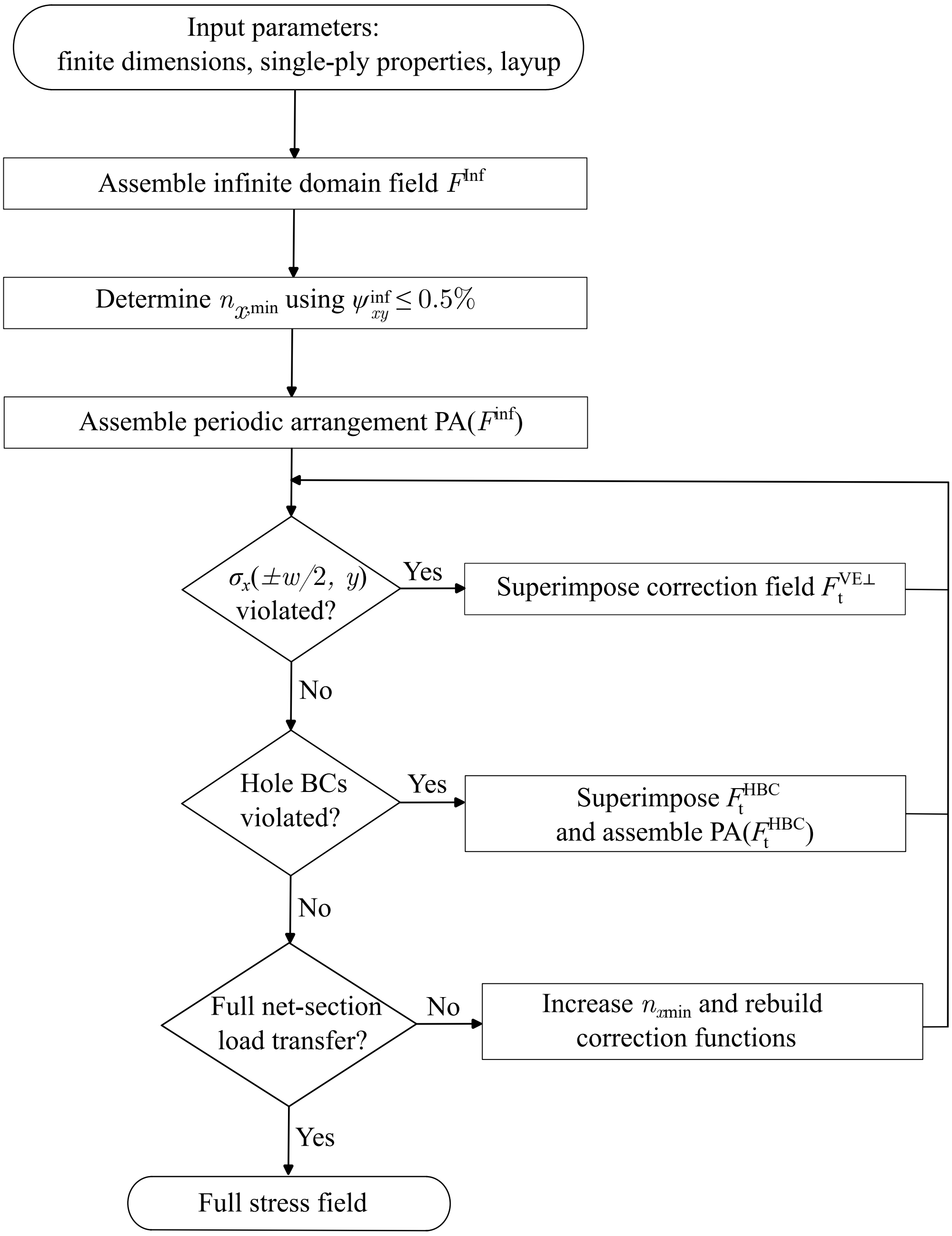

Figure 4.21: Flowchart for stress calculus of finite-width plates with open and filled holes, adapted from reference [14].

and checking the convergence criteria, with the following expressions.

Open hole:

$$
\begin{aligned}
\psi_{\sigma_r} &= \frac{R}{P_{\mathrm{By}}} \int_0^{2\pi} \sqrt{\sigma_r(R,\varphi)^2}\, \sin\varphi \, d\varphi \leq 0.01, \\
\psi_{\tau_{r\varphi}} &= \frac{R}{P_{\mathrm{By}}} \int_0^{2\pi} \sqrt{\tau_{r\varphi}(R,\varphi)^2}\, \cos\varphi \, d\varphi \leq 0.01, \\
\psi_{\sigma_x} &= \frac{4}{P_{\mathrm{By}}} \int_0^{l_{Fo}/2} \sqrt{\sigma_x(\pm w/2, y)^2}\, dy \leq 0.01, \\
\psi_{\tau_{xy}} &= \frac{4}{P_{\mathrm{By}}} \int_0^{\infty} \sqrt{\tau_{xy}(\pm w/2, y)^2}\, dy \leq 0.01, \\
\psi_{\sigma_y^{\mathrm{inf}}} &= \frac{2}{P_{\mathrm{By}}} \int_0^{w/2} \sqrt{\big(\sigma_y(x, \pm l_{Fo}/2) - \sigma_0\big)^2}\, dx \leq 0.01, \\
\chi_{\sigma_y} &= \frac{2}{P_{\mathrm{By}}} \int_R^{w/2} \sigma_y(x,0)\, dx, \qquad \text{with } \left|\chi_{\sigma_y} - 1\right| \leq 0.01.
\end{aligned}
\tag{4.75}
$$

Filled hole:

$$
\begin{aligned}
\psi_{\sigma_r} &= \frac{R}{P_{\mathrm{Bea}}} \int_0^{2\pi} \sqrt{\sigma_r(R,\varphi)^2}\, \sin\varphi \, d\varphi \leq 0.01, \\
\psi_{\tau_{r\varphi}} &= \frac{R}{P_{\mathrm{Bea}}} \int_0^{2\pi} \sqrt{\tau_{r\varphi}(R,\varphi)^2}\, \cos\varphi \, d\varphi \leq 0.01, \\
\psi_{\sigma_x} &= \frac{2}{P_{\mathrm{Bea}}} \int_0^{e} \sqrt{\sigma_x(\pm w/2, y^*)^2}\, dy^* \leq 0.01, \\
\psi_{\tau_{xy}} &= \frac{2}{P_{\mathrm{Bea}}} \int_{-l_{Fo}/2}^{e} \sqrt{\tau_{xy}(\pm w/2, y)^2}\, dy \leq 0.01, \\
\chi_{\sigma_r} &= \frac{R}{P_{\mathrm{Bea}}} \int_0^{\pi} \sigma_r(R,\varphi)\, \sin\varphi \, d\varphi, \qquad \text{with } \left|\chi_{\sigma_r} - 1\right| \leq 0.01, \\
\chi_{\sigma_y} &= \frac{2}{P_{\mathrm{Bea}}} \int_R^{w/2} \sigma_y(x,0)\, dx, \qquad \text{with } \left|\chi_{\sigma_y} - 1\right| \leq 0.01.
\end{aligned}
\tag{4.76}
$$

Where ψ_{σ_r}, $\psi_{\tau_{r\varphi}}$, ψ_{σ_x}, $\psi_{\tau_{xy}}$ indicate deviations in the corresponding stress-free BCs, which can be corrected by increasing the number of iterations L. In the periodic Fourier series expansion, the upper and lower limits of the integral in ψ_{σ_x} are set to $y = \pm l_{Fo}/2$, under the conservative assumption that within half the wavelength l_{Fo}, Gibbs' phenomenon has only a negligible effect. This ensures that an undisturbed uniaxial stress state can develop in that region. Inaccurate load transfer ratios χ_{σ_y} and χ_{σ_r} arise from either an excessive force flux through the hole edge or elevated shear stresses along the vertical boundaries at $x = \pm w/2$. The former can be corrected by introducing additional correction functions F_l^{HBC}, while the latter is addressed by increasing the minimum number of plates $n_{x,\min}$. The correction functions must then be recalculated accordingly.

4.2.5 Analysis of Characteristic Stresses

Now we verify if the formulation was well implemented by comparing the results with numerical simulations for the open hole problem at $w/d = \{3, 10, 20\}$ and for the filled hole problem at $w/d = \{3, 10, 20\}$ with $e/d = \{2.5, 10\}$. In addition, our results are compared with those reported by Nguyen-Hoang and Becker [8, 9], authors of the formulation, which present results for the open hole case at $w/d = \{3, 20\}$ and for the filled hole case at $w/d = \{3, 20\}$ with $e/d = \{3, 10\}$. For the filled hole case, we select $e/d = 2.5$, in line with industry standards for bolt edge distance in aircraft composite laminates, where $e/d = 2.5$. Additionally, Nguyen-Hoang and Becker [8, 9] demonstrated that this approach provides a more accurate solution than the heuristic method proposed by Tan and Tan-Heywood [5–7].

4.2.5.1 Analysis of the Finite-Width Solution: Open Hole

The stresses are presented in Figure 4.22, Figure 4.23, Figure 4.24, Figure 4.25, and Figure 4.26 for the different laminates. The relative errors calculated against using as reference value the numerical results are presented in Table 4.3. Nguyen-Hoang and Becker [9] obtained a maximum error magnitude of 1.4 % for the [±45°] laminate, whereas in our analysis, we obtained a maximum error of 3.96%, for the same laminate. This deviation can be clearly observed in Figure 4.25. The underlying reason, was that as mentioned in subsection 4.1.2, along the vertical edge $x = \pm w/2$, a sign change must be accounted for when the real part of the complex constant μ_k is non-zero. It should also be noted that the influence of this effect diminishes as w/d increases. As future work, this condition should be incorporated into the code. For the present, we conclude that the formulation has been correctly implemented for laminates with $\text{Re}[\mu_k] \approx 0$ as well as to cases with $w/d \geq 10$.

Table 4.3: Maximum stress relative error (%) in open hole tension for various laminate configurations comparing numerical results with the analytical solution, at different w/d values.

	[0°]	Quasi-isotropic	$[0°/90°]_s$	$[\pm45°]_s$	$[0^\circ_5\,/\,(\pm45°)_2\,/\,90°]_s$
$w/d = 3$	-1.17%	-0.44%	-0.71%	-3.96%	-1.34%
$w/d = 10$	-1.21%	-0.87%	-0.70%	-1.99%	-0.93%
$w/d = 20$	-0.82%	-0.21%	-0.19%	-0.69%	- 0.36%

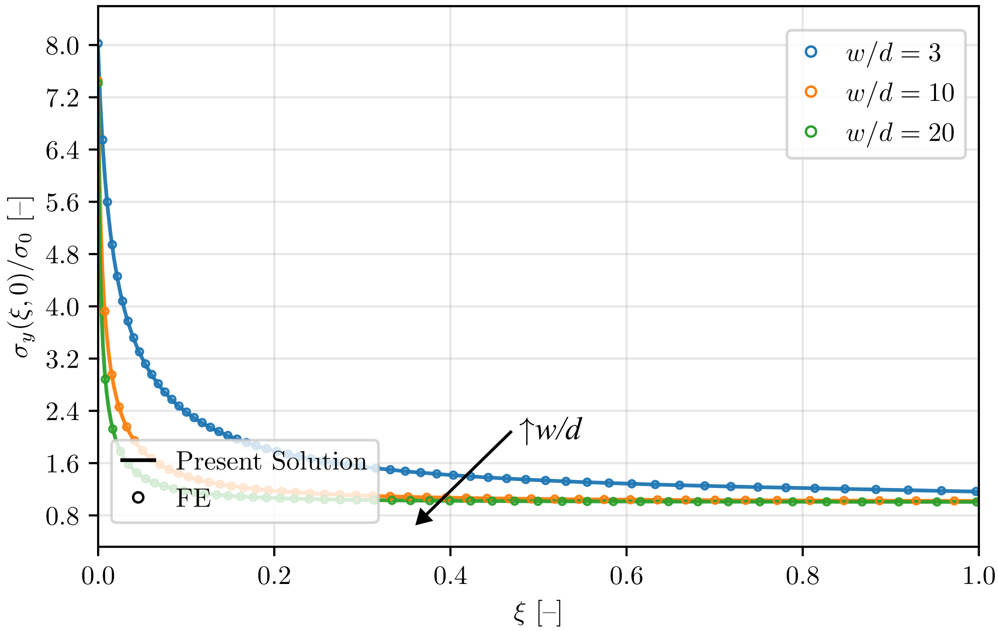

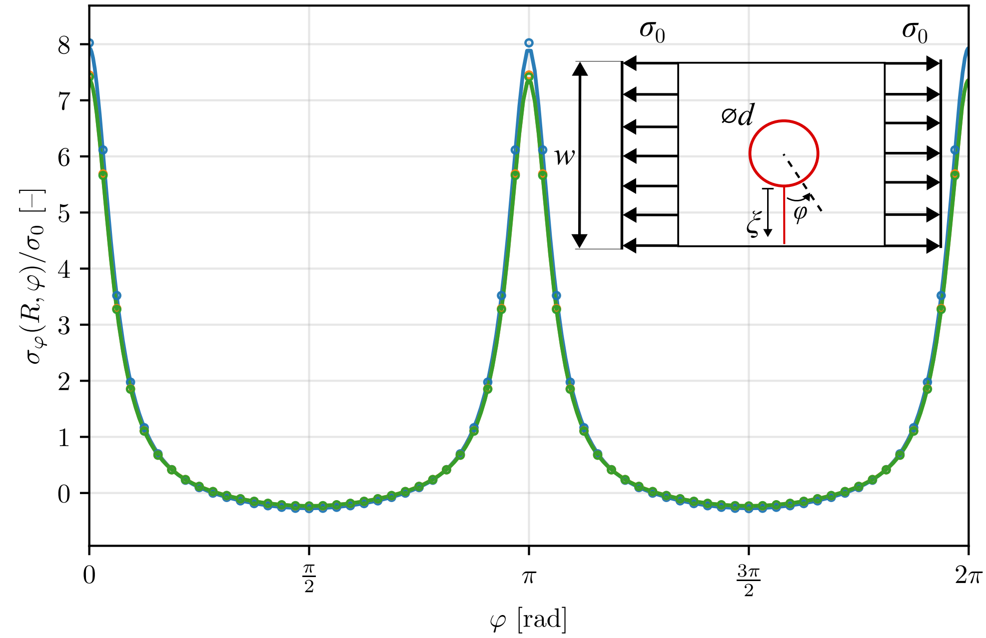

Figure 4.22: Open hole tension finite-width plate, comparison between analytical and FE solution for the [0°] laminate, for $w/d = \{3, 10, 20\}$. The upper plot shows the normalised net-section stresses, while the lower plot shows the normalised circumferential stresses.

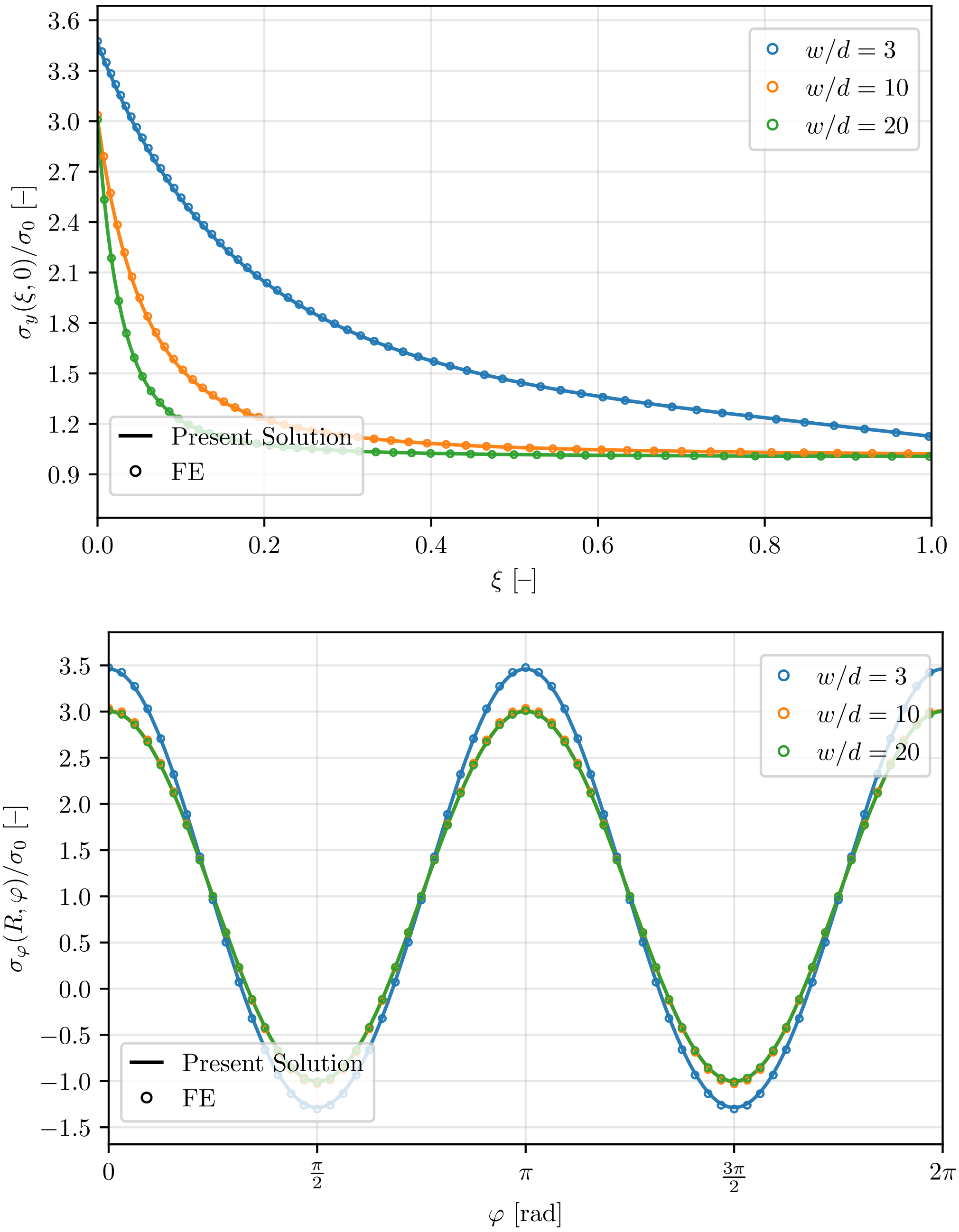

Figure 4.23: Open hole tension finite-width plate, comparison between analytical and FE solution for the quasi-isotropic laminate, for $w/d = \{3, 10, 20\}$. The upper plot shows the normalised net-section stresses, while the lower plot shows the normalised circumferential stresses.

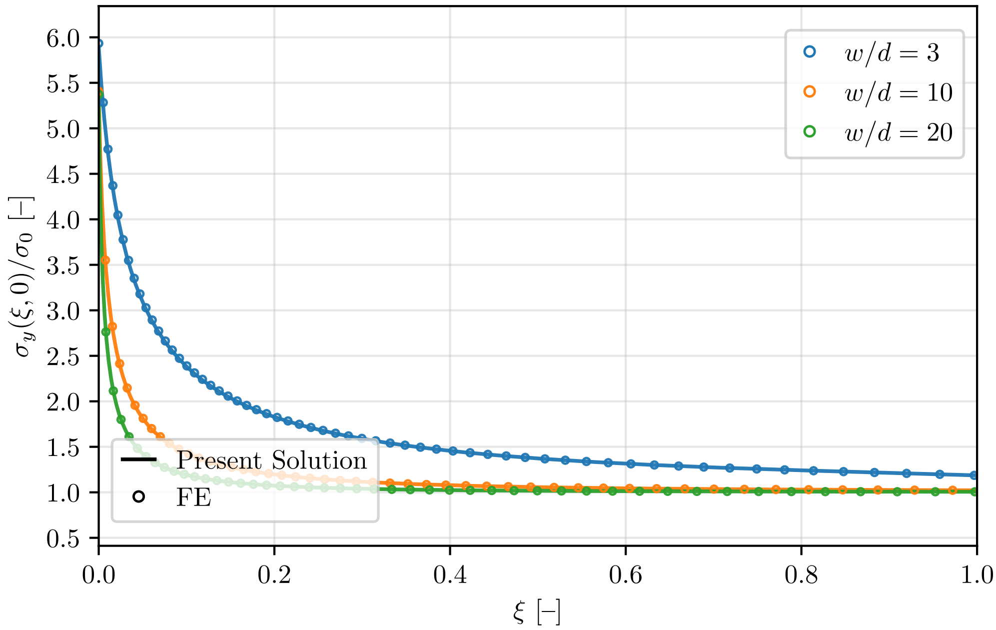

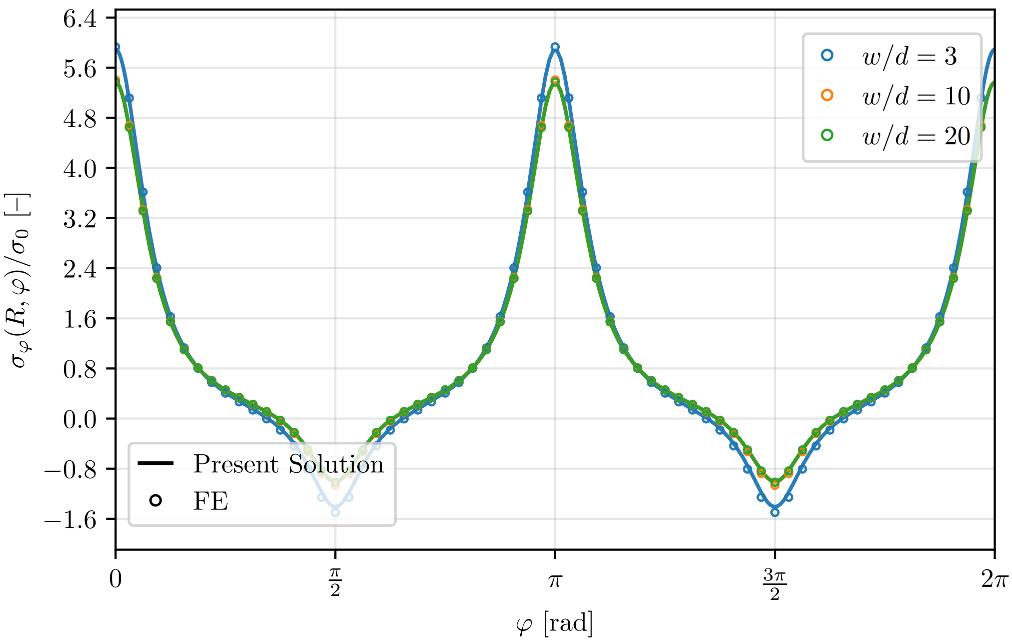

Figure 4.24: Open hole tension finite-width plate, comparison between analytical and FE solution for the $[0°/90°]_s$ laminate, for $w/d = \{3, 10, 20\}$. The upper plot shows the normalised net-section stresses, while the lower plot shows the normalised circumferential stresses.

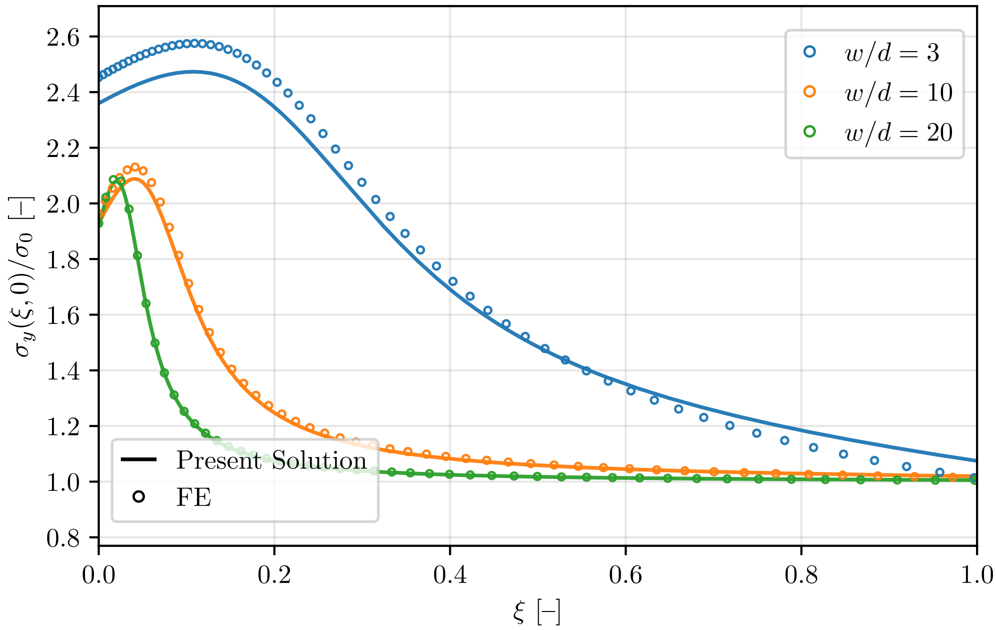

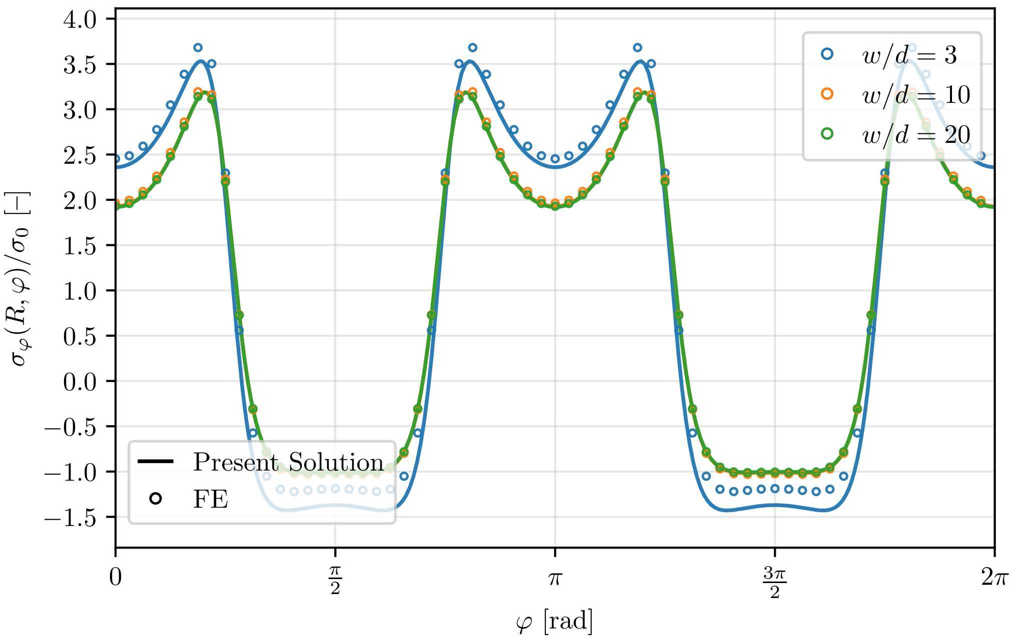

Figure 4.25: Open hole tension finite-width plate, comparison between analytical and FE solution for the $[\pm 45°]_s$ laminate, for $w/d = \{3, 10, 20\}$. The upper plot shows the normalised net-section stresses, while the lower plot shows the normalised circumferential stresses.

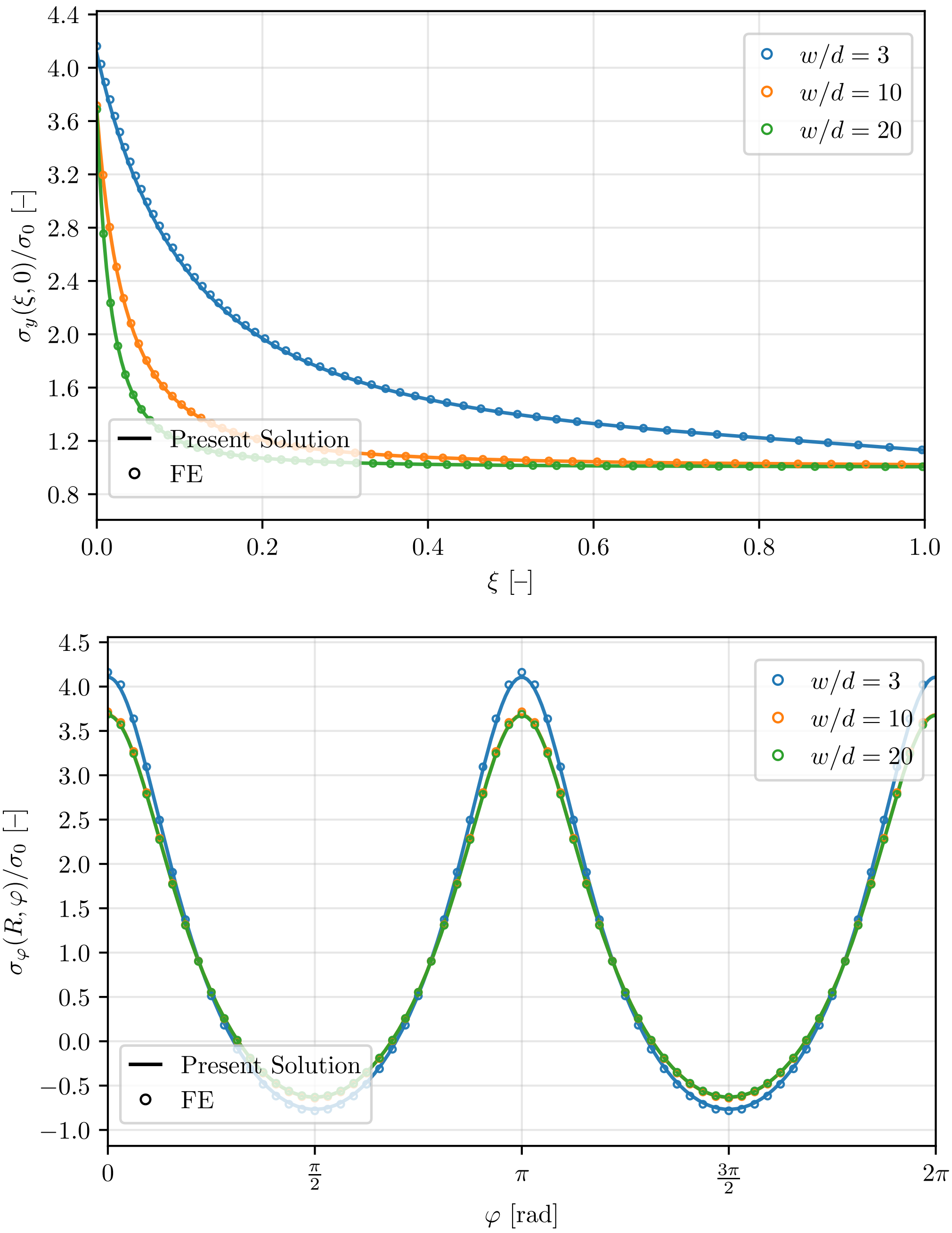

Figure 4.26: Open hole tension finite-width plate, comparison between analytical and FE solution for the $[0^\circ_5\,/\,(\pm 45^\circ)_2\,/\,90^\circ]_\mathrm{s}$ laminate, for $w/d = \{3, 10, 20\}$. The upper plot shows the normalised net-section stresses, while the lower plot shows the normalised circumferential stresses.

4.2.5.2 Analysis of the Finite-Width Solution: Filled Hole

For the finite-width filled hole case with $e/d = 2.5$, the stress distributions for each laminate are shown in Figure 4.27, Figure 4.28, Figure 4.29, Figure 4.30, and Figure 4.31. For $e/d = 10$, the corresponding results are presented in Figure 4.32, Figure 4.33, Figure 4.34, Figure 4.35, and Figure 4.36. The results obtained do fit Nguyen-Hoang and Becker [8] results, for all laminates except for the $[\pm 45°]_s$ laminate, which was not dealt in its study for filled holes. Similarly, to the reference, when the effect by finite dimensions is dominantly or even only caused by a small end distance as for in our case $e/d = 2.5$, $w/d = 3$, slight deviations are observable in the characteristic stresses. This is due to the remaining shear stresses $\tau_{xy}(x, e)$ along the horizontal boundary $y = e$, which were not covered by the formulation, the solution to this is presented in subsection 4.2.2. Due to its complexity, this was not implemented in the present work; however, it may be addressed in future studies. Overall, the formulation provides satisfactory results; nevertheless, if the finite dimensions effect is predominantly governed by the end distance e, a safety coefficient should be applied to ensure that stresses are not underpredicted.

Table 4.4: Maximum stress relative error (%) in finite-width filled hole for various laminate configurations comparing numerical results with the analytical solution at different w/d values, for $e/d = 2.5$ and $e/d = 10$.

	$[0°]$	Quasi-isotropic	$[0°/90°]_s$	$[\pm 45°]_s$	$[0^\circ_5\,/\,(\pm 45°)_2\,/\,90°]_s$
			$e/d = 2.5$		
$w/d = 3$	-8.93%	-1.81%	-2.51%	-4.38%	-3.90%
$w/d = 10$	-10.46%	-7.64%	-3.77%	-15.91%	-9.23%
$w/d = 20$	-10.41%	-7.14%	-3.60%	-19.80%	-9.03%
			$e/d = 10$		
$w/d = 3$	-1.01%	-1.42%	-0.57%	-4.76%	-1.05%
$w/d = 10$	-2.50%	0.14%	-0.36%	0.16%	-0.31%
$w/d = 20$	-3.29%	-0.96%	-0.71%	-1.30%	-1.76%

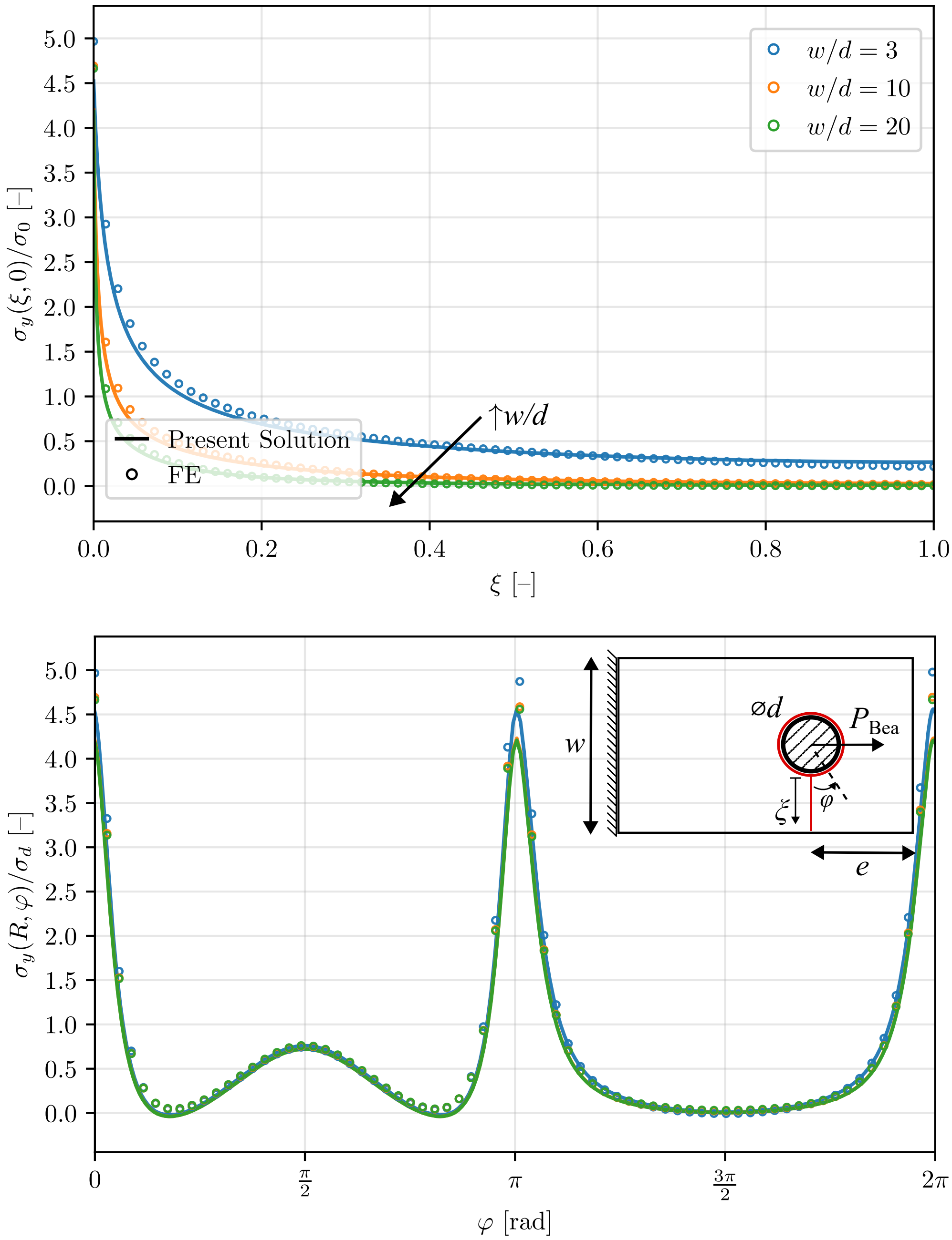

Figure 4.27: Filled hole finite-width plate, comparison between analytical and FE solutions for the [0°] laminate, with $e/d = 2.5$. The upper plot shows the normalised net-section stresses, while the lower plot shows the normalised circumferential stresses.

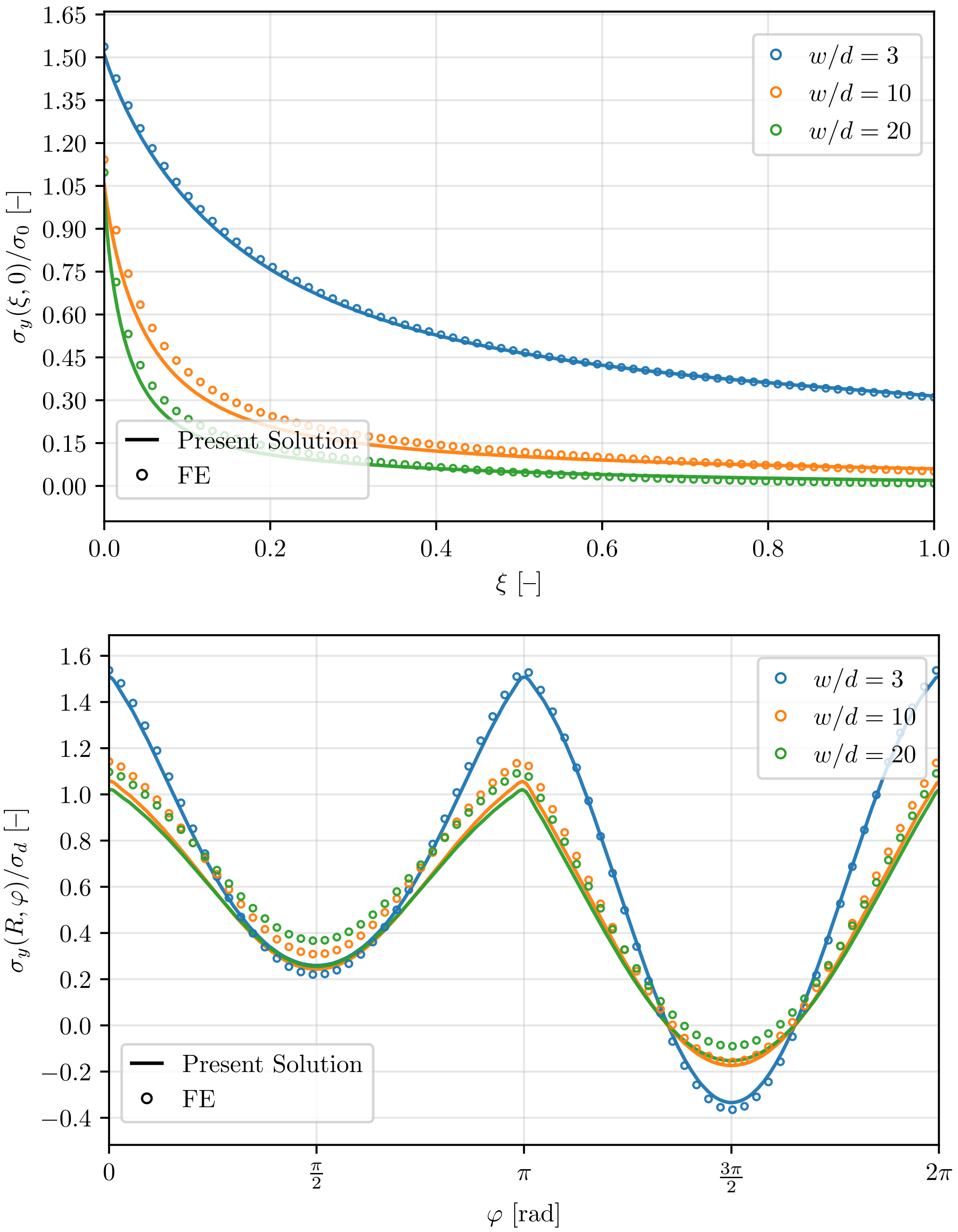

Figure 4.28: Filled hole finite-width plate, comparison between analytical and FE solutions for the quasi-isotropic quasi-isotropic laminate, with $e/d = 2.5$. The upper plot shows the normalised net-section stresses, while the lower plot shows the normalised circumferential stresses.

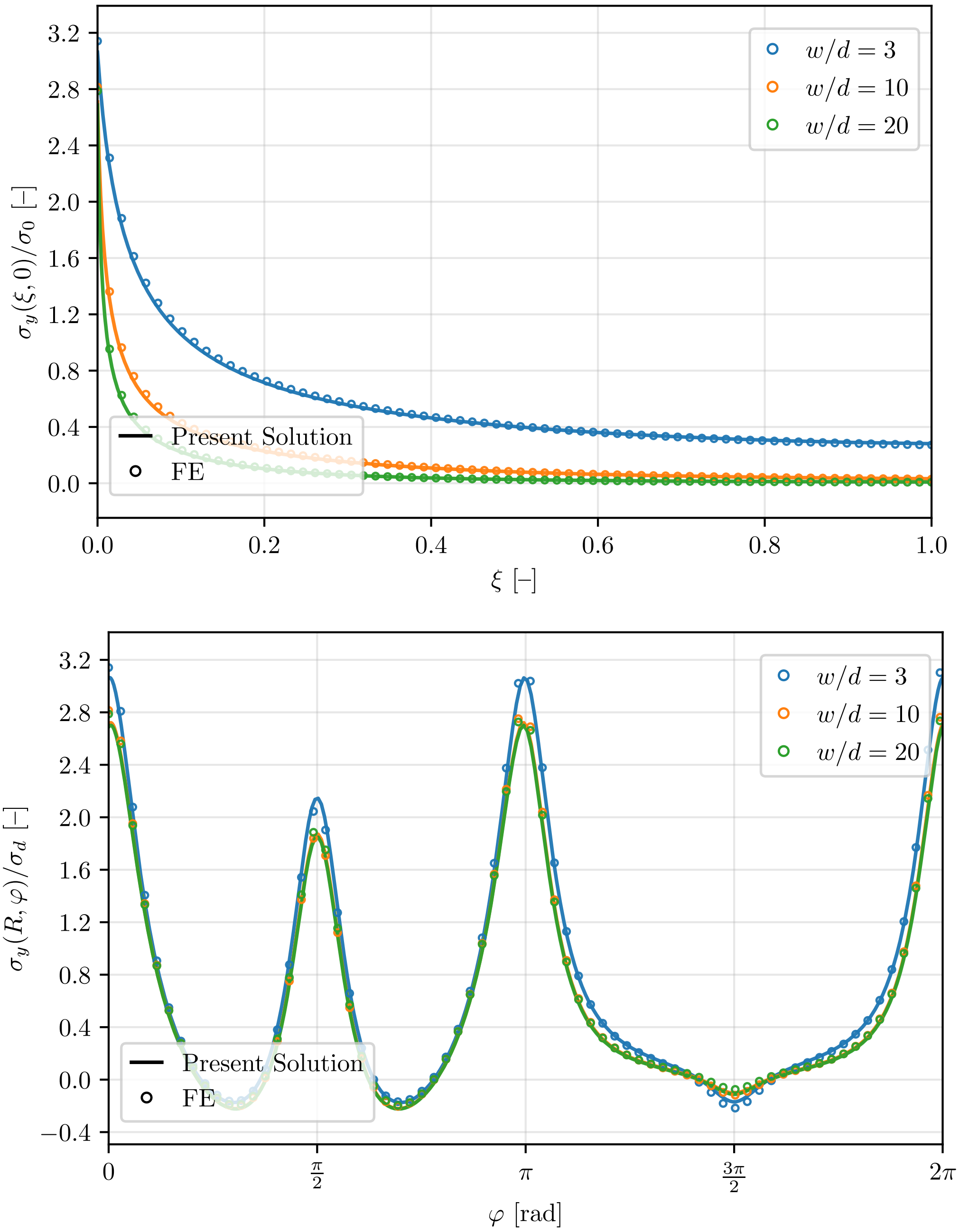

Figure 4.29: Filled hole finite-width plate, comparison between analytical and FE solutions for the $[0°/90°]_s$ laminate, with $e/d = 2.5$. The upper plot shows the normalised net-section stresses, while the lower plot shows the normalised circumferential stresses.

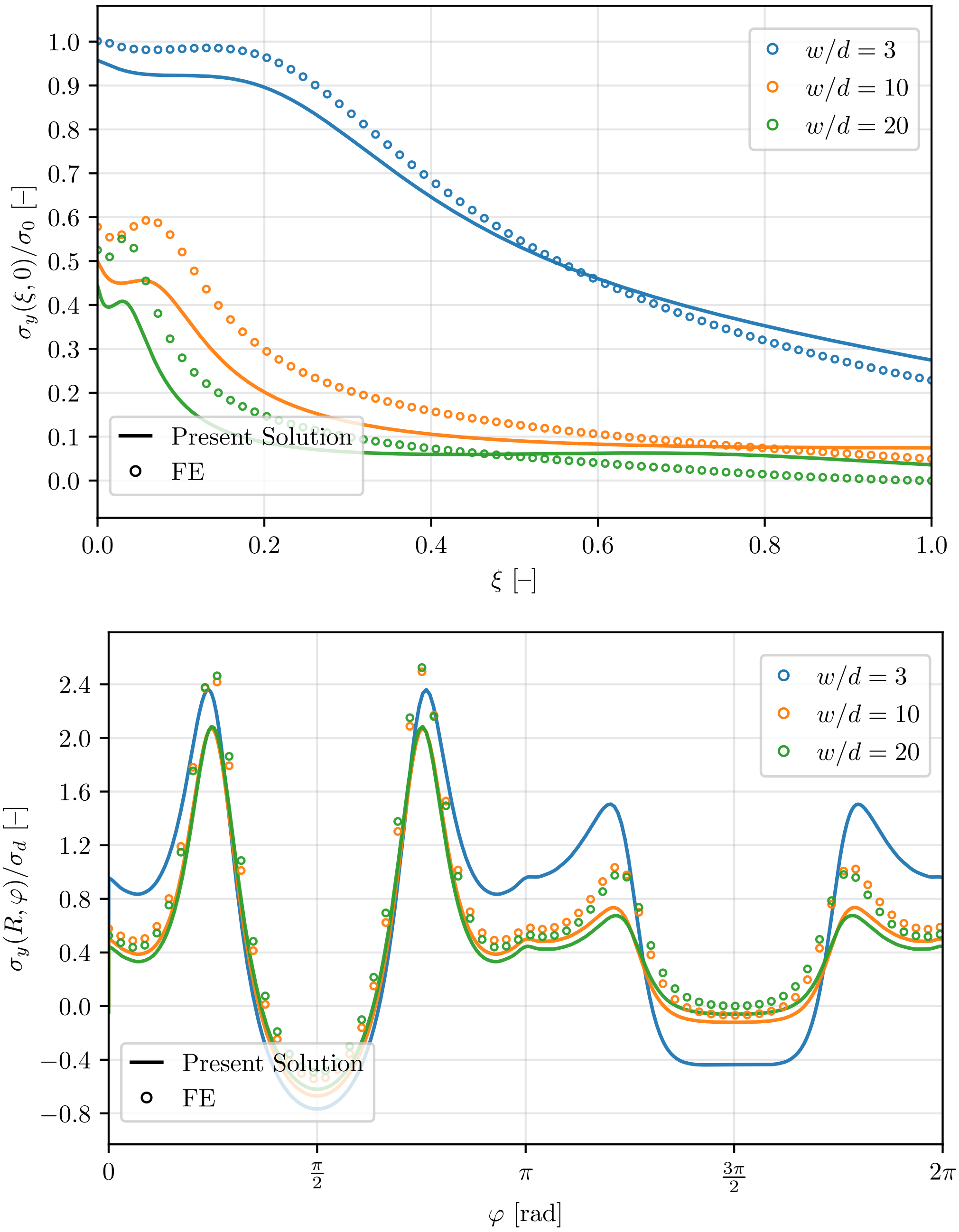

Figure 4.30: Filled hole finite-width plate, comparison between analytical and FE solutions for the $[\pm 45°]_s$ laminate, with $e/d = 2.5$. The upper plot shows the normalised net-section stresses, while the lower plot shows the normalised circumferential stresses.

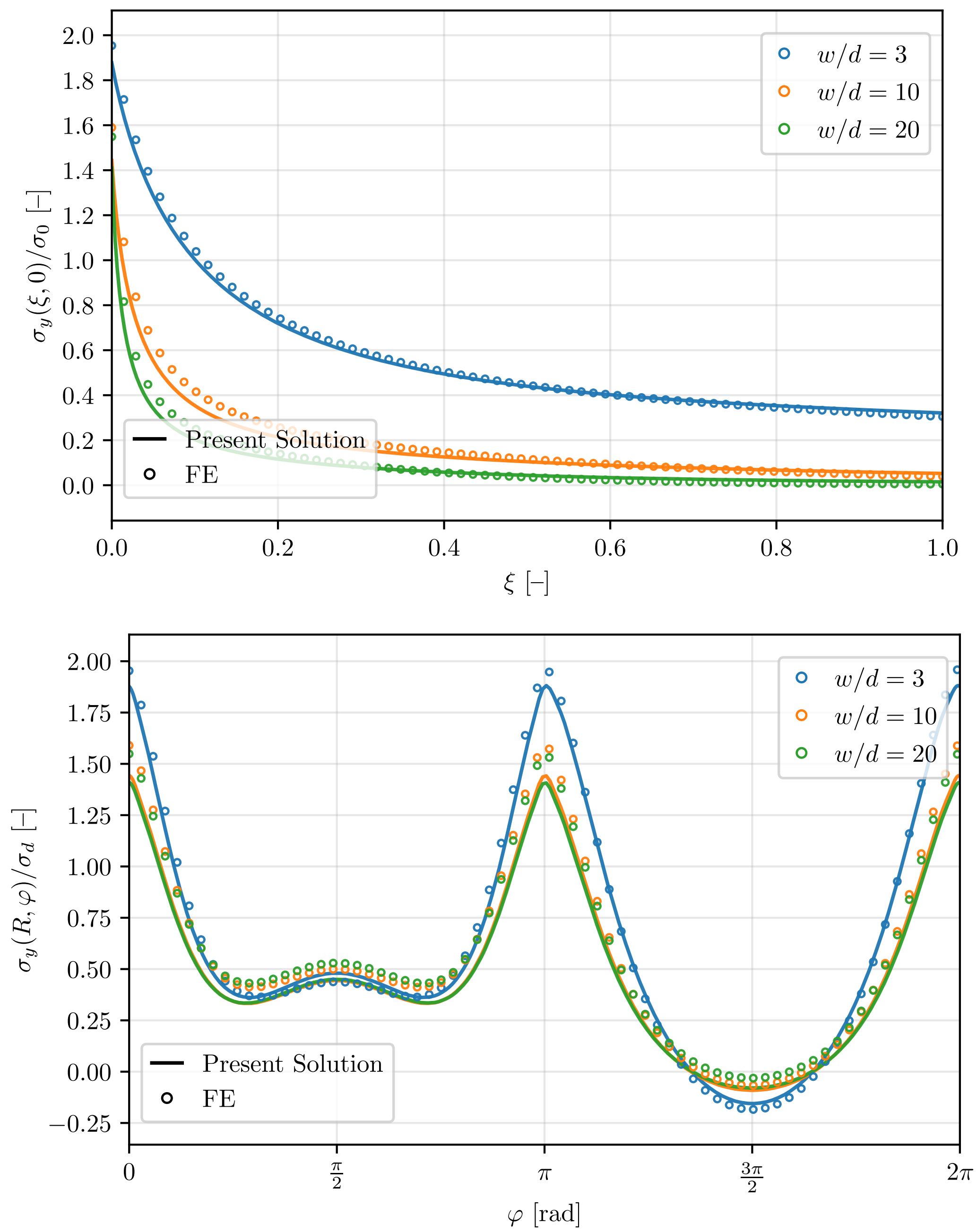

Figure 4.31: Filled hole finite-width plate, comparison between analytical and FE solutions for the $[0^\circ_5 \,/\, (\pm 45^\circ)_2 \,/\, 90^\circ]_s$ laminate, with $e/d = 2.5$. The upper plot shows the normalised net-section stresses, while the lower plot shows the normalised circumferential stresses.

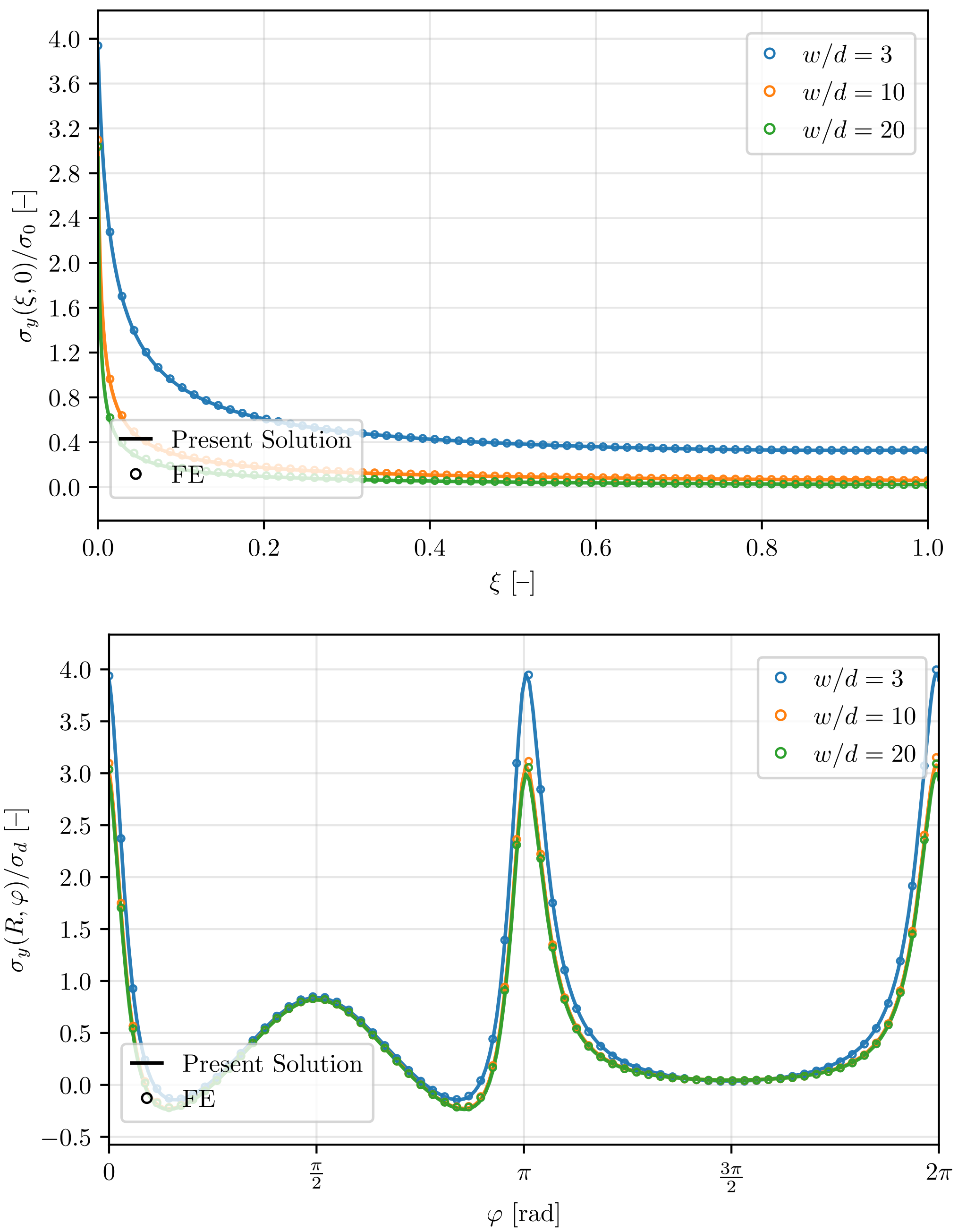

Figure 4.32: Filled hole finite-width plate, comparison between analytical and FE solutions for the [0°] laminate, with $e/d = 10$. The upper plot shows the normalised net-section stresses, while the lower plot shows the normalised circumferential stresses.

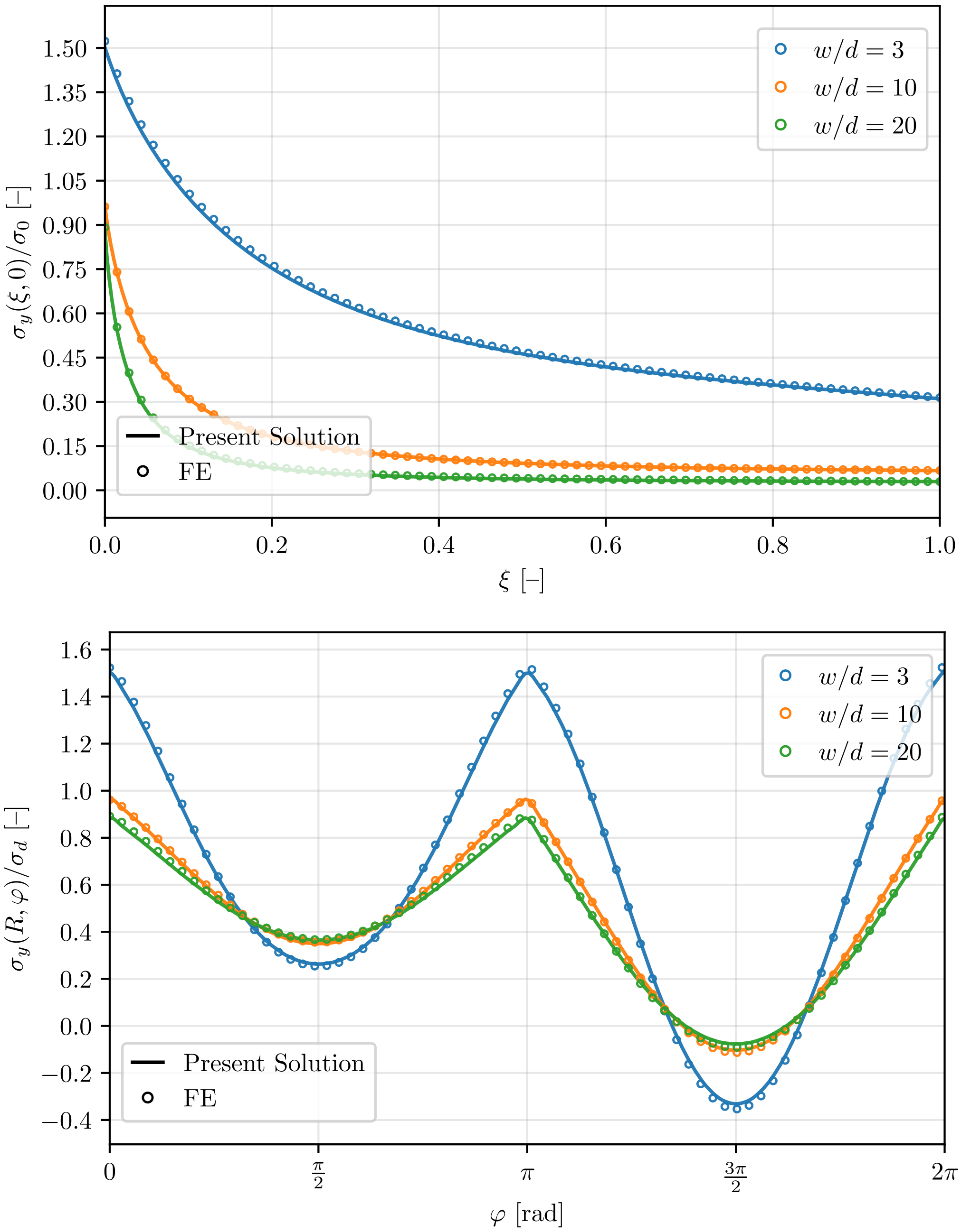

Figure 4.33: Filled hole finite-width plate, comparison between analytical and FE solutions for the quasi-isotropic laminate, with $e/d = 10$. The upper plot shows the normalised net-section stresses, while the lower plot shows the normalised circumferential stresses.

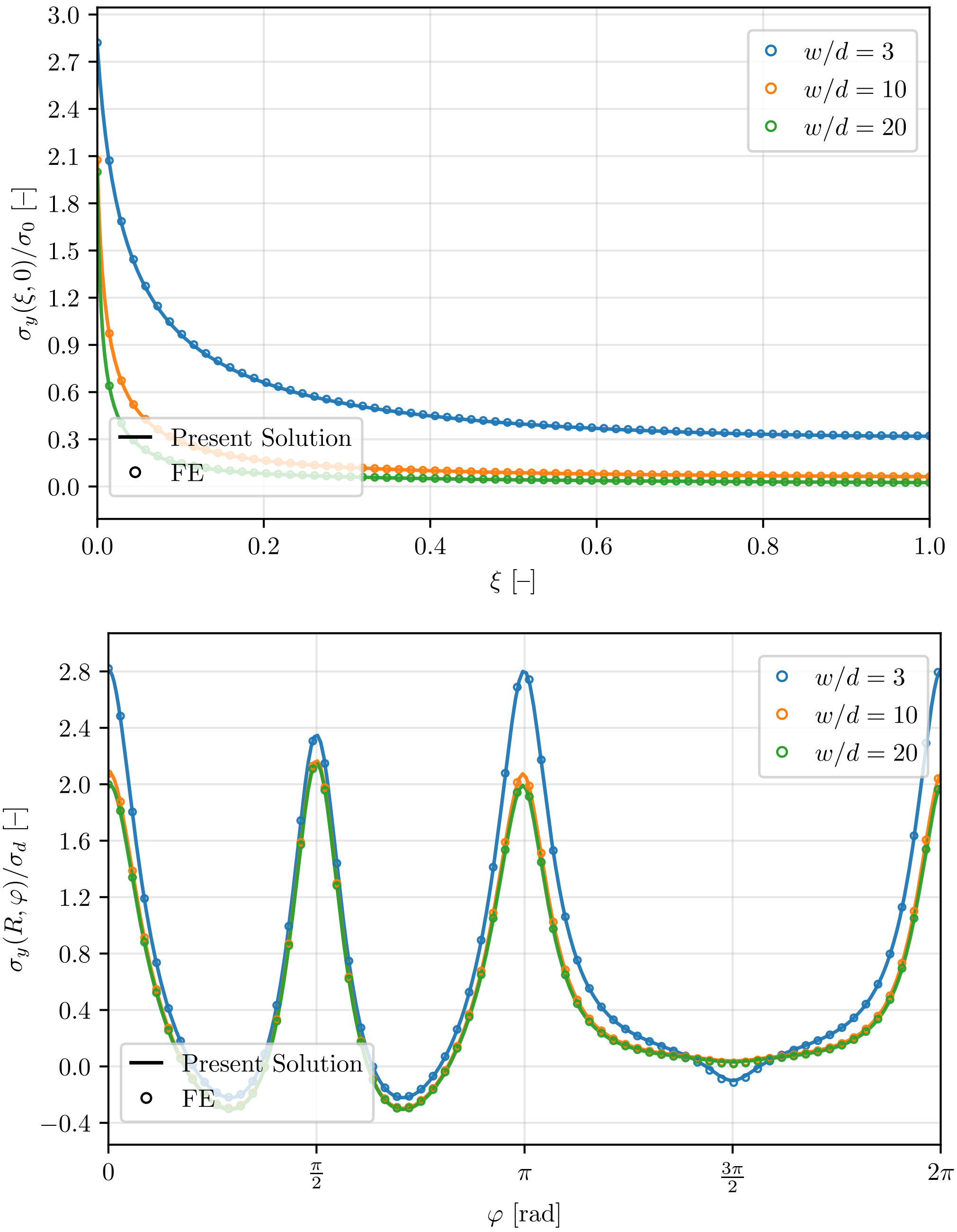

Figure 4.34: Filled hole finite-width plate, comparison between analytical and FE solutions for the $[0°/90°]_s$ laminate, with $e/d = 10$. The upper plot shows the normalised net-section stresses, while the lower plot shows the normalised circumferential stresses.

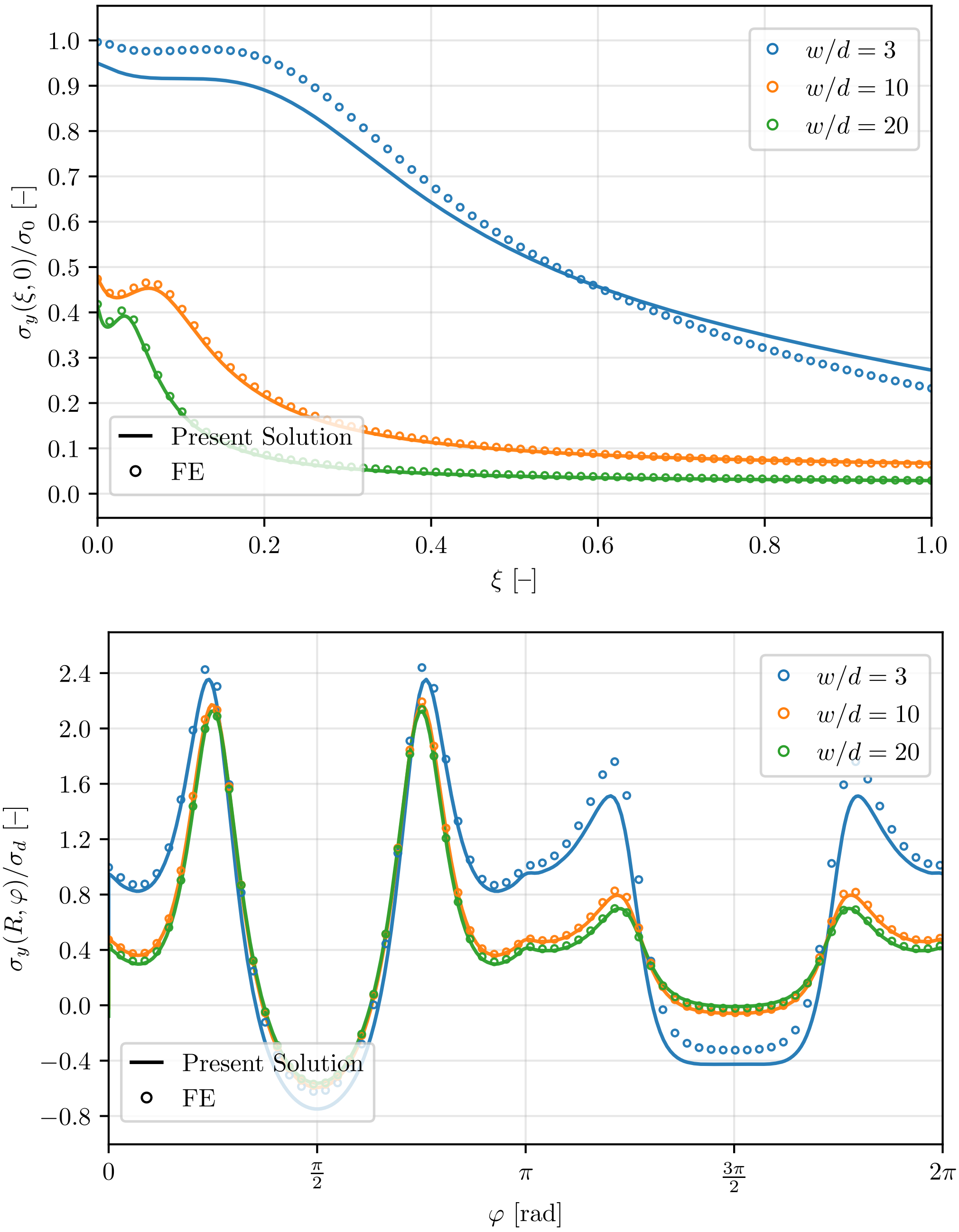

Figure 4.35: Filled hole finite-width plate, comparison between analytical and FE solutions for the $[\pm 45°]_s$ laminate, with $e/d = 10$. The upper plot shows the normalised net-section stresses, while the lower plot shows the normalised circumferential stresses.

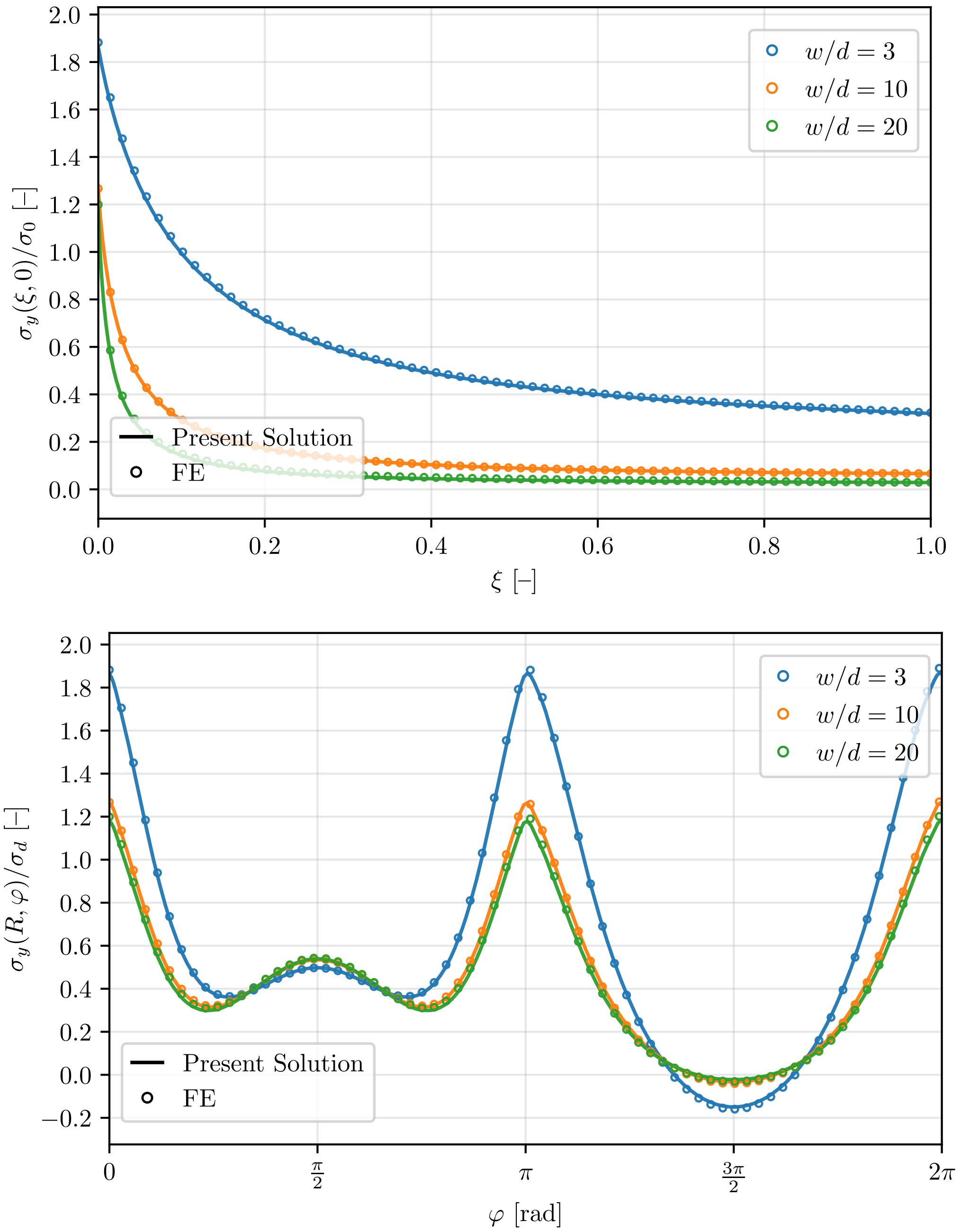

Figure 4.36: Filled hole finite-width plate, comparison between analytical and FE solutions for the $[0^\circ_5\,/\,(\pm 45^\circ)_2\,/\,90^\circ]_\mathrm{s}$ laminate, with $e/d = 10$. The upper plot shows the normalised net-section stresses, while the lower plot shows the normalised circumferential stresses.

4.3 Analysis of Biaxial Loading Case

The biaxial loading case can be solved for the infinite domain case, by imposing the following BCs:

$$\lim_{x\to\pm\infty} \sigma_x(x,y) = \sigma_x^{\mathrm{By}}, \quad \lim_{y\to\pm\infty} \sigma_y(x,y) = \sigma_y^{\mathrm{By}}, \quad \lim_{\substack{x\to\pm\infty \\ y\to\pm\infty}} \tau_{xy}(x,y) = 0. \tag{4.77}$$

where σ_x^{By} and σ_x^{By} are the bypass loads in the x and y directions, respectively, this BCs are illustrated in Figure 4.37.

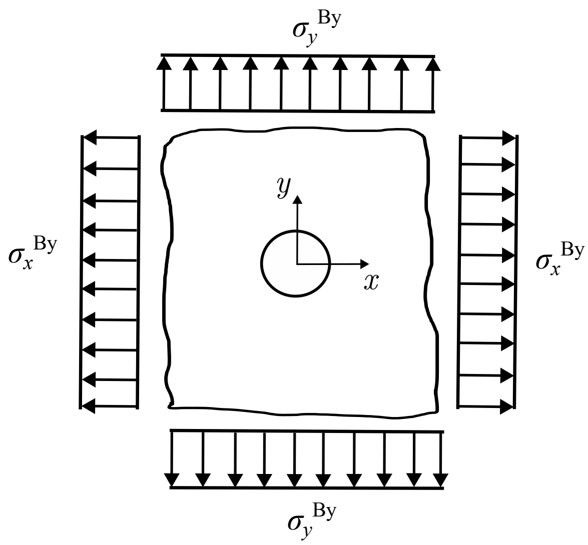

Figure 4.37: Schematic of the boundary conditions of the infinite-plate open hole configuration, subjected to uniform remote bypass stresses σ_x^{By} and σ_x^{By} at $x \to \pm\infty$ and $y \to \pm\infty$, respectively.

By following the same procedure described in subsection 4.1.3, it leads to the potentials

$$\begin{aligned} \Phi_1'^{\text{OH-II,inf}}(z_1) &= R\,\frac{\sigma_x^{\mathrm{By}}\, i - \sigma_y^{\mathrm{By}}\, \mu_2}{2(\mu_1 - \mu_2)\sqrt{z_1^2 - R^2(1+\mu_1^2)}}\,\zeta_1^{-1}, \\ \Phi_2'^{\text{OH-II,inf}}(z_2) &= -R\,\frac{\sigma_x^{\mathrm{By}}\, i - \sigma_y^{\mathrm{By}}\, \mu_1}{2(\mu_1 - \mu_2)\sqrt{z_2^2 - R^2(1+\mu_2^2)}}\,\zeta_2^{-1}. \end{aligned} \tag{4.78}$$

These expressions define the stress field under biaxial loading conditions, assuming an infinite domain, following Lekhnitskii's [10] formalism.

To solve the finite dimensions problem under the biaxial loading case, the solution can be obtained for different plate side dimensions by first solving the uniaxial finite-width problem in each direction and then superimposing the resulting stress fields.

To avoid solving the finite-width problem for loading along the x-axis, the author recommends rotating the plate's reference system by $-\pi/2$ rad and subsequently rotating the stress field back to the original coordinate system. This approach enables the superposition of stress fields corresponding to loadings in both directions. Leading to

$$F = F_x^{\mathrm{By}} + F_y^{\mathrm{By}} = (1-\alpha)F_x^{\mathrm{By}} + \alpha F_x^{\mathrm{By},\perp}, \quad \alpha = \frac{P_y^{\mathrm{By}}}{P}, \tag{4.79}$$

where $P = P_x^{\mathrm{By}} + P_y^{\mathrm{By}}$. Here, P denotes the sum of the two bypass loadings. Although this summation is not physically meaningful, since the loads act in perpendicular directions, it is introduced merely as a notational convenience to simplify the presentation of their relation.

4.3.1 Analysis of the Finite-Plate Solution: Open Hole Biaxial Tension

The biaxial open hole stress distributions are presented in Figure 4.38, Figure 4.41, Figure 4.40, Figure 4.39, and Figure 4.42, where $w_x/d = w_y/d = 10$, are respectively the width and height of the plate, note that we are normalising the stresses to σ_y^{By} for $\alpha = 1$. Note that here, we are focusing on a finite-plate problem, as neither of the plate's dimensions are infinite, therefore , this formulation will be highly influenced by e_{load}/d. This is because the solution corresponds to the superposition of two finite-width plates, which considers the loads is applied at infinity, however, we are in reality, applying σ_x^{By} at $e_{\mathrm{load},x} = 0.5\, w_y$ and σ_y^{By} at $e_{\mathrm{load},y} = 0.5\, w_x$. In subsection 4.1.5, it was shown that $e_{\mathrm{load}}/d = 2.5$ resulted in large deviations, particularly for the $[0°]$ laminate. Therefore, in this analysis we selected $e_{\mathrm{load}}/d = 5$, which for $w/d = 10$ yields an absolute maximum relative error of 3.40% for the $[0°]$ laminate. The following ratios were evaluated: $\alpha = \{0, 0.1, 0.5, 0.9, 1\}$, and the corresponding relative errors are reported in Table 4.5. The cases $\alpha = 1$ and $\alpha = 0$ represent uniaxial loading in the longitudinal and transverse directions, respectively, while $\alpha = 0.5$ corresponds to a biaxial loading scenario where equal tensions are applied at each edge. Overall, the analytical solution shows good agreement with the numerical results. However, for the $[0°]$ laminate the deviations are significant, particularly in the $\alpha = 0.5$ loading case, where the absolute relative error reaches 19.13%. Nevertheless, this ratio is not critical, as the stress concentrations are 4.9 times lower than those observed under uniaxial tension in the longitudinal direction.

Table 4.5: Normalised maximum stress relative error (%) for different laminate configurations under biaxial loading for various α, for $w_x/d = w_y/d = 10$.

	$[0°]$	Quasi-isotropic	$[0°/90°]_s$	$[\pm45°]_s$	$[0^\circ_5\,/\,(\pm45°)_2\,/\,90°]_s$
$\alpha = 0$	-6.00%	-1.43%	-1.75%	-2.18%	-0.70%
$\alpha = 0.1$	-8.33%	-0.96%	-1.60%	-2.10%	-1.89%
$\alpha = 0.5$	-19.13%	-0.66%	-0.91%	-2.39%	-1.21%
$\alpha = 0.9$	5.02%	-0.96%	-1.60%	-2.10%	-1.44%
$\alpha = 1$	4.43%	-1.43%	-1.75%	-3.21%	-1.79%

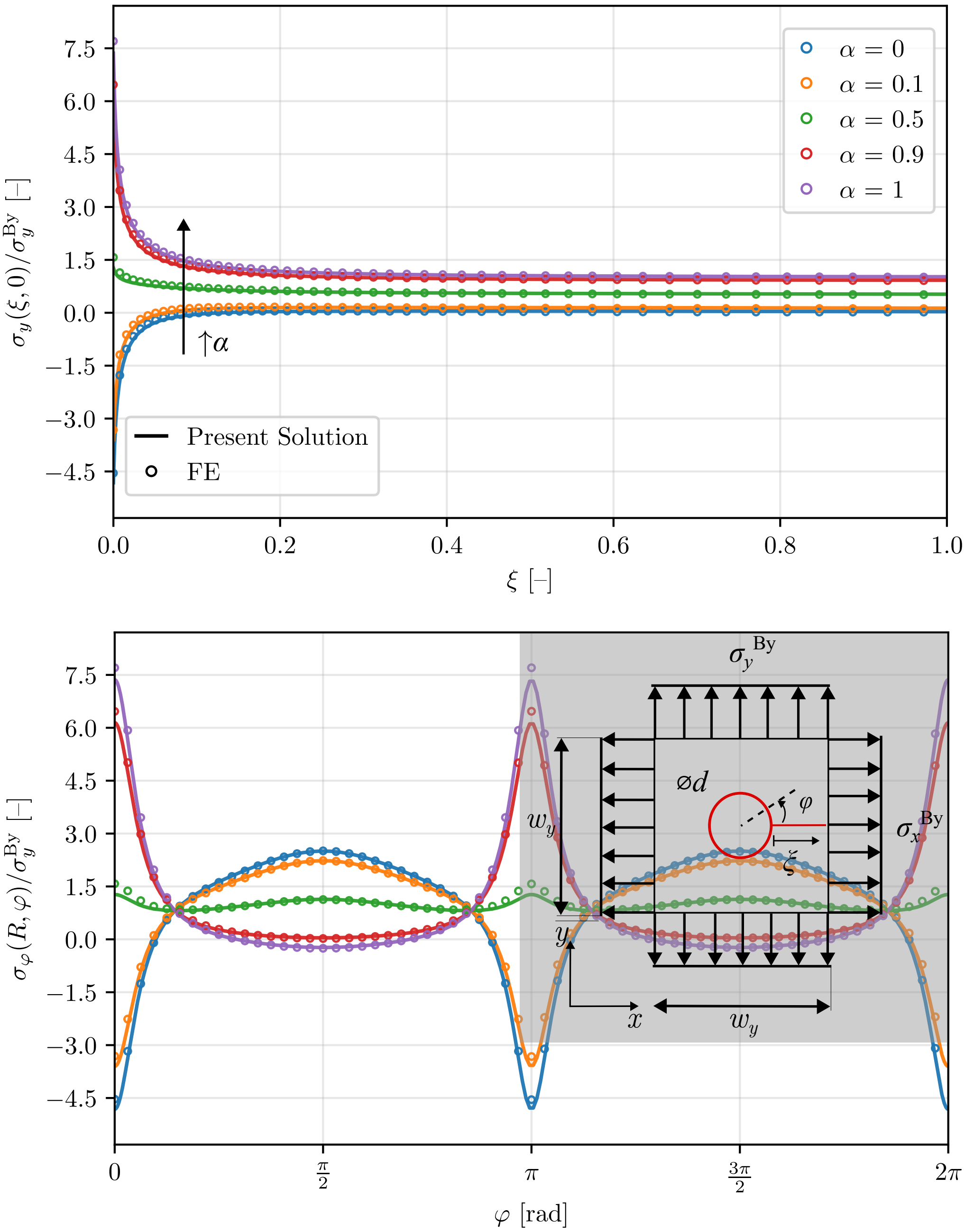

Figure 4.38: Biaxial open hole finite-width plate, comparison between analytical and FE solutions for the [0°] laminate, with $w_x/d = 10$, $w_y/d = 10$ and $\alpha = \{0, 0.1, 0.5, 0.9, 1\}$. The upper plot shows the normalised net-section stresses, while the lower plot shows the normalised circumferential stresses. Stresses normalised by σ_y^{By} for $\alpha = 1$.

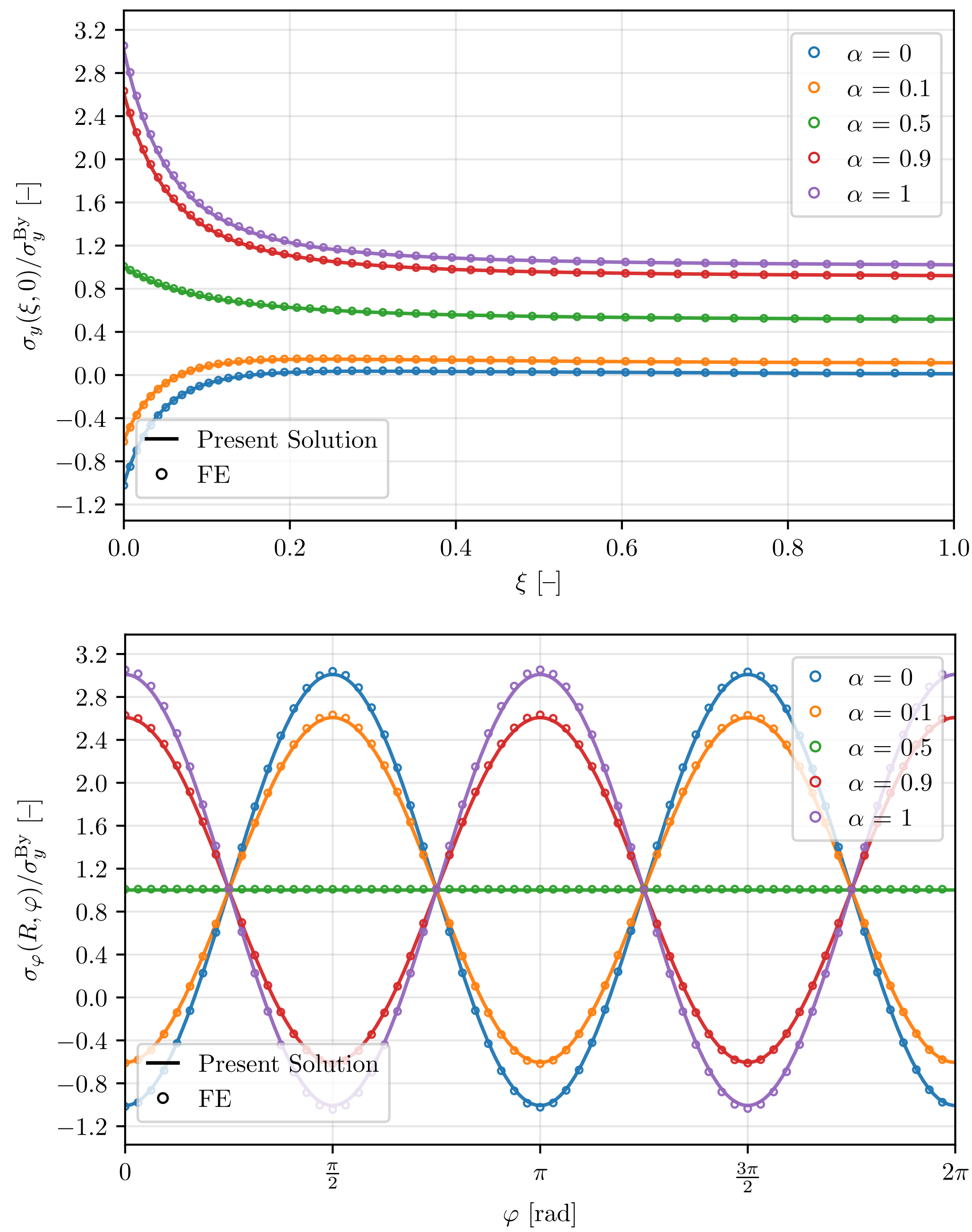

Figure 4.39: Biaxial open hole finite-width plate, comparison between analytical and FE solutions for the quasi-isotropic laminate, with $w_x/d = 10$, $w_y/d = 10$ and $\alpha = \{0, 0.1, 0.5, 0.9, 1\}$. The upper plot shows the normalised net-section stresses, while the lower plot shows the normalised circumferential stresses. Stresses normalised by σ_y^{By} for $\alpha = 1$.

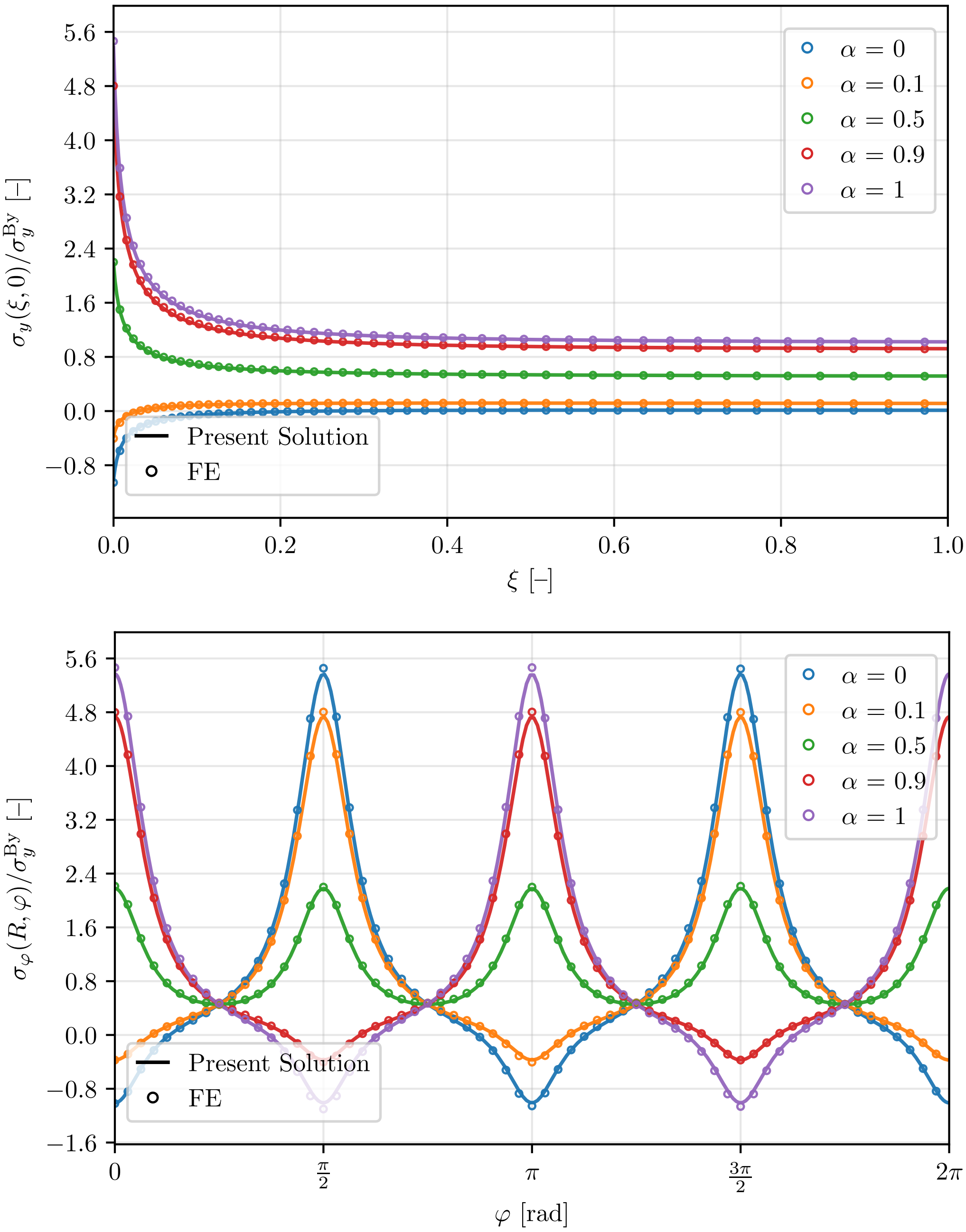

Figure 4.40: Biaxial open hole finite-width plate, comparison between analytical and FE solutions for the $[0°/90°]_s$ laminate, with $w_x/d = 10$, $w_y/d = 10$ and $\alpha = \{0, 0.1, 0.5, 0.9, 1\}$. The upper plot shows the normalised net-section stresses, while the lower plot shows the normalised circumferential stresses. Stresses normalised by σ_y^{By} for $\alpha = 1$.

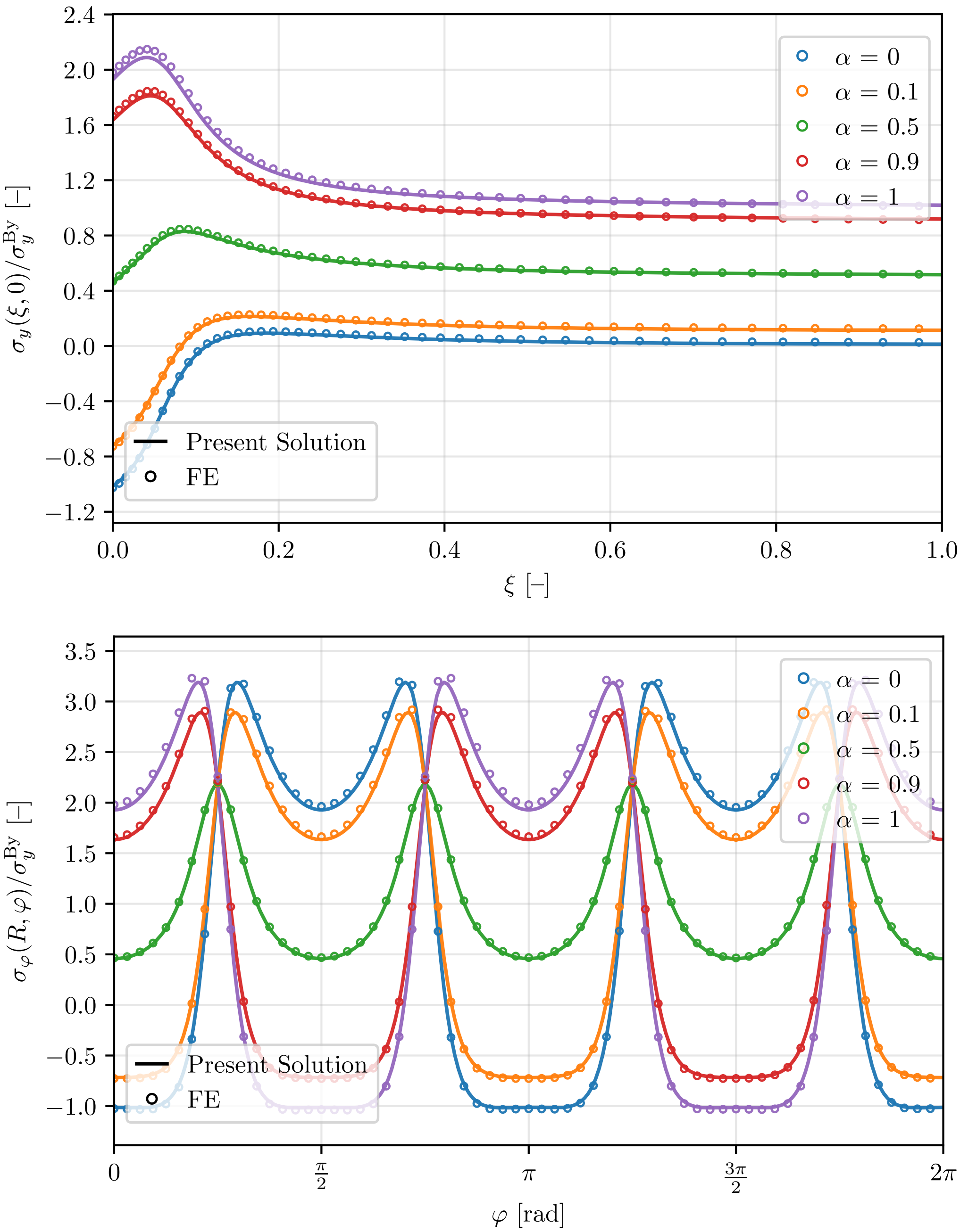

Figure 4.41: Biaxial open hole finite-width plate, comparison between analytical and FE solutions for the $[\pm 45°]_\mathrm{s}$ laminate, with $w_x/d = 10$, $w_y/d = 10$ and $\alpha = \{0, 0.1, 0.5, 0.9, 1\}$. The upper plot shows the normalised net-section stresses, while the lower plot shows the normalised circumferential stresses. Stresses normalised by σ_y^{By} for $\alpha = 1$.

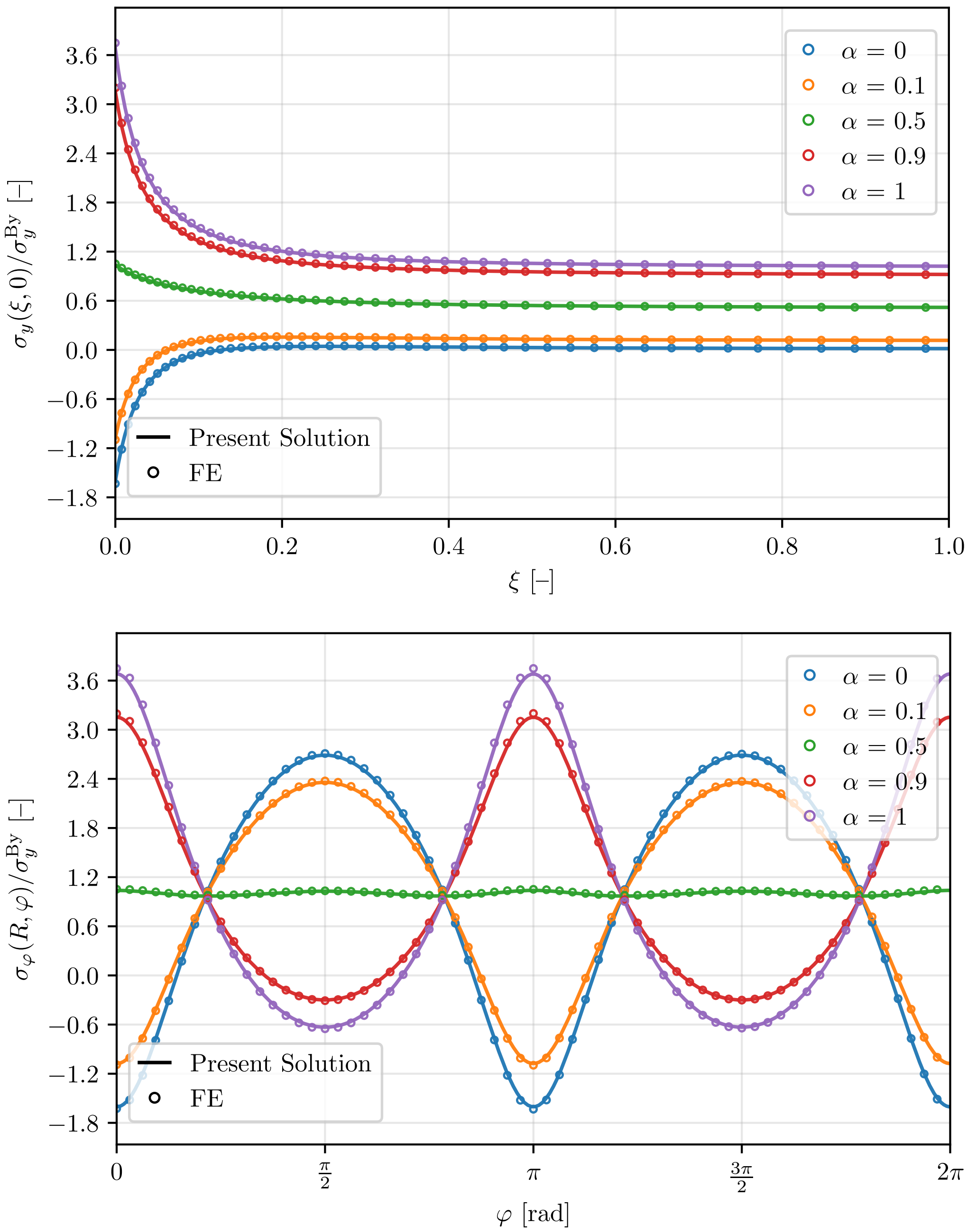

Figure 4.42: Biaxial open hole finite-width plate, comparison between analytical and FE solutions for the $[0^\circ_5\,/\,(\pm 45^\circ)_2\,/\,90^\circ]_\mathrm{s}$ laminate, with $w_x/d = 10$, $w_y/d = 10$ and $\alpha = \{0, 0.1, 0.5, 0.9, 1\}$. The upper plot shows the normalised net-section stresses, while the lower plot shows the normalised circumferential stresses. Stresses normalised by σ_y^{By} for $\alpha = 1$.

4.4 Out-of-Axis Bearing Loading Case

The out-of-axis bearing loading case (Figure 4.43) in an infinite domain can be addressed using the procedure in subsection 4.1.4, which assumes the load is aligned with the x-axis. For loads not aligned with the laminate's material coordinate system, two equivalent strategies are available: introduce a local coordinate system aligned with the bearing load, solve in that system, and then rotate the resulting stress field back to the reference frame; or retain the reference frame but modify the BCs in the formulation and re-derive the coefficients $\bar{\alpha}_m$ and $\bar{\beta}_m$. For practicality, the first approach was adopted.

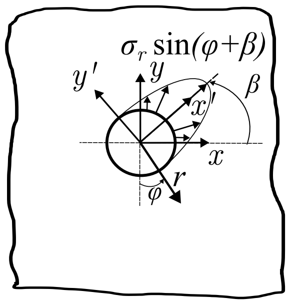

Figure 4.43: Out-of-axis bearing load: a local coordinate system (x', y') is introduced so that x' aligns with the bearing direction, which forms an angle β with the global x-axis.

The finite-domain methodology used for the filled hole problem is applicable only when the load's symmetry axis is parallel to the plate edges, if this condition is not satisfied, as in out-of-axis bearing loading, the method does not apply [8].

4.5 Analysis of the Bearing-bypass Interactions

In the previous sections, we successfully solved the open and filled hole problems using complex potentials combined with the boundary collocation method. In this section, the objective is to define the bearing-bypass interaction, following the methodology of Nguyen-Hoang and Becker, which studied the interaction for the uniaxial loading case, and therefore, for further details, refer to reference [14]. The bearing-bypass, with biaxial bypass will be studied.

First, lets formulate the uniaxial bearing-bypass interaction, constructed by Nguyen-Hoang and Becker [14], which idealized the bolted-joint as the superposition of the open hole and filled hole problems, following the approach presented by Camanho and Lambert [65]. Let F^{OH} and F^{FH} be the Airy stress functions for the open hole and filled hole problems, respectively. For the combined load $P = P_{\mathrm{Bea}} + P_{\mathrm{By}}$, the bolted joint under bearing–bypass loading has the stress function, by superposition

$$F^{\mathrm{BBI}} = (1-\beta)\, F^{\mathrm{OH}} + \beta\, F^{\mathrm{FH}}, \qquad \beta = \frac{P_{\mathrm{Bea}}}{P}. \tag{4.80}$$

For $\beta = 0$ this formulation specializes to the open hole problem and for $\beta = 1$ the filled hole problem. The filled hole case ($\beta = 1$) was deemed the most critical, yielding higher stress concentrations than the open hole ($\beta = 0$) and bearing-bypass ($0 < \beta < 1$) loading cases, and the open hole case was considered the less critical one.

4.6 Final Remarks

This chapter established an analytical framework to predict stress fields in laminates with open and filled circular holes, spanning infinite and finite domains. The formulation builds on Lekhnitskii's [10] complex potentials and conformal mappings for the infinite domain and extends to finite-width plates via auxiliary functions and periodic arrangements following Nguyen–Hoang and Becker [8, 9, 14]. All expressions were implemented in *Python* and verified against *Abaqus* FE results, with accuracy quantified across layups, geometric ratios, and loading cases (uniaxial, biaxial, bearing–bypass). In section 7.4, we present an overview of the stress-field implementation methodology, identify remaining gaps, and delineate the formulations' domain of applicability.

5. Failure Analysis

In failure analysis, the primary objective of the tool is to adopt a highly conservative approach. Therefore, First Ply Failure (FPF) was established as the failure philosophy for the tool. The premise of this criterion is that failure of a single ply implies failure of the entire laminate.

In the previous section, a laminate-level approach to the problem has been adopted, allowing the definition of the stress field within the laminate using its homogenized properties. However, the FPF criterion is based on a local analysis of the laminate, as it determines failure by evaluating each individual lamina. As a result, the laminate-level stress field needs to be transformed into a lamina-level stress field for each ply, using the Classical Laminate Theory presented in subsection 2.2.2.

5.1 Methodology for Computation of the Lamina-Level Stress Field

The strain distribution through the laminate thickness varies linearly with the distance from the midplane, as shown in Equation 5.1, where the slope of the curve is the curvature of the plate, κ. This parameter is considered null, therefore the strain in the laminate is given by the following expression:

$$\boldsymbol{\varepsilon}(z) = \boldsymbol{\varepsilon}^0. \tag{5.1}$$

This indicates that the strain remains equal to the midplane strain through the laminate thickness, hence, all plies experience the same strain field. By applying the Hook's law to each lamina, and using its transformed stiffness matrix $\bar{\boldsymbol{Q}}_{\mathrm{k}}$, in the global coordinate system, the stress field within each ply can be determined from the midplane strain-field.

Combining Equation 2.16 with $\boldsymbol{\kappa} = [0, 0, 0]^T$, the midplane strain is obtained:

$$\boldsymbol{\varepsilon}^{\mathbf{0}} = \boldsymbol{A}^{-1}\,\boldsymbol{N}. \tag{5.2}$$

Subsequently, using Equation 2.12 the stress field in the k$^{\text{th}}$ ply is given by:

$$\boldsymbol{\sigma}_{\text{k}} = \bar{\boldsymbol{Q}}_{\text{k}}\,\boldsymbol{\varepsilon}^{\mathbf{0}}. \tag{5.3}$$

5.1.1 Analysis of the Lamina-Level Characteristic Stresses

In this Subsection, we validate the methodology for computing the lamina-level stress field against FE results. The FE model was largely similar to the one presented in section 3.2; however, in this case, S8R shell elements (8-node quadratic quadrilaterals with reduced integration) were employed, as three-dimensional shell elements were required in order to define the plate with a composite layup, enabling the direct extraction of the lamina-level stresses. The methodology was tested for open hole tension and filled hole bearing cases, $w/d = 10$, $e_{\text{load}}/d = 80$, and, for the filled hole configuration $e/d = 20$. This configuration was selected to minimize the errors associated with the finite-width solution, thereby allowing a clearer assessment of the errors arising from the methodology developed in this chapter. Additionally, stresses are shown only for half of the laminate plies, specifically those above the midplane, since all laminates considered are symmetric. Ply numbering is assigned from the outer ply down to the middle ply and the stresses will be presented in the lamina's local coordinate system.

5.1.1.1 Analysis of the Lamina-Level Solution: Open Hole

The validation of the analytical formulation against the FE results for different laminate configurations is illustrated in Figure 5.1, Figure 5.2, Figure 5.3, and Figure 5.4. Each figure shows the comparison of the normalized stress distributions at each lamina local coordinate system. In Table 5.1, the relative errors of the highest absolute normalised stress values in each lamina, obtained from the analytical model and compared to the numerical results, are presented. Overall, the results are satisfactory. The 90° plies, which are subjected to compressive stresses near the hole, present higher deviations, particularly for the $[0°/90°]_{\text{s}}$ laminate. From the circumferential stresses shown in Figure 5.2, it is evident that the observed error is not critical, as it arises in a region where the stress levels are very low. In fact, the difference between the maximum stresses is only $\sigma_{\varphi}(R,\pi)/\sigma_0 = 0.16$. Furthermore, for the laminates analyzed under open hole tension, the 90° plies are never critical. For all laminates, except the $[\pm45°]_{\text{s}}$ laminate, the 0° ply is the most critical one, additionally, the stresses in this ply show excellent agreement, with a maximum relative error of only 1.03% for this ply. For the $[\pm45°]_{\text{s}}$ laminate, the ±45° plies are critical one, with a relative error of 1.79%.

Table 5.1: Maximum lamina-level stress relative error (%) in open hole tension for various laminate configurations comparing numerical results with the analytical solution with $w/d = 10$. Ply numbering is assigned from the outer ply down to the middle ply.

	Quasi-isotropic	$[0°/90°]_s$	$[\pm45°]_s$	$[0^\circ_5\,/\,(\pm45°)_2\,/\,90°]_s$
Ply-1	0.62%	1.03%	1.79%	0.58%
Ply-2	1.07%	-1564.97%	1.79%	1.75%
Ply-3	1.07%	-	-	1.75%
Ply-4	-4.02%	-	-	-8.26%

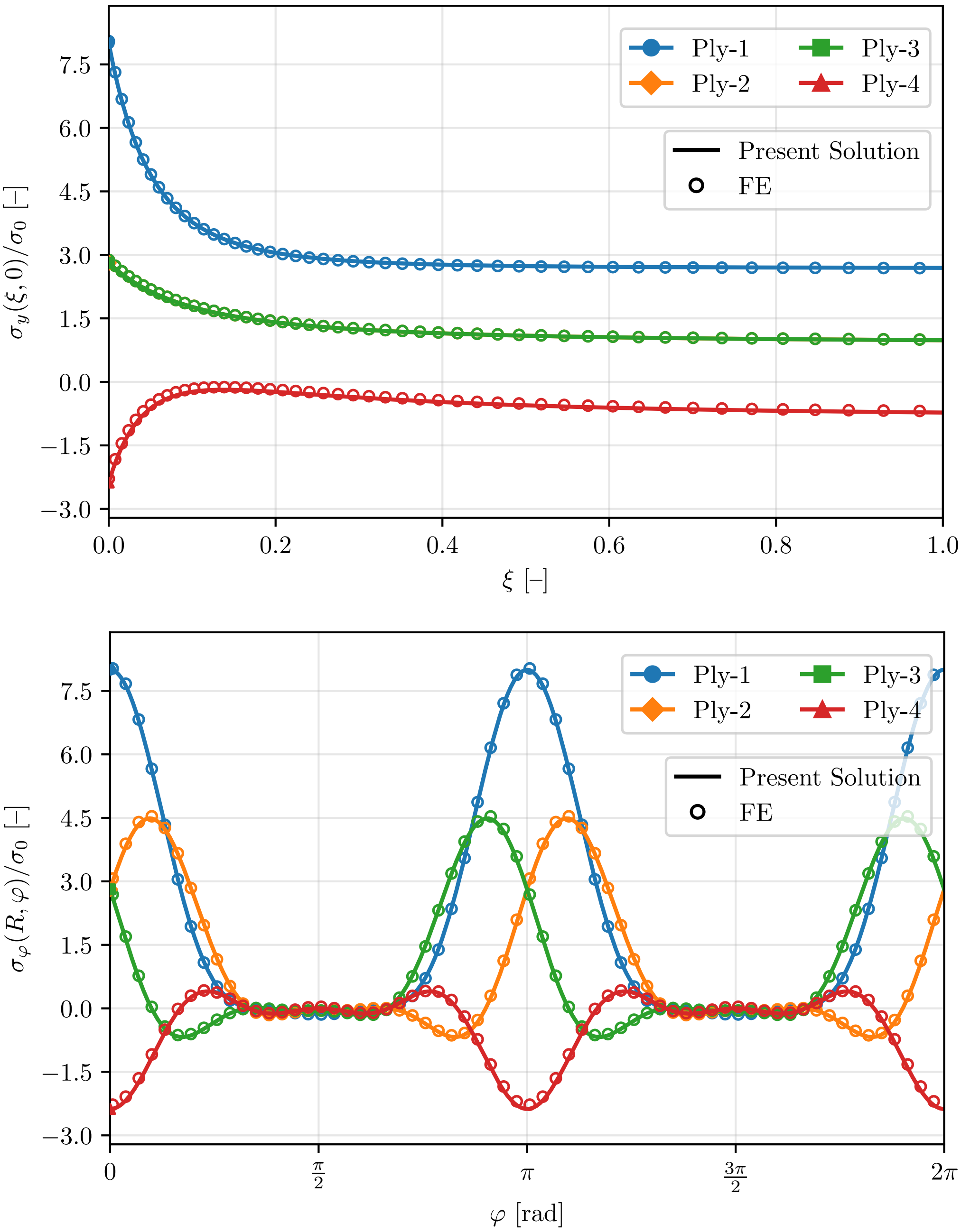

Figure 5.1: Comparison of analytical and FE solutions for lamina-level stresses in the quasi-isotropic laminate with an open hole finite-width plate, evaluated at $w/d = 10$. The top plot presents the normalised net-section stresses, while the bottom plot shows the normalised circumferential stresses. Ply numbering is assigned from the outer ply down to the middle ply.

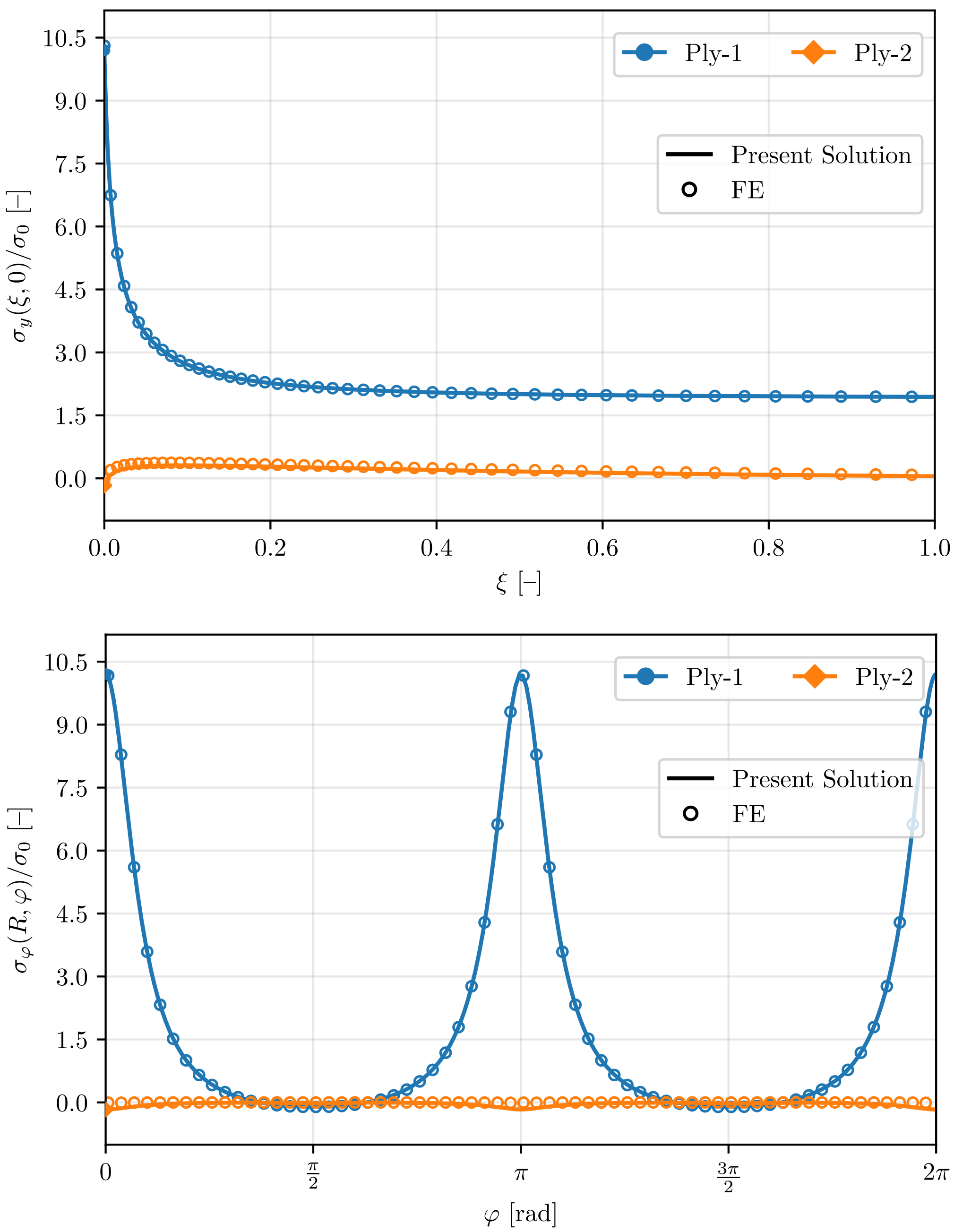

Figure 5.2: Comparison of analytical and FE solutions for lamina-level stresses in the $[0°/90°]_s$ laminate with an open hole finite-width plate, evaluated at $w/d = 10$. The top plot presents the normalised net-section stresses, while the bottom plot shows the normalised circumferential stresses. Ply numbering is assigned from the outer ply down to the middle ply.

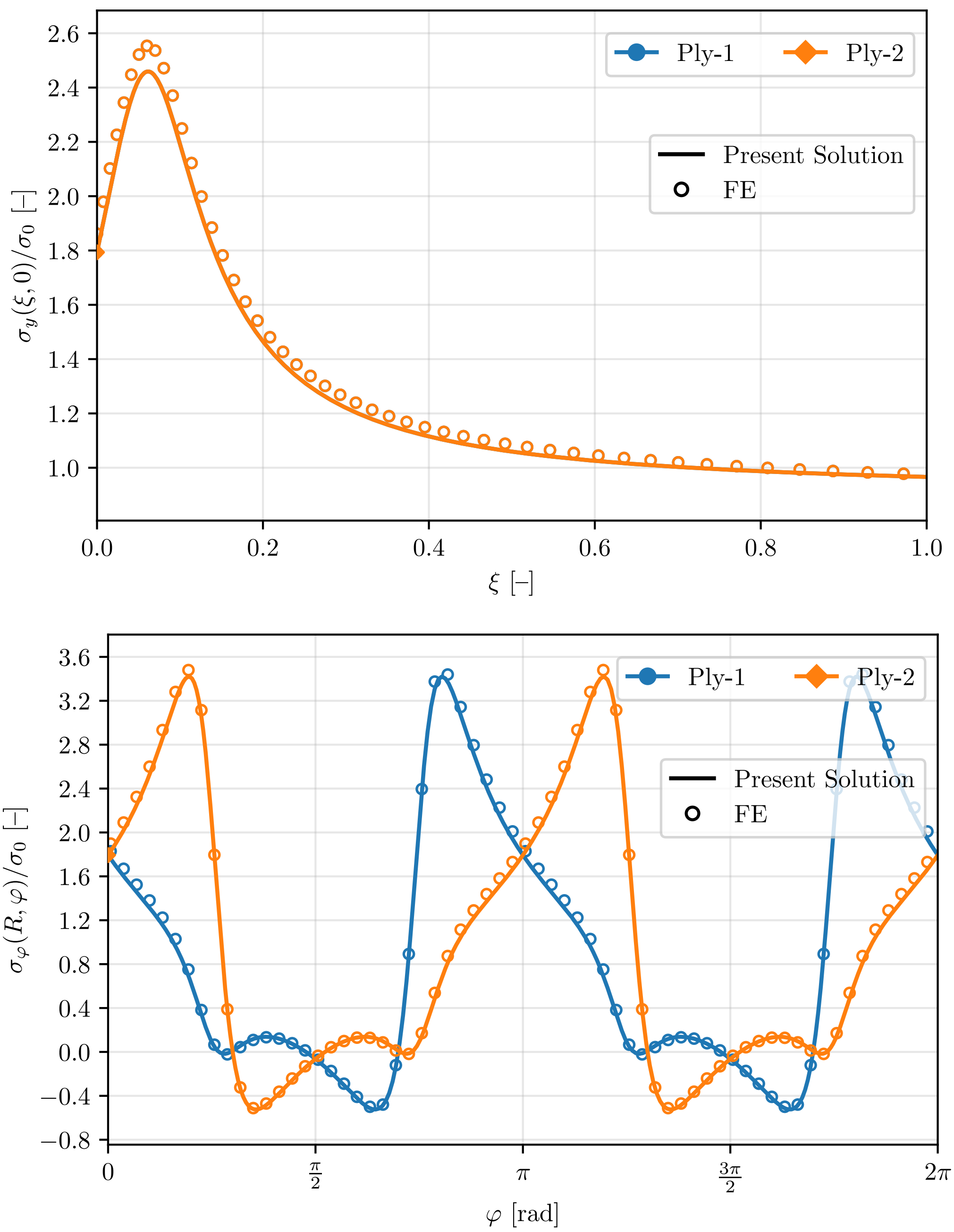

Figure 5.3: Comparison of analytical and FE solutions for lamina-level stresses in the $[\pm 45°]_s$ laminate with an open hole finite-width plate, evaluated at $w/d = 10$. The top plot presents the normalised net-section stresses, while the bottom plot shows the normalised circumferential stresses. Ply numbering is assigned from the outer ply down to the middle ply.

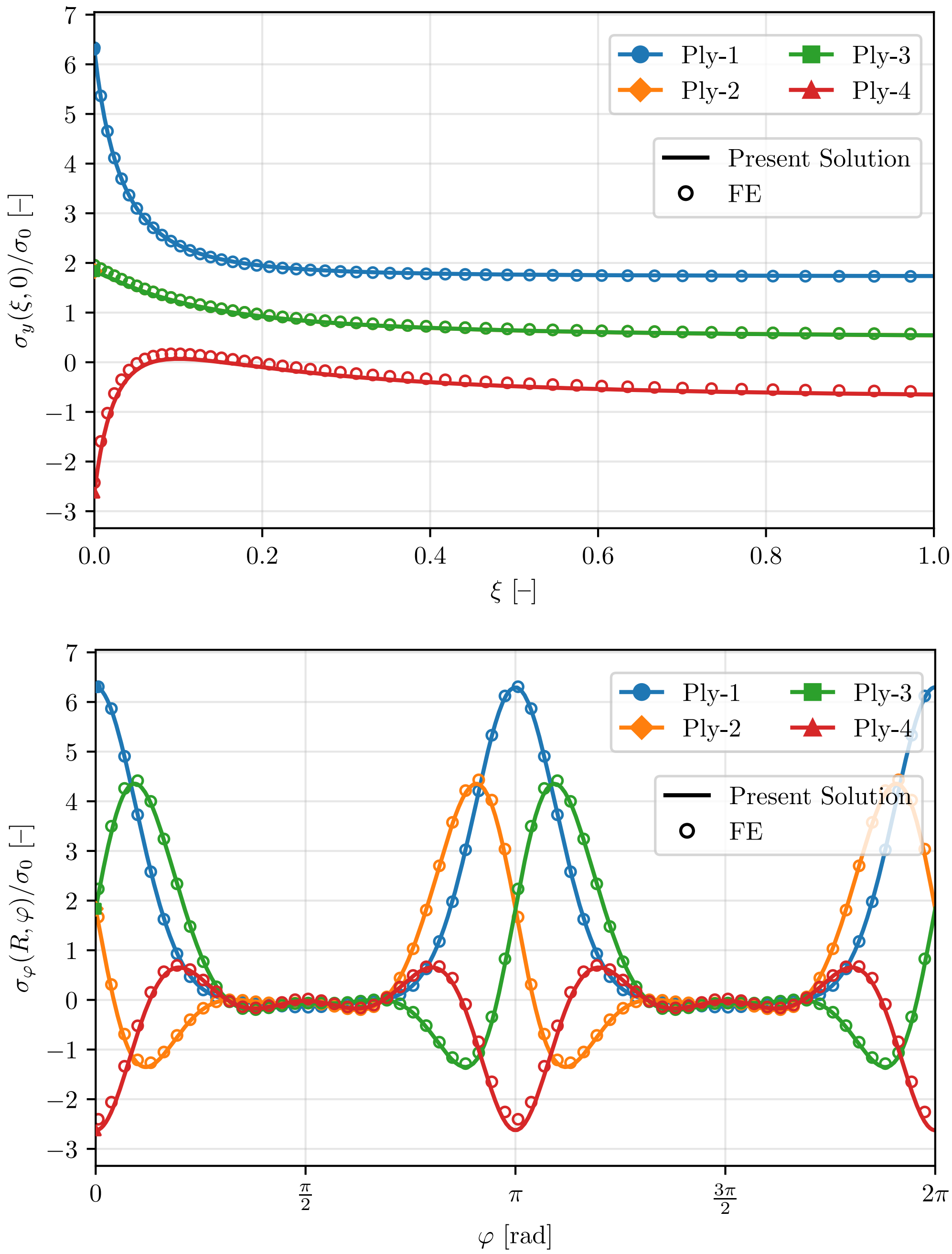

Figure 5.4: Comparison of analytical and FE solutions for lamina-level stresses in the $[0^\circ_5\,/\,(\pm45^\circ)_2\,/\,90^\circ]_s$ laminate with an open hole finite-width plate, evaluated at $w/d = 10$. The top plot presents the normalised net-section stresses, while the bottom plot shows the normalised circumferential stresses. Ply numbering is assigned from the outer ply down to the middle ply.

5.1.1.2 Analysis of the Lamina-Level Stress Field: Filled Hole

The validation of the analytical formulation for the filled hole case against FE results for different laminate configurations is illustrated in Figure 5.5, Figure 5.6, Figure 5.7, and Figure 5.8. Each figure presents a comparison of the normalized stress distributions in the local coordinate system of each lamina. The corresponding relative errors of the maximum absolute normalised stresses, obtained from the analytical model and compared with the FE results, are summarized in Table 5.2. As in the open hole case, the 90° ply exhibits the largest absolute relative errors; however, the results are satisfactory, with a maximum absolute relative error of 2.15%.

Table 5.2: Relative errors for different layups.

	Quasi-isotropic	$[0°/90°]_s$	$[\pm45°]_s$	$[0^\circ_5\,/\,(\pm45°)_2\,/\,90°]_s$
Ply-1	-0.08%	0.06%	-1.25%	-0.09%
Ply-2	-1.02%	0.05%	-1.26%	-1.19%
Ply-3	-1.09%	–	–	-1.19%
Ply-4	-1.86%	–	–	-2.15%

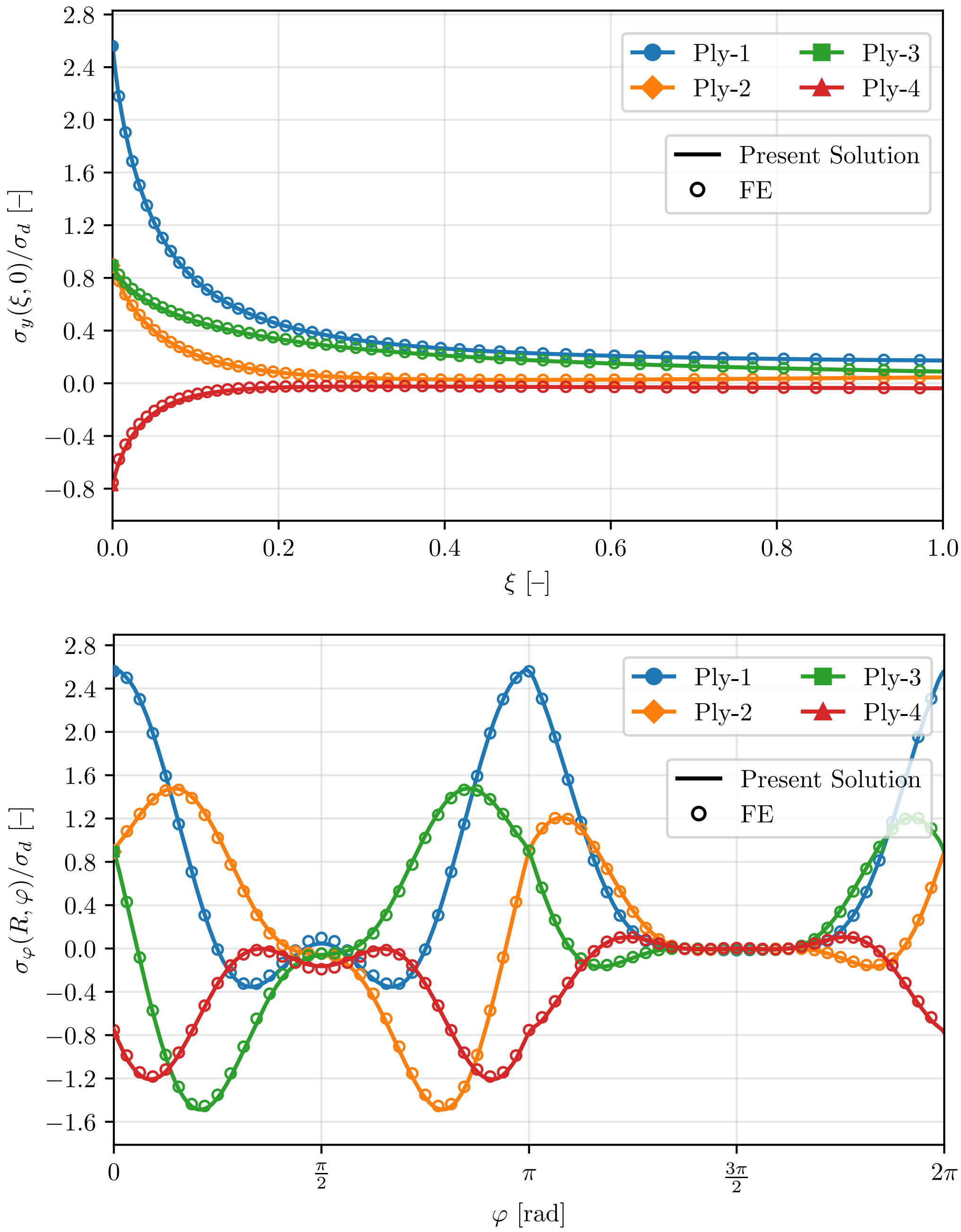

Figure 5.5: Comparison of analytical and FE solutions for lamina-level stresses in the quasi-isotropic laminate with a filled hole finite-width plate, evaluated at $w/d = 10$ and $e/d = 20$. The top plot presents the normalised net-section stresses, while the bottom plot shows the normalised circumferential stresses. Ply numbering is assigned from the outer ply down to the middle ply.

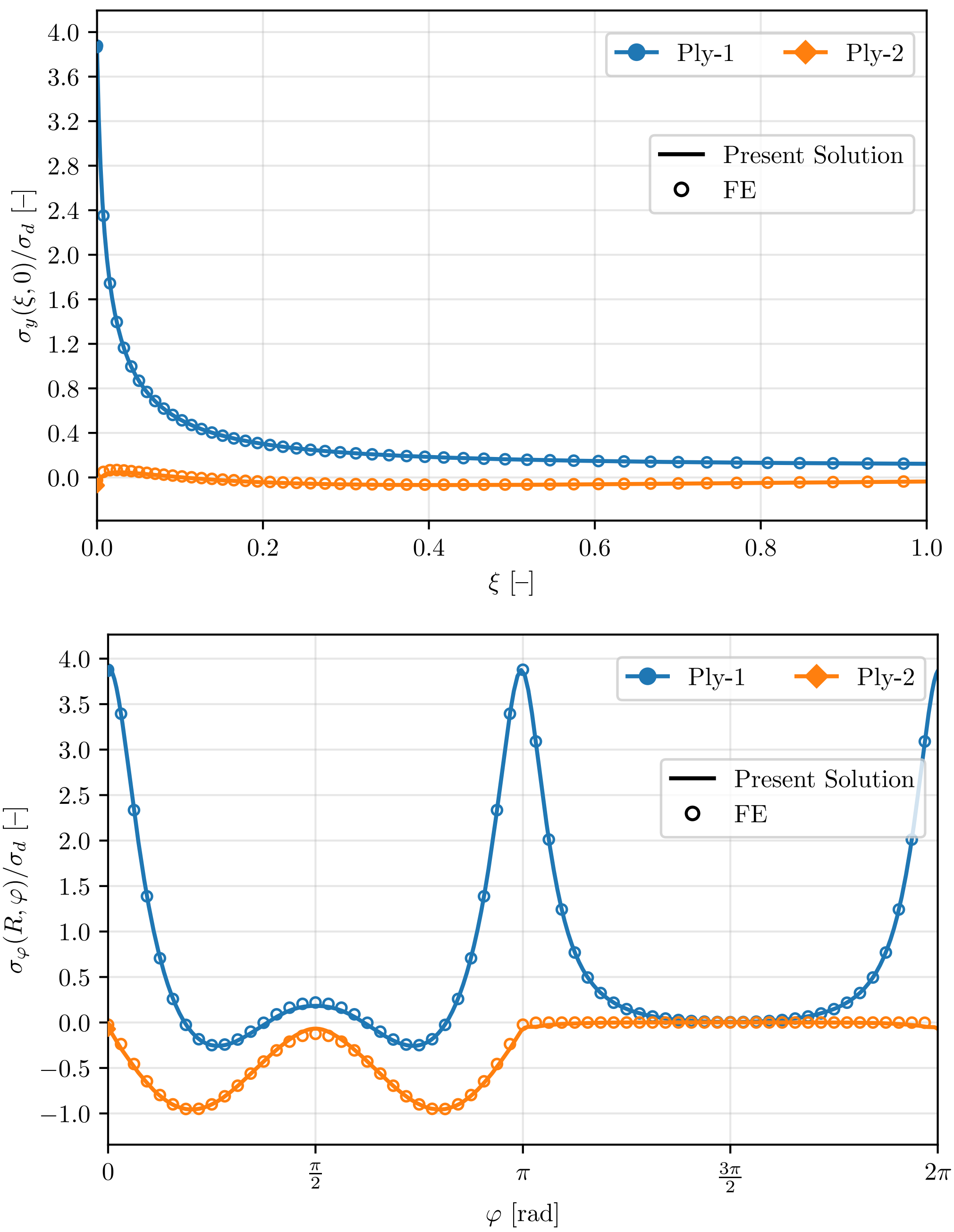

Figure 5.6: Comparison of analytical and FE solutions for lamina-level stresses in the $[0°/90°]_s$ laminate with a filled hole finite-width plate, evaluated at $w/d = 10$ and $e/d = 20$. The top plot presents the normalised net-section stresses, while the bottom plot shows the normalised circumferential stresses. Ply numbering is assigned from the outer ply down to the middle ply.

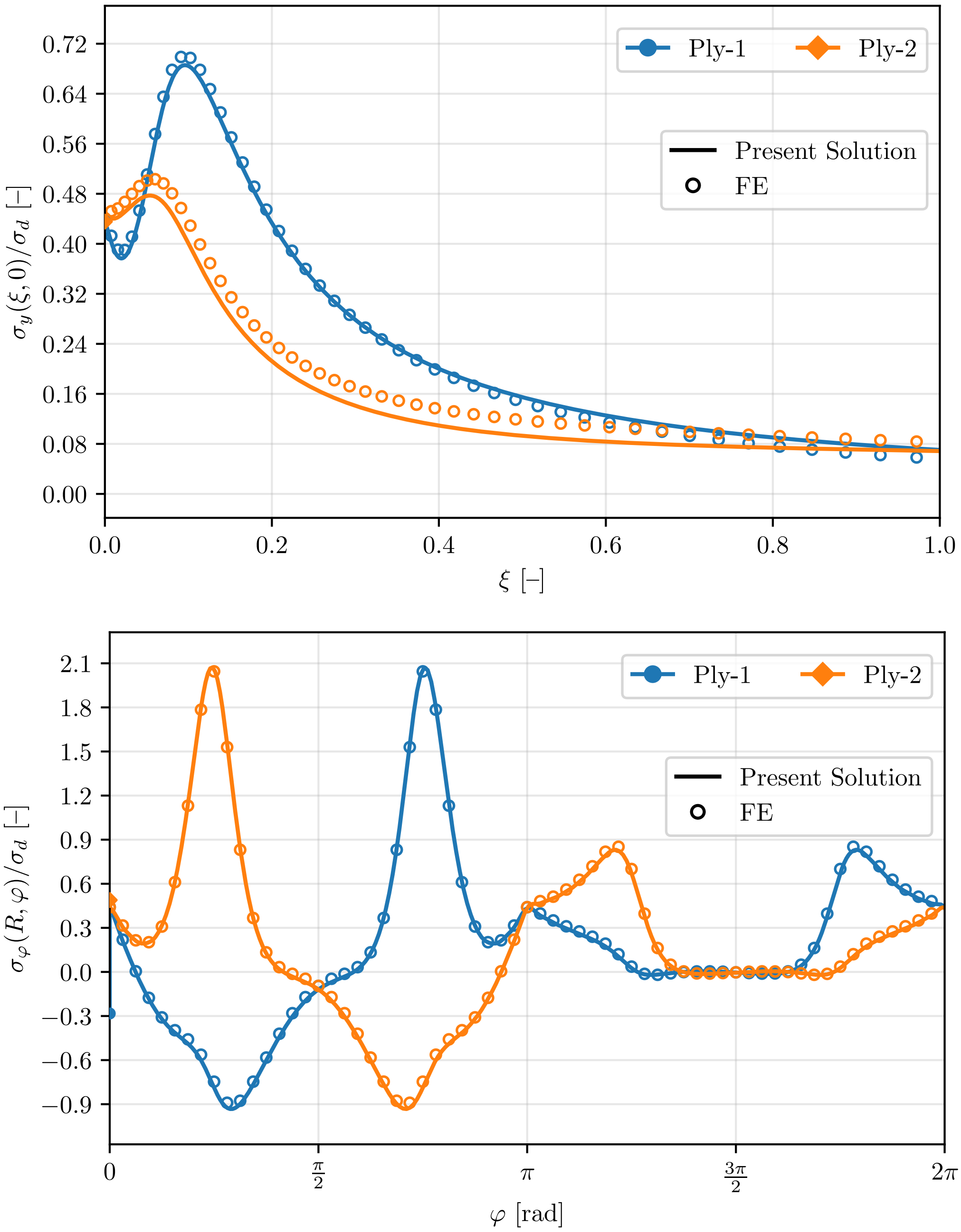

Figure 5.7: Comparison of analytical and FE solutions for lamina-level stresses in the $[\pm 45°]_s$ laminate with a filled hole finite-width plate, evaluated at $w/d = 10$ and $e/d = 20$. The top plot presents the normalised net-section stresses, while the bottom plot shows the normalised circumferential stresses. Ply numbering is assigned from the outer ply down to the middle ply.

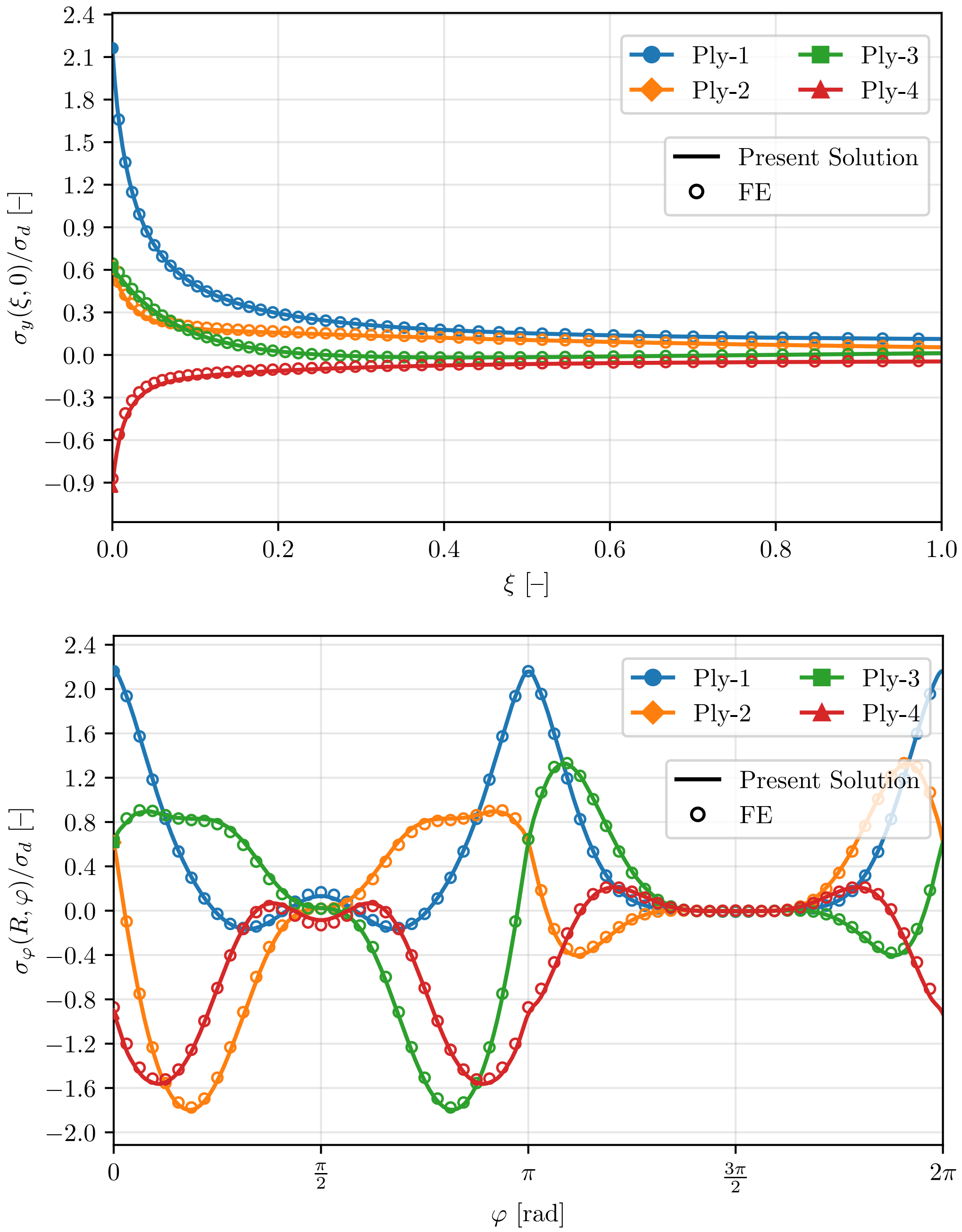

Figure 5.8: Comparison of analytical and FE solutions for lamina-level stresses in the $[0^\circ_5\,/\,(\pm 45^\circ)_2\,/\,90^\circ]_\mathrm{s}$ laminate with a filled hole finite-width plate, evaluated at $w/d = 10$ and $e/d = 20$. The top plot presents the normalised net-section stresses, while the bottom plot shows the normalised circumferential stresses. Ply numbering is assigned from the outer ply down to the middle ply.

5.2 Computation of Failure

The formulation for transforming the laminate-level stresses to the lamina-level stresses was successfully presented and validated in the last Section. Now we will be presenting the failure critera used to compute ply failure. Four different failure criteria were considered, all of them phenomenological in nature, meaning they do not distinguish between specific failure modes, instead, failure is assumed to occur once the conditions defined by the criterion are met [69]. This type of criterion was selected due to its ease of implementation and minimal material-specific inputs requirements, making it to be applied in design checks and global failure assessment. The selected criteria were: maximum failure stress criterion, maximum failure strain criterion, Tsai-Hill criterion and Tsai-Wu criterion.

5.2.1 Maximum Failure Stress Criterion

The maximum failure stress criterion suggests a comparison between the stress components expressed in the principal material directions of the lamina to their corresponding allowable stress limits, as follows:

Tension:

$$\sigma_1 < X_t \quad ; \quad \sigma_2 < Y_t. \tag{5.4}$$

Compression:

$$\sigma_1 > X_c \quad ; \quad \sigma_2 > Y_c. \tag{5.5}$$

Shear:

$$|\tau_{12}| < S_{12}. \tag{5.6}$$

Where X_t and X_c represent the allowable longitudinal tensile and compressive strengths respectively, Y_t and Y_c are the allowable transverse tensile and compressive strengths respectively, and S_{12} is the allowable in-plane shear strength. The terms σ_1 and σ_2 are the maximum acting in-plane normal stresses in the principal material directions, while τ_{12} is the maximum shear stress.

The safety margins are calculated as follows:

$$MS = \frac{X_T}{\sigma_1} - 1 \quad \text{or} \quad MS = \frac{X_c}{\sigma_1} - 1, \tag{5.7}$$

$$MS = \frac{Y_T}{\sigma_2} - 1 \quad \text{or} \quad MS = \frac{Y_c}{\sigma_2} - 1, \tag{5.8}$$

$$MS = \frac{S_{12}}{|\tau_{12}|} - 1. \tag{5.9}$$

One of the key advantages of this criterion is its simplicity in identifying the failure mode. It distinguishes between two primary modes: fiber-related and matrix-related failure. The criterion assumes that the stress components act independently, which simplifies the analysis and eliminates the need for complex interaction calculations.

5.2.2 Maximum Failure Strain Criterion

The maximum failure strain criterion compares the strain components expressed in the principal material directions of the lamina to their corresponding allowable strain limits, as follows:

Tension:

$$\varepsilon_1 < X_t'; \qquad \varepsilon_2 < Y_t'. \tag{5.10}$$

Compression:

$$\varepsilon_1 > X_c'; \qquad \varepsilon_2 > Y_c'. \tag{5.11}$$

Shear:

$$|\gamma_{12}| < S_{12}'. \tag{5.12}$$

Where X_t' and X_c' are the allowable longitudinal tensile and compressive failure strain respectively, Y_t' and Y_c' are the allowable transverse tensile and compressive failure strain respectively, and S_{12}' is the allowable in-plane shear strain. The terms ε_1 and ε_2 are the maximum acting in-plane normal strains in the principal material directions, while γ_{12} is the maximum shear strain.

The safety margins can be calculated using the following expressions:

$$MS = \frac{X_T'}{\varepsilon_1} - 1 \quad \text{or} \quad MS = \frac{X_c'}{\varepsilon_1} - 1, \tag{5.13}$$

$$MS = \frac{Y_T'}{\varepsilon_2} - 1 \quad \text{or} \quad MS = \frac{Y_c'}{\varepsilon_2} - 1, \tag{5.14}$$

$$MS = \frac{S'_{12}}{|\gamma_{12}|} - 1. \tag{5.15}$$

Similar to the maximum failure stress criterion, the maximum failure strain criterion is distinguished by its simplicity and its ability to clearly indicate the specific mode of failure.

5.2.3 Tsai-Hill Criterion

The Tsai-Hill [70] criterion, assumes interaction between the in-plane stress components of the lamina and defines the failure envelope as follows:

$$f(\sigma) = \left(\frac{\sigma_1}{X}\right)^2 + \left(\frac{\sigma_2}{Y}\right)^2 - \left(\frac{\sigma_1\sigma_2}{X^2}\right) + \left(\frac{\tau_{12}}{S_{12}}\right)^2 \tag{5.16}$$

The safety margin can be calculated using the following expression:

$$MS_{\mathrm{TH}} = \frac{1}{\sqrt{f(\sigma)}} - 1, \tag{5.17}$$

where X and Y correspond to either the tensile or compressive allowable values, depending on the sign of the most critical acting stress. A key advantage of this criterion is that it accounts for interaction between the in-plane stress components of the lamina. However, it does not provide information about the specific failure mode.

5.2.4 Tsai-Wu Criterion

The Tsai-Wu [71] criterion, just like the Tsai-Hill Criterion, considers the interaction between the in-plane stress components of the lamina and defines the failure envelope using the following polynomial expression:

$$f(\sigma) = F_1\sigma_1 + F_2\sigma_2 + F_{11}\sigma_1^2 + F_{22}\sigma_2^2 + F_{66}\tau_{12}^2 + 2F_{12}\sigma_1\sigma_2 = 1, \tag{5.18}$$

where coefficients F_i and F_{ij} are functions of the tensile and compressive strengths of the material allowables and are defined as:

$$F_1 = \left(\frac{1}{X_T} + \frac{1}{X_C}\right), F_2 = \left(\frac{1}{Y_T} + \frac{1}{Y_C}\right), \tag{5.19}$$

$$F_{12} = -\frac{1}{2}\sqrt{\frac{1}{X_T X_C}\frac{1}{Y_T Y_C}}, F_{11} = -\frac{1}{X_T X_C}, F_{22} = -\frac{1}{Y_T Y_C}, F_{66} = \frac{1}{S_{12}^2}. \tag{5.20}$$

The margin of safety for the Tsai-Wu criterion represents the scalar factor by which the actual in-plane stress components of the lamina must be increased to reach failure. It is calculated as

$$MS_{\mathrm{TW}} = \frac{-C_1 + R}{2C_2} - 1, \tag{5.21}$$

where:

$$C_1 = F_1\sigma_1 + F_2\sigma_2, \tag{5.22}$$

$$C_2 = F_{11}\sigma_1^2 + F_{22}\sigma_2^2 + F_{66}\sigma_{12}^2 + 2F_{12}\sigma_1\sigma_{2,} \tag{5.23}$$

$$R = \sqrt{|C_1^2 + 4C_2|}. \tag{5.24}$$

An advantage of the Tsai-Wu criterion is its ability to capture stress interactions within the plane of the lamina. This is achieved through the inclusion of coupling terms between different stress components, allowing for a more realistic and continuous representation of multiaxial loading conditions. However, similar to the Tsai-Hill criterion, the Tsai-Wu criterion does not provide information about the specific failure mode.

6. Extraction of Bearing and By-pass Loads from Finite Element Analysis Outputs

The bearing and bypass loads used to calculate the stress fields around the hole, are taken directly from the FE analysis results, therefore, to automate the extraction of these loads, a custom tool was developed specifically for *Simcenter Femap* with *Nastran*, using *VBA* and the *Simcenter Femap* API.

This section outlines a methodology for load extraction adapted to a specific joint representation commonly used in the industry. The objective is to validate the proposed approach and to identify potential issues arising from current joint modeling practices.

6.1 Joint Representation

It is important to note that the joint modeling approach which is described bellow is applied within the context of global structural analysis, where the fasteners are not explicitly modeled. From this model, the next step would be to perform a local analysis in which the loads obtained from the global model are transferred to a more refined model. In this local model, the fasteners are explicitly represented, allowing for a more detailed assessment of the joint behavior.

6.1.1 Plate

The plate is modeled with four-node quadrilateral shell elements (CQUAD4), and for composite regions, element properties were defined via a laminate section. The mesh size is selected independently of the fastener diameter, being represented by quadrangular elements in the zones where the fasteners are represented. The laminate section is defined using the lamina properties and the specific stacking sequence of the composite layup.

6.1.2 Fastener

The fasteners are not explicitly represented, therefore, contact interactions between the fasteners and the surrounding material are not considered. Additionally, the fastener holes are not represented geometrically, instead, the region of the plate where the fastener would be located is modeled as continuous, filled material.

The fastener is represented using a four-point configuration, with four nodes arranged in a cross pattern on the surface of each plate and the fastener is modeled as a CBUSH element (two-node, 6-DOF generalized spring–damper), that was positioned between two nodes located at the center of the fastener. For each plate surface, the corresponding four-node set should be chosen so that the CBUSH element lies at the geometric center of the set. For efficiency of the modeling process, these four nodes are taken as the ones closest to the central node. The CBUSH nodes are not part of the plate mesh but are auxiliary nodes introduced specifically for the fastener representation. Each CBUSH end node was connected to the four nearest plate surface nodes using an RBE3 interpolation element. The RBE3 distributes loads through weighted interpolation from the independent nodes to the dependent node, where the independent nodes are those that drive the motion, and the dependent node is stiffness-free and follows accordingly. In this case, the CBUSH node was defined as the dependent node, and the surrounding plate surface nodes as the independent nodes. This configuration allows for the transfer of loads while avoiding artificial stiffness. A schematic of the joint is shown in Figure 6.1, where the RBE3 element is depicted in blue, the CBUSH element in red, the plate-mesh nodes in blue and nodes shared by the CBUSH and RBE3 elements in black.

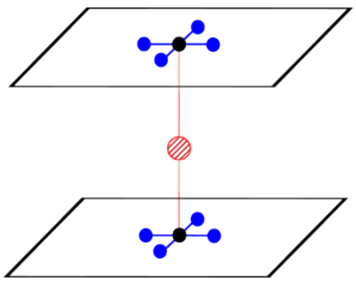

Figure 6.1: Schematic representation of the fastener modeling strategy. The fastener is represented by a CBUSH element (shown in red) positioned at the geometric center of a four-node set on the plate surface. Each CBUSH end node is connected to the surrounding four plate surface nodes through RBE3 interpolation elements (shown in black), which distribute the loads without introducing artificial stiffness. The plate mesh nodes connected through the RBE3 are shown in blue.

To define the CBUSH elements, its stiffness is defined using the Huth formula [72], which is a formulation that provides an empirical estimation of fastener stiffness based on joint geometry and the material properties of the fastener and plates.

6.2 Load Extraction Methodology

The following section presents the load extraction methodology adopted, which is based on an internal classified report from Jet Aviation.

The load extraction process starts with the definition of a load extraction area, defined around the bolt node in the plate. Each fastener has two load extraction points, corresponding to its two CBUSH nodes. The associated load extraction areas and the resulting bypass loads may differ between the area surrounding this two nodes. However, the bearing load remains identical for both, as it is derived directly from the shared CBUSH element representing the fastener.

The bypass load will be calculated based on the resultant membrane forces within the load extraction area, while the bearing load, as stated above will be directly extracted from the CBUSH element forces. To ensure the results are meaningful, it is important to always correctly define the orientation of the CBUSH elements, as well as aligning the laminate element directions with the material coordinate system. This alignment is fundamental, as the approach is developed for orthotropic materials.

6.2.1 Bypass and Bearing Loads Calculation

To calculate the bypass load, a squared shaped load extraction area, with a side length of a is initially considered, as pictured in Figure 6.2.

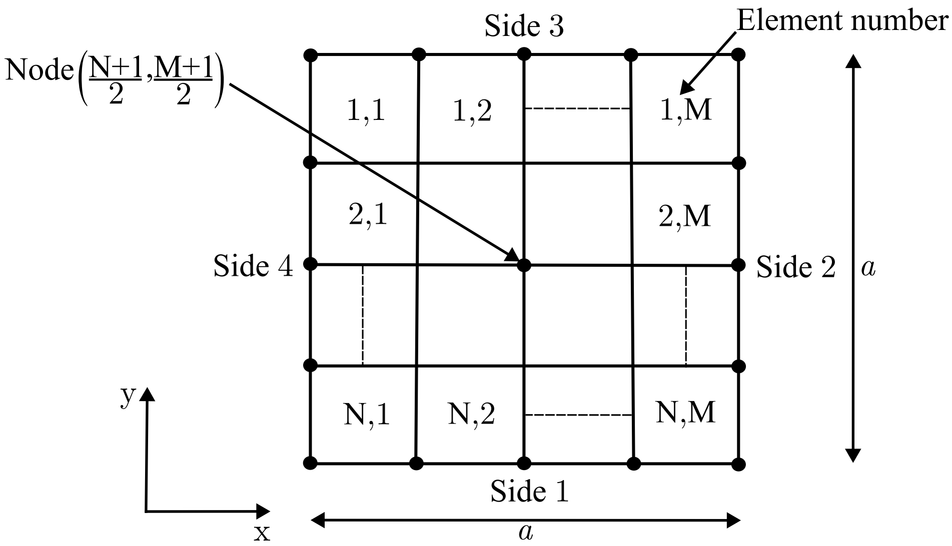

Figure 6.2: Schematic of the square-shaped load extraction area used to calculate the bypass load. The area has a side length a and is centered at the node $\left(\frac{N+1}{2}, \frac{M+1}{2}\right)$. The load is extracted along the four sides (1–4), with element numbers defined in the (i, j) notation.

To extract the direct membrane fluxes, the average flux is first computed on each side of the extraction area by considering the flux component perpendicular to the side under analysis. Specifically, for sides 2 and 4, the P_x component is extracted, while for sides 1 and 3, the P_y component is used. This results in the following expressions:

$$\begin{aligned} P_y^{\text{side1}} &= \text{Average}\left(P_y^{\text{N},1}, P_y^{\text{N},2}, \ldots, P_y^{\text{N},\text{M}}\right) \\ P_x^{\text{side2}} &= \text{Average}\left(P_x^{1,\text{M}}, P_x^{2,\text{M}}, \ldots, P_x^{\text{N},\text{M}}\right) \\ P_y^{\text{side3}} &= \text{Average}\left(P_y^{1,1}, P_y^{1,2}, \ldots, P_y^{1,\text{M}}\right) \\ P_x^{\text{side4}} &= \text{Average}\left(P_x^{1,1}, P_x^{2,1}, \ldots, P_x^{\text{N},1}\right) \end{aligned} \tag{6.1}$$

To determine the bypass and total membrane fluxes in each direction, the following conditions are applied:

$$\begin{aligned} P_x^{\text{By}} &= \begin{cases} P_x^{\text{side2}} & \text{if } \left|P_x^{\text{side2}}\right| \leq \left|P_x^{\text{side4}}\right| \\ P_x^{\text{side4}} & \text{if } \left|P_x^{\text{side4}}\right| < \left|P_x^{\text{side2}}\right| \end{cases}, \quad P_x^{\text{Total}} = \begin{cases} P_x^{\text{side2}} & \text{if } \left|P_x^{\text{side2}}\right| > \left|P_x^{\text{side4}}\right| \\ P_x^{\text{side4}} & \text{if } \left|P_x^{\text{side4}}\right| \geq \left|P_x^{\text{side2}}\right| \end{cases}, \\ P_y^{\text{By}} &= \begin{cases} P_y^{\text{side1}} & \text{if } \left|P_y^{\text{side1}}\right| \leq \left|P_y^{\text{side3}}\right| \\ P_y^{\text{side3}} & \text{if } \left|P_y^{\text{side3}}\right| < \left|P_y^{\text{side1}}\right| \end{cases}, \quad P_y^{\text{Total}} = \begin{cases} P_y^{\text{side1}} & \text{if } \left|P_y^{\text{side1}}\right| > \left|P_y^{\text{side3}}\right| \\ P_y^{\text{side3}} & \text{if } \left|P_y^{\text{side3}}\right| \geq \left|P_y^{\text{side1}}\right| \end{cases}. \end{aligned} \tag{6.2}$$

A similar methodology is applied for the evaluation of shear fluxes, however, it uses the average shear fluxes on all four sides of the extraction region. The following procedure is adopted:

$$\begin{aligned} P_{xy}^{\text{side1}} &= \text{Average}\left(P_{xy}^{\text{N},1}, P_{xy}^{\text{N},2}, \ldots, P_{xy}^{\text{N},\text{M}}\right) \\ P_{xy}^{\text{side2}} &= \text{Average}\left(P_{xy}^{1,\text{M}}, P_{xy}^{2,\text{M}}, \ldots, P_{xy}^{\text{N},\text{M}}\right) \\ P_{xy}^{\text{side3}} &= \text{Average}\left(P_{xy}^{1,1}, P_{xy}^{1,2}, \ldots, P_{xy}^{1,\text{M}}\right) \\ P_{xy}^{\text{side4}} &= \text{Average}\left(P_{xy}^{1,1}, P_{xy}^{2,1}, \ldots, P_{xy}^{\text{N},1}\right) \end{aligned} \tag{6.3}$$

$$P_{xy}^{\mathrm{By}} = \begin{cases} P_{xy}^{\mathrm{side1}} & \text{if } \left|P_{xy}^{\mathrm{side1}}\right| = \min\left(\left|P_{xy}^{\mathrm{side1}}\right|, \left|P_{xy}^{\mathrm{side2}}\right|, \left|P_{xy}^{\mathrm{side3}}\right|, \left|P_{xy}^{\mathrm{side4}}\right|\right) \\ P_{xy}^{\mathrm{side2}} & \text{if } \left|P_{xy}^{\mathrm{side2}}\right| = \min\left(\left|P_{xy}^{\mathrm{side1}}\right|, \left|P_{xy}^{\mathrm{side2}}\right|, \left|P_{xy}^{\mathrm{side3}}\right|, \left|P_{xy}^{\mathrm{side4}}\right|\right) \\ P_{xy}^{\mathrm{side3}} & \text{if } \left|P_{xy}^{\mathrm{side3}}\right| = \min\left(\left|P_{xy}^{\mathrm{side1}}\right|, \left|P_{xy}^{\mathrm{side2}}\right|, \left|P_{xy}^{\mathrm{side3}}\right|, \left|P_{xy}^{\mathrm{side4}}\right|\right) \\ P_{xy}^{\mathrm{side4}} & \text{if } \left|P_{xy}^{\mathrm{side4}}\right| = \min\left(\left|P_{xy}^{\mathrm{side1}}\right|, \left|P_{xy}^{\mathrm{side2}}\right|, \left|P_{xy}^{\mathrm{side3}}\right|, \left|P_{xy}^{\mathrm{side4}}\right|\right) \end{cases}$$

$$P_{xy}^{\mathrm{Total}} = \begin{cases} P_{xy}^{\mathrm{side1}} & \text{if } \left|P_{xy}^{\mathrm{side1}}\right| = \max\left(\left|P_{xy}^{\mathrm{side1}}\right|, \left|P_{xy}^{\mathrm{side2}}\right|, \left|P_{xy}^{\mathrm{side3}}\right|, \left|P_{xy}^{\mathrm{side4}}\right|\right) \\ P_{xy}^{\mathrm{side2}} & \text{if } \left|P_{xy}^{\mathrm{side2}}\right| = \max\left(\left|P_{xy}^{\mathrm{side1}}\right|, \left|P_{xy}^{\mathrm{side2}}\right|, \left|P_{xy}^{\mathrm{side3}}\right|, \left|P_{xy}^{\mathrm{side4}}\right|\right) \\ P_{xy}^{\mathrm{side3}} & \text{if } \left|P_{xy}^{\mathrm{side3}}\right| = \max\left(\left|P_{xy}^{\mathrm{side1}}\right|, \left|P_{xy}^{\mathrm{side2}}\right|, \left|P_{xy}^{\mathrm{side3}}\right|, \left|P_{xy}^{\mathrm{side4}}\right|\right) \\ P_{xy}^{\mathrm{side4}} & \text{if } \left|P_{xy}^{\mathrm{side4}}\right| = \max\left(\left|P_{xy}^{\mathrm{side1}}\right|, \left|P_{xy}^{\mathrm{side2}}\right|, \left|P_{xy}^{\mathrm{side3}}\right|, \left|P_{xy}^{\mathrm{side4}}\right|\right) \end{cases} \tag{6.4}$$

The bearing load can be obtained directly from the CBUSH forces, as previously described. However, since it must also be in equilibrium with the total and bypass membrane force fluxes, P_{Total} and P_{By}, respectively, in the plate around the fastener, the bearing flux in each direction could also be determined through the following relation:

$$P_{\mathrm{Bea}} = P_{\mathrm{Total}} - P_{\mathrm{By}}. \tag{6.5}$$

However, this alternative approach propagates any errors inherent of the bypass flux calculation into the resulting bearing load estimation.

6.2.2 Load Extraction Area Definition

The load extraction area, is directly linked to several geometrical parameters, represented in Figure 6.3.

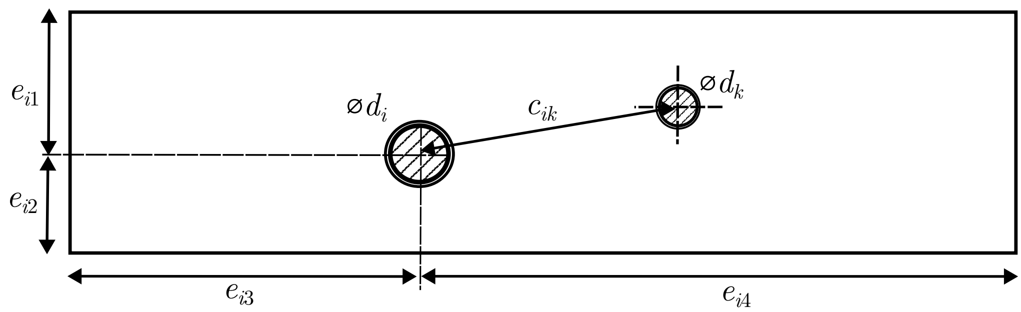

Figure 6.3: Geometrical parameters associated with the load extraction area. The parameter e_{ij} denotes the distance from the edge of the hole of diameter d_i to edge j, while c_{ik} represents the distance between the centers of the holes with diameters d_i and d_k.

The parameter e_{ij} is the distance from the hole of diameter d_i to the edge j and C_{ik} the distance between the hole of diameter d_i and the hole of diameter d_k.

The bypass loads should be extracted at a sufficient distance from the hole to minimize stress field disturbances caused by the hole itself, while also ensuring the location is not so far that it becomes influenced by adjacent holes, imposed boundary conditions, or free edges. The defined extraction area should also be adapted to the element size, in this approach, the area was rounded up to the nearest value that accommodates the mesh discretisation. However the side length could alternatively be rounded down or an interpolation between the rounded-up and rounded-down values could be employed to achieve a more balanced representation.

Following this set of criteria the size of the load extraction area side is

$$a = 2 \times \min\left(e_{i1}, e_{i2}, e_{i3}, e_{i4}, C_{ik}\frac{d_i}{d_i + d_k}\right) + \varepsilon, \tag{6.6}$$

where ε represents the calibration offset used to ensure that the area accommodates the mesh discretisation.

6.3 Analysis of the Load Extraction Method

This section evaluates the joint representation and load-extraction procedure, focusing on the selection of independent nodes for the RBE3 used to distribute the fastener load into the plate, as well as the accuracy of the bearing and bypass loads extracted.

In Jet Aviation's joint design procedure, the RBE3 elements are defined by selecting the nodes closest to the central node, without accounting for the fastener diameter. This approach avoids the need for local mesh refinement in the fastener region. However, as noted in [73], the independent nodes of these elements should ideally lie within the fastener's influence zone, i.e., the portion of the plate surface that realistically transfers load into or out of the fastener, typically bounded by the diameter of the fastener head and nut. Consequently, this study evaluates the company's joint load representation procedure by considering differently mesh sizes, which inherently alter the positioning of the RBE3 element independent nodes. The analysis will be made for a double lap joint under uniaxial loading, with two consecutive fasteners positioned along the centerline of the plate's width. The BCs, loading scenario and overall dimensions, defined relative to the fastener diameter, are illustrated in Figure 6.4.

The FE model's mesh was chosen to allow for $\varepsilon = 0$. The value of the load extraction area side length is $a = 10\,d$. Figure 6.5 illustrates the membrane force distribution along the x-direction, expressed in force per unit length (N mm^{-1}), within this area for the rightmost fastener (corresponding to the largest x value).

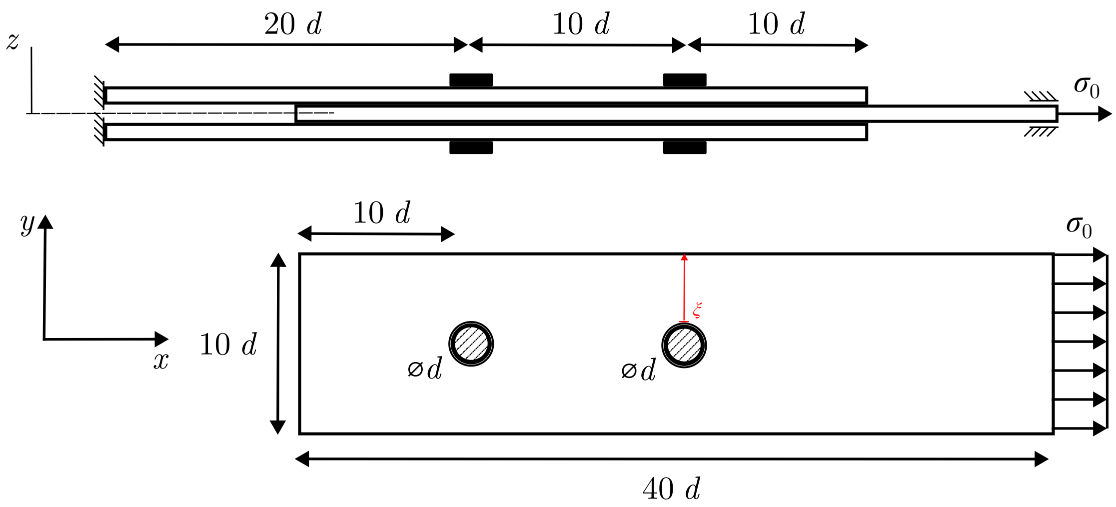

Figure 6.4: Model description of the double-lap joint under uniaxial loading, showing boundary conditions, loading configuration, and overall dimensions defined relative to the fastener diameter.

The results are presented for the central plate. The total load is $\sigma_0 = 1$ N mm^{-2}. The laminate is a $[0°/90°]_s$ configuration, based on the properties in Table 3.1, with the fibers oriented along the x-direction. The displays indicate that increasing the element size, leads to a reduction in the stress concentrations. This behavior arises because a coarser mesh, distributes the bearing load over a larger effective area, resulting in lower stress concentrations.

The extracted bypass and bearing load fluxes are compared in Table 6.1, where $\beta = P/P_{\mathrm{Bea}}$ and the total load is given by $P = P_{\mathrm{Bea}} + P_{\mathrm{By}}$. A coarser mesh leads to an higher β, and as $\beta > 0.5$ in all cases, this indicates that more load is being transferred through this fastener to the adjacent plates compared to the other one. Therefore, we can conclude that a coarser mesh results in a less balanced load transfer, meaning the load is distributed less equally between the fasteners. Additionally, the extracted bearing and bypass loadings were used to calculate the stress concentration factor $K_t = \sigma_x(x, \xi = 0)/\sigma_0$ in the middle plate, using the methodology developed in this thesis. A larger element size leads to higher stress concentrations. Moreover, in this connection, a larger element size causes more load to be transferred through the fastener, consistent with Nguyen-Hoang and Becker's [14] conclusion that the filled hole case is the most critical condition in a joint under bearing–bypass loading.

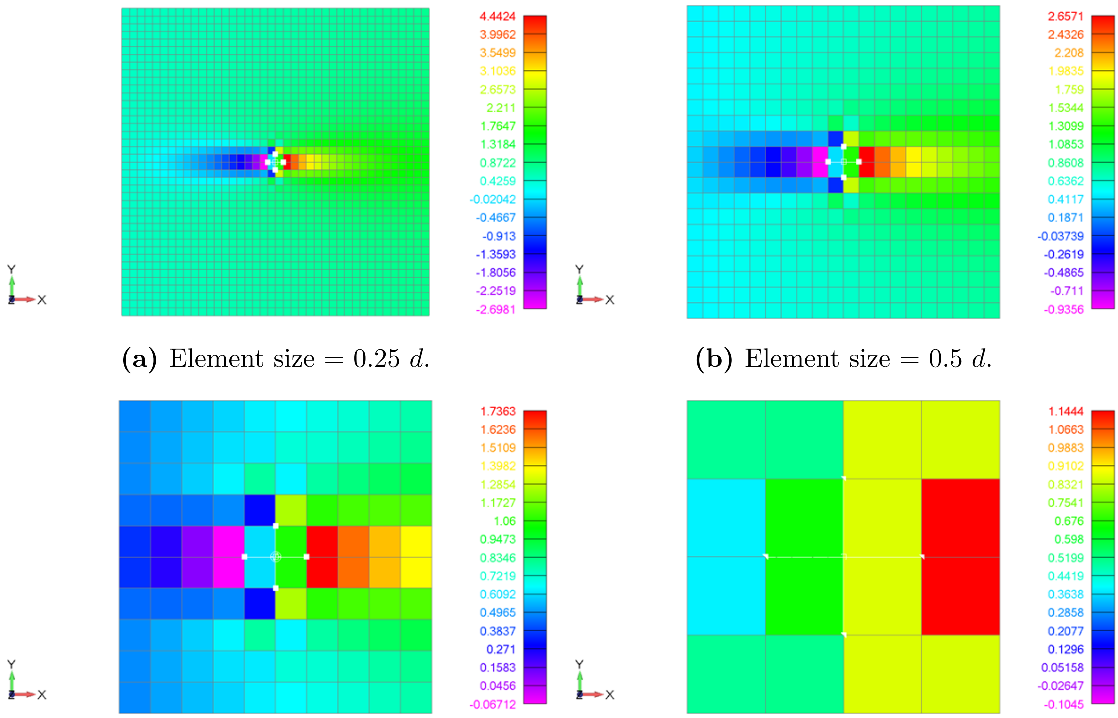

(a) Element size = 0.25 d.

(b) Element size = 0.5 d.

(c) Element size = 1.00 d.

(d) Element size = 2.50 d.

Figure 6.5: Effect of element size and opposite-node spacing on membrane force distribution (N mm^{-1}), with $d = 1$ mm and using the non-deformed display option. Opposite-node spacing is set to twice the element size.

Table 6.1: Bearing and bypass loads extracted from the FE model for various element sizes. Listed are the bypass load P_x^{By} and the bearing load P_{Bea} defined as force per unit thickness (in N mm^{-1}), together with β and the stress-concentration factor K_t .

Element size [mm]	P_x^{By} [N mm^{-1}]	P_{Bea} [N mm^{-1}]	β [-]	K_t [-]
0.25 d	9.38	10.62	0.531	13.32
0.5 d	9.26	10.74	0.537	13.40
1.0 d	9.18	10.90	0.545	13.55
2.5 d	8.81	11.19	0.559	13.74

7. Operational Details and Limitations of the Developed Tool

The methodology developed in this thesis was translated into a tool for the analysis of filled and open holes, intended to support the design process by providing rapid failure predictions. This chapter explains how the tool operates, summarises its limitations, presents an example application, and concludes with a brief reflection of its overall performance.

7.1 Tool Operation

The main workflow of the tool is shown in Figure 7.1. The process begins with a *VBA* script that uses the *Femap* API to identify and map the holes in the FE model. Each hole is then analysed individually according to the procedure outlined in Figure 7.2. As part of this step, the API checks whether each hole satisfies the assumptions of the methodology developed in this thesis, classifies it as either an open or filled hole, and verifies compliance with the constraints established for the tool's applicability.

From the FE model, the laminate properties, geometric parameters, and loadings are subsequently extracted, with the latter following the methodology described in Table 6.3. These inputs are then processed in *Python*, where laminate-level stresses are computed using the formulation presented in section 4.6. The lamina-level stress field is then derived, and the margins of safety are evaluated using the formulation described in Equation 5.2.4, ultimately determining whether failure occurs. This process is repeated for all holes in the global model, providing an estimation of the critical holes within the structure under analysis.

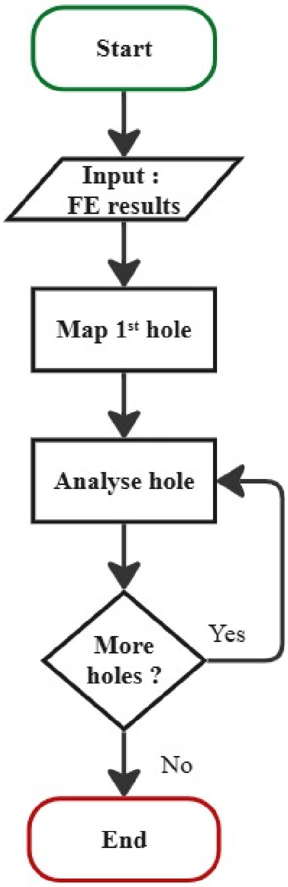

Figure 7.1: Overall workflow of the developed tool.

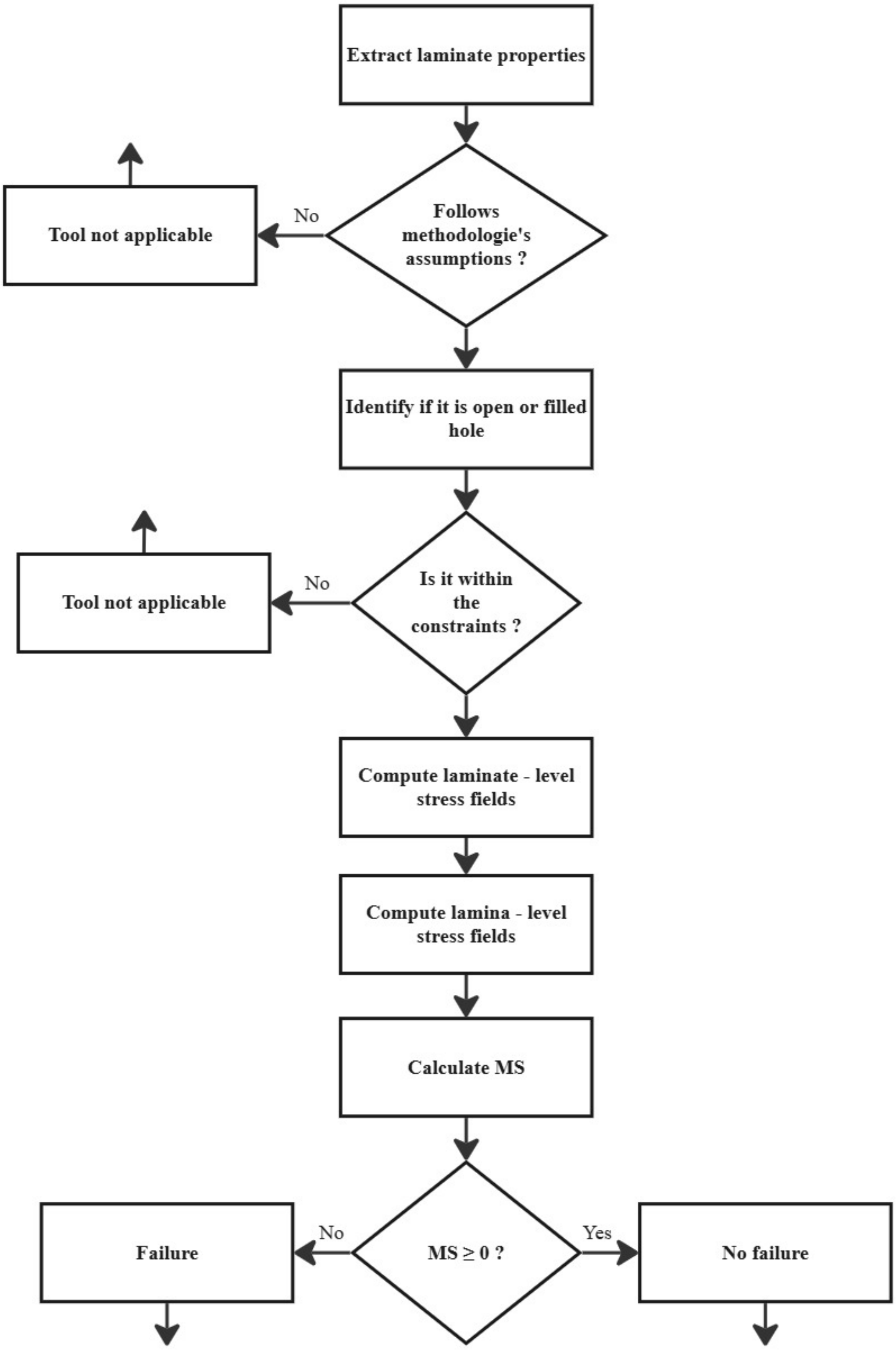

Figure 7.2: Hole analysis subroutine, executed iteratively for all holes in the global model.

7.2 Assumptions and Limitations of the Developed Tool

In this Section we will summarise the assumptions and limitations, defining the main envelop within which the tool should be used.

7.2.1 Tool Assumptions

The development of the tool was carried out under the following main assumptions:

- Symmetric laminate layups.
- Two-dimensional, linear, plane-stress formulation.
- Joint symmetry to eliminate secondary bending by avoiding load-path eccentricity.
- Frictionless fastener–hole contact idealized by sinusoidal radial tractions over half of the hole circumference, with a perfect fit (no clearance) between fastener and hole.
- In-plane loading.

7.2.2 Tool Limitations

This subsection presents the tool's limitations and provides guidance on how they can be further addressed.

In Table 7.1, we summarise the geometric configurations for open and filled holes in which, for the laminates analysed in this thesis, the analytical solutions for infinite-width and finite-width plates show absolute relative errors below 4% when compared with finite element results. Recall that when the roots of the characteristic equation have a nonzero real part, $\mathrm{Re}(\mu_k) \neq 0$, as in angle-ply laminates, a sign change in the mapping function must be applied at the plate edges, $x = \pm w/2$, in accordance with Equation 4.15. To apply the analytical model, it is important to delimit the range of e_{load}/d values for which the tool is valid. Table 7.2 summarises the configurations where the load application distance yields absolute relative errors below 5%. This step is not yet implemented in the tool. For the biaxial loading case, only a square plate with $w_x/d = w_y/d = 10$ was analysed. Further work should examine the influence of the plate aspect ratio (w_x/w_y) and test the implementation for other dimension ratios, particularly $w_x/d < 10$ and/or $w_y/d < 10$, where the distance for load application may be more influential. Additionally, the load application distance study was performed only for uniaxial loading; therefore, future work should investigate how the load distance varies under biaxial loading and how it compares with the uniaxial case. For the conditions of this study we can state that the open hole under biaxial tension loading for $w_x/d = w_y/d = 10$, presents absolute relative errors bellow 4% for all laminates, and ratios α studied, except for the [0°] laminate, where the errors are above 5%. The analytical solution for biaxial loading in an infinite plate was formulated, and also implemented, however, its results were not analysed and verified. Despite this, the uniaxial implementation was verified. We can therefore state that the overall workflow of the code is correct: it correctly determines the roots of the characteristic equation Equation 2.32 and the mapping functions Equation 4.3 for the infinite plate. Consequently, any remaining implementation error is likely in the determination of the complex conjugates $\bar{\alpha}_m$ and $\bar{\beta}_m$ for the biaxial loading case with infinite plate boundary conditions. The off-axis bearing case was formulated and implemented but not tested. It follows the same logic as the biaxial infinite plate formulation; therefore, any potential error is likely in the determination of the complex conjugates $\bar{\alpha}_m$ and $\bar{\beta}_m$ for the boundary conditions. Finally, no analysis was conducted for the filled hole under combined bearing and bypass loading, since this case is obtained by superposing the bearing stress routine with the open hole uniaxial stress routine, which were verified individually; this approach is validated in [8].

Regarding the lamina stress calculations, analyses were performed only for the open hole tension and filled hole bearing configurations with $w/d = 10$ and $e_{\text{load}}/d = 80$; for the filled hole case we additionally considered $e/d = 20$. The critical plies and their associated critical stresses were correctly identified. For the open hole case, the maximum absolute relative error was 1.79%. Although the 90° plies exhibited relative stress errors exceeding 4%, these plies are not critical under uniaxial tension. The filled hole case showed good agreement with the numerical results, including the 90° plies, with a maximum absolute relative error of 2.15%. We therefore consider the methodology suitable for predicting first ply failure, however, further studies should be conducted to determine the range of dimensions over which this methodology may fail, particularly since the tests were performed on geometries that exhibited small errors in laminate-level stress calculations. In addition, the method was not tested under biaxial loading, and therefore this case should be analysed further.

Regarding the load extraction methodology, different mesh sizes were compared to assess Jet Aviation's joint design procedure and its influence on the loads extracted from the FE model. The results show that a coarser mesh leads to a less balanced load transfer, with the load being distributed less evenly between fasteners of identical stiffness. It should be noted, however, that the joint representation was only evaluated for the $[0^\circ/90^\circ]_s$ laminate. Further studies are therefore recommended for other laminate configurations, loading conditions, and geometries.

In this study, the extraction area was defined using both the edge distance and the spacing between consecutive holes as the governing minimum values, and the analysis was limited to uniaxial loading. It remains important to investigate the individual influence of each geometric parameter on the extracted loads. Moreover, since the methodology has also been developed and adapted for biaxial loading, the same validation procedures should be extended to that context.

Table 7.1: Summary of geometric configurations for an open hole under uniaxial tension and a filled hole under bearing in infinite width and finite width plates, where for the laminates analysed in this thesis the analytical solutions show absolute relative errors below 4% compared with FE results.

Open Hole: Uniaxial Tension					
	$[0^\circ]$	Quasi-isotropic	$[0^\circ/90^\circ]_s$	$[\pm 45^\circ]_s$	$[0^\circ_5 / (\pm 45^\circ)_2 / 90^\circ]_s$
Infinite-width	$w/d \geq 5$	$w/d \geq 10$	$w/d \geq 5$	$w/d \geq 10$	$w/d \geq 10$
Finite-width	$w/d \geq 3$	$w/d \geq 3$	$w/d \geq 3$	$w/d \geq 3$	$w/d \geq 3$
Filled Hole: Bearing					
	$[0^\circ]$	Quasi-isotropic	$[0^\circ/90^\circ]_s$	$[\pm 45^\circ]_s$	$[0^\circ_5 / (\pm 45^\circ)_2 / 90^\circ]_s$
Infinite-width	$w/d \geq 80$ AND $e/d \geq 80$	($w/d \geq 80$ AND $e/d \geq 20$) OR ($w/d > 40$ AND $e/d \geq 80$)	$w/d \geq 40$ AND $e/d \geq 80$	($w/d \geq 80$ AND $e/d \geq 20$) OR ($w/d \geq 80$ AND $e/d \geq 80$)	$w/d \geq 40$ AND $e/d \geq 80$
Finite-width	$w/d \geq 3$ AND $e/d \geq 10$	($w/d = 3$ AND $e/d \geq 2.5$) OR ($w/d \geq 3$ AND $e/d \geq 10$)	$w/d \geq 3$ AND $e/d \geq 2.5$	$w/d \geq 10$ AND $e/d \geq 10$	($w/d = 3$ AND $e/d \geq 2.5$) OR ($w/d \geq 3$ AND $e/d \geq 10$)

Table 7.2: Summary of geometric configurations for an open hole and a filled hole under different load application distances, where for the laminates analysed in this thesis the analytical solutions show absolute relative errors below 5% compared with FE results.

Open Hole: Uniaxial Tension					
	$[0°]$	Quasi-isotropic	$[0°/90°]_s$	$[\pm 45°]_s$	$[0^\circ_5\,/\,(\pm 45°)_2\,/\,90°]_s$
$e_{load}/d = 2.5$	$\times$	$w/d \leq 20$	$w/d \leq 10$	$w/d \leq 20$	$w/d \leq 20$
$e_{load}/d = 5$	$w/d \leq 20$	$w/d \leq 20$	$w/d \leq 20$	$w/d \leq 20$	$w/d \leq 20$
$e_{load}/d = 10$	$w/d \leq 20$	$w/d \leq 20$	$w/d \leq 20$	$w/d \leq 20$	$w/d \leq 20$
Filled Hole: Bearing					
$e/d = 2.5$					
	$[0°]$	Quasi-isotropic	$[0°/90°]_s$	$[\pm 45°]_s$	$[0^\circ_5\,/\,(\pm 45°)_2\,/\,90°]_s$
$e_{load}/d = 2.5$	$w/d \leq 5$	$w/d \leq 20$	$w/d \leq 5$	$w/d \leq 10$	$w/d \leq 10$
$e_{load}/d = 5$	$w/d \leq 20$	$w/d \leq 20$	$w/d \leq 20$	$w/d \leq 20$	$w/d \leq 20$
$e_{load}/d = 10$	$w/d \leq 20$	$w/d \leq 20$	$w/d \leq 20$	$w/d \leq 20$	$w/d \leq 20$
$e/d = 10$					
	$[0°]$	Quasi-isotropic	$[0°/90°]_s$	$[\pm 45°]_s$	$[0^\circ_5\,/\,(\pm 45°)_2\,/\,90°]_s$
$e_{load}/d = 2.5$	$w/d \leq 5$	$w/d \leq 20$	$w/d \leq 5$	$w/d \leq 10$	$w/d \leq 10$
$e_{load}/d = 5$	$w/d \leq 5$	$w/d \leq 20$	$w/d \leq 10$	$w/d \leq 20$	$w/d \leq 20$
$e_{load}/d = 10$	$w/d \leq 20$	$w/d \leq 20$	$w/d \leq 20$	$w/d \leq 20$	$w/d \leq 20$
$e/d = 20$					
	$[0°]$	Quasi-isotropic	$[0°/90°]_s$	$[\pm 45°]_s$	$[0^\circ_5\,/\,(\pm 45°)_2\,/\,90°]_s$
$e_{load}/d = 2.5$	$w/d \leq 5$	$w/d \leq 10$	$w/d \leq 5$	$w/d \leq 10$	$w/d \leq 5$
$e_{load}/d = 5$	$w/d \leq 5$	$w/d \leq 20$	$w/d \leq 10$	$w/d \leq 20$	$w/d \leq 20$
$e_{load}/d = 10$	$w/d \leq 20$	$w/d \leq 20$	$w/d \leq 20$	$w/d \leq 20$	$w/d \leq 20$

7.3 Example of Application of the Tool

In this section, we show an example of application of the tool using the FE model presented in section 6.3 as input, focusing on the same connection studied there. The bearing and bypass loads used correspond to the solutions for the element size of $1.0\,d$. The tool proceeds through the following steps until it determines if the plate will fail or not.

1. **Inputs:**
   - Loading Case: Filled hole; Uniaxial Bypass;Bearing - $P_{\text{By}} = 9.18$ N mm^{-1}; $P_{\text{Bea}} = 10.90$ N mm^{-1}.
   - Geometrical Configuration: $w/d = 10$; $e/d = 20$; $d = 2$ mm.
   - Layup - $[0°/90°]_s$; $t_k = 0.125$ mm per ply.
   - Elastic Ply Properties - $E_x = 171.40$ GPa; $E_y = 9.10$ GPa; $G_{xy} = 9.10$ GPa; $\nu = 0.016$.
   - Stress Allowables (obtained from reference [74]): $X_T = 2326.2$ MPa; $X_C = 1200.1$ MPa, $Y_T = 62.3$ MPa, $Y_C = 199.8$ MPa; $S_{12} = 62.3$ MPa.
2. **Computation of Laminate-level stresses:**
   - Calculation of stress field using the laminate's equivalent elastic properties (Figure 7.3).

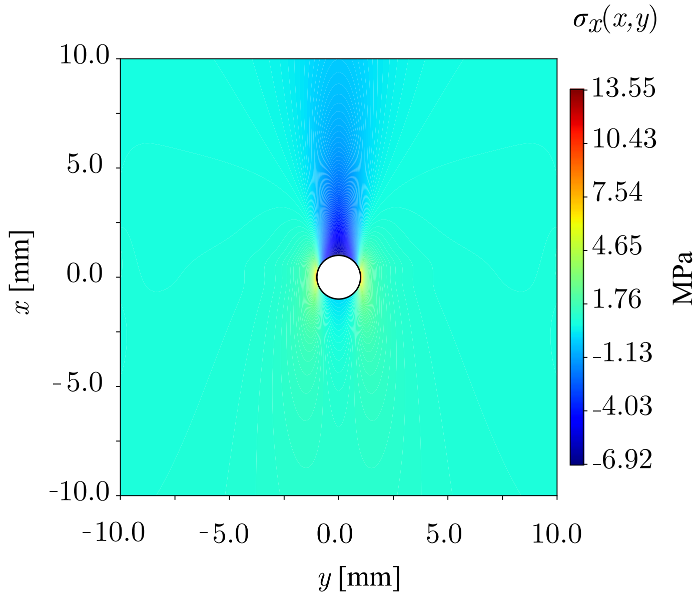

Figure 7.3: Laminate-level net-section stresses, $\sigma_x(x, y)$.

3. **Computation of Lamina-level stresses**

   - In Figure 7.4, lamina-level stresses are shown around the hole and along a line at $y = 0$ perpendicular to the loading direction, as this is the critical zone where failure is most likely to occur.

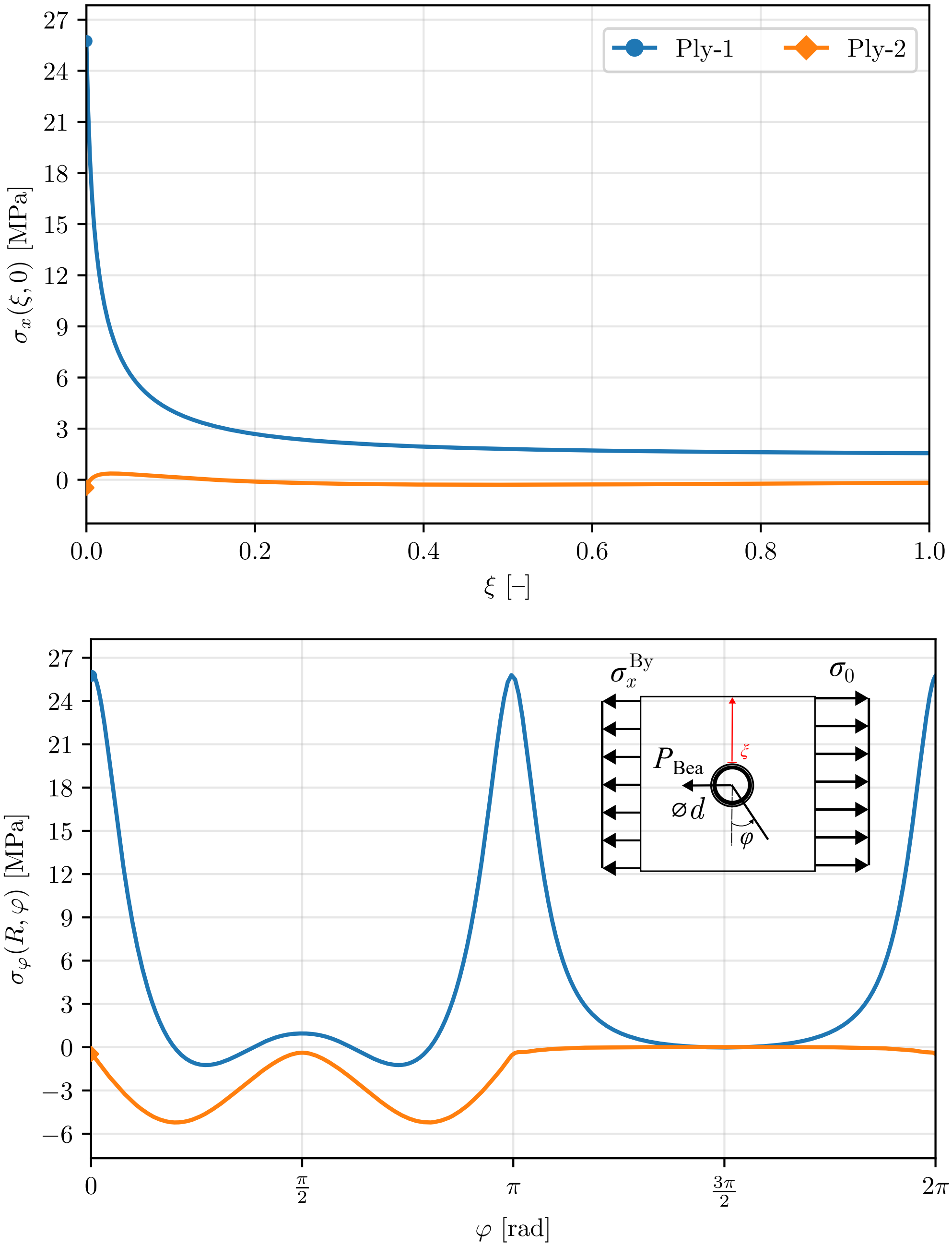

Figure 7.4: Lamina-level stresses, wehere Ply-1 is the 0° ply and Ply-2 the 90° ply. The upper plot shows the net-section stresses, while the lower plot shows the circumferential stresses.

4. **Failure Calculation**

   - The lamina's margins of safety at the critical location are reported in Table 7.3. They were computed for the Maximum Stress, Tsai-Hill and Tsai-Wu failure criteria. Since no ply exhibits MS < 0, no failure is predicted.

Table 7.3: Margins of safety for lamina failure, using Maximum Stress, Tsai-Hill and Tsai-Wu failure criteria.

Ply	MS σ_{11}	MS σ_{22}	MS τ_{12}	MS Tsai-Hill	MS Tsai-Wu
1	6.4E3	1.4E0	5.9E4	1.4E0	1.4E0
2	1.7E3	4.3E2	5.9E4	4.1E2	3.9E2
3	1.7E3	4.3E2	5.9E4	4.1E2	3.9E2
4	6.4E3	1.4E0	5.9E4	1.4E0	1.4E0

Comparison with FE Results

The results from the tool are now compared against FE analysis in which the fasteners are modeled as rigid bodies to represent the fastener–plate contact interaction (see Figure 7.5). The model BCs and loads are the same as those used in section 6.3. A *hard contact* formulation is applied in the normal direction, with the *augmented Lagrange* method used for contact constraint enforcement. The mesh follows the guidelines presented in section 6.3. In addition, S8R shell elements were employed in order to analyse the lamina-level stresses.

In Figure 7.6, the stress field for the 0° (critical) ply is shown. The maximum stress predicted by the analytical model is 1.04 times the numerical value (i.e., about 4% higher). This discrepancy may stem from the load-extraction procedure as in earlier sections the relative error was negative, implying the analytical result should be lower, disregarding the filled-hole case where this error was positive but it was roughly twenty times smaller than for the open hole case. In Table 7.1, the margins of safety are summarised. For the critical components (lower MS values), the MS from the analytical model closely matches the FE results. Larger MS values show more noticeable relative deviations, which is expected because they correspond to very low stress levels, and so small absolute differences translate into large percentage errors.

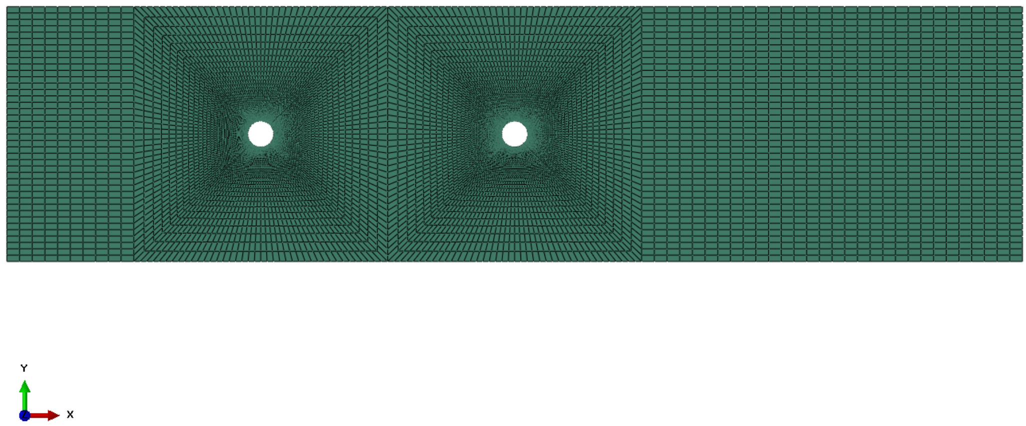

(a) Mid-plate mesh.

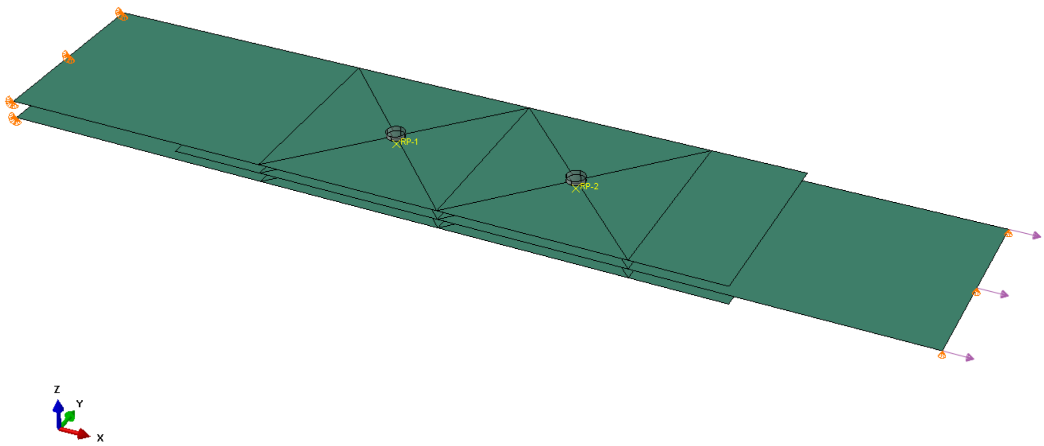

(b) FE model geometry, boundary conditions, and loads.

Figure 7.5: FE model with contact using rigid bodies as fasteners. The specimen is a double-lap joint under tension; the model was implemented in *Abaqus*.

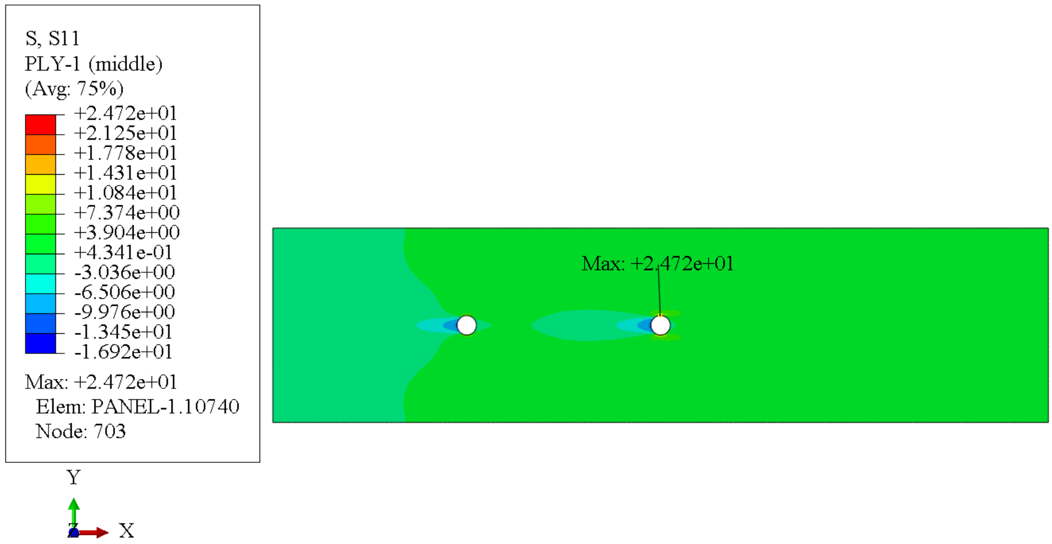

Figure 7.6: Laminate-level net-section stresses, $\sigma_x(x, y)$.

Table 7.4: Margins of safety of the FE results for lamina failure, using Maximum Stress, Tsai-Hill and Tsai-Wu failure criteria.

Ply	MS σ_{11}	MS σ_{22}	MS τ_{12}	MS Tsai-Hill	MS Tsai-Wu
1	9.52E3	1.51E0	6.46E4	1.51E0	1.51E0
2	1.77E3	2.32E3	6.36E1	6.35E1	6.65E1
3	1.77E3	2.32E3	6.36E1	6.35E1	6.65E1
4	9.52E3	1.51E0	6.46E4	1.51E0	1.51E0

7.4 Qualitative Analysis of the Tool's Performance

This section presents a qualitative analysis of the tool's overall performance based on the author's experience utilising it.

Overall the tool performs very efficiently, computing failure in under half a minute for infinite-domain assumptions. The bottleneck of the tool, is definitely the finite-width calculations, specifically, the cancellation of tractions perpendicular to the load direction because the number of plates required for a periodic arrangement can be very large. This is particularly inefficient for the filled hole, especially when the end-edge distance is very low. The hole BC imposition routine is usually the most efficient one, but the traction-cancellation step can be problematic because it relies on hyperbolic functions, which can lead to *overflow errors*. Therefore, parameters must be carefully calibrated, particularly the virtual wavelength (l_{Fo}), to mitigate the Gibbs phenomenon.

To boost the tool's performance, the author proposes transforming the stress-calculation routine into a surrogate model capable of generating new fitting functions for different load cases, geometries, and layups. With this approach, lamina-level stresses could be obtained directly from the applied loads without repeatedly running the complex and sometimes inefficient, finite-width stress-field formulation.

Additionally, as shown in previous sections, the relative error in the laminate stress field is negative in most cases, indicating that the stresses are underpredicted. This runs counter to the conservative philosophy adopted for the tool. It would therefore be prudent to apply a safety factor to the load to ensure that stresses are not underestimated.

8. Conclusion and Future Work

8.1 Conclusion

Pursuing lighter and more fuel-efficient aircraft, the aerospace industry has increasingly adopted composite materials in aircraft structures. The Boeing 787 Dreamliner and Airbus A350 XWB were the first commercial aircraft to feature more than 50% of their structural weight in composites. While these materials enable significant performance gains, they also introduce considerable complexity into the structural design process due to their anisotropic behavior. Aiming to start working more intensively with composite aircraft structures, Jet Aviation proposed this thesis with the objective of developing a tool capable of efficiently analyzing stress concentration zones and calculate failure around open and filled holes in composite laminates, thereby supporting preliminary design activities.

The tool developed in this thesis was based on analytical methods, with the objective of reducing reliance on numerical simulations during the design process. The problem was simplified by adopting a two-dimensional linear plane stress formulation and restricting the analysis to symmetric laminates. A FE methodology was established to provide reference solutions and to validate the analytical models.

Analytical solutions for determining the stress field in open and filled holes in both infinite and finite plates were divised and tested against FE results. Lekhnitskii's [10] complex potential method was used for infinite-domain problems, while the formulations of Nguyen-Hoang and Becker [8, 9] enabled finite-width solutions. The approach was further extended to biaxial loading through superposition of loading cases, and additional cases, such as out-of-axis bearing and bearing–bypass loading, were also considered.

Failure was addressed through the conservative First Ply Failure (FPF) criterion, whereby the failure of one ply implies the failure of the laminate. Lamina-level stresses were computed from laminate strains by exploiting midplane symmetry and applying Hooke's law. The methodology was validated against FE results and different criteria for computing lamina's failure was presented.

Finally, since the input bypass and bearing loads for stress calculations were obtained from FE models, a dedicated extraction methodology was developed and validated. This approach was tailored to Jet Aviation's modeling practices, reducing modeling effort while ensuring accuracy in the preliminary design phase.

In conclusion, this thesis successfully presents a state of the art approach for the fast analysis of open and filled holes in composite structures. It relies entirely on analytical methods to evaluate stresses, avoiding the commonly used heuristic approaches, which lack physical justification and are particularly unreliable for filled holes. In addition, a conservative and efficient analytical framework for predicting failure based on First Ply Failure is implemented. Finally, the methodology is integrated with a feature that extracts loads directly from FE results, ensuring full connectivity.

With the tool fully developed, its domain of applicability was rigorously assessed and its limitations clearly defined, resulting in a robust and bounded methodology tailored to industrial needs. Overall, the methodology has proven highly reliable across all tested configurations, enabling the creation of a tool that accepts a global FE model as input and provides a detailed local analysis of all holes within its applicability domain as output.

8.2 Future Work and Gaps to be Fulfilled

With the goal of continuously improving the analysis of open and filled holes in aircraft composite laminates, we will now address current gaps of the tool and propose future works, in other to improve the tool's range of applications and accuracy of results.

Gaps to be fulfilled:

- Add the sign change in mapping function at the plate's edges when $\mathrm{Re}[\mu_k] \neq 0$, allowing for better result for angle-ply laminates.
- Extend the validation of stress fields under biaxial loading to different plate geometries, load application distances and lamina-level analysis.
- Perform verification of the out-of-axis bearing and infinite plate biaxial loading cases, as well as explore their limitations.
- Perform a quantitative analysis of the tool's performance.
- Extend the load extraction methodology by testing additional laminate configurations, evaluating the individual influence of each geometric parameter on the extracted loads, and expanding the validation procedure to biaxial loading.

- Cancel shear stresses $\tau_{xy}(x, e)$ along the horizontal boundary $y = e$ (method for solving the problem presented in subsection 4.2.2).

Future Work:

- Validate the formulation for a wider range of orthotropic laminates by performing a detailed assessment of the methodology, with particular focus on the influence of stiffness properties.
- Perform a parametric study on plate curvature to define the range within which the tool remains valid without significant deviations from the real solution. This is particularly relevant since aircraft fuselages often exhibit high curvature relative to the diameters of most joint holes, making it essential to establish clear applicability limits for the tool.
- Develop fitting functions to estimate lamina-level stresses by accounting for geometry, laminate properties, and ply distribution. This would transform the stress routine into a surrogate model, significantly reducing computational time. Such an improvement is particularly relevant for finite-width solutions, which can be computationally expensive when evaluated repeatedly, especially for filled hole configurations where a single hole analysis could take several minutes per hole, in some geometrical configurations.

References

[1] Marsh G. Airbus takes on boeing with reinforced plastic a350 xwb. Reinforced Plastics 2007;51(11):26–9.

[2] Nagaraju SB, Priya H, Girijappa YGT, Puttegowda M. 9 - lightweight and sustainable materials for aerospace applications. In: Rangappa SM, Doddamani SM, Siengchin S, Doddamani M, editors. Lightweight and Sustainable Composite Materials. Woodhead Publishing. ISBN 978-0-323-95189-0; 2023, p. 157–78.

[3] Riccio A, Caprio FD, Tsai S, Russo A, Sellitto A. Optimization of composite aeronautical components by re-designing with double-double laminates. Aerospace Science and Technology 2024;151:109304.

[4] Tan SC. Fracture strength of composite laminates with an elliptical opening. Composites Science and Technology 1987;29(2):133–52.

[5] Tan S. Finite-width correction factors for anisotropic plate containing a central opening. Journal of Composite Materials 1988;22(11):1080–97.

[6] Tan S, Kim R. Strain and stress concentrations in composite laminates containing a hole. Experimental Mechanics 1990;30(4):345–51.

[7] Tan S. Stress Concentrations in Laminated Composites. London: CRC Press; 1994.

[8] Nguyen-Hoang M, Becker W. Stress analysis of finite orthotropic plates loaded by a bolted joint. Composite Structures 2021;276:114454.

[9] Nguyen-Hoang M, Becker W. Open holes in composite laminates with finite dimensions: structural assessment by analytical methods. Archive of Applied Mechanics 2022;92:1101–25.

[10] Lekhnitskii S. Anisotropic Plates. London: Gordon and Breach Science Publishers; 1968.

[11] Nguyen-Hoang M, Becker W. Open Circular Hole in a Finite Plate Under Tension Treated by Airy Stress Function Method. Cham: Springer International Publishing. ISBN 978-3-030-47491-1; 2020, p. 311–30.

[12] Nguyen-Hoang M, Becker W. Tension failure analysis for bolted joints using a closed-form stress solution. Composite Structures 2020;238:111931.

[13] Nguyen-Hoang M, Becker W. Stress analysis of finite dimensions bolted joints using the airy stress function. International Journal of Solids and Structures 2021;224:111023.

[14] Nguyen-Hoang M, Becker W. Stress analysis of a bolted finite dimensions plate under bearing-bypass load interaction using the airy stress function. Engineering Structures 2022;256:113943.

[15] Kirsch G. Die theorie der elastizitat und die bedurfnisse der festigkeitslehre. Zentralblatt Verlin Deutscher Ingenieure 1898;42:797–807.

[16] Timoshenko S, Goodier J. Theory of Elasticity. New York: McGraw-Hill Book Company Inc; 1951.

[17] Sadd M. Elasticity: Theory, Applications, and Numerics. 2nd ed.; New York: Elsevier, Butterworth-Heinemann; 2005.

[18] Ukadgaonker V. Theory of Elasticity and Fracture Mechanics. Delhi: PHI Learning Pvt. Ltd; 2015.

[19] Inglis C. Stresses in a plate due to the presence of cracks and sharp corners. Transactions of the Institution of Naval Architects 1913;55:219–30.

[20] Westergaard H. Bearing pressures and cracks. Journal of Applied Mechanics 1939;6:A49–53.

[21] Irwin G. Analysis of stresses and strains near the end of a crack traversing a plate. Journal of Applied Mechanics 1957;24:361–4.

[22] Kolosov G. An application of complex function theory to a plane problem of the mathematical theory of elasticity. 1909.

[23] Muskhelishvili N. Some Basic Problems of the Mathematical Theory of Elasticity. Groningen: Noordhoff; 1963.

[24] Szachter O, Katzav E, Adda-Bedia M, Moshe M. Nonlinear extension of kolosov-muskhelishvili stress function formalism. 2022.

[25] Savin G. Stress Concentration Around Holes. New York: Pergamon Press; 1961.

[26] Becker W. Complex method for the elliptical hole in an unsymmetric laminate. Archive of Applied Mechanics 1993;63:159–69.

[27] Ukadgaonker V, Rao D. A general solution for stress resultants and moments

around holes in unsymmetric laminates. Composites Structures 2000;49(1):27–39.

[28] Ukadgaonker V, Rao D. A general solution for stresses around holes in symmetric laminates under inplane loading. Composite Structures 2000;49(3):339–54.

[29] Waszczak J, Cruse T. Failure mode and strength predictions of anisotropic bolt bearing specimens. Journal of Composite Materials 1971;5(3):421–5.

[30] Sundaram N, Farris T. The generalized advancing conformal contact problem with friction, pin loads and remote loading – case of rigid pin. International Journal of Solids and Structures 2010;47(6):801–15.

[31] Johnson KL. Contact Mechanics. Cambridge: Cambridge University Press; 1987.

[32] Persson A. On the stress distribution of cylindrical elastic bodies in contact. Phd thesis; Chalmers University of Technology; 1964.

[33] Gladwell GM. Contact Problems in the Classical Theory of Elasticity. Dordrecht: Springer Netherlands; 1980.

[34] Ciavarella M, Baldini A, Barber JR, Strozzi A. Reduced dependence on loading parameters in almost conforming contacts. International Journal of Mechanical Sciences 2006;48(9):917–25.

[35] To Q, He QC, Cossavella M, Morcant K, Panait A. Closed-form solution for the contact problem of reinforced pin-loaded joints used in glass structures. International Journal of Solids and Structures 2007;44(11):3887–903.

[36] Sundaram N, Farris T. Mechanics of advancing pin-loaded contacts with friction. Journal of the Mechanics and Physics of Solids 2010;58(11):1819–33.

[37] Hou JP, Hills DA. Contact between a pin and a plate with a hole under interference-fit and clearance-fit conditions. Proceedings of the Institution of Mechanical Engineers, Part C: Journal of Mechanical Engineering Science 2001;215(6):629–39.

[38] Zhang KD, Ueng CE. Stresses around a pin-loaded hole in orthotropic plates. Journal of Composite Materials 1984;18(5):432–46.

[39] Zhang KD, Ueng CE. Stresses around a pin-loaded hole in orthotropic plates with arbitrary loading direction. Composite Structures 1985;3(2):119–43.

[40] Hyer M, Klang E. Contact stresses in pin-loaded orthotropic plates. International Journal of Solids and Structures 1985;21(9):957–75.

[41] Hyer M, Klang E, Cooper D. The effects of pin elasticity, clearance, and friction on the stresses in a pin-loaded orthotropic plate. Journal of Composite Materials 1987;21(3):190–206.

[42] Dundurs J, Stippes M. Role of elastic constants in certain contact problems. Journal of Applied Mechanics 1970;37:965–70.

[43] Catalanotti G, Camanho P. A semi-analytical method to predict net-tension failure of mechanically fastened joints in composite laminates. Composites Science and Technology 2013;76:69–76.

[44] Heywood R. Designing by Photoelasticity. New York: Chapman & Hall; 1952.

[45] Bickley WG. The distribution of stress round a circular hole in a plate. Philosophical Transactions of the Royal Society of London Series A 1928;227:383–415.

[46] Knight R. The action of a rivet in a plate of finite breadth. Philosophical Magazine 1935;19(7):517–40.

[47] de Jong T. Spanningen rond een gat in een elastisch orthotrope of isotrope plaat, belast door een pen die zich daarin wrijvingsloos kan bewegen. Ph.D. thesis; Technische Hogeschool Delft, Afdeling der Luchtvaart- en Ruimtevaarttechniek; 1976. Rapport LR-223.

[48] de Jong T, Vuil HA. Stresses around pin-loaded holes in elastically orthotropic plates with arbitrary load direction. Tech. Rep. Report LR-333; Delft University of Technology, Department of Aerospace Engineering; 1981.

[49] Berbinau P, Soutis C. A new approach for solving mixed boundary value problems along holes in orthotropic plates. International Journal of Solids and Structures 2001;38(1):143–59.

[50] de Jong T. Stresses around pin-loaded holes in elastically orthotropic or isotropic plates. Journal of Composite Materials 1977;11:313–31.

[51] Echavarría C, Haller P, Salenikovich A. Analytical study of a pin-loaded hole in elastic orthotropic plates. Composite Structures 2007;79(1):107–12.

[52] Ogonowski J. Analytical study of finite geometry plates with stress concentrations. In: 21st Structures, Structural Dynamics, and Materials Conference. 1980, p. 778.

[53] Pilkey W, Pilkey D. Peterson's Stress Concentration Factors. New York: Wiley; 2008.

[54] Hufenbach W, Kroll L. Stress analysis of notched anisotropic finite plates under mechanical and hygrothermal loads. Arch Appl Mech 1999;69(3):145–59.

[55] Hufenbach W, Grüber B, Gottwald R, Lepper M, Zhou B. Analytical and experimental analysis of stress concentration in notched multilayered composites with finite outer boundaries. Mechanics of Composite Materials 2010;46(5):531–8.

[56] Hufenbach W, Grüber B, Lepper M, Zhou B. An analytical method for the determination of stress and strain concentrations in textile-reinforced gf/pp composites with elliptical cutout and a finite outer boundary and its numerical verification. Arch Appl Mech 2013;83:125–35.

[57] Kratochvil J, Becker W. Structural analysis of composite bolted joints using the complex potential method. Composite Structures 2010;92(10):2512–6.

[58] Grüber B, Hufenbach W, Kroll L, Lepper M, Zhou B. Stress concentration analysis of fibre-reinforced multilayered composites with pin-loaded holes. Composites Science and Technology 2007;67:1439–50.

[59] Grüber B, Gude M, Hoyer T, Gottwald R, Lepper M, Zhou B. Calculation method for the determination of stress concentrations in fibre-reinforced multilayered composites due to metallic interference-fit bolt. Journal of Composite Materials 2018;52(18):2415–29.

[60] Lekhnitskii S. Anisotropic Plates. London: Gordon and Breach Science Publishers; 1968, p. 5–18.

[61] Nettles AT. Basic mechanics of laminated composite plates. NASA Reference Publication NASA-RP-1351; National Aeronautics and Space Administration (NASA); Washington, DC; 1994. Also published as M-764; NAS 1.61:1351.

[62] Kollár LP, Springer GS. Laminated Composites. Cambridge University Press; 2003, p. 63–88.

[63] Tsai S, Pagano N. Invariant properties of composite materials. In: Tsai S, Halpin J, Pagano N, editors. Composite Materials Workshop. Stamford, CT: Technomic Publishing Co.; 1968, p. 233.

[64] Galińska A. Mechanical joining of fibre reinforced polymer composites to metals—a review. part i: Bolted joining. Polymers 2020;12.

[65] Camanho P, Lambert M. A design methodology for mechanically fastened joints in laminated composite materials. Composites Science and Technology 2006;66(15):3004–20.

[66] Camanho P, Erçin G, Catalanotti G, Mahdi S, Linde P. A finite fracture mechanics model for the prediction of the open-hole strength of com-

posite laminates. Composites Part A: Applied Science and Manufacturing 2012;43(8):1219–25.

[67] Tung T. On computation of stresses around holes in anisotropic plates. Journal of Composite Materials 1987;21(2):100–4.

[68] Horgan CO. Saint-venant end effects in composites. Journal of Composite Materials 1982;16(5):411–22.

[69] Cabrero J, Blanco C, Gebremedhin K, Martín-Meizoso A. Assessment of phenomenological failure criteria for wood. European Journal of Wood and Wood Products 2012;70.

[70] Tsai S. Strength characteristics of composite materials. Tech. Rep. CR-224; NASA; 1965.

[71] Tsai SW, Wu EM. A general theory of strength for anisotropic materials. Journal of Composite Materials 1971;5:58–80.

[72] Eremin V, Bolshikh A, Koroliskii V, Shelkov K. Methods for flexibility determination of bolted joints: empirical formula review. Journal of Physics: Conference Series 2021;1925:012058.

[73] Madier D. Practical Finite Element Analysis for Mechanical Engineers. First ed.; Canada: FEA Academy; 2020. ISBN 978-1-9990475-0-4.

[74] Camanho P, Maimí P, Dávila C. Prediction of size effects in notched laminates using continuum damage mechanics. Composites Science and Technology 2007;67(13):2715–27.

A. Stress Analysis

A.1 Load Application Distance Results

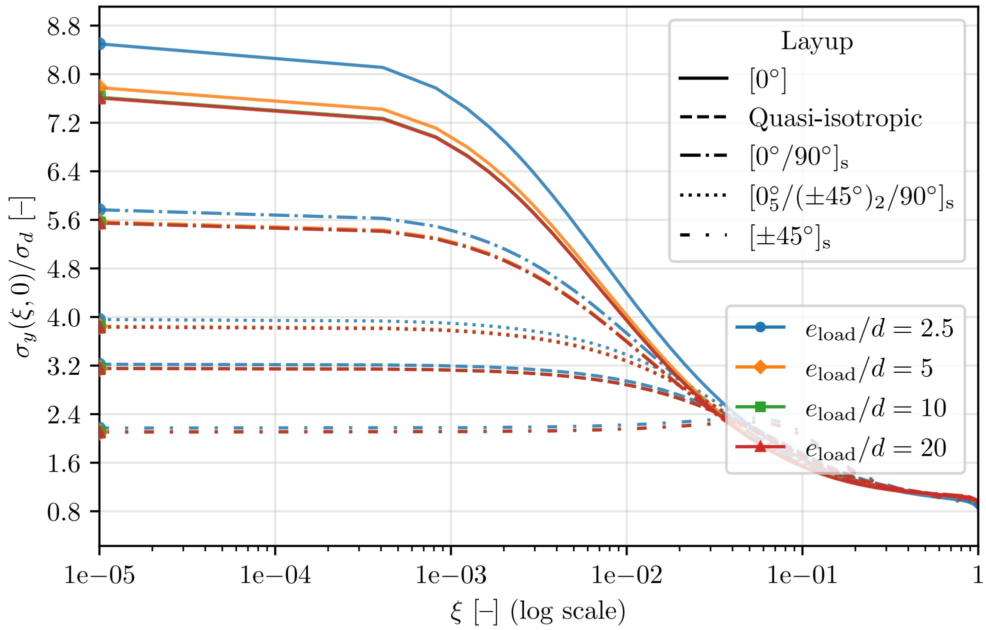

(a) $w/d = 5$.

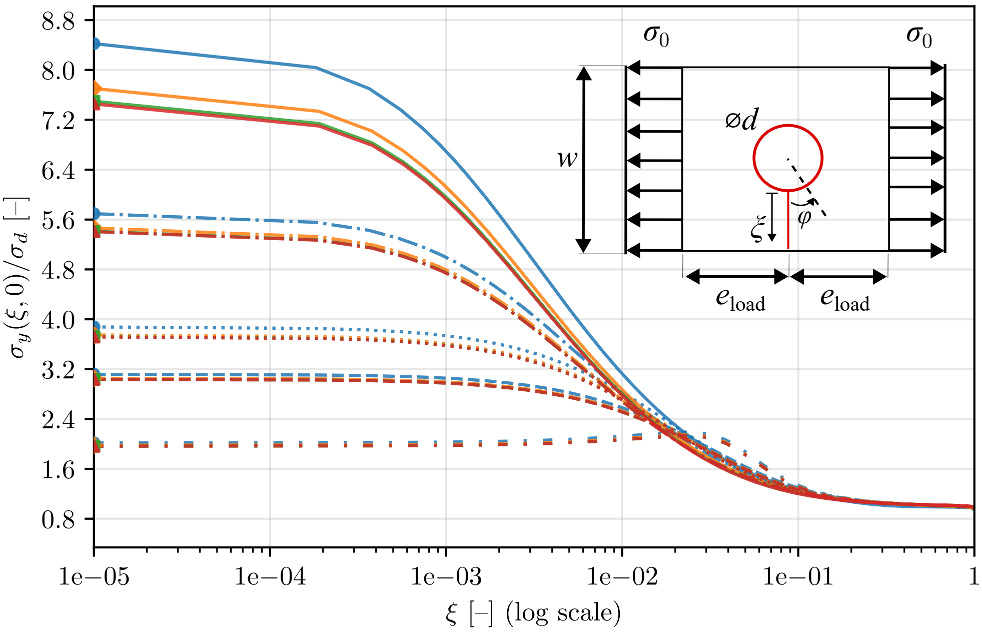

(b) $w/d = 10$.

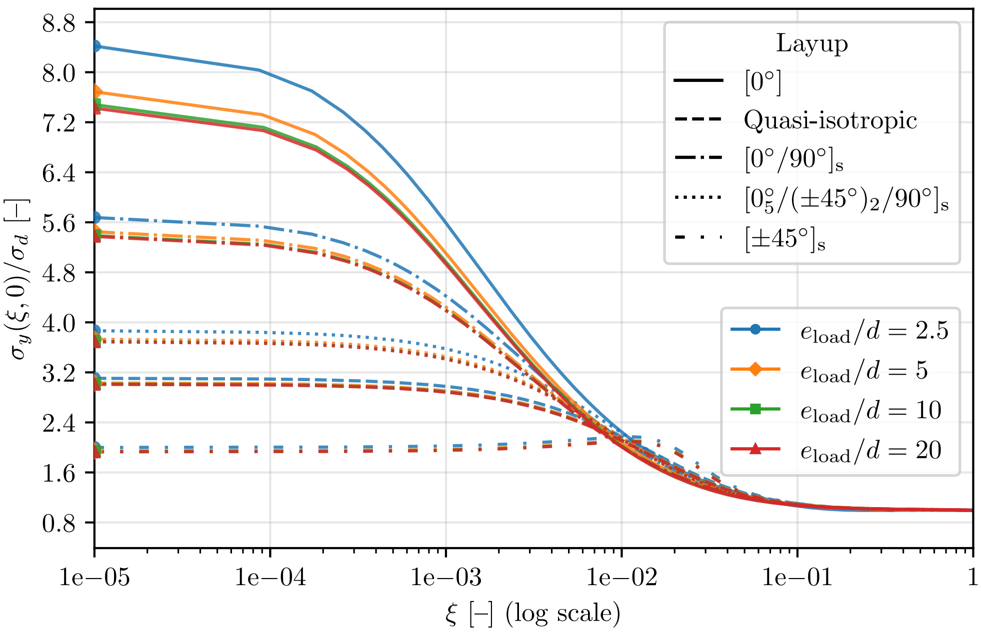

(c) $w/d = 20$.

Figure A.1: Open hole tension normalised net-section stresses for each laminate at different e_{load}/d values, with $w/d = \{5, 10, 20\}$.

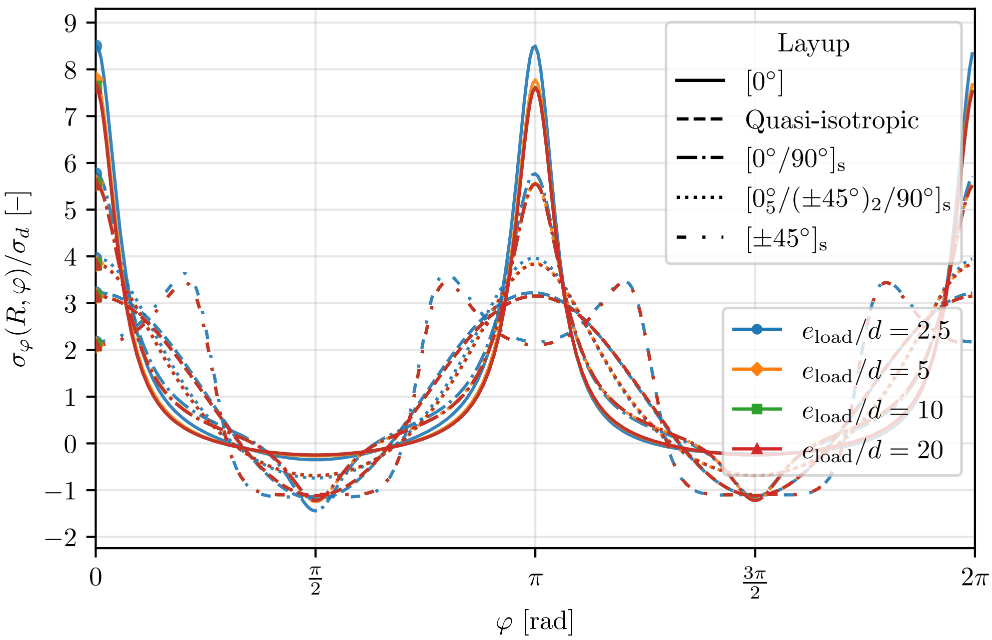

Layup
[0°]
Quasi-isotropic
[0°/90°]$_s$
[0$^\circ_5$/(±45°)$_2$/90°]$_s$
[±45°]$_s$
$e_{load}/d = 2.5$
$e_{load}/d = 5$
$e_{load}/d = 10$
$e_{load}/d = 20$
$\sigma_\varphi(R,\varphi)/\sigma_d$ [−]
φ [rad]

(a) $w/d = 5$.

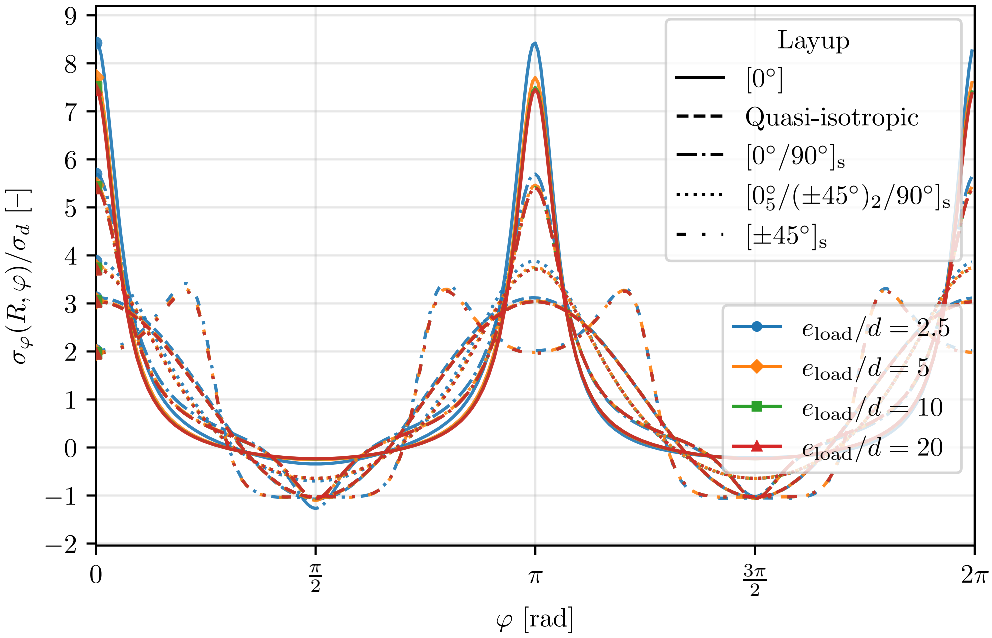

(b) $w/d = 10$.

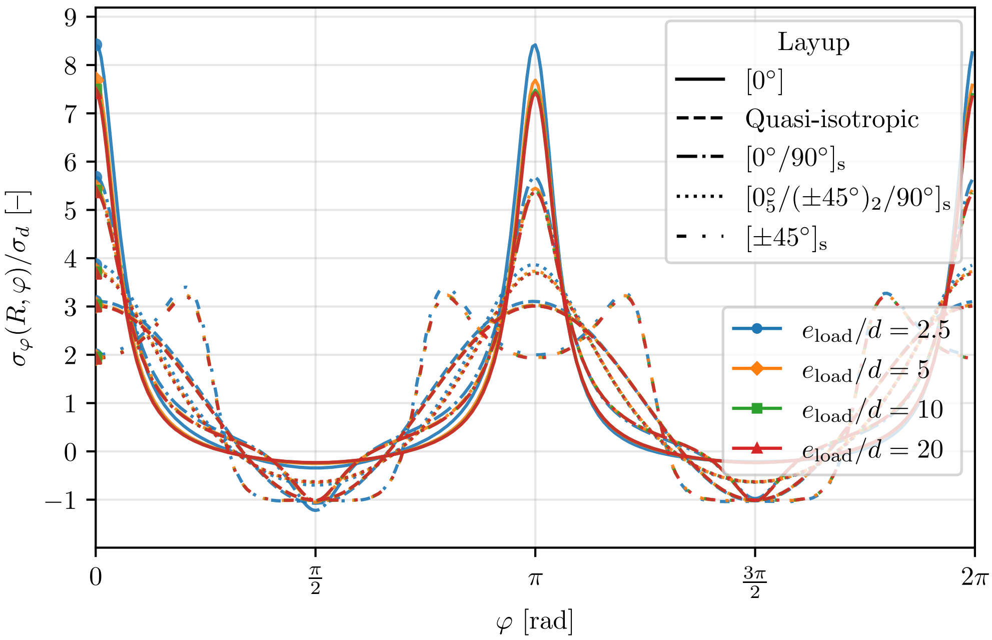

(c) $w/d = 20$.

Figure A.2: Open hole tension normalised circumferential stresses for each laminate at different e_{load}/d values, with $w/d = \{5, 10, 20\}$.

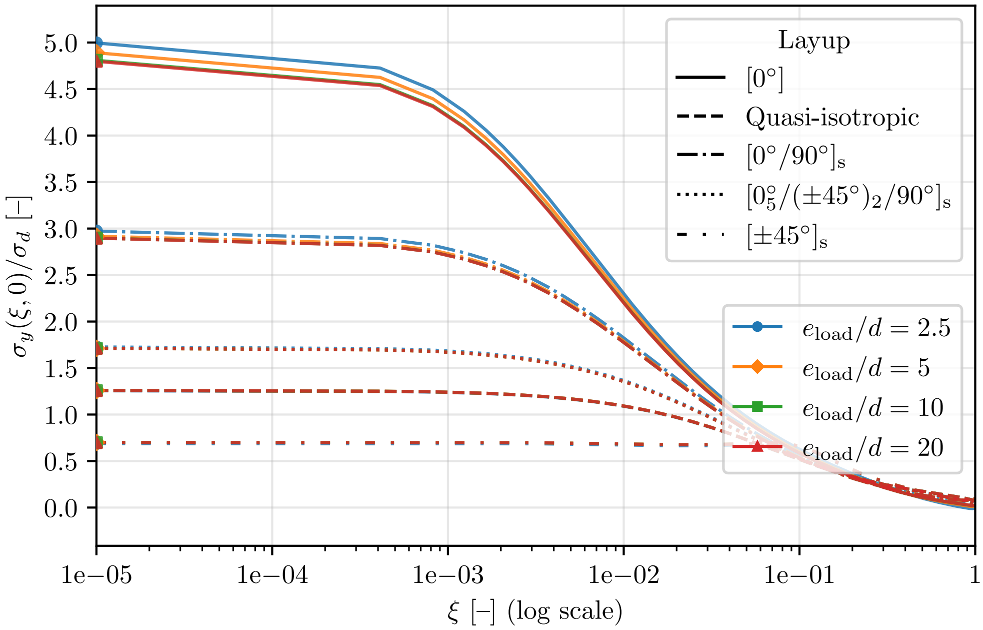
Layup
[0°]
Quasi-isotropic
[0°/90°]s
[0°5/(±45°)2/90°]s
[±45°]s
eload/d = 2.5
eload/d = 5
eload/d = 10
eload/d = 20
σy(ξ, 0)/σd [–]
ξ [–] (log scale)
5.0
4.5
4.0
3.5
3.0
2.5
2.0
1.5
1.0
0.5
0.0
1e−05
1e−04
1e−03
1e−02
1e−01
1

(a) $w/d = 5$.

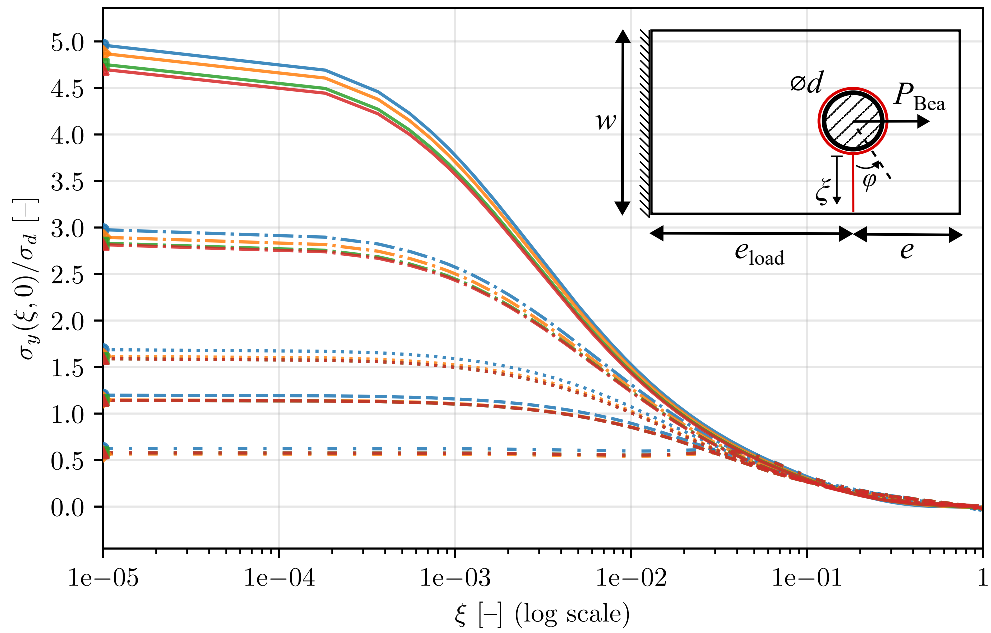

(b) $w/d = 10$.

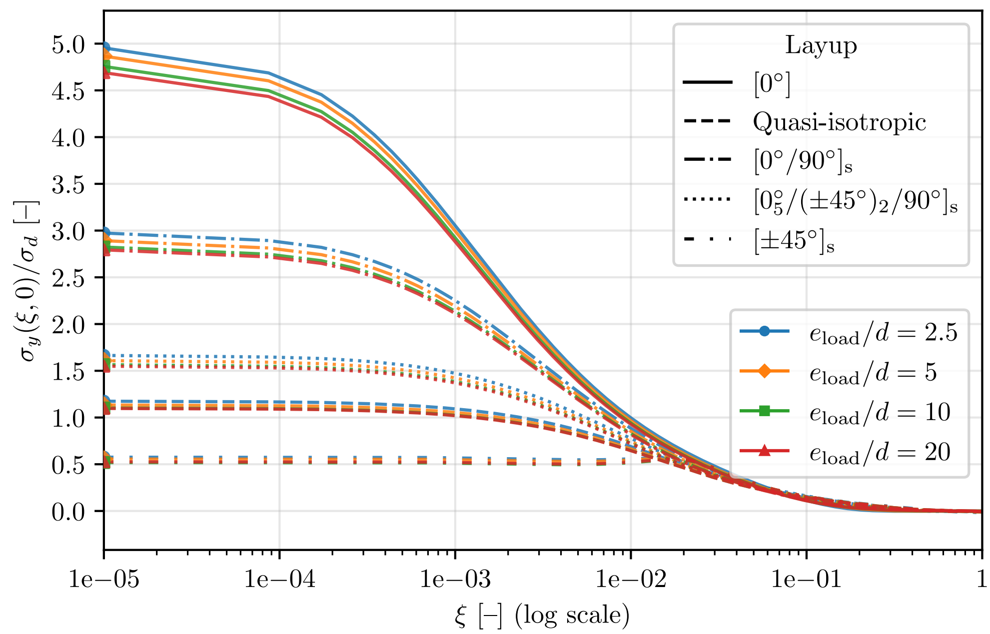

(c) $w/d = 20$.

Figure A.3: Filled hole net section stresses for each laminate at different e_{load}/d values, with $w/d = \{5, 10, 20\}$ and $e/d = 2.5$.

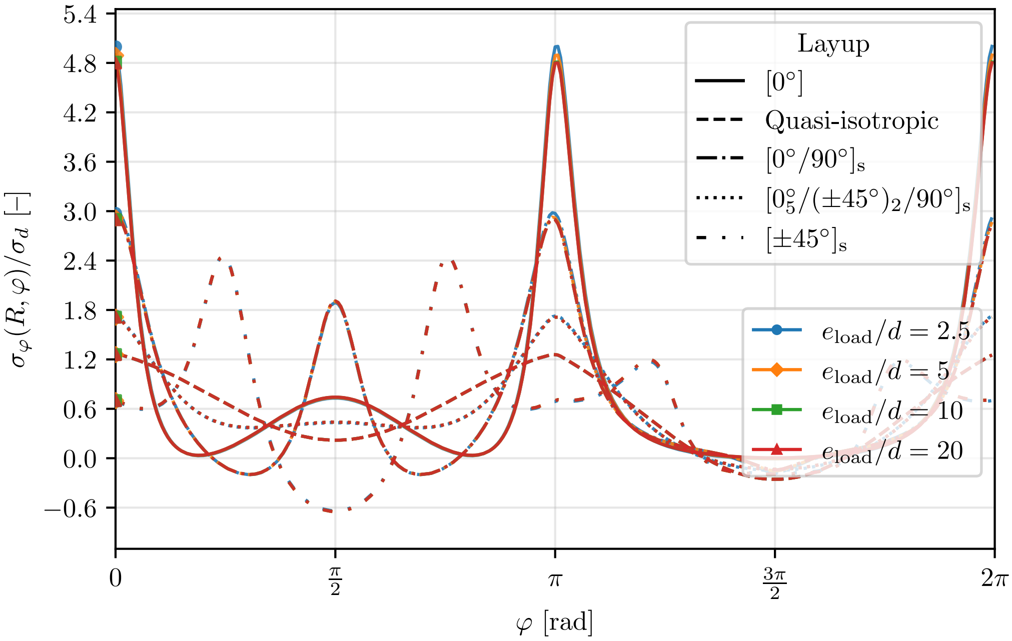

5.4
4.8
4.2
3.6
3.0
2.4
1.8
1.2
0.6
0.0
−0.6
$\sigma_\varphi(R,\varphi)/\sigma_d$ [−]
0
$\frac{\pi}{2}$
π
$\frac{3\pi}{2}$
2π
φ [rad]
Layup
[0°]
Quasi-isotropic
[0°/90°]$_s$
$[0^\circ_5/(\pm 45^\circ)_2/90^\circ]_s$
[±45°]$_s$
$e_{\mathrm{load}}/d = 2.5$
$e_{\mathrm{load}}/d = 5$
$e_{\mathrm{load}}/d = 10$
$e_{\mathrm{load}}/d = 20$

(a) $w/d = 5$.

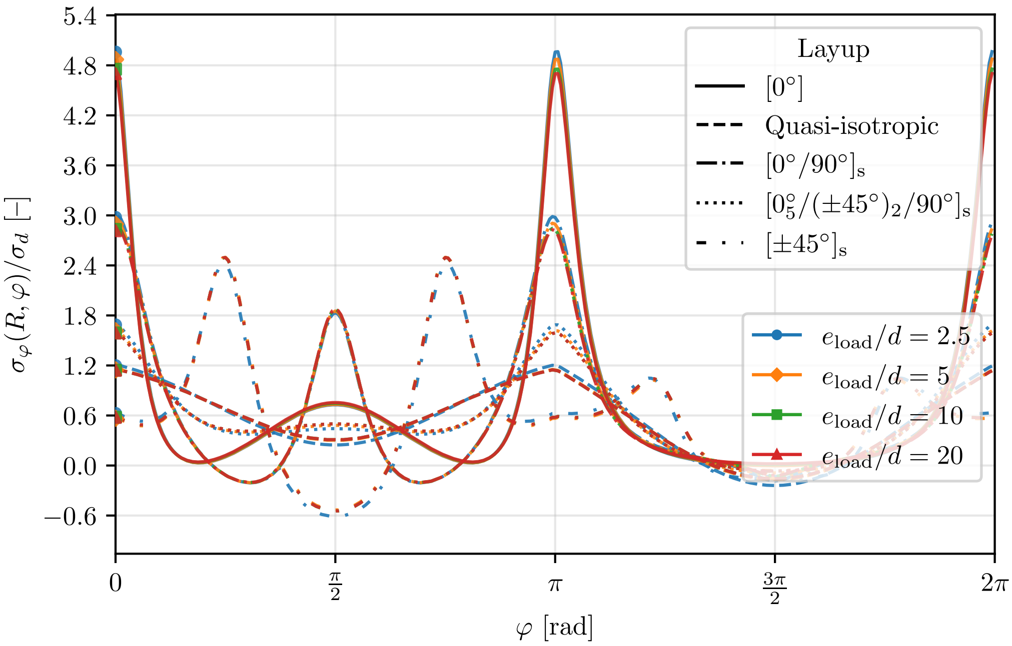

(b) $w/d = 10$.

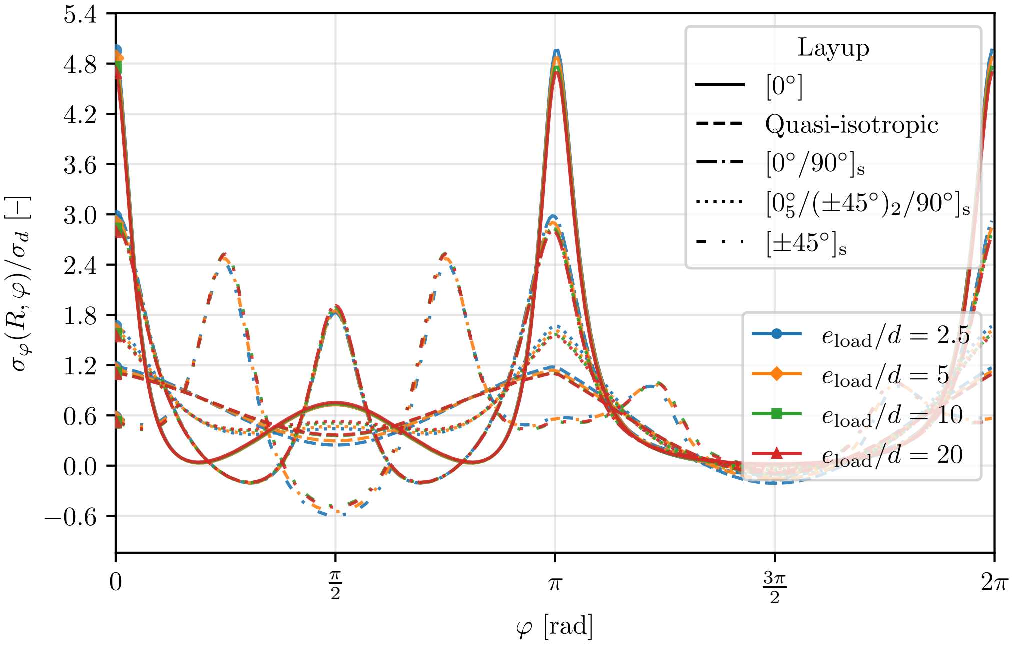

(c) $w/d = 20$.

Figure A.4: Filled hole circumferential stresses for each laminate at different e_{load}/d values, with $w/d = \{5, 10, 20\}$ and $e/d = 2.5$.

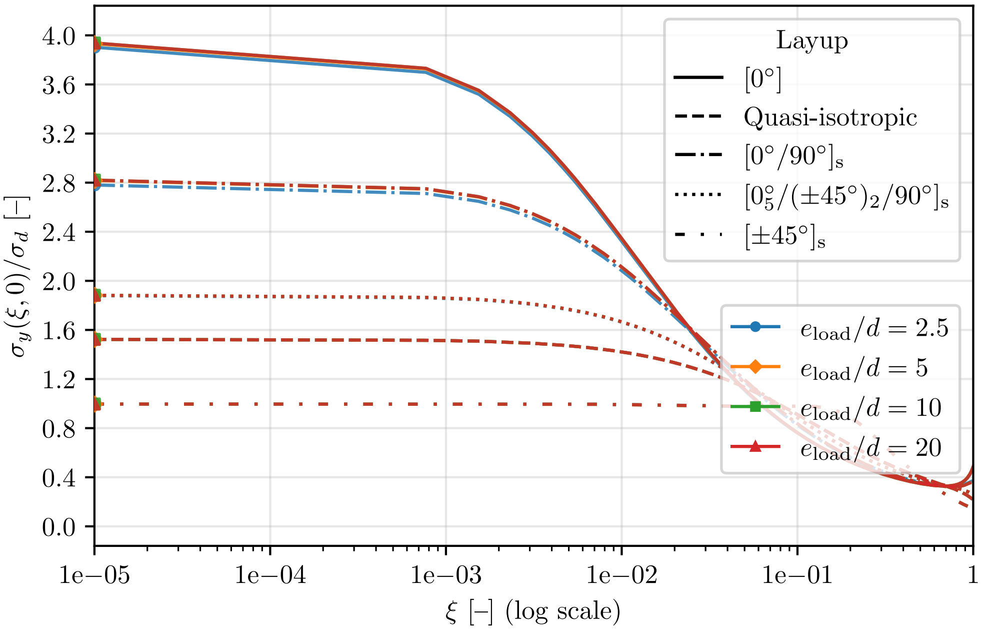

Layup
[0°]
Quasi-isotropic
[0°/90°]$_s$
[0°$_5$/(±45°)$_2$/90°]$_s$
[±45°]$_s$
$e_{load}/d = 2.5$
$e_{load}/d = 5$
$e_{load}/d = 10$
$e_{load}/d = 20$
$\sigma_y(\xi, 0)/\sigma_d$ [–]
ξ [–] (log scale)
4.0
3.6
3.2
2.8
2.4
2.0
1.6
1.2
0.8
0.4
0.0
1e−05
1e−04
1e−03
1e−02
1e−01
1

(a) $w/d = 3$.

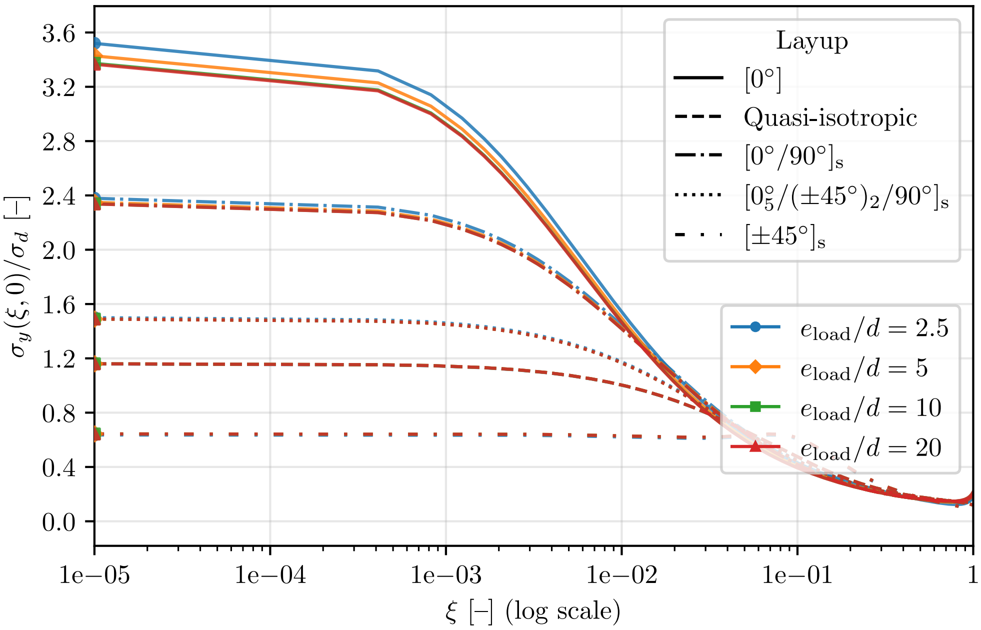

Layup
[0°]
Quasi-isotropic
[0°/90°]$_s$
[0°$_5$/(±45°)$_2$/90°]$_s$
[±45°]$_s$
$e_{load}/d = 2.5$
$e_{load}/d = 5$
$e_{load}/d = 10$
$e_{load}/d = 20$
$\sigma_y(\xi, 0)/\sigma_d$ [–]
ξ [–] (log scale)
3.6
3.2
2.8
2.4
2.0
1.6
1.2
0.8
0.4
0.0
1e−05
1e−04
1e−03
1e−02
1e−01
1

(b) $w/d = 5$.

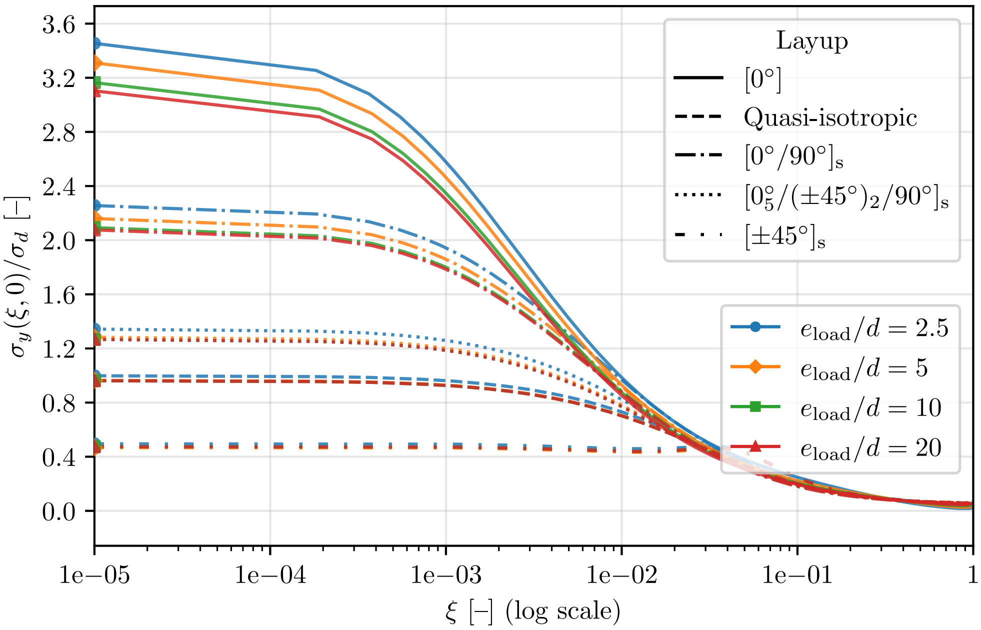

(c) $w/d = 10$.

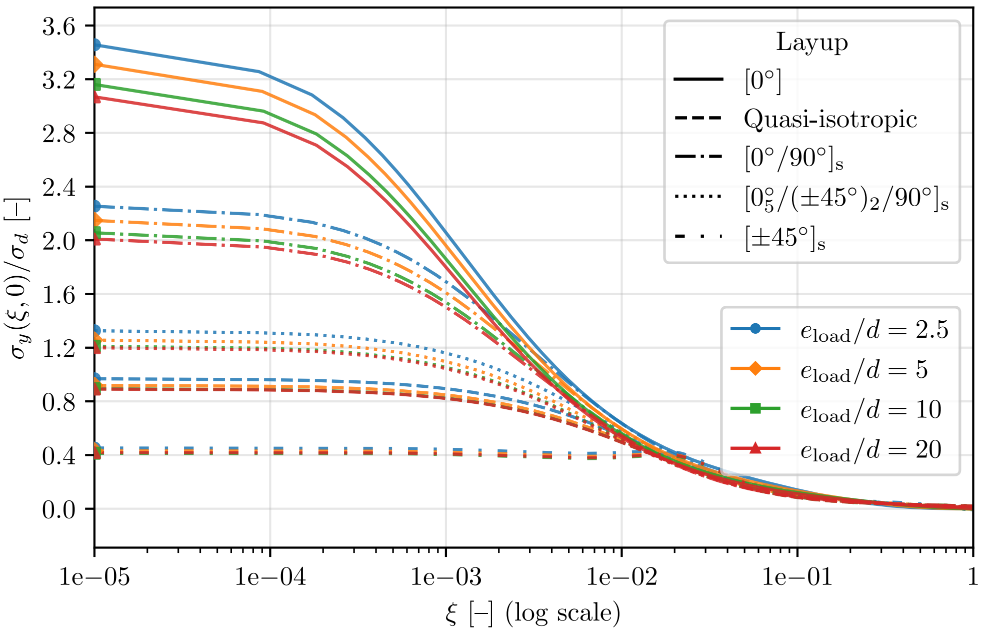

(d) $w/d = 20$.

Figure A.5: Filled hole net section stresses for each laminate at different e_{load}/d values, with $w/d = \{3, 5, 10, 20\}$ and $e/d = 10$.

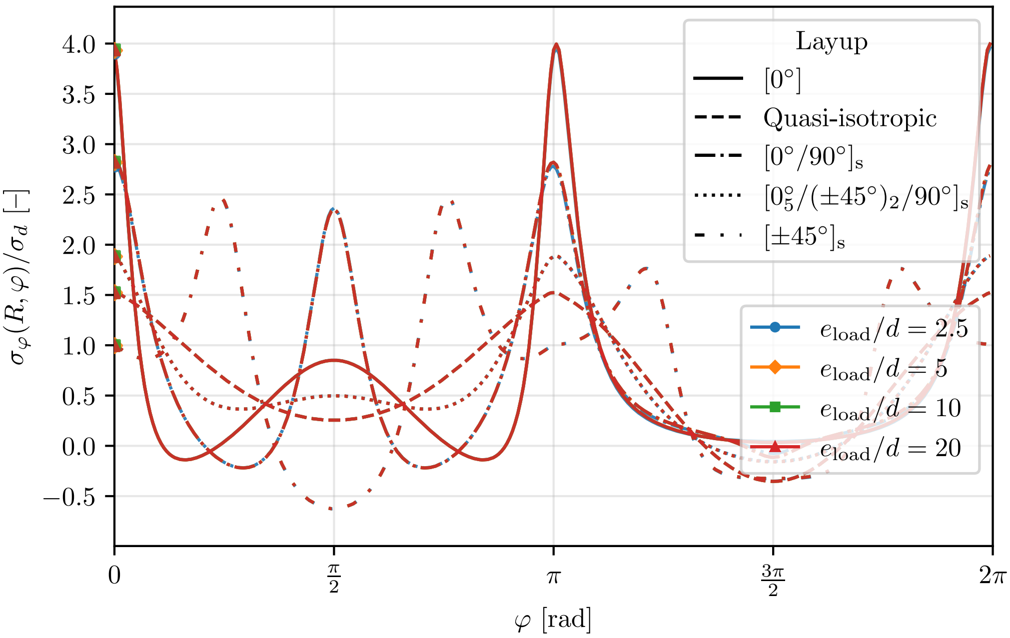

Layup
[0°]
Quasi-isotropic
[0°/90°]s
[0°5/(±45°)2/90°]s
[±45°]s
eload/d = 2.5
eload/d = 5
eload/d = 10
eload/d = 20
σφ(R, φ)/σd [−]
φ [rad]

(a) $w/d = 3$.

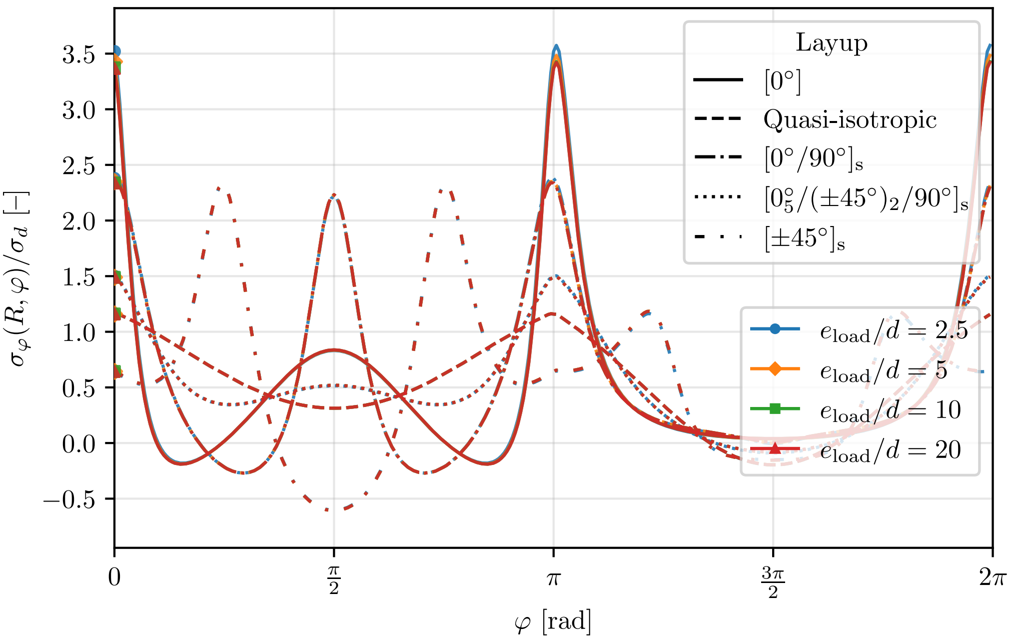

Layup
[0°]
Quasi-isotropic
[0°/90°]s
[0°5/(±45°)2/90°]s
[±45°]s
eload/d = 2.5
eload/d = 5
eload/d = 10
eload/d = 20
σφ(R, φ)/σd [−]
φ [rad]

(b) $w/d = 5$.

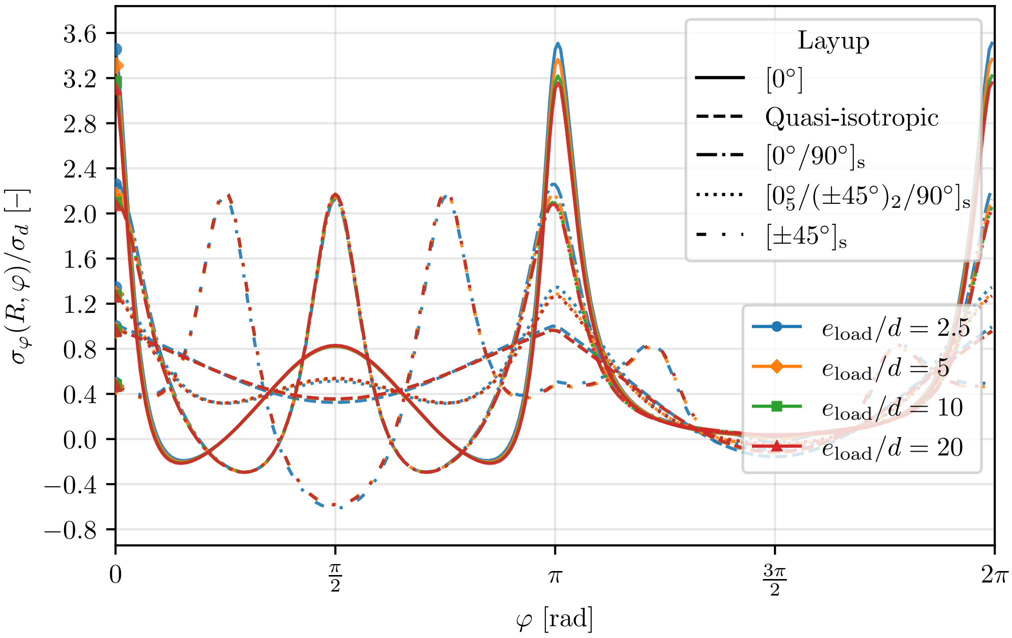

(c) $w/d = 10$.

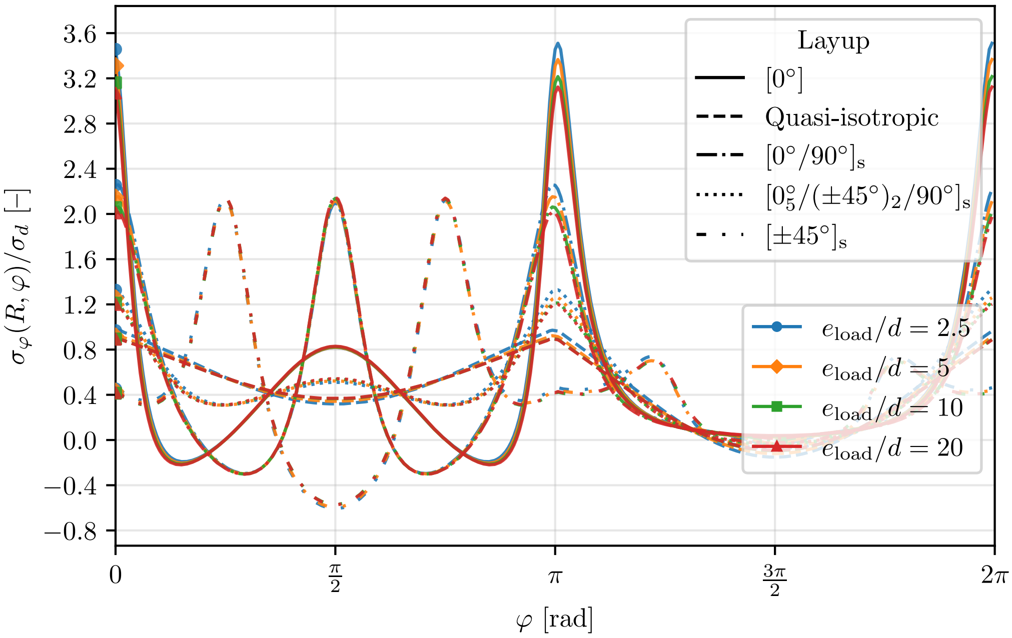

(d) $w/d = 20$.

Figure A.6: Filled hole circumferential stresses for each laminate at different e_{load}/d values, with $w/d = \{5, 10, 20\}$ and $e/d = 10$.

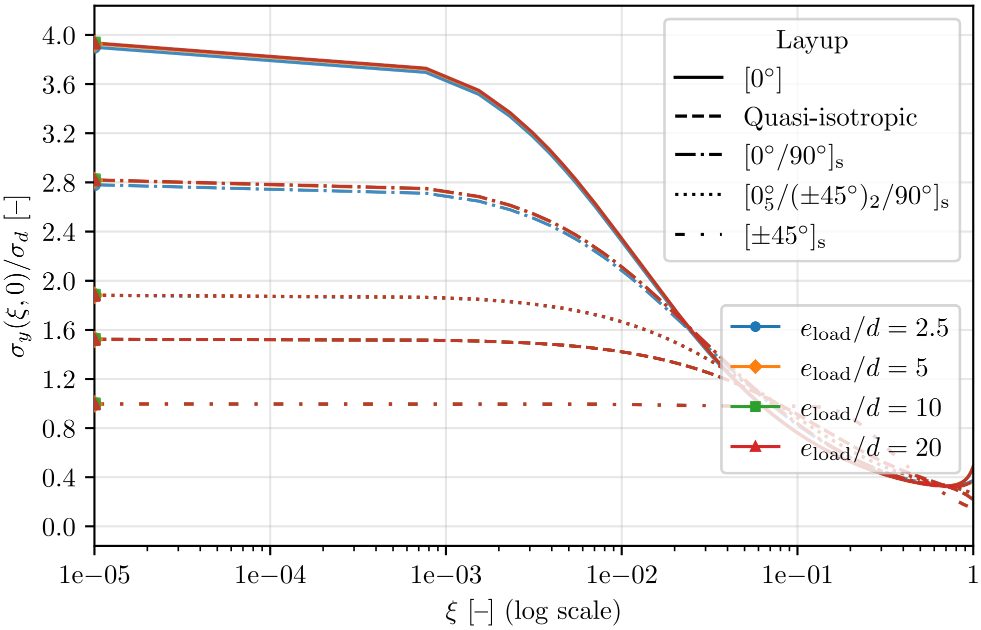

Layup
[0°]
Quasi-isotropic
[0°/90°]s
[0°5/(±45°)2/90°]s
[±45°]s
eload/d = 2.5
eload/d = 5
eload/d = 10
eload/d = 20
σy(ξ, 0)/σd [–]
ξ [–] (log scale)

(a) $w/d = 3$.

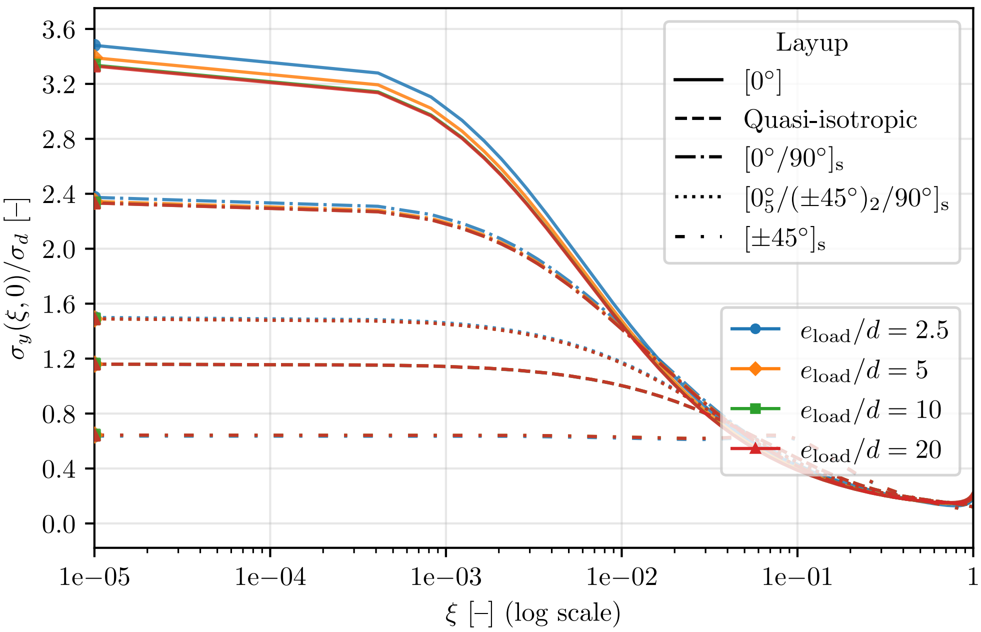

Layup
[0°]
Quasi-isotropic
[0°/90°]s
[0°5/(±45°)2/90°]s
[±45°]s
eload/d = 2.5
eload/d = 5
eload/d = 10
eload/d = 20
σy(ξ, 0)/σd [–]
ξ [–] (log scale)

(b) $w/d = 5$.

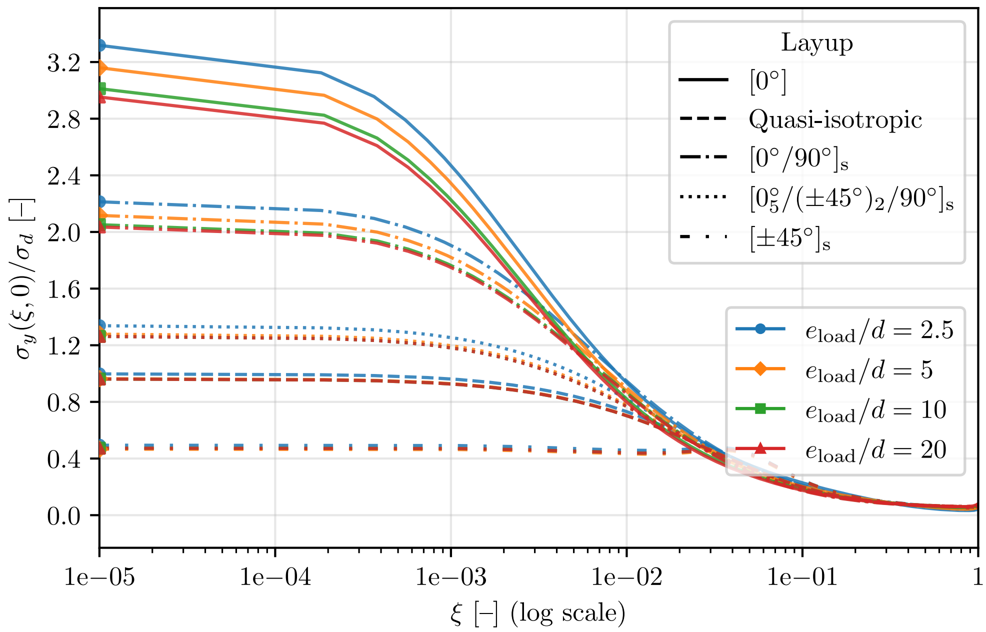

(c) $w/d = 10$.

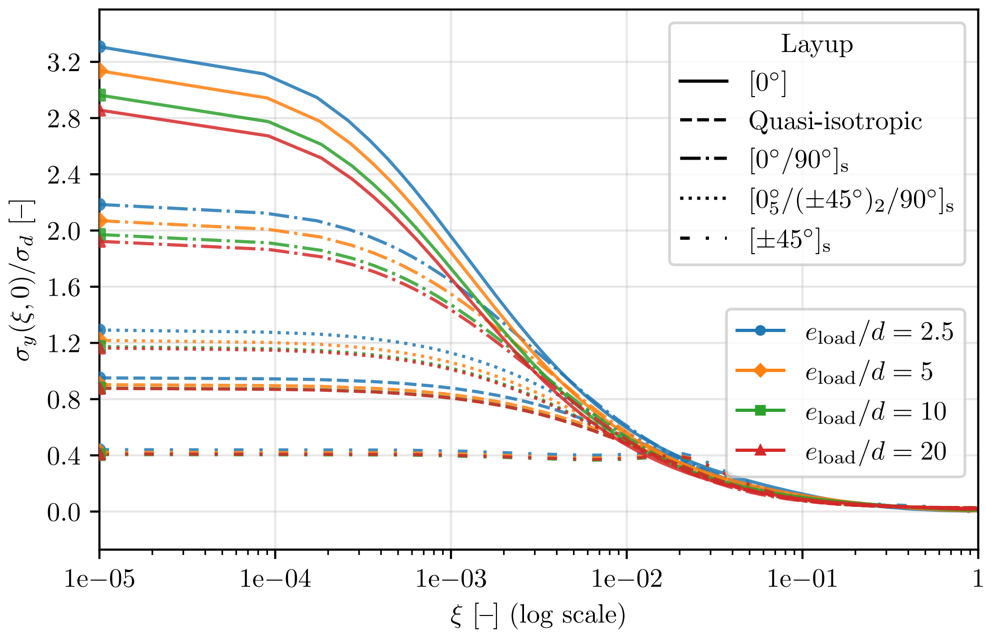

(d) $w/d = 20$.

Figure A.7: Filled hole net section stresses for each laminate at different e_{load}/d values, with $w/d = \{3, 5, 10, 20\}$ and $e/d = 20$.

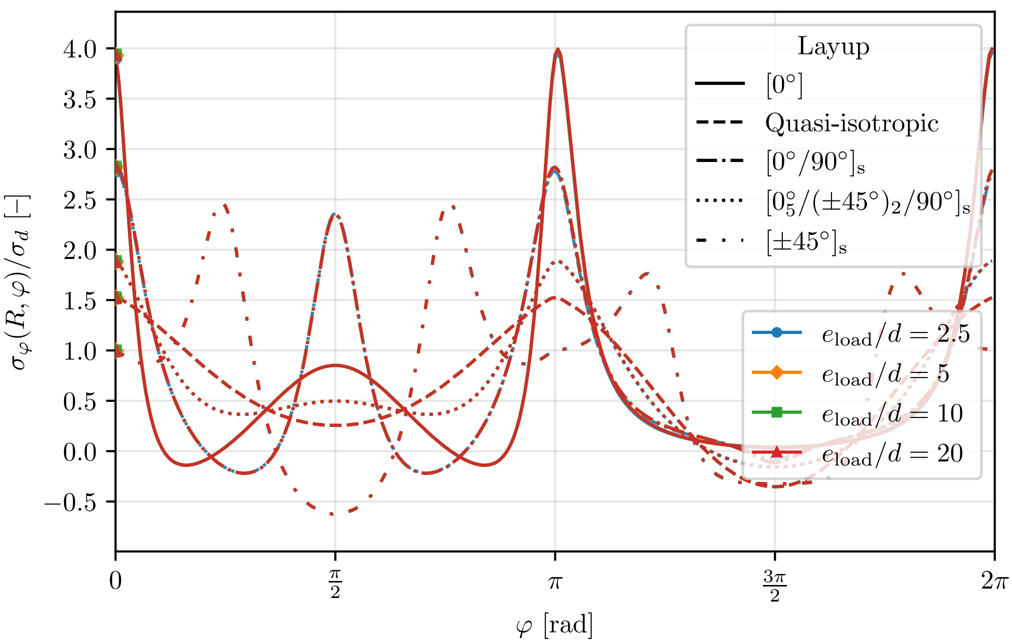

Layup
[0°]
Quasi-isotropic
[0°/90°]s
[0°5/(±45°)2/90°]s
[±45°]s
eload/d = 2.5
eload/d = 5
eload/d = 10
eload/d = 20
σφ(R, φ)/σd [−]
φ [rad]

(a) $w/d = 3$.

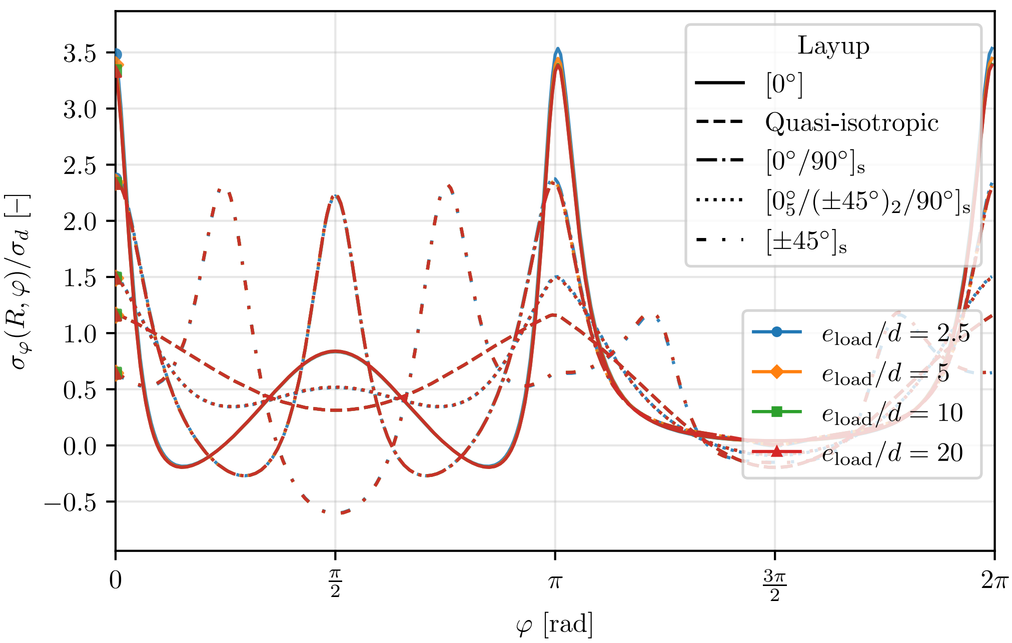

Layup
[0°]
Quasi-isotropic
[0°/90°]s
[0°5/(±45°)2/90°]s
[±45°]s
eload/d = 2.5
eload/d = 5
eload/d = 10
eload/d = 20
σφ(R, φ)/σd [−]
φ [rad]

(b) $w/d = 5$.

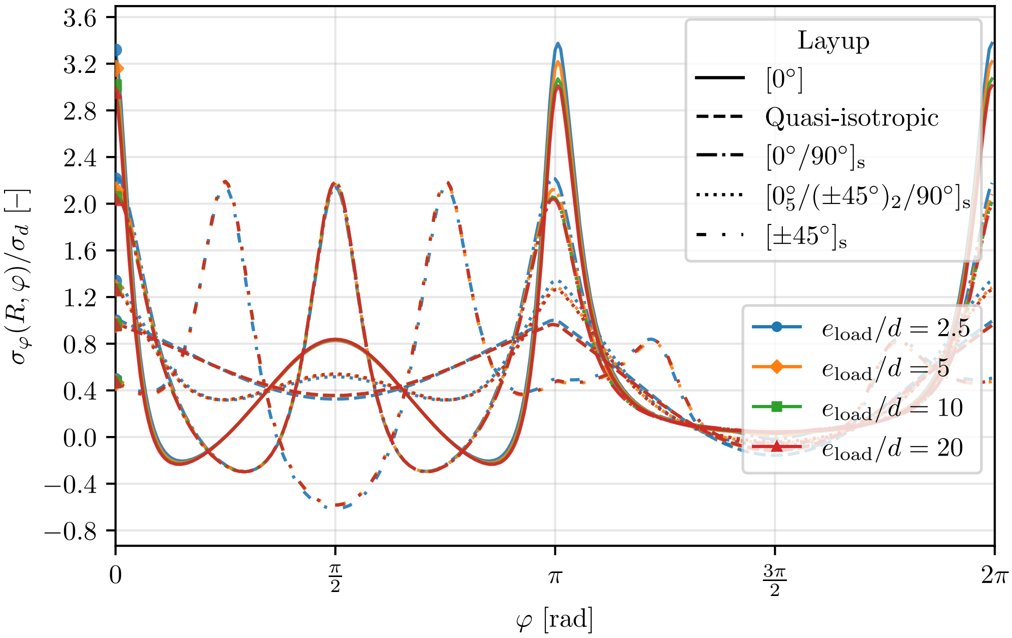

(c) $w/d = 10$.

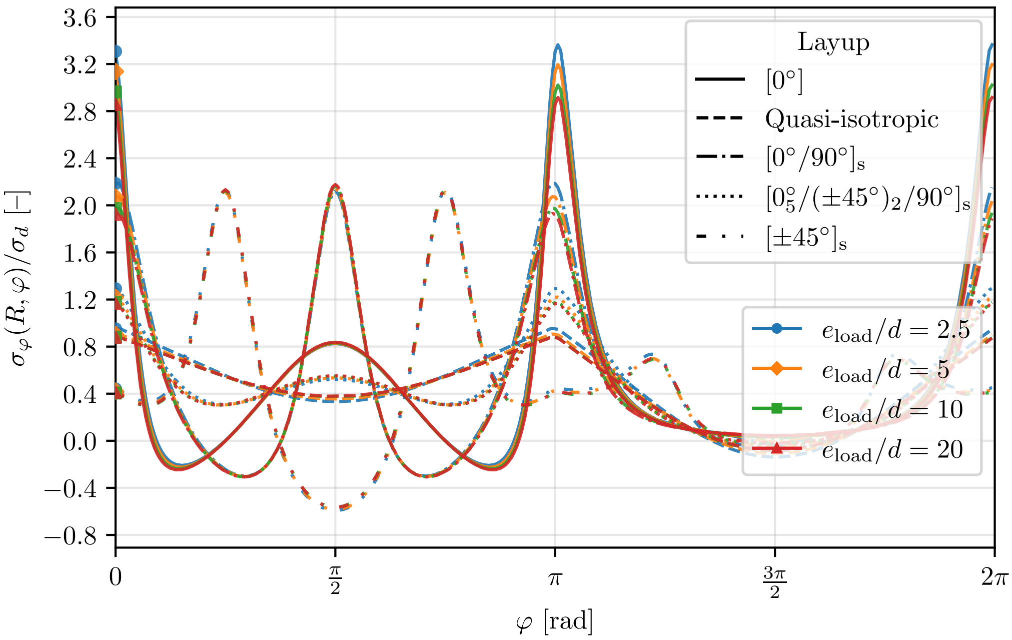

(d) $w/d = 20$.

Figure A.8: Filled hole circumferential stresses for each laminate at different e_{load}/d values, with $w/d = \{5, 10, 20\}$ and $e/d = 20$.

A.2 Infinite-Domain Filled Hole Solutions

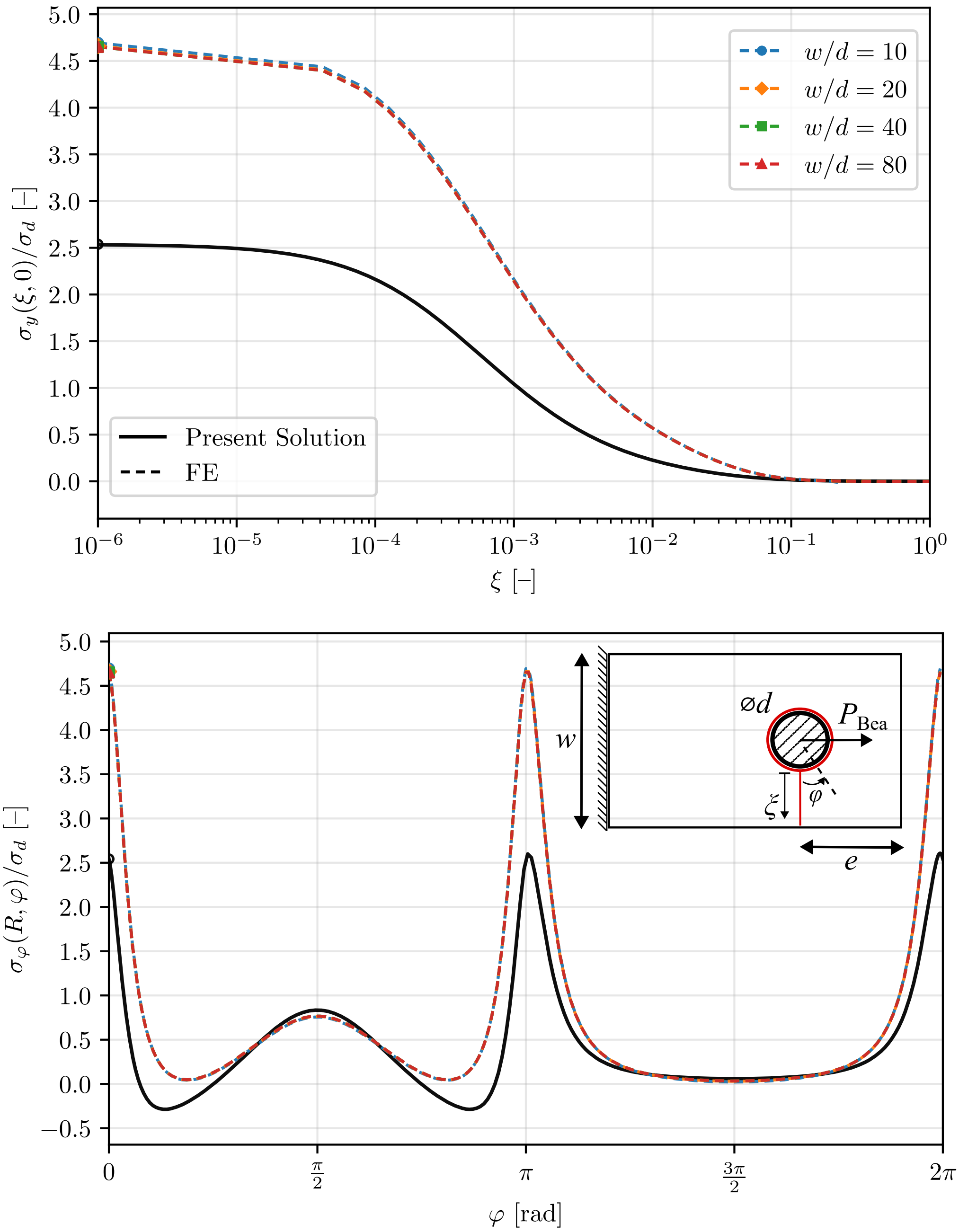

Figure A.9: Filled hole infinite plate, comparison between analytical and FE solutions for the [0°] laminate, for $w/d = \{10, 20, 40, 80\}$ and $e/d = 2.5$. The upper plot shows the normalised net-section stresses, while the lower plot shows the normalised circumferential stresses.

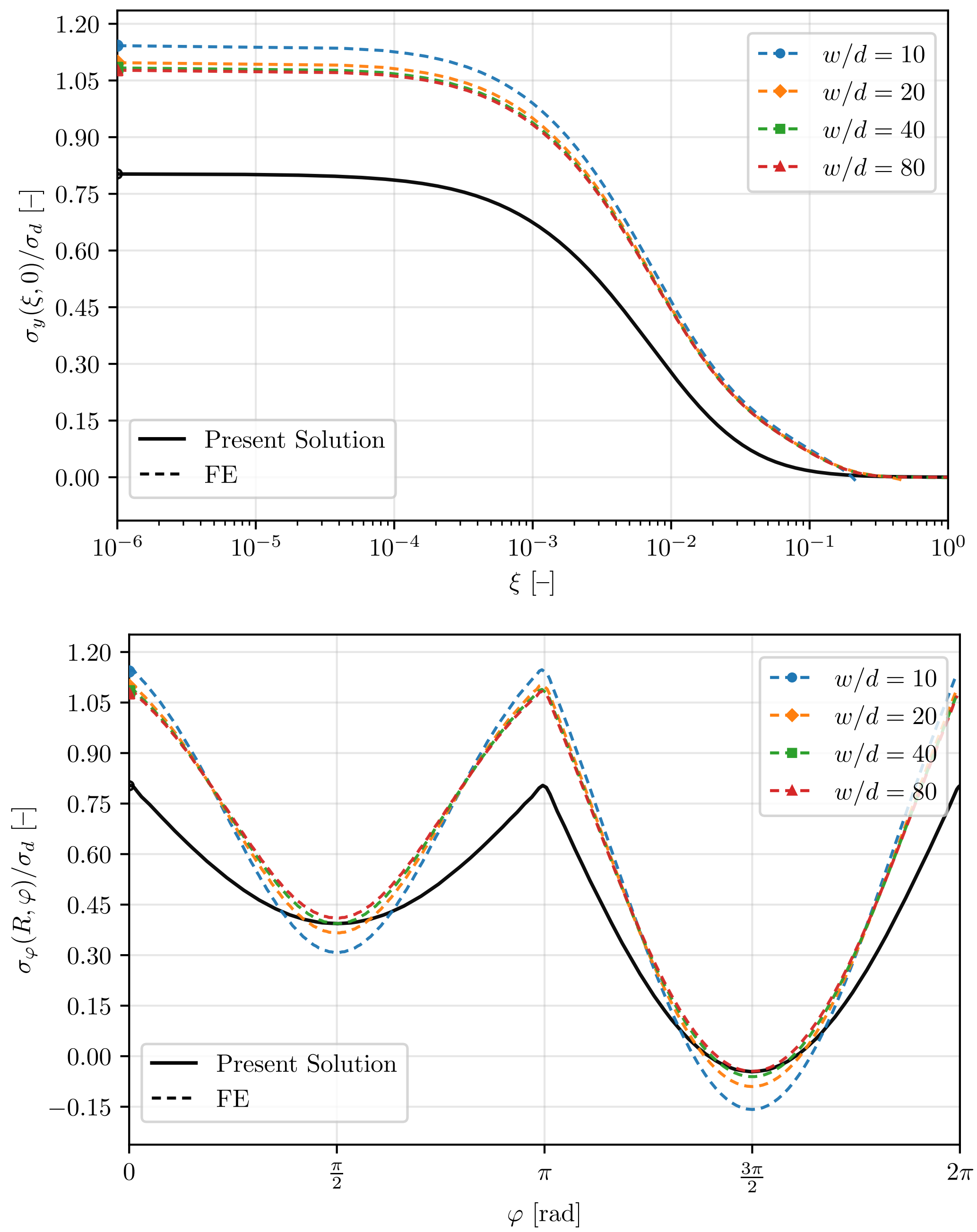

Figure A.10: Filled hole infinite plate, comparison between analytical and FE solutions for the quasi-isotropic $[0^\circ_5\,/\,(\pm 45^\circ)_2\,/\,90^\circ]_\mathrm{s}$ laminate, for $w/d = \{10, 20, 40, 80\}$ and $e/d = 2.5$. The upper plot shows the normalised net-section stresses, while the lower plot shows the normalised circumferential stresses.

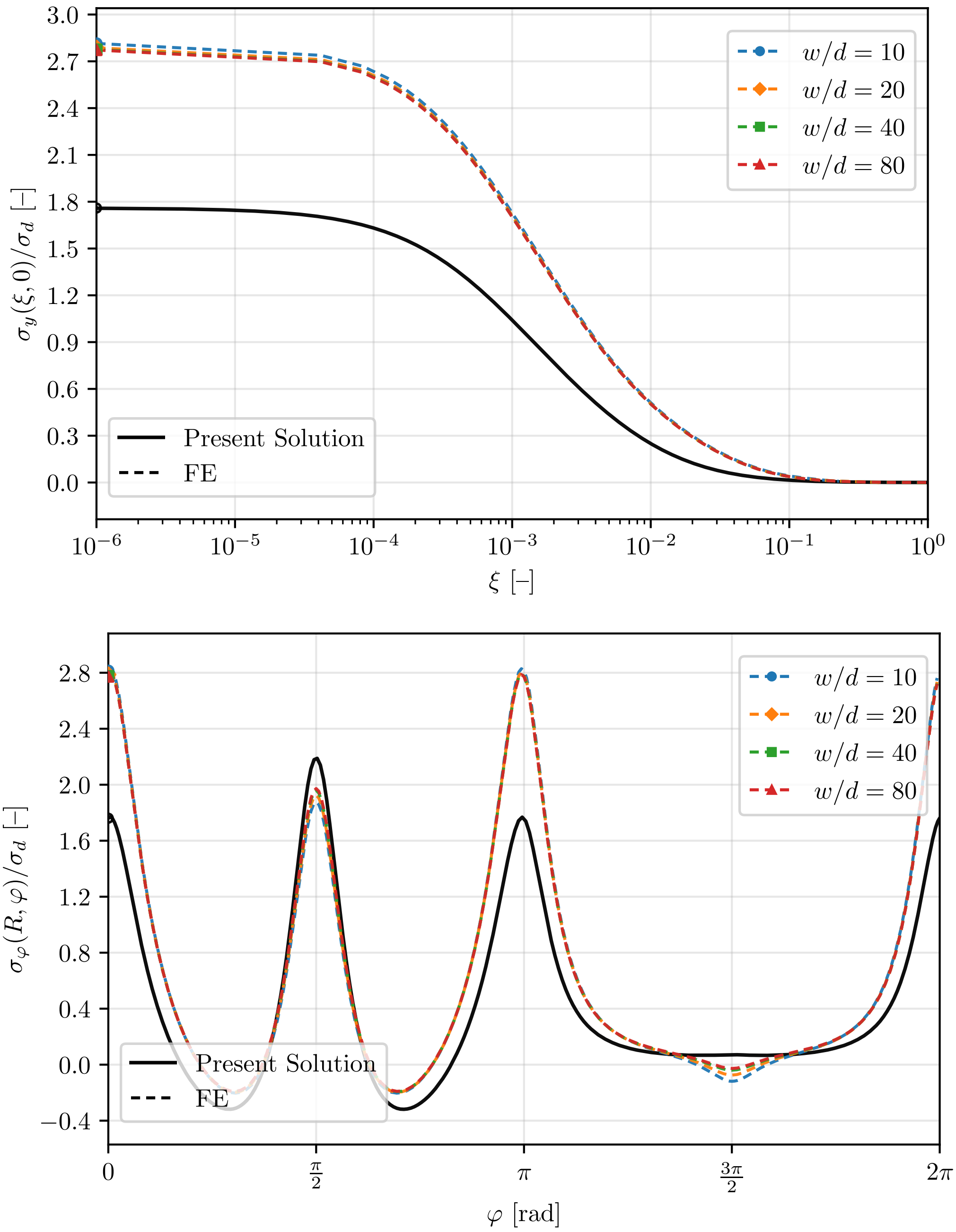

Figure A.11: Filled hole infinite plate, comparison between analytical and FE solutions for the $[0°/90°]_s$ laminate, for $w/d = \{10, 20, 40, 80\}$ and $e/d = 2.5$. The upper plot shows the normalised net-section stresses, while the lower plot shows the normalised circumferential stresses.

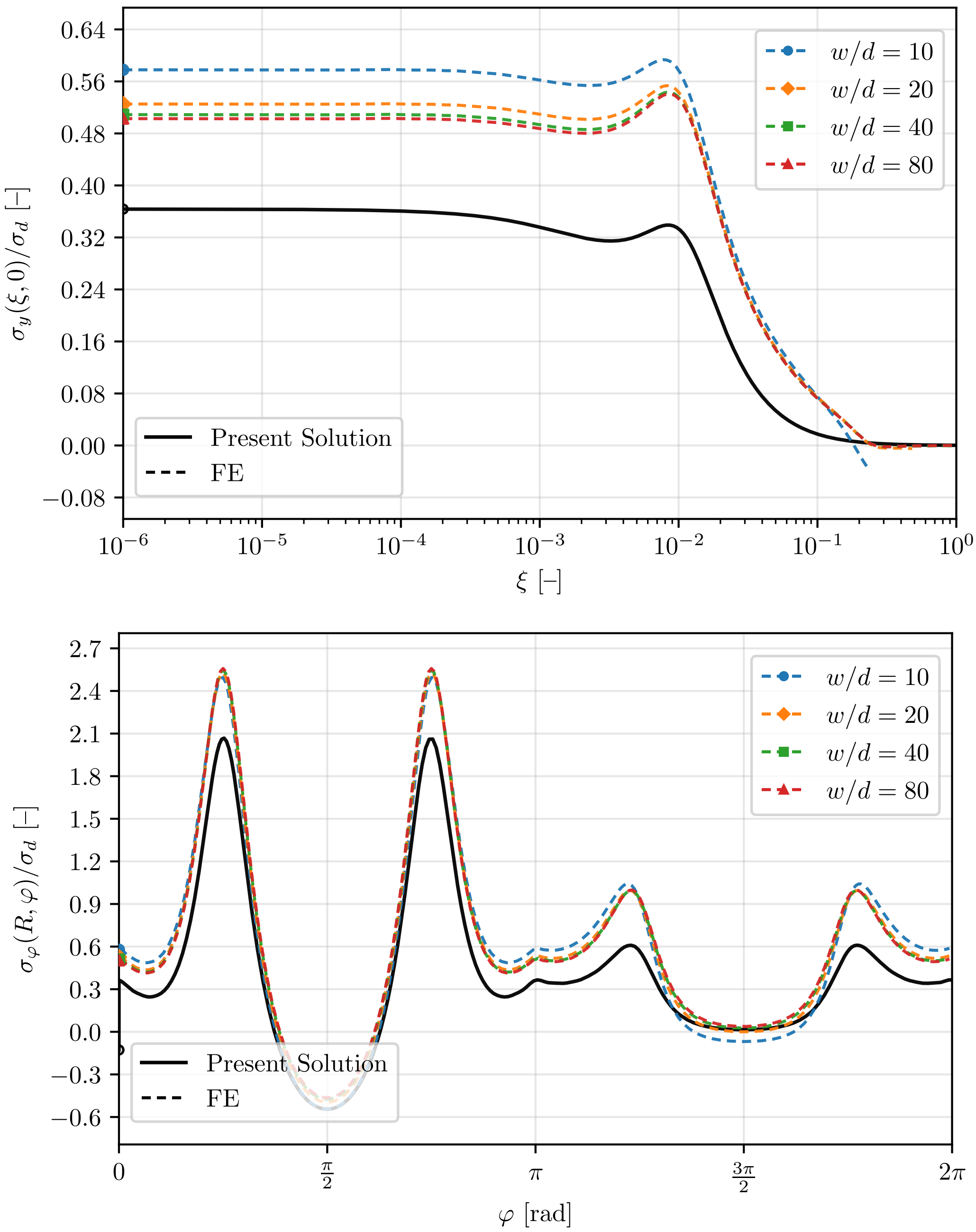

Figure A.12: Filled hole infinite plate, comparison between analytical and FE solutions for the $[\pm 45°]_s$ laminate, for $w/d = \{10, 20, 40, 80\}$ and $e/d = 2.5$. The upper plot shows the normalised net-section stresses, while the lower plot shows the normalised circumferential stresses.

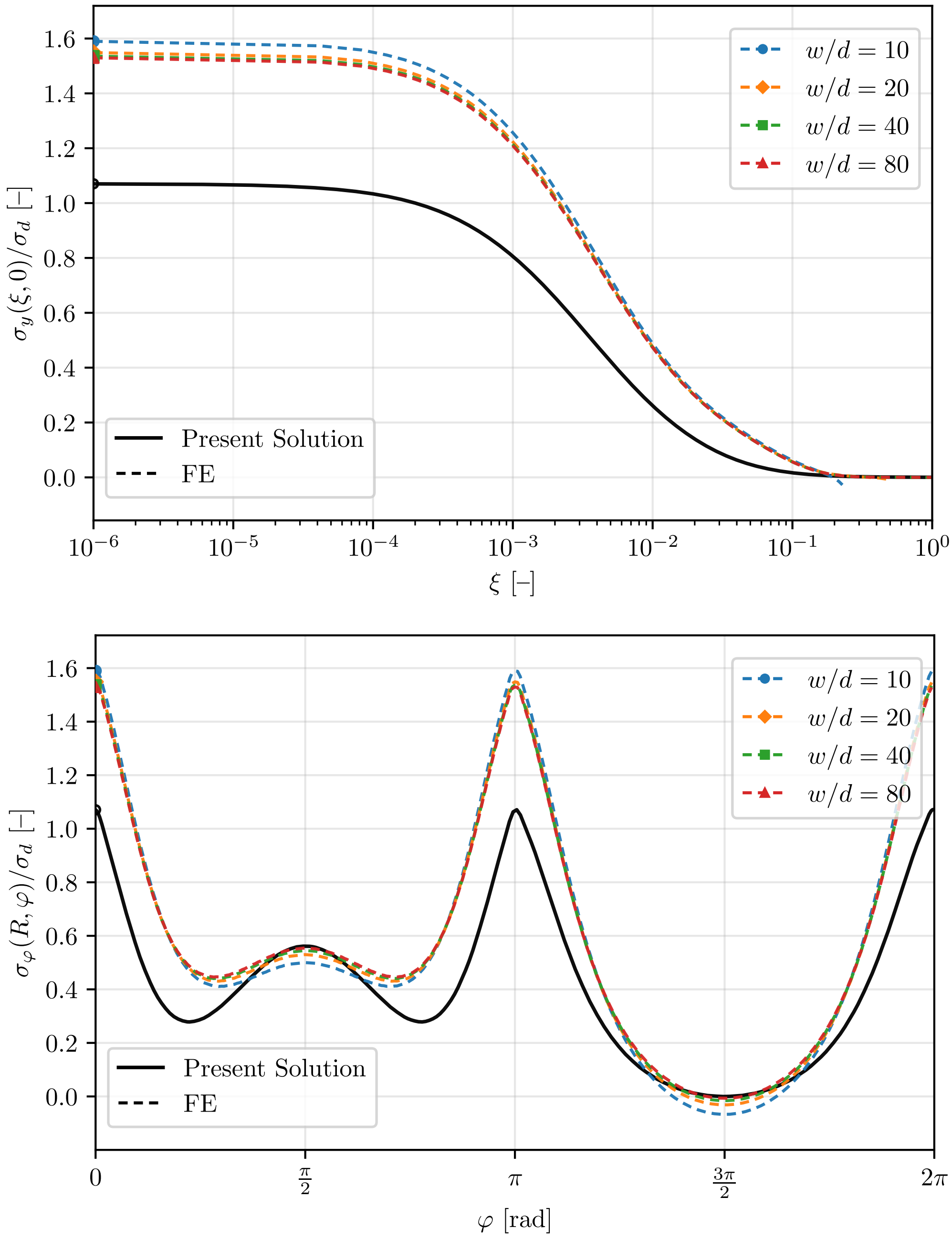

Figure A.13: Filled hole infinite plate, comparison between analytical and FE solutions for the $[0^\circ_5\,/\,(\pm 45^\circ)_2\,/\,90^\circ]_\mathrm{s}$ laminate, for $w/d = \{10, 20, 40, 80\}$ and $e/d = 2.5$. The upper plot shows the normalised net-section stresses, while the lower plot shows the normalised circumferential stresses.

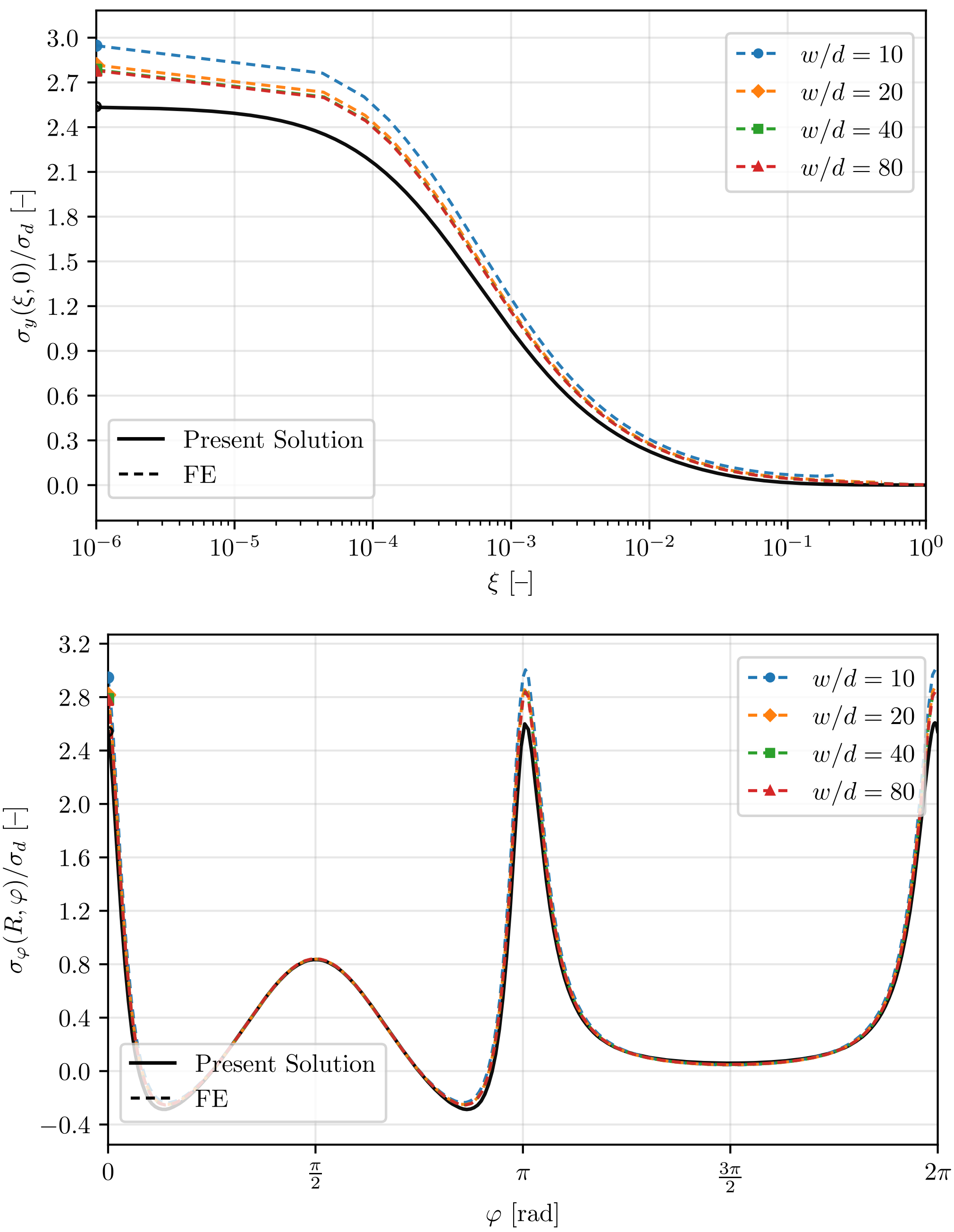

Figure A.14: Filled hole infinite plate, comparison between analytical and FE solutions for the $[0°]$ laminate, for $w/d = \{10, 20, 40, 80\}$ and $e/d = 20$. The upper plot shows the normalised net-section stresses, while the lower plot shows the normalised circumferential stresses.

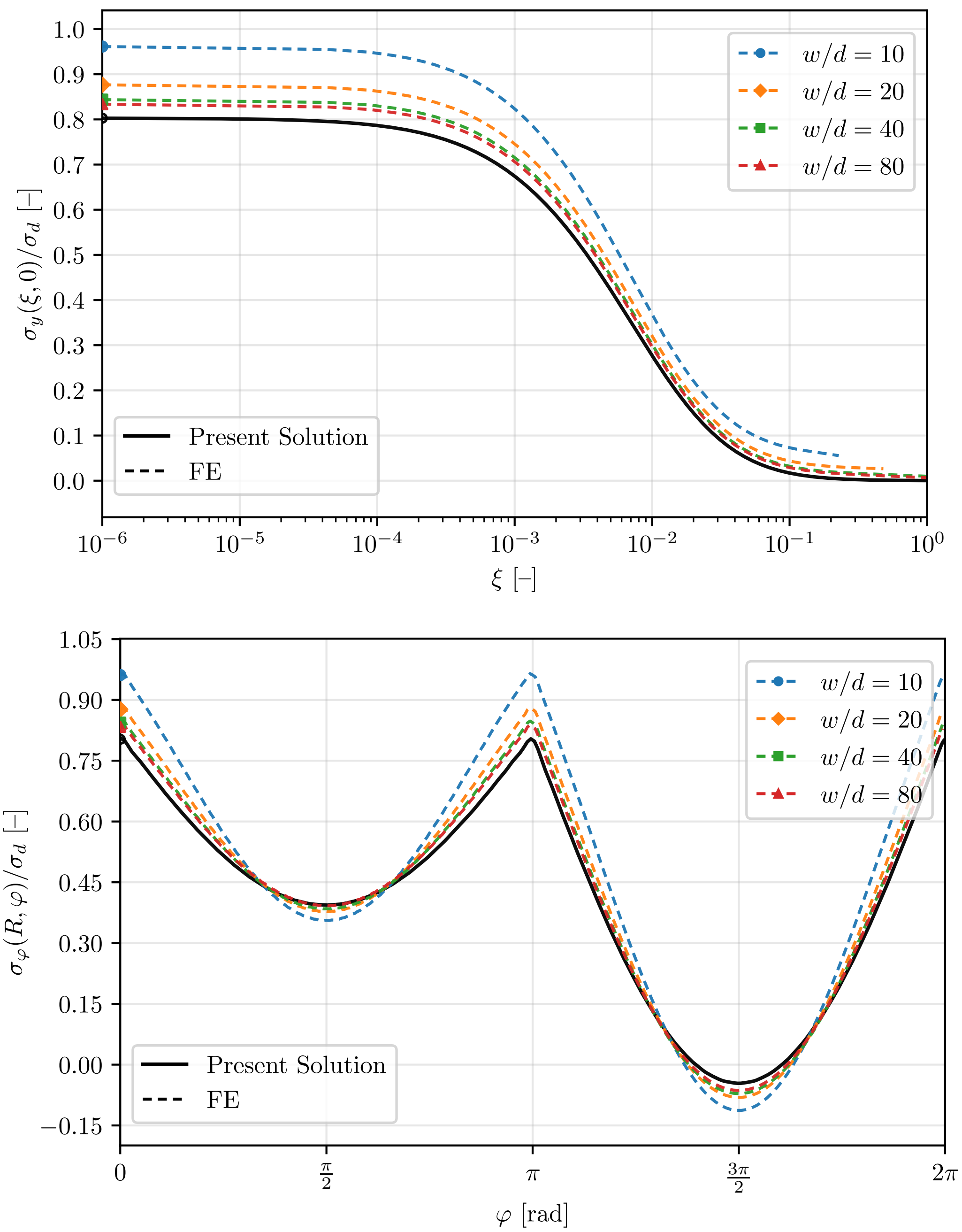

Figure A.15: Filled hole infinite plate, comparison between analytical and FE solutions for the $[0^\circ_5\,/\,(\pm 45^\circ)_2\,/\,90^\circ]_\mathrm{s}$ laminate, for $w/d = \{10, 20, 40, 80\}$ and $e/d = 20$. The upper plot shows the normalised net-section stresses, while the lower plot shows the normalised circumferential stresses.

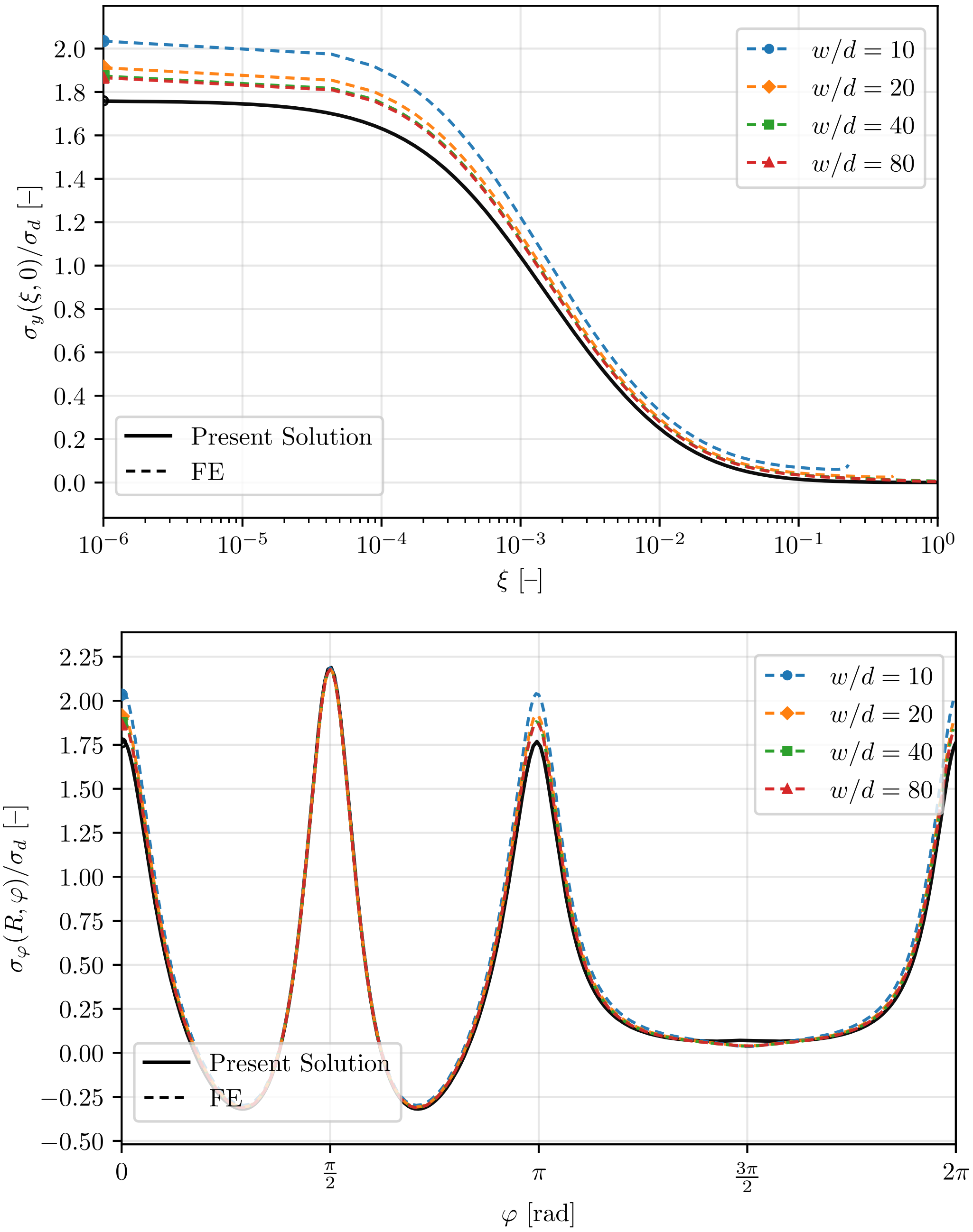

Figure A.16: Filled hole infinite plate, comparison between analytical and FE solutions for the $[0°/90°]_s$ laminate, for $w/d = \{10, 20, 40, 80\}$ and $e/d = 20$. The upper plot shows the normalised net-section stresses, while the lower plot shows the normalised circumferential stresses.

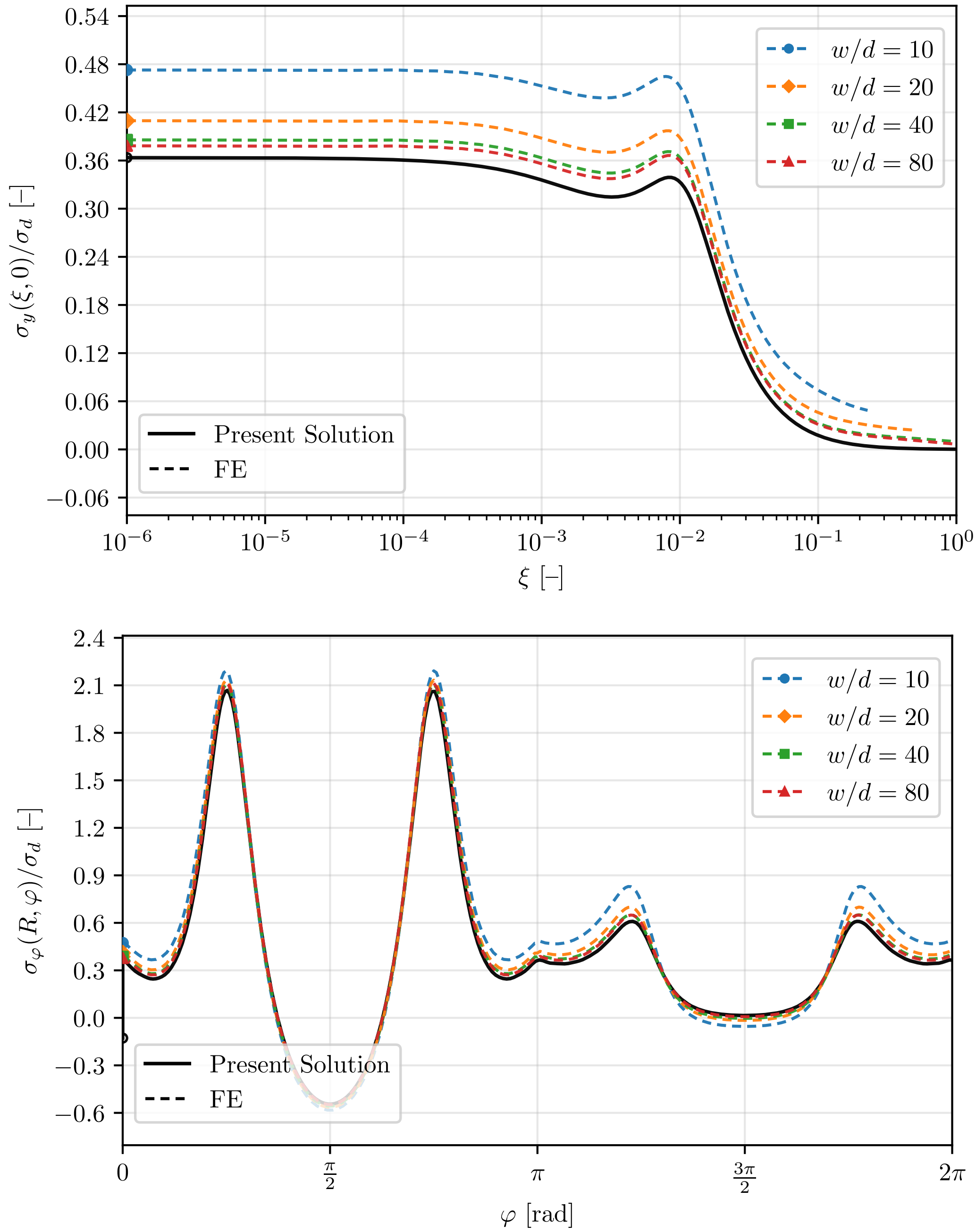

Figure A.17: Filled hole infinite plate, comparison between analytical and FE solutions for the $[\pm 45°]_s$ laminate, for $w/d = \{10, 20, 40, 80\}$ and $e/d = 20$. The upper plot shows the normalised net-section stresses, while the lower plot shows the normalised circumferential stresses.

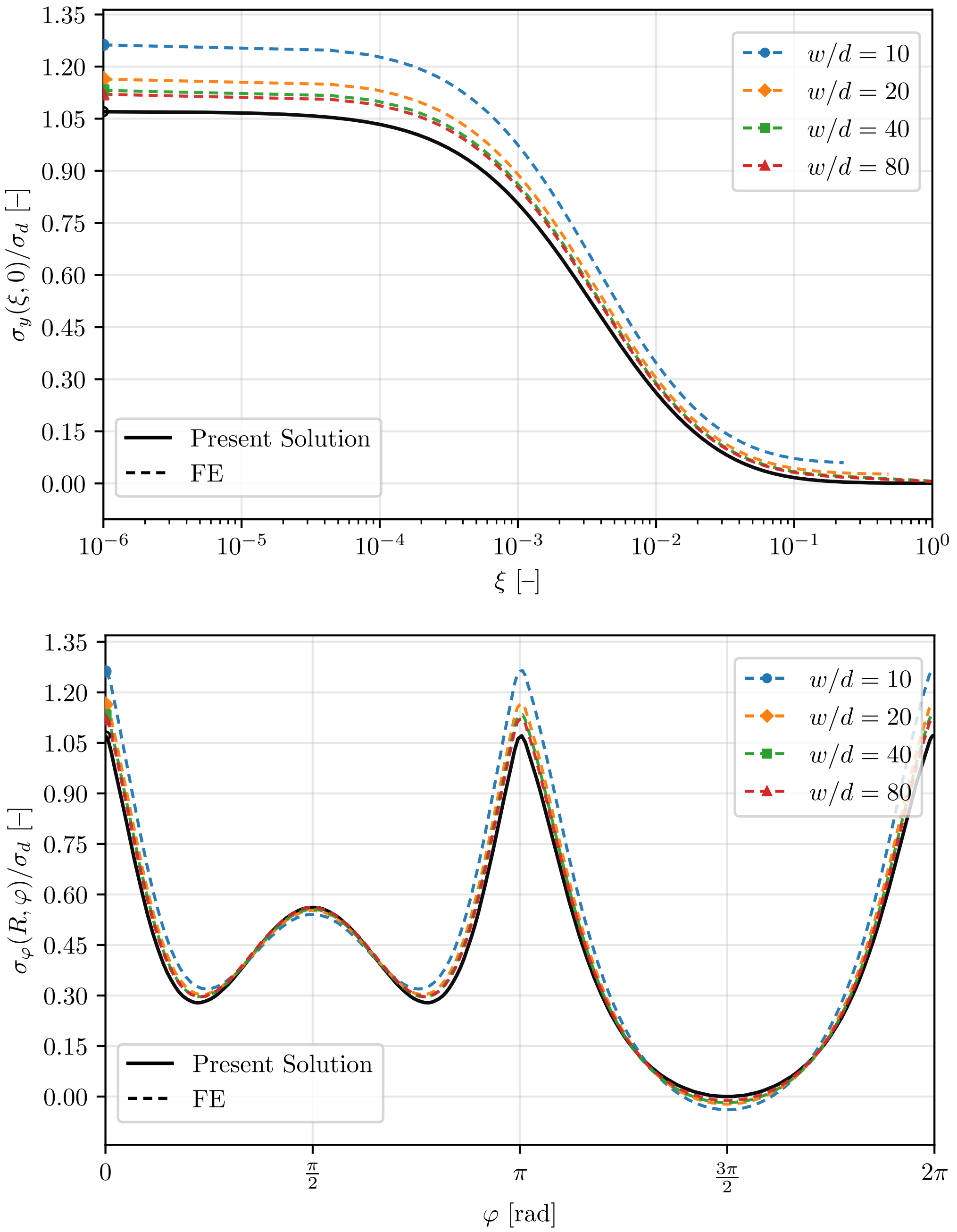

Figure A.18: Filled hole infinite plate, comparison between analytical and FE solutions for the $[0^\circ_5\,/\,(\pm45^\circ)_2\,/\,90^\circ]_s$ laminate, for $w/d = \{10, 20, 40, 80\}$ and $e/d = 20$. The upper plot shows the normalised net-section stresses, while the lower plot shows the normalised circumferential stresses.